ULTRAVIOLET SPECTROSCOPY AND REMOTE SENSING OF THE UPPER ATMOSPHERE

R. R. MEIER

E. O. Hulburt Center for Space Research, Naval Research Laboratory, Washington, DC 20375, U.S.A.

Abstract. The Earth's ultraviolet airglow contains fundamental diagnostic information about the state of its upper atmosphere and ionosphere. Our understanding of the excitation and emission processes which are responsible for the airglow has undergone dramatic evolution from the earliest days of space research through the past several years during which a wealth of new information has been published from high-resolution spectroscopy and imaging experiments. This review of the field begins with an overview of the phenomenology: how the Earth looks in the ultraviolet. Next the basic processes leading to excitation of atomic and molecular energy states are discussed. These concepts are developed from first principles and applied to selected examples of day and night airglow; a detailed review of radiation transport theory is included. This is followed by a comprehensive examination of the current status of knowledge of individual emission features seen in the airglow, in which atomic physics issues as well as relevant atmospheric observations of major and minor neutral and ionic constituents are addressed. The use of airglow features as remote sensing observables is then examined for the purpose of selecting those species most useful as diagnostics of the state of the thermosphere and ionosphere. Imaging of the plasmasphere and magnetosphere is also briefly considered. A summary of upcoming UV remote sensing missions is provided.

Table of Contents

Space Science Reviews **58:** 1–185, 1991.

1. Introduction

In 1955, far ultraviolet (FUV) remote sensing of the upper atmosphere began with the discovery of atomic hydrogen Lα radiation in the night sky using a sounding rocket payload (Byram *et al.*, 1957; Kupperian *et al.*, 1959). It was actually six years earlier that the era of exploration of the upper atmosphere from space had been born when Friedman *et al.* (1951) determined molecular oxygen concentrations above 70 km by measuring the absorption of solar ultraviolet radiation with a rocket experiment. In the intervening years, ultraviolet instrumentation has been included in the payloads of many spaceflight missions to measure the components of the Earth's upper atmosphere as well as those of the planets, comets, and the interplanetary medium. Many important discoveries of the composition, energetic and dynamics of the thermosphere and ionosphere have been made using UV observations.

The Sun is ultimately the dominant source of energy for the terrestrial atmosphere. Absorption of solar radiation in the upper atmosphere results in excitation, dissociation, and ionization. Fluorescence usually follows excitation. Ionization and dissociation can also lead to fluorescence from excited fragment species, from chemical reactions, or from collisional excitation by energetic photoelectrons. Fluorescence in the upper atmosphere is commonly known as airglow. When the atmosphere is sunlit, the day airglow (or dayglow) spectrum contains signatures of the composition of the thermosphere and ionosphere, and their responses to external energy inputs. In the absence of sunlight, energy stored in dissociation or ionization products is released through recombination or photochemical reactions, and generates the night airglow (nightglow).

Resonance fluorescence involves excitation of electronic transitions between the ground state and excited states of an atom or molecule, so that the emission rate is proportional to the concentration of the species in question. Resonance emission lines of the atomic and molecular components of the thermosphere (N_2, O_2, O, O^+, and minor species) are mostly in the ultraviolet region of the airglow spectrum (defined here as wavelengths between 4000 Å and about 100 Å). Consequently, remote sensing of that spectral regime offers an attractive approach to measuring the composition of the upper atmosphere. Background radiation is minimal because pure absorption in and below the thermosphere prevents both scattering from the Earth's surface of radiation below 3000 Å and Rayleigh scattering below 2000 Å. This is especially advantageous for observing minor species whose concentrations may be too low to be measured by other techniques, but which may have an emission feature observable above the background. For low altitude spacecraft, remote sensing can provide altitude distributions of atmospheric species on a fairly localized scale. For high altitude spacecraft, remote sensing is the only practical way to observe the upper atmospheric environment on a truly global scale. It provides an approach for routine monitoring of thermospheric and ionospheric 'weather'.

There are three pre-requisites for obtaining quantitative information about the atmospheric composition from remote sensing observations. Firstly, the excitation source for each emission line must be specified; secondly, the atomic physics of the process must be known accurately; and thirdly, numerical algorithms must be devised in order to extract local compositional information from line-of-sight observations. It has taken a long time to develop and validate the required analysis techniques. Consequently, modern thermospheric general circulation models (TGCM) (e.g., see Roble *et al.*, 1987 or Rees and Fuller-Rowell, 1988) and empirical models (e.g., see Hedin, 1987; Jacchia, 1977) of the thermospheric composition have thus far relied most heavily on mass spectrometer observations, incoherent radar backscatter and satellite drag determinations of concentration and temperature, rather than from the products of remote sensing.

During the past decade, substantial progress has been made on virtually all fronts of UV remote sensing. New high reliability models of the airglow have evolved, advances have been made in radiative transport theory, critical measurements of excitation cross

sections and transition probabilities have been made in the laboratory, new inversion techniques are now available for obtaining local concentration information, and state of the art instrumentation for high-resolution spatial and spectral imaging has been constructed. The field has matured significantly.

In the future, ultraviolet remote sensing may be expected to play a prominent role in global studies of thermospheric and ionospheric weather. Spectacular data sets have already been acquired, especially in the area of global imaging, and new analysis models are being applied to these data. Experiments planned for the future offer the possibility of routine UV monitoring of the upper atmosphere.

This review is intended to provide a comprehensive overview of the ultraviolet airglow and recent theoretical and experimental developments in UV remote sensing. It is not historical in scope; there is simply too much material to include. But it is more than a progress report. Basic principles, figures and tables of emission rates, and atomic and molecular spectroscopic data are included so that the review will be useful to the expert as well as the casual reader. Summaries of thermospheric airglow research since the early 1980's have been published by Vallance Jones *et al.* (1985) and Meier (1987a). Section 2 of this review contains observations selected to illustrate the salient spectral and spatial properties of the airglow. Section 3 covers the excitation and emission processes, including derivation of the relationships between airglow emission rates and composition. Radiation transport and opacity effects are discussed in some detail. The current level of understanding of individual emission features in the ultraviolet spectrum is reviewed critically in Section 4. The merits and disadvantages of each emission feature as a diagnostic of the emitting species are considered. Section 5 provides a limited description of expected emission rate variations over a range of conditions encountered by idealized observing systems. Monochromatic global images of the UV airglow are presented. Prospects for planned observing systems are considered in Section 6, followed by concluding remarks.

The definitions of various spectral bands used in this paper are: near ultraviolet (NUV): 4000–3000 Å; middle ultraviolet (MUV): 3000–2000 Å; far ultraviolet (FUV): 2000–1000 Å; extreme ultraviolet (EUV): 1000–100 Å. (Also see Figure 3 for band identifications.) The boundaries of the bands are not always defined the same way by all researchers, but these are commonly in use. Also there are technological reasons why these are convenient boundaries because they identify rough intervals in which various detectors, filters, and windows begin or end their sensitivity or transmissivity.

2. The Ultraviolet Earth

The intent of this section is to provide an overview of observations of the spectral composition of the UV airglow, its global morphology, and its temporal variability. Salient features of the ultraviolet spectra of both the Sun and the terrestrial dayglow are briefly described, followed by a more detailed examination of the spectral content of the various UV bands. A similar account of the UV nightglow is then given. Global variations of brightness levels of prominent emission features are presented using

selected low-altitude satellite observations. Finally, images of the UV airglow made from high-altitude vantage illustrate the global perspective.

2.1. The Sun and the Dayglow

The upper panel in Figure 1 shows the solar ultraviolet spectral irradiance for conditions of low solar activity. This spectrum is a combination mainly of two data sets. The portion of the spectrum from 18 to 1100 Å is taken from the quiet-Sun reference spectrum of Hinteregger *et al.* (1981) (available from the National Space Science Data Center as SC No. 21REF, date of issue: 9 April, 1981), which was measured from the Atmospheric Explorer *AE–E* satellite data near the minimum level of activity between solar cycles 20 and 21 (July 1976) normalized to a rocket measurement in 1974. The assignment of absolute value to the *AE–E* spectrum is discussed by Hinteregger *et al.* (1981). At wavelengths longer than 1207 Å, the irradiance is from the Solar Ultraviolet Spectral Irradiance Monitor (SUSIM) on Spacelab 2, which flew in July/August, 1985 also near the minimum of solar activity (Brueckner and Van Hoosier, 1990). In the wavelength interval between the C I (neutral carbon) continuum edge at 1100 Å and the merger with the SUSIM data at 1207 Å, the SC No. 21REF tabulation contains only a few strong emission features, whereas the actual solar irradiance consists of quite weak C I, C III, and other lines (Cohen *et al.*, 1978). To account for these poorly-measured lines, the compilation of Donnelly and Pope (1973) in 10 Å bands (also listed in Timothy, 1977) was included in Figure 1(a) as a pseudo-continuum, with the bright emission lines from the SC No. 21REF spectrum superimposed.

Thus the spectrum in Figure 1 is representative of the solar radiation output at solar min. The variability from the minimum to maximum of the solar activity cycle is less than 1% at wavelengths longer than 3000 Å, but increases with decreasing wavelength. At the short wavelength end of the FUV band, the min to max irradiance ratio approaches a factor of two; at EUV wavelengths the ratio is as much as an order of magnitude for some coronal emission lines. This variability is displayed in the lower panels of Figure 1 taken from Lean (1987). Additionally, there is a rotation modulation superimposed on the 11 year solar cycle variation. For detailed information on the solar cycle variability, rotation modulation and other periodicities, as well as their relationships to solar parameters monitored from the ground (such as radio wavelength emissions, the plage index and sunspots) the reader is referred to the book edited by White (1987), and the reviews by Lean (1988) and Lean (1987) which discuss the EUV and FUV, respectively.

The opacity of the atmosphere is a strong function of wavelength in the UV. Figure 2, taken from Lean (1987) (adapted from Chamberlain, 1978), shows the altitude at which solar radiation, vertically incident at the top of the atmosphere, is reduced by a factor of e^{-1}. Solar radiation at wavelengths longer than about 3000 Å can reach the surface. In the MUV, sunlight is attenuated by strong ozone absorption, primarily in the stratosphere. In the FUV, O_2-band and continuum absorption stop solar radiation in the mesosphere and lower thermosphere. In the EUV, all of the major atmospheric species absorb sunlight, producing the ionosphere and heating the thermosphere. Ionization thresholds for some atmospheric gases are indicated in Figure 2.

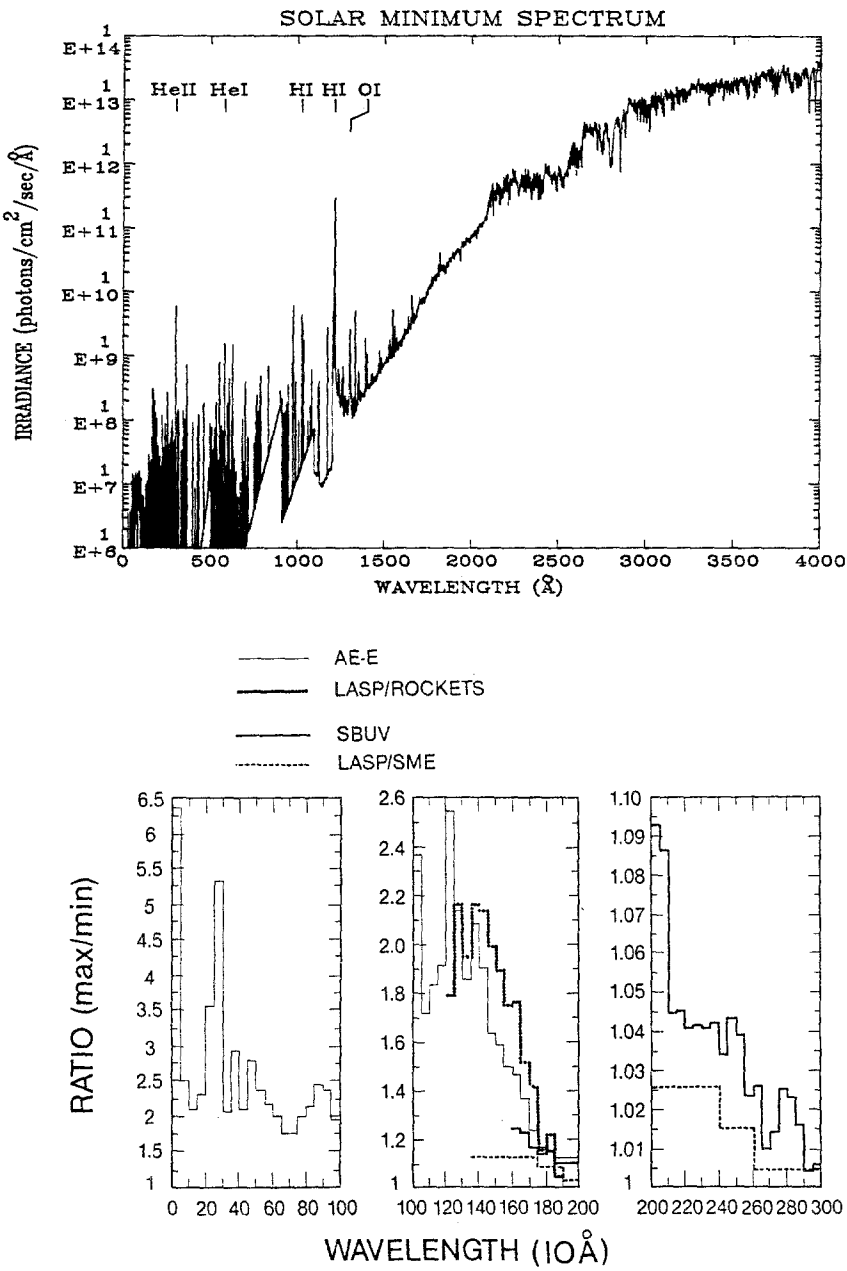

Fig. 1. *Upper panel*: Composite solar spectral irradiance for solar minimum conditions. SUSIM data at 1.5 Å resolution (Brueckner and VanHoosier, 1991) are used from 1207 to 4000 Å. These data were obtained during the Spacelab 2 mission in July, 1985. From 18 to 1100 Å, the Hinteregger *et al.* (1981) quiet-Sun reference spectrum (SC No. 21REF) appropriate to July 1976 is used after binning into 1 Å intervals. The Donnelly and Pope (1973) representation of weak lines, superimposed on strong lines from the SC No. 21REF tabulation is used to fill the gap between 1100 and 1207 Å (see text). *Lower panel*: Ratio of maximum to minimum solar irradiances during solar cycle 21. *AE – E* is from Hinteregger *et al.* (1981) and Torr and Torr (1985); LASP/ROCKETS is from Mount and Rottman (1983, and references); SBUV is from Heath and Schlesinger (1984); LASP/SME is from Rottman (1985a, b, and references). More recent analyses indicate that the SME curve underestimates the solar variability and the ROCKETS curve overestimates the variability (J. Lean, private communication, 1990). Figure taken from Lean (1988).

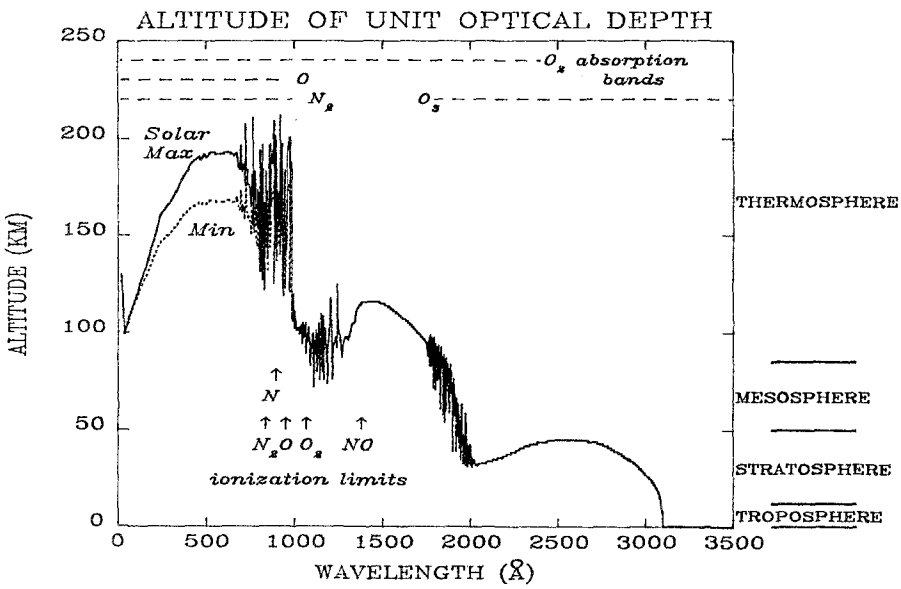

Fig. 2. Altitude at which vertically incident UV radiation is attenuated by e^{-1}. Dashed lines at top identify spectral regions where extinction by the indicated species is significant. Arrows give the ionization thresholds of important atmospheric species. Atmospheric regions are given on the right. Altitudes for solar max and min were obtained using the MSIS-86 model (see Section 3.2.1.1) above 90 km; below 90 km, the US standard atmosphere was used. Absorption cross sections were taken from Conway (1988) for N_2, O_2, O in EUV, from Watanabe (1958), Blake *et al.* (1986), Yoshino *et al.* (1983), and Nicolet and Kennes (1988b) for O_2 in the FUV and MUV, and from Molina and Molina (1986) for O_3. Earlier versions of these curves appeared in Lean (1987) and Chamberlain (1978).

The terrestrial UV radiance is more difficult to display since no simultaneous measurements of all the bands exist. A representative spectrum shown in Figure 3 was compiled from several sources. The EUV portion of the spectrum was taken from the rocket data of Gentieu *et al.* (1979), the FUV from the S3-4 satellite observations of Huffman *et al.* (1980), the MUV, the rocket data of Barth (1965), and the NUV was calculated assuming the ground to be a Lambertian surface with an albedo of 0.3. The various spectra were adjusted to vertical viewing downward from 200 km with the Sun approximately overhead. Since the data were taken under widely differing conditions, the accuracy of the combined spectrum is not expected to be high, but is unlikely to be worse than a factor of two in representing moderate solar activity conditions. The observing details for each of the airglow observations used in this paper, as well as of the solar spectra, are provided in Table I.

The composite spectral radiance shown in Figure 3 is in the form of the 'apparent' column emission rate in units of Rayleighs per 10 Å. While the photometric unit Rayleigh applies to an omnidirectional emission rate in an optically thin column, it is commonly used as a measure of radiance in the following way: if I is the radiance in megaphoton $cm^{-2}\ s^{-1}\ ster^{-1}$, $4\pi I$ is the equivalent radiance expressed in Rayleighs.

The physical processes responsible for producing the Earth's UV spectral radiance

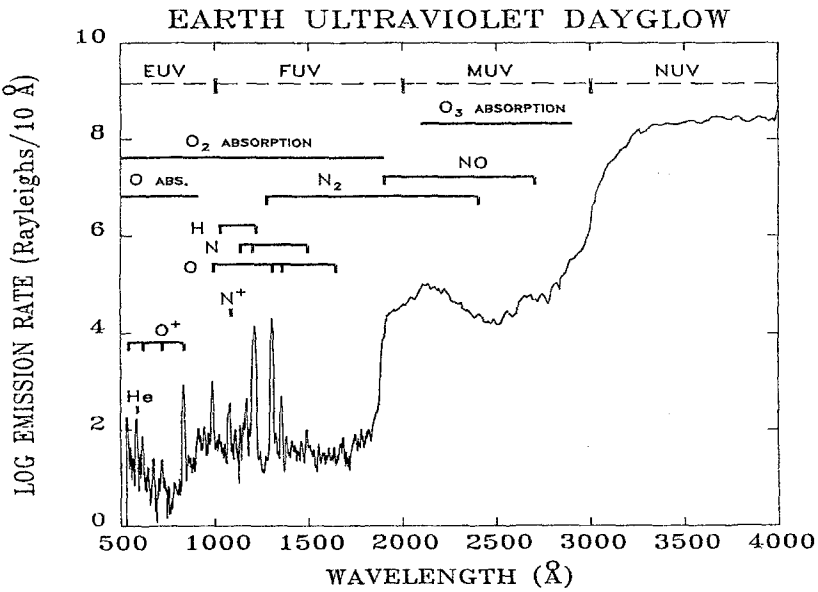

Fig. 3. Complete Earth dayglow spectrum, adjusted to nadir viewing from 200 km at midmorning. The various spectral bands defined at the top of the figure are the extreme, far, middle, and near-ultraviolet. Regions of absorption by oxygen species are indicated by thick horizontal lines; emission band intervals are shown for N_2 and NO, and the stronger emission lines of atomic and ionic species are shown. The NUV emission rate was calculated assuming an Earth albedo of 0.3 and a smoothed solar irradiance, the MUV was taken from Barth (1965), the FUV from Huffman *et al.* (1980), and the EUV from Gentieu *et al.* (1979).

during the day reflect widely diverse phenomena. The radiation sources range from low altitude Rayleigh and surface scattering at the longer wavelengths, through molecular and atomic emissions from solar fluorescence and photoelectron impact, to the more energetic emissions produced through ionization-excitation at the shortest wavelengths. In the NUV, the actual spectrum is dominated by surface and cloud reflection, and Rayleigh and aerosol scattering of sunlight. The calculated (NUV only) spectrum shown in Figure 3 includes surface reflection and Rayleigh scattering only. The large decrease in the radiance from 2500 to 3000 Å is a convolution of decreasing sunlight and strongly increasing O_3 absorption. Little solar radiation below 3000 Å reaches the ground. The MUV radiance is mostly due to Rayleigh scattering by the atmosphere above the stratosphere (see Figure 2). Although N_2 and NO molecular emissions from the thermosphere and mesosphere (above 90 km) are present in the MUV, they cannot be seen above the much brighter Rayleigh scattering in Figure 3. The molecular emissions are, however, observable above the Earth limb and at twilight since Rayleigh scattering is much weaker there. The O_3 absorption cross section is largest near 2550 Å and decreases with decreasing wavelength below that peak (e.g., Molina and Molina, 1986, and Figure 2). As a result, there is some recovery in the radiance from 2500 to 2100 Å. Measurement of this differential absorption is a standard technique for monitoring the column concentration of ozone. Below 2000 Å, absorption in the Schumann–Runge

Spectrum	Mission	Date	$F_{10.7}$ (1 AU)	A_p	Solar zenith angle (deg)	Observation zenith angle (deg)	Altitude (km)	References
				Solar				
FUV, MUV	Spacelab 2	4 Aug., 1985	79	–	–	–	–	Brueckner and Van Hoosier (1991)
EUV (SC No. 21 REF)	AE-E	13–28 July, 1976	~68	–	–	–	–	Hinteregger *et al.* (1981)
				Earth/Spectroscopy				
MUV	Rocket	13 June, 1969	229	15	10	180	168	Barth (1988, private communication)
FUV	S3–4	9 Apr., 1978	156	6	25	180	200	Conway *et al.* (1988) Huffman *et al.* (1980)
FUV, EUV	Rocket	9 Jan., 1978	106	23	56	40, 90, 180	100–265	Gentieu *et al.* (1979) Meier *et al.* (1980)
FUV, EUV	Rocket	27 June, 1980	219	3	9	90–98	140–260	Eastes *et al.* (1985) Gentieu *et al.* (1981, 1984)
EUV	STP 78–1	5–15 Mar., 1979	~185	~12	0–180	120–150	600	Chakrabarti *et al.* (1983) Chakrabarti *et al.* (1984)
NUV, MUV	Rocket	30 Nov., 1965	71	11	170	90	184	Hennes (1966)
MUV	Rocket	2 Nov., 1978	159	10	104	90	115–150	Sharp and Rusch (1981)
				Earth/Photometry				
FUV	OGO-4	Aug. 1967–Jan. 1969	–	–	0–180	180	400–900	Meier and Mange (1970, 1973) Meier and Prinz (1971) Prinz and Meier (1971)
EUV	STP 72–1	Oct. 1972–Jan. 1974	–	–	0–180	25–155	740	Weller and Meier (1974) Meier and Weller (1974, 1975) Anderson *et al.* (1976)
				Earth/Imaging				
FUV	Apollo-16	21 Apr., 1972	122	19	105	180	Moon	Carruthers and Page (1976) Carruthers *et al.* (1976)
FUV	DE-1	Aug. 1981–Present	–	–	–	180	570–23000	Franck and Craven (1988)

bands and continuum of O_2 in the mesosphere and lower thermosphere mark the end of significant Rayleigh scattering since solar radiation cannot penetrate to lower altitudes. The radiance in the FUV and EUV is comprised of molecular, atomic, and ionic line emission. Calculations of UV backgrounds, including Rayleigh scattering, have been made by Strickland and Christensen (1988), Strickland *et al.* (1988), and Anderson and Strickland (1988).

The positions of some of the important emission lines and bands, as well as the locations of absorption regions, are identified in Figure 3. These lines and bands contain signatures of the concentrations of major and minor atmospheric species as well as information about the strengths of the excitation mechanisms. The absorption bands can be used to determine the O_2 and O_3 concentrations. The emission rates can vary significantly with geographic location, local time, and solar and geomagnetic activity. These dependences will be explored later in this section and in Section 5.

A quantity of general interest to planetary astronomers is the planetary albedo, defined as the full planetary disk irradiance for a particular Sun-planet-observer phase angle, divided by the incident solar irradiance. An exact calculation would require specification of all emission and scattering processes throughout the atmosphere followed by integration along every line-of-sight in the direction of the chosen phase angle and integration across the solid angle subtended by the projected planetary disk. With a few assumptions, however, the albedo can be readily estimated for the Earth using Figures 1 and 3, without resorting to the much more difficult exact calculation. Assuming a zero-degree phase angle (overhead Sun; approximately correct for Figure 3) and an isotropic radiance (Lambertian surface or optically thick emission), the irradiance is π times the radiance. (See, for example, Appendix 1 of Yung and Goody, 1976). This further assumes a planar atmosphere and surface and, therefore, ignores brightening or darkening of the radiance at the limb. Alternatively, for an optically thin airglow layer, the radiance increases as the cosecant of the angle from the local vertical (for a planar geometry), and the irradiance is 2π times the radiance. The isotropic case chosen for the estimate here is appropriate for scattering in the MUV and NUV. There are also a number of optically thick airglow emission features at shorter wavelengths which exhibit approximate isotropy.

Applying this simplified approach leads to the estimated albedo plotted as a solid line in Figure 4. It was obtained by converting Figure 3 into radiance units, smoothing the solar irradiance in Figure 1 over a 10 Å full width at half maximum (FWHM) triangular response function to be compatible with the airglow, and taking the ratio. The overplotted histogram sums the respective irradiances in 100 Å bins before taking the ratio. In the NUV, the albedo is near 0.3 as expected from the value assumed in Figure 3. The structure simply reflects differences in solar spectral detail between the simplified spectrum used to calculate the surface and Rayleigh scattering in Figure 3 and the SUSIM spectrum. In the MUV, O_3 absorption causes the albedo to drop to very low levels, but with some recovery near 2000 Å, until O_2 absorption produces the deep decrease in the FUV. At even shorter wavelengths, the albedo actually rises again, fluctuates, and at some places substantially exceeds unity. This behavior reflects the

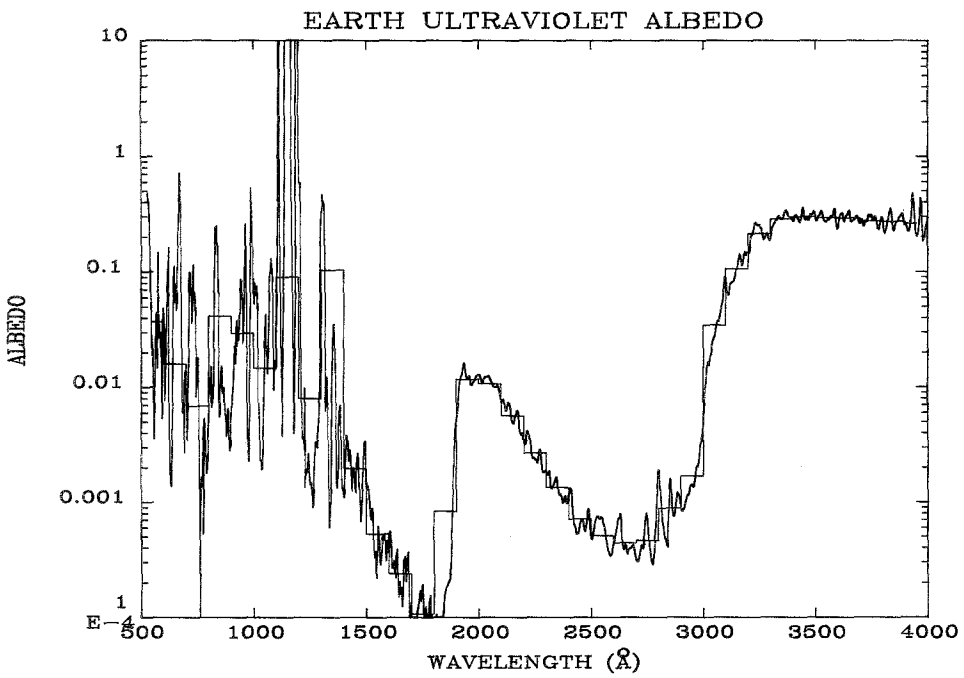

Fig. 4. Earth UV albedo, obtained by dividing the Earth spectrum in Figure 3 (after conversion to irradiance; see text) by the solar spectrum in Figure 1 (after smoothing over a 10 Å FWHM triangular function). The histogram is the albedo obtained by integrating the two irradiances over 100 Å intervals before dividing. The large excursions in the FUV and EUV are due to structure in the spectra. The solar spectral irradiance is especially weak between 1100 and 1240 Å, causing the albedo to rise significantly above unity. Because much of the airglow below 2000 Å results from absorption of sunlight at much shorter wavelengths, the albedo does not have the same meaning as for scattering or reflection processes.

gradual evolution with decreasing wavelength of the solar continuum into line emissions and atomic free-bound continua, with regions of low emission in between. These low-intensity wavelength regions in the solar spectrum can contain strong lines and bands in the airglow spectrum because the excitation of most FUV and EUV atmospheric emissions is by photoelectrons, created originally by sunlight at much shorter wavelengths. Since the albedo is defined as the ratio of Earth-to-solar irradiances at the same wavelength, the albedo in the FUV and EUV is not very meaningful. There is no simple way to calculate an albedo there because solar ionizing radiation ultimately is (partially) converted into a steady-state flux of photoelectrons whose energy function depends on many energy loss processes. (It is for this reason that no attempt was made to adjust the solar and terrestrial spectra to precisely the same activity level.) For general interest, the integrals of the Earth irradiance from 500 to 1000 Å and the solar irradiance from 18 to 1000 Å were computed; the ratio of the two is about 0.02. To reiterate, the albedo plotted in Figure 4 should only be considered representative, since at the longer wavelengths, surface scattering, cloud cover, and O_3 concentrations can vary significantly and at the shorter wavelengths, the albedo is an ill-defined quantity.

The dayglow spectrum in Figure 3 is too condensed to resolve more than the few features indicated. For the purpose of identifying the spectral content in more detail,

examples of observations from each of the UV bands have been chosen for illustration without regard to standardization of observing conditions. These data are considered next. Discussion of the specific physical processes which give rise to the emissions and energy level diagrams which show the atomic and molecular states involved are given in Section 4.

Beginning at longer wavelengths, Figure 5 shows the NUV and MUV dayglow obtained from a rocket flight in which the spectrometer was pointed at 90 deg from the

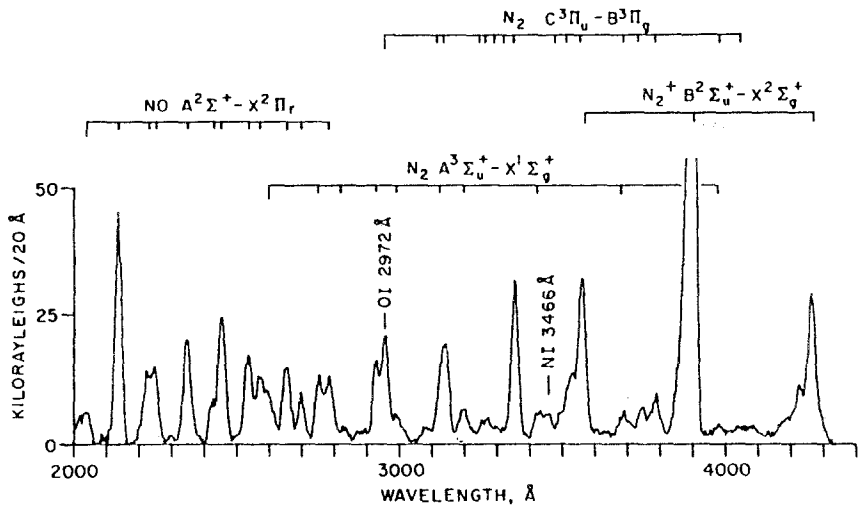

Fig. 5. MUV and NUV dayglow obtained from a rocket experiment launched from White Sands, NM on 13 June, 1969. The payload viewed the airglow horizontally at 150 km, thereby excluding Rayleigh and surface scattering from low altitudes. Prominent molecular and atomic features are identified. The N_2^+ emission at 4278 Å has been truncated. Courtesy of C. Barth. Also see Sharp (1986).

local vertical (C. Barth, private communication, 1988; Sharp, 1986). Since the lower atmosphere was not within the line-of-sight, emissions from the thermosphere are not overwhelmed by the Rayleigh and surface scattering present in the nadir-viewing spectrum of Figure 3. The NUV is dominated by molecular nitrogen emissions. The first negative (1 NG) bands at at 3914 and 4278 Å are produced through resonant scattering of sunlight by N_2^+, and both the second positive (2 PG) $B \rightarrow C$ and Vegard–Kaplan (VK) $A \rightarrow X$ emissions are induced by photoelectron impact excitation of ground state $N_2(X)$. (These states are identified later in the energy level diagram in Figure 39.) The VK-bands are relatively weak because of quenching of $N_2(A)$ by atomic oxygen below 150 km (see Table 4.7 of Vallance Jones, 1974). The atomic oxygen transition at 2972 Å accompanies the O I 5577 Å green line and is produced by a variety of processes in the dayglow (see the reviews by Sharp, 1986; Torr and Torr, 1982, and references therein). There may be a weak N I forbidden line at 3466 Å, which would be produced by dissociative excitation of N_2 and by electron impact on N. In the MUV, nitric oxide δ- and γ-bands result from solar stimulated fluorescence (Cleary, 1986; McCoy, 1983a, b, and references therein). The so-called auroral 'mystery' feature at 2143 Å is also present in

the dayglow. The controversy over its identification is now resolved in favor of N^+, produced in the dayglow by photodissociative ionization excitation of N_2 (Cleary and Barth, 1987, and their references). Below 2600 Å, N_2 Lyman–Birge–Hopfield (LBH)-bands occur as the result of photoelectron impact excitation of N_2, but do not achieve significant brightness until the FUV (for identifications of MUV LBH-bands, see the synthetic auroral spectrum in Figure 1 of Ishimoto *et al.*, 1988).

The FUV dayglow at 7 Å is shown in Figure 6(a). The data were taken from the S3-4 nadir-viewing satellite (Conway *et al.*, 1988; Huffman *et al.*, 1980). Since the LBH emissions in the S3-4 data were found to be contaminated by spacecraft glow (Conway *et al.*, 1987, 1988), the spectrum shown in Figure 6(a) should be used for band identifi-

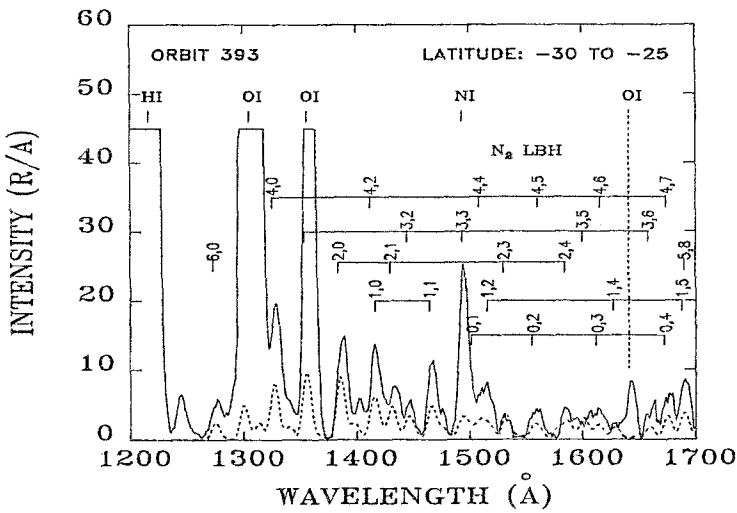

Fig. 6a. S3-4 FUV dayglow spectrum (solid line) on 9 April, 1978 for nadir viewing from 205 km (Conway *et al.*, 1988; Huffman *et al.*, 1980). The spectral resolution is 7 Å. The dashed curve is the prediction of the N_2 LBH band band spectrum using a photoelectron model appropriate to the observation conditions and a Franck–Condon theoretical spectrum (R. Conway, private communication, 1988). No O, H, or N emission features were included in the theory. The excess emission seen in the S3-4 N_2 data is the result of spacecraft glow (Conway *et al.*, 1987, 1988). The bright H I and O I features in the S3-4 data have been truncated.

cation only. The underlying dotted line shows the theoretical prediction of LBH emission rates for the conditions of the satellite observation (Conway, private communication, 1988). Comparison of the theoretical and observed band structures shows that the vibrational distribution of the contaminated signal does not follow the predictions based on Franck–Condon theory. To better identify the emission features, the dayglow at 4 Å resolution obtained in the rocket experiment of Eastes *et al.* (1985) is shown in Figure 6(b). There is no contribution from spacecraft glow in these rocket data.

Atomic oxygen lines are seen at 1356 and 1304 Å and at 1641 Å in Figure 6(a). There is no evidence for contamination of the atomic oxygen lines by S3-4 spacecraft glow: no O I emission at night, other than the tropical arcs. The 1641 Å feature comes from an occasional branch to $O(^1D)$ from the $O(^3S)$ parent state of the 1304 Å line (Meier

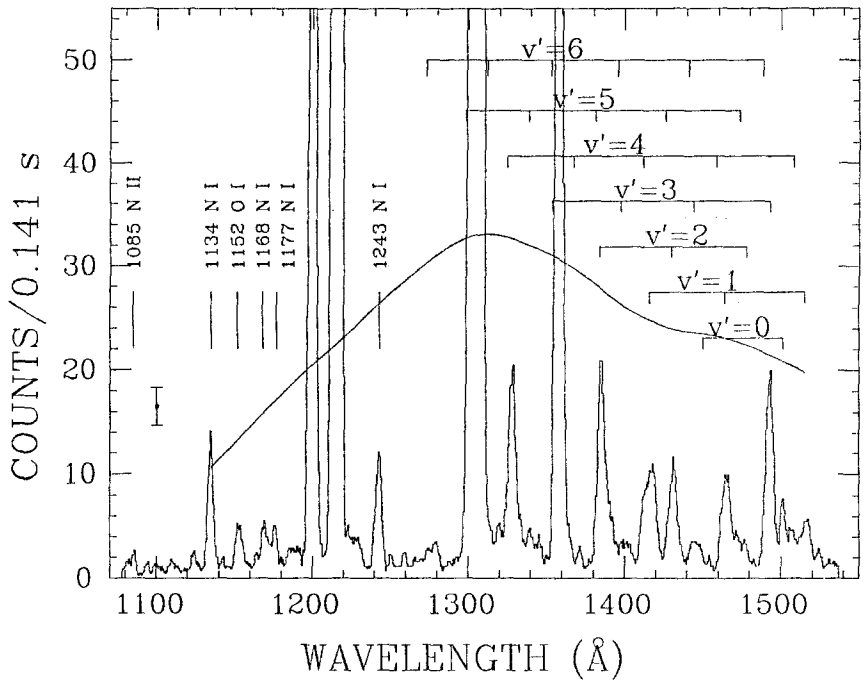

Fig. 6b. FUV dayglow spectrum taken by horizontally-viewing rocket spectrometer on 27 June, 1980. Twenty-two scans between 190 and 240 km were summed. The spectral resolution was 3.5 Å. Positions of N_2 LBH bands for $v' < 7$ progressions and several atomic lines are indicated. The smooth curve indicates the response of the spectrometer to a uniform source of 160 R Å^{-1}. Taken from Eastes *et al.* (1985).

and Conway, 1985; Erdman and Zipf, 1986a; Conway *et al.*, 1988). (These atomic states are identified in the energy level diagram in Figure 48.) Photoelectron excitation of O as well as resonant scattering of the solar 1304 Å triplet are responsible for the 1304 and 1641 Å features. Photoelectron excitation produces the forbidden O I 1356 Å line. A weak contribution to all of these lines from O_2 dissociation can be ignored in the dayglow.

There are a number of atomic nitrogen lines present in the FUV. The strongest of these are at 1134, 1168, 1177, 1200, and 1493 Å (Meier *et al.*, 1980; Eastes *et al.*, 1985; also see Figure 7). Electron impact on N_2 and N, and photodissociative excitation of N_2 contribute variously to the excitation of these N lines.

The ubiquitous hydrogen Lα line at 1216 Å is present in all FUV spectra. Resonant scattering of the solar Lα line is the excitation source in the day-and-night airglow.

Moving into the EUV, the dayglow observed from the rocket experiment of Gentieu *et al.* (1981) is shown in remarkable detail at 3.5 Å spectral resolution in Figure 7. Myriad N_2, N I, N II, O I, and O II lines are present. Except for the H and He emissions, which come from resonant scattering of the solar lines, all other lines are produced by photoelectron impact and photoionization excitation processes. The EUV spectrum is continued down to 530 Å in Figure 8 (Gentieu *et al.*, 1984). The important O II 834 Å, He I 584 Å, and other lines are discussed later in more detail.

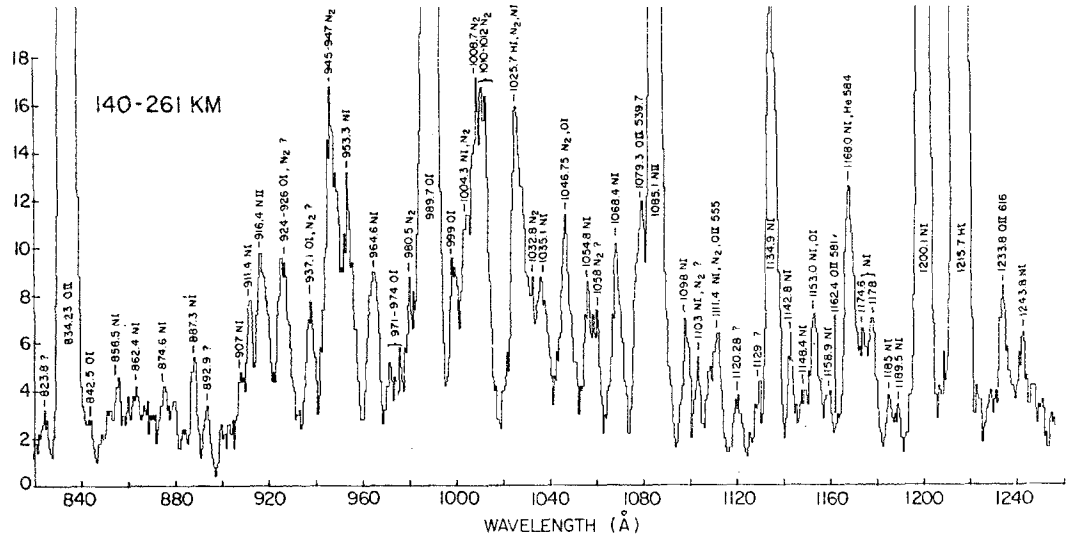

Fig. 7. EUV/FUV spectrum obtained from horizontally viewing rocket experiment on 27 June, 1980, taken from Gentieu *et al.* (1981). The data are a coherent sum of all spectra taken between 140 and 261 km. The spectral resolution is 3.5 Å. The stronger features have been truncated.

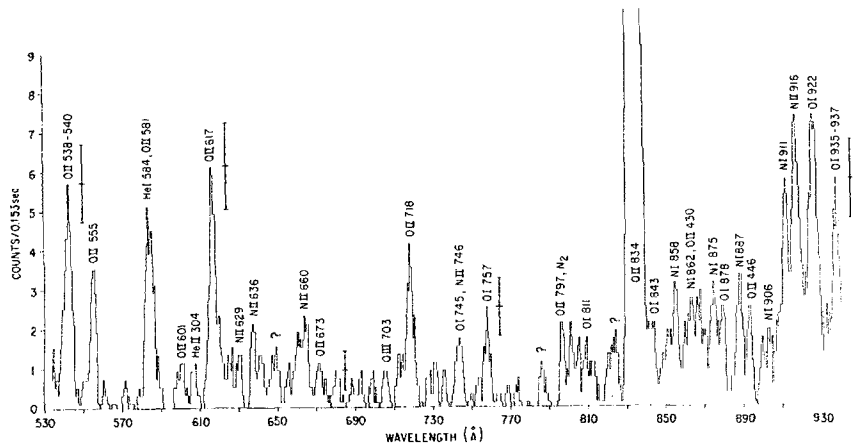

Fig. 8. Continuation of 1980 rocket data into EUV (Gentieu *et al.*, 1984). The data are the sum of 12 spectral scans obtained between 196 and 242 km when the experiment viewed at 90 deg from the zenith, and 12 scans between 246 and 261 km when the view direction was 98 deg. One sigma statistical error bars are given at several places. Some second-order features are indicated.

Table II contains a listing of the identifications of major dayglow emission features, along with nadir-viewing emission rates (except for He 304 Å which is for zenith viewing from 740 km (Weller and Meier, 1974)). For wavelengths between 430 and 1356 Å the entries have been taken from the Space Test Program STP 78-1 satellite observations in March 1979, as reported in Table I of Chakrabarti *et al.* (1983). (Some errors in notation and wavelength identification have been corrected.) At longer wavelengths ($>$ 1356 Å), the column emission rates were calculated for the conditions of the S3-4 satellite (see Table I) using the photoelectron model of Strickland and Meier (1982), but updated with revised cross sections. As an accuracy check, the calculated LBH-bands

TABLE II

UV dayglow in nadir[a] from 600 km

Species	Wavelength (Å)	Transition	Column emission rate (R)
N_2^+	3914	$B\,^2\Sigma_u^+ - X\,^2\Sigma_g^+$	6700
O_2	2500–2900	Herzberg bands	–
N II	2143	$2s\,2p^3\,^5S - 2s^2 2p^2\,^3P$	300
NO	2363	$A\,^2\Sigma^+ + X\,^2\Pi$ (γ band) (0, 1)	369
NO	2262	$A\,^2\Sigma^+ + X\,^2\Pi$ (γ band) (0, 0)	265
NO	2239	$A\,^2\Sigma^+ + X\,^2\Pi$ (γ band) (1, 1)	206
NO	2216	$A\,^2\Sigma^+ + X\,^2\Pi$ (γ band) (2, 2)	82
NO	2149	$A\,^2\Sigma^+ + X\,^2\Pi$ (γ band) (1, 0)	752
NO	2047	$A\,^2\Sigma^+ + X\,^2\Pi$ (γ band) (2, 0)	197
NO	2030	$A\,^2\Sigma^+ + X\,^2\Pi$ (γ band) (3, 1)	29
NO	2000–2700	Gamma bands	
N_2	Total	$A\,^3\Sigma_g^+ - X\,^1\Sigma_g^+$ (VK)	6820 (excitation only)
N_2	Total	$a\,^1\Pi_g - X\,^1\Sigma_g^+$ (LBH)	4560
N_2	2000–2400	Subtotal (LBH)	273
N_2	1947	$a\,^1\Pi_g - X\,^1\Sigma_g^+$ (4, 11)	70
N_2	1930	$a\,^1\Pi_g - X\,^1\Sigma_g^+$ (3, 10)	71
N_2	1856	$a\,^1\Pi_g - X\,^1\Sigma_g^+$ (3, 9)	95
N_2	1839	$a\,^1\Pi_g - X\,^1\Sigma_g^+$ (2, 8), (6, 11)	100
N_2	1771	$a\,^1\Pi_g - X\,^1\Sigma_g^+$ (2, 7), (6, 10)	127
N_2	1754	$a\,^1\Pi_g - X\,^1\Sigma_g^+$ (1, 6), (5, 9)	113
N_2	1690	$a\,^1\Pi_g - X\,^1\Sigma_g^+$ (1, 5), (5, 8)	116
N_2	1675	$a\,^1\Pi_g - X\,^1\Sigma_g^+$ (4, 7), (0, 4)	98
O I	1641	$2p^4\,^1D - 2p^3\,^3s\,^3S^0$	50
N_2	1602	$a\,^1\Pi_g - X\,^1\Sigma_g^+$ (3, 5)	87
N_2	1586	$a\,^1\Pi_g - X\,^1\Sigma_g^+$ (2, 4)	73
N_2	1558	$a\,^1\Pi_g - X\,^1\Sigma_g^+$ (0, 2), (4, 5)	87
N_2	1531	$a\,^1\Pi_g - X\,^1\Sigma_g^+$ (2, 3)	104
N_2	1511	$a\,^1\Pi_g - X\,^1\Sigma_g^+$ (4, 4), (1, 2)	127
N_2	1495	$a\,^1\Pi_g - X\,^1\Sigma_g^+$ (3, 3), (6, 5)	109
N I	1493	$2p^3\,^2D^0 - 3s^2P$	91 ($e + N_2$)
N_2	1465	$a\,^1\Pi_g - X\,^1\Sigma_g^+$ (1, 1)	144
N_2	1446	$a\,^1\Pi_g - X\,^1\Sigma_g^+$ (3, 2)	93
N_2	1431	$a\,^1\Pi_g - X\,^1\Sigma_g^+$ (2, 1), (5, 3)	144
N_2	1416	$a\,^1\Pi_g - X\,^1\Sigma_g^+$ (4, 2), (1, 0)	207
N_2	1398	$a\,^1\Pi_g - X\,^1\Sigma_g^+$ (6, 3), (3, 1)	62
N_2	1384	$a\,^1\Pi_g - X\,^1\Sigma_g^+$ (2, 0), (5, 2)	267
O I	1356	$2p^4\,^3P - 2p^3\,3s\,^5S^0$	1068
N_2	1354	$a\,^1\Pi_g - X\,^1\Sigma_g^+$ (3, 0)	222
N_2	1325	$a\,^1\Pi_g - X\,^1\Sigma_g^+$ (4, 0)	200
O I	1304	$2p^4\,^3P - {}^2P^3\,3s\,^3S^0$	10498
N_2	1298	$a\,^1\Pi_g - X\,^1\Sigma_g^+$ (5, 0)	(111)
N_2	1273	$a\,^1\Pi_g - X\,^1\Sigma_g^+$ (6, 0)	<70
N_2	1259	$b\,^1\Pi_g - X\,^1\Sigma_g^+$ (1, 10) (BH)	<30
N I	1243	$2p^3\,^2D^0 - 2p^2\,3s'\,^2D$	150
H I	1216	$1s^2S - 2p^2P^0$	35000
N I	1200	$2p^3\,^4S^0 - 2p^2\,3s\,^4P$	1500
O I	1173	$2p^4\,^1D_2 - 3s'\,^3D^0$	
N I	1176–1177	$2p^3\,^2D^0 - 2p^2(^3P)4s\,^2P$	<160
N I	1168	$2p^3\,^2D^0 - 2p^2\,3d\,^4P$	170
O I	1152	$2p^4\,^1D - 3s'\,^1D^0$	150

Table II (continued)

Species	Wavelength (Å)	Transition	Column emission rate (R)
N I	1143	$3p^3\ ^2P^0 - 2p^2\ 3s^2S$	<45
N I	1134	$2s^2\ 2p^3\ ^4S - 2s\ 2p^4\ ^4P$	400
N_2	1110	$b\ ^1\Pi_u - X\ ^1\Sigma_g^+$ (1, 5)	<50
N I	1100	$2p^3\ ^2D^0 - 2p^2(^3P)5s\ ^2P$	55
N I	1097–1099	$2p^3\ ^2D^0 - 2p^2(^3P)4d\ (^2P$ and $^4F)$	55
N II	1085	$2s^2\ 2p^2\ ^3P - 2s\ 2p^3\ ^3D^0$	500
N I	1067–1068	$2p^3\ ^2D^0 - 2p^2(^3P)5d\ (^{2,4}D$ and $^{2,4}F)$	<120
N_2	1058	$b\ ^1\Pi_u - X\ ^1\Sigma_g^+$ (1, 3)	<120
O I	1040	$2p^4\ ^3P - 2p^3 4s\ ^3S^0$	60
N_2	1033	$b\ ^1\Pi_u - X\ ^1\Sigma_g^+$	(149)
O I	1027	$2p^4\ ^3P - 3d\ ^3D^0$	340
H I	1026	$1s\ ^2S - 3p\ ^2P^0$	
N_2	1009	$b\ ^1\Pi_u - X\ ^1\Sigma_g^+$ (1, 1)	150
O I	989	$2p^4\ ^3P - 2p^3(^2D^0)3s'\ ^3D^0$	850
N_2	985	$b\ ^1\Pi_u - X\ ^1\Sigma_g^+$ (1, 0)	95
H I	973	$1s\ ^2S - 4p\ ^2P^0$	14
N I	964–965	$2p^3\ ^4S^0 - 2p^2(^3P)4s\ ^4P$	80
N I	953	$2p^3\ ^4S^0 - 2p^2(^3P)3d\ ^4P$	125
N II	916	$2s^2\ 2p^2\ ^3P - 2s\ 2p^3\ ^3P^0$	185
N I	910	$2p^3\ ^4S^0 - 2p^2(^3P)5s\ ^4P$	90
N I	907	$2p^3\ ^4S - 2p^2(^3P)4d\ ^2P\ ^4P^4F$	<80
N I	887	$2p^3\ ^4S - 2p^2(^3P)6s\ ^4P^2P$	<40
N I	875	$2p^3\ ^4S - 2p^2(^3P)6d\ ^4P\ ^4D$	<35
N I	862	$2p^3\ ^4S - 2p^2(^3P)9d\ ^4P\ ^4D$	<35
N I	859	$2p^3\ ^4S - 2p^2(^3P)11d\ ^4P\ ^4D$	<35
O II	834	$2s^2\ 2p^3\ ^4S^0 - 2s\ 2p^4\ ^4P$	580
N II	776	$2s^2\ 2p^2\ ^1D - 2s\ 2p^3\ ^1D^0$	<5
N II	747	$2p^2\ ^1D - 2p\ 3s\ ^1P^0$	<4
O II	718	$2s^2\ 2p^3\ ^2D^0 - 2s\ 2p^4\ ^2D$	17
O II	673	$2p^3\ ^2P^0 - 2p^2(^3P)3s\ ^2P$	6.5
N II	671	$2p^2\ ^3P - 2p\ 3s\ ^3P^0$	
N II	645	$2s^2\ 2p^2\ ^3P - 2s\ 2p^3\ ^3S^0$	7
O II	644	$2s^2\ 2p^3\ ^2P^0 - 2s\ 2p^4\ ^2S$	
N II	629	$2s\ 2p^3\ ^5S^0 - 2s\ 2p^2(^4P)3s\ ^5P$	3
O II	617	$2p^3\ ^2D^0 - 2p^2(^3P)3s\ ^2P$	60
O II	601	$2p^3\ ^2P^0 - 3s'\ ^2D$	9
He I	584	$1s^2\ ^1S - 1s2p\ ^1P^0$	330
O II	581	$2s^2\ 2p^3\ ^2P^0 - 2s\ 2p^4\ ^2P$	<20
O II	555	$2p^3\ ^2D^0 - 3s'\ ^2D$	15
O II	539	$2p^3\ ^4S^0 - 3s\ ^4P$	115
O II	538	$2s^2\ 2p^3\ ^2D^0 - 2s\ 2p^4\ ^2P$	
He I	537	$1s^2\ ^1S - 1s3p\ ^1P^0$	
He I	522	$1s^2\ ^1S - 1s4p\ ^1P^0$	8.5
O II	515	$2p^3\ ^2D - 2p^2(^3P)3d\ ^2P^0$	
O II	482	$2p^3\ ^2D^0 - 2p^2(^3P)3d\ ^2D$	8
O II	470	$2p^3\ ^2P^0 - 2p^2(^1D)3d'\ ^2D$	<8
O II	442	$2p^3\ ^2D^0 - 2p^2(^1D)3d'\ ^2D$	12
O II	430	$2p^3\ ^4S^0 - 2p^2(^3P)3d\ ^4P$	12
He II	304	$1s^2S - 2p\ ^2P^0$	5 (Zenith)

[a] Background below 100 km not included.

and O I lines below 1356 Å were found to be in good agreement with observed values given in the table of Chakrabarti *et al.* The N_2 VK-band entry gives the total population of the A state from direct photoelectron impact excitation, including cascade from the C, B, and W states; quenching is not included. The NO γ-band emission rates are fluorescence calculations based on the discussions of Sections 3.2.1.2 and 4.2.1. The fluorescence efficiency for the δ-bands is somewhat uncertain (Cleary, 1986). The N^+ emission rate at 2143 Å was calculated by D. Cleary (private communication, 1988) for zenith viewing above 100 km at the equator under solar maximum conditions. The N_2^+ emission rate is from Zipf and Fastie (1964). Thus Table II provides average daytime UV intensities under moderately active solar conditions (see Table I). Note that the emission rates in Table II may not always agree with those in Figures 3–8 because of different observation conditions.

2.2. The Nightglow

A composite nightglow spectrum analogous to Figure 3 was constructed, again using data from several sources. The viewing condition chosen for this example is downward from 600 km near midnight in the equatorial zone. Between 2500 and 3800 Å, the spectrum of Hennes (1966) is used. The data of Sharp and Rusch (1981) are used in the 1900 to 2300 Å interval. A theoretical NO spectrum fills in the gap from 2300 to 2500 Å, and the data of Broadfoot and Kendall (1968) are used between 3800 and 4000 Å. All of the spectra were placed on the same scale by normalizing to the S3-4 satellite data of Huffman *et al.* (1980) after converting the spectrum in the center panel of their Figure 12 to absolute units. At shorter wavelengths, the ionospheric lines of atomic oxygen were taken from Chakrabarti *et al.* (1984). All data were degraded to a spectral resolution of 15 Å FWHM. No attempt was made to include Rayleigh or ground scattering in the nightglow spectrum.

The resulting radiance is shown in Figure 9. The nightglow is produced by atom-atom and ionic recombination and is expected to be highly variable, both spatially and temporally. The spectrum in Figure 9 should be considered as representative of moderately active conditions in March 1978 and April 1979 near the equator at midnight, only. The composite spectrum is sparse. There are apparently no emissions in between the features shown. N_2 LBH-band emissions, orginally thought to be nightglow (Huffman *et al.*, 1980; Meier and Conway, 1983; Torr *et al.*, 1985), have now been attributed to interaction of the spacecraft with the atmosphere (Conway *et al.*, 1987; Swensen and Meyerott, 1988; Kofsky, 1988).

The NUV nightglow spectrum is shown in more detail in Figure 10, taken from Hennes (1966). The rocket observation was made in the direction of the limb, but the spectrum was adjusted to zenith by Hennes. The instrumental resolution was stated to be 12 Å but the emission rate was given by Hennes in R Å^{-1}. Band identifications for the $O_2(A \rightarrow X)$ Herzberg I system were adopted from Degen (1969). Hennes calculated the O_2 Herzberg I system vertical column emission rate to be 600 R and the O I emission at 2972 Å to be 9 R. In constructing Figure 9, normalization of the Hennes spectrum to the nadir-viewing S3-4 observations of Huffman *et al.* (1980) required scaling the O_2

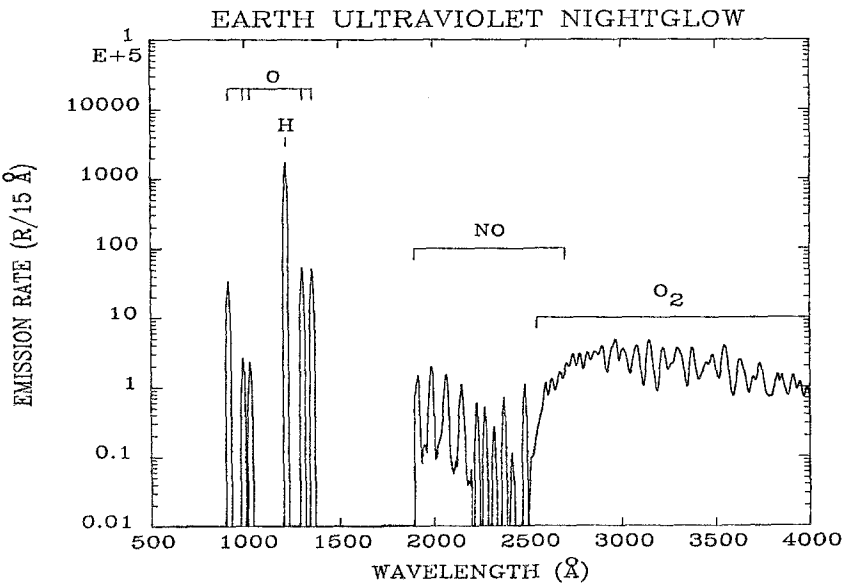

Fig. 9. Composite UV nightglow spectrum adjusted to nadir viewing from 600 km in equatorial region. All spectral features have been smoothed to 15 Å resolution. The O_2 and NO molecular, the H geocoronal resonant scattering, and the $O^+ + e \rightarrow O$ recombination emissions are indicated. The O_2 spectrum was taken from the Hennes (1966) rocket experiment, the NO spectrum from the Sharp and Rusch (1981) rocket data, and the O I and H I lines from the STP 78-1 satellite data of Chakrabarti *et al.* (1984). The absolute values of the O_2 and NO bands were obtained by normalizing to the Huffman *et al.* (1980) S3-4 equatorial spectrum (after converting the S3-4 data to absolute units). The nightglow varies strongly with geographic position, local time, and solar activity.

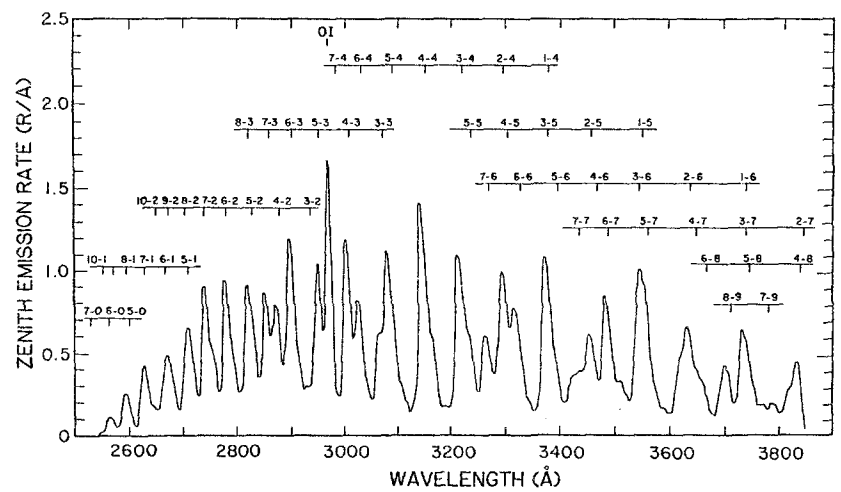

Fig. 10. MUV and NUV spectra at 12 Å resolution obtained on 30 November, 1964 from a horizontally viewing rocket experiment at 184 km (after Hennes, 1966). The O_2 Herzberg I band identifications were taken from Degen (1969). The intensity scale was obtained after adjustment to zenith by Hennes, giving 600 *R* in the Herzberg I band. The O I line at 2973 Å is indicated at the top.

Herzberg I to 225 R, a value in agreement with the rocket observations of Murtagh *et al.* (1986). While the Hennes spectrum seems to be well accounted for by the Herzberg I system, there are weaker contributions present from the O_2 Herzberg II and Chamberlain systems, especially at the longer wavelengths (see Slanger and Degen, 1986, for band identifications). Murtagh *et al.* (1986) estimated the total band intensity ratio of Herzberg I to II to be 4 : 1, and Herzberg I to Chamberlain to be 2 : 1. The Herzberg I-bands are produced by the three-body process: $O + O + M \rightarrow O_2(A) + M$ (see Parisot, 1986; Murtagh *et al.*, 1986, and their references). Quenching of this metastable state is important at low altitudes. (See the energy level diagram in Figure 45 for identification of these band systems.)

At night, the lower wavelength end of the MUV is poulated by NO δ- and γ-bands (Sharp and Rusch, 1981; Tennyson *et al.*, 1986). The spectrum of Sharp and Rusch is shown in Figure 11, for horizontal viewing from a rocket between 115 and 150 km. The

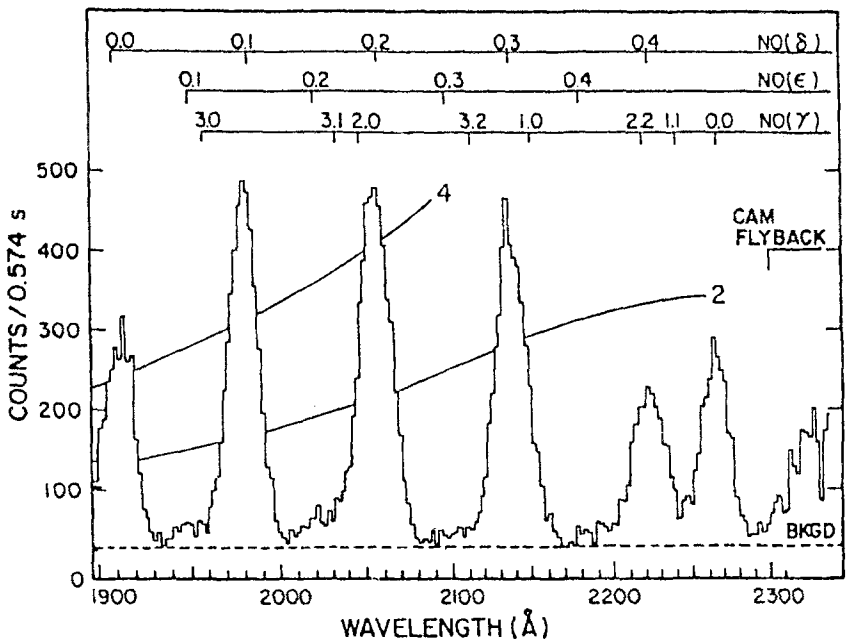

Fig. 11. NO nightglow at 15 Å resolution viewing horizontally between 115 and 150 km from a rocket experiment launched on 2 November, 1978 (Sharp and Rusch, 1981). Band identifications are given at the top. Curves giving the absolute instrument response at 2 and 4 R are plotted as solid lines. The dashed line indicates the instrument background level.

vibrational distributions of the bands are consistent with $N(^4S) + O(^3P)$ association.

In the FUV and EUV, a series of O I lines are present from radiative recombination of $O^+ + e$. These are seen spectroscopically in the STP 78-1 observations which are reproduced from Chakrabarti *et al.* (1984) in Figure 12. A narrow continuum is present at 911 Å as O^+ ions recombine into the ground state of O. There may also be a contribution to the nightglow at 1304 and 1356 Å from ring current particles which have been neutralized and which precipitate into the equatorial region (Abreu *et al.*, 1986).

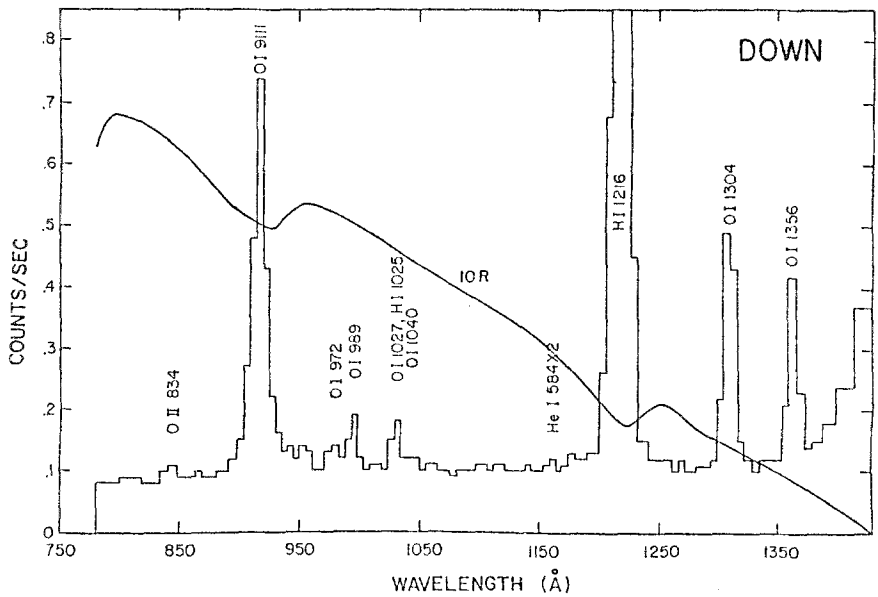

Fig. 12. Average EUV and FUV nightglow spectrum from the STP 78-1 spacecraft at 600 km obtained by summing all nadir viewing (120–150 deg observation zenith angle) data taken within 40 deg of the magnetic equator between 7 and 9 April, 1979 (Chakrabarti *et al.*, 1984). The smooth solid line gives the absolute instrument calibration at 10 *R* per wavelength bin. Note that a single line profile extends over several bins.

Tinsley and colleagues have detected related visible emissions from H, O^+, He^+, and N_2^+ (Tinsley, 1979; Tinsley *et al.*, 1982; Rohrbaugh *et al.*, 1983). Ishimoto *et al.* (1986) have observed N_2^+ 1 NG and N_2 2 PG emissions at mid-latitudes during the night. However, these appear to be associated with auroral precipitation. Cazes and Emerich (1980) observed H Lα enhancements at low- and mid-latitudes which they correlated to magnetic activity. Meier and Weller (1975) found He^+ and associated He^{++} recombination emissions of up to several Rayleighs during periods of ring-current disturbances. Paresce (1979) confirmed the Meier and Weller observations and reported evidence for emission below 150 Å, possibly due to ionized oxygen. The Lα nightglow is due to solar radiation multiply scattered into the night sector by high altitude geocoronal hydrogen. The possible presence of other weak features is indicated in Figure 12.

Table III lists the emission rates used in the creation of Figure 9. He II 304 Å due to ring-current precipitation (Meier and Weller, 1975) is included in the table but not in Figure 9. As noted before, the nightglow is highly variable, depending mostly on the products of the recombining species or geomagnetic activity. In the next section, the variability of selected emission features in both the dayglow and nightglow is reviewed.

2.3. Airglow Variability

The UV airglow has been observed from many rockets and satellites under widely diverse conditions, too many to include here in a comprehensive way. Consequently,

TABLE III

UV nightglow in nadir from 600 km

Species	Wavelength (Å)	Transition	Column emission rate (R)
O_2	Total	$A\,^3\Sigma_u^+ - X\,^3\Sigma_g^-$ (Herzberg I)	225
O I	2972	$2p^4\,^1S - 2p^4\,^3P$	9
NO	1900	$C\,^2\Pi - X\,^2\Pi$ (δ band) (0, 0)	5.5
NO	1980	$C\,^2\Pi - X\,^2\Pi$ (δ band) (0, 1)	7.9
NO	2055	$C\,^2\Pi - X\,^2\Pi$ (δ band) (0, 2)	6.5
NO	2134	$C\,^2\Pi - X\,^2\Pi$ (δ band) (0, 3)	4.0
NO	2219	$C\,^2\Pi - X\,^2\Pi$ (δ band) (0, 4)	2.1
NO	2310	$C\,^2\Pi - X\,^2\Pi$ (δ band) (0, 5)	0.93
NO	2406	$C\,^2\Pi - X\,^2\Pi$ (δ band) (0, 6)	0.38
NO	2509	$C\,^2\Pi - X\,^2\Pi$ (δ band) (0, 7)	0.16
NO	2620	$C\,^2\Pi - X\,^2\Pi$ (δ band) (0, 8)	0.06
NO	2262	$A\,^2\Sigma^+ - X\,^2\Pi$ (γ band) (0, 0)	1.8
NO	2363	$A\,^2\Sigma^+ - X\,^2\Pi$ (γ band) (0, 1)	2.4
NO	2471	$A\,^2\Sigma^+ - X\,^2\Pi$ (γ band) (0, 2)	3.8
NO	2587	$A\,^2\Sigma^+ - X\,^2\Pi$ (γ band) (0, 3)	1.5
NO	2713	$A\,^2\Sigma^+ - X\,^2\Pi$ (γ band) (0, 4)	0.5
O I	1356	$2p^4\,^3P - 2s\,^5S^0$	52
O I	1304	$2p^4\,^3P - 3s\,^3S^0$	54
H I	1216	$1s\,^2S - 2p\,^2P$	1712
H I, O I	1026	$1s\,^2S - 2p^2P^0$, $2p^4\,^3P - 3d^3D^0$	2.3
O I	989	$2p^4\,^3P - 3s'\,^3D^0$	2.6
O I	911	$2p^4\,^3P - \infty$	34.5
He II	304	$1s\,^2S - 2p\,^2P^0$	0.1–5

only satellite observations have been selected to display the spatial and temporal variability of airglow emissions. Full spatial and temporal characterization of many UV airglow features is not yet available. Those for which a reasonable database has been obtained are reviewed in this section. Details of the excitation and emission processes are discussed in Sections 4 and 5.

A number of observations in the NUV and MUV to date have been made from spinning satellites, but to avoid contamination of the airglow emissions by low altitude scattering, only data obtained when viewing above the limb have been analyzed. Most of the data have been published in the form of volume emission rates derived from the inversion of limb-scan radiances. References to observations from the Atmospheric Explorer (AE) satellites of the N_2^+ 1 NG and N_2 2 PG-bands are given in the review by Hays *et al.* (1988). Analysis of observations of NO emissions from $AE-C$ are discussed by Cravens and Killeen (1988, and papers referenced by them). The actual measurements of radiances from these species are apparently not in the literature. Theoretical calculations of some NUV and MUV radiances are presented in Section 4.2.1.

N_2 LBH-bands in the FUV show behavior typical of photoelectron-excited dayglow emissions. Vertical column emission rates seen in the nadir from above the atmosphere are of order 4 to 8 kR for the entire LBH-band system, with a variation in the sunlit atmosphere approximately following the cosine of the solar zenith angle. This is seen in data from the polar Orbiting Geophysical Observatory OGO-4, which are reproduced in Figure 13 (Prinz and Meier, 1971). These data were obtained photometrically with

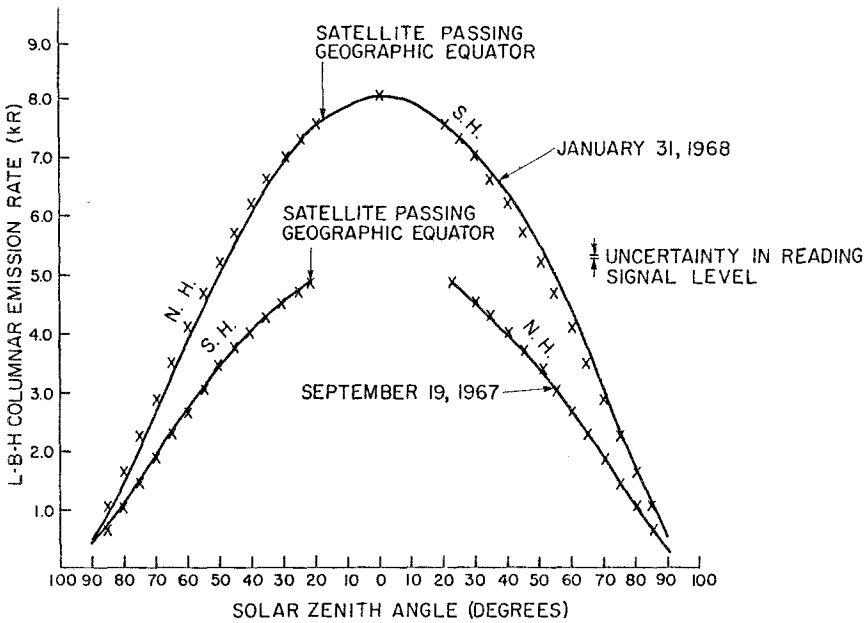

Fig. 13. N_2 LBH total band emission rate in the nadir vs solar zenith angle for orbits of the OGO-4 satellite near solstice and equinox (Prinz and Meier, 1971). The high signal-to-noise data are given by the solid lines and the X's are a representation provided by the inverse of the Chapman function to provide a symmetric reference. The photometric data were converted to total band emission rates using a synthetic spectrum convoluted with and the instrument sensitivity function. Northern and southern hemispheres are indicated by N.H. and S.H., respectively.

entire band emission rates deduced from an assumed synthetic spectral distribution. Superimposed on this strong variation with solar zenith angle is a weaker temporal dependence on both the ionizing solar flux and geomagnetic activity. Figure 14, also taken from Prinz and Meier, shows this long-term variability in the LBH airglow at a fixed solar zenith angle (60 deg), along with simultaneous solar X-ray and 10.7 cm radio fluxes. The LBH radiance only approximately tracks the solar irradiance variations. Undoubtedly this is due to changes in thermospheric composition as well as to nonlinear dependences of the solar X-rays and radio emissions on the actual EUV lines responsible for producing the energetic photoelectrons. In addition to these 'routine' variations, Opal (1973) found a strong enhancement in the photoelectron-excited dayglow accompanying solar flares. This is not unexpected since strong increases in the solar EUV irradiance occur during flares.

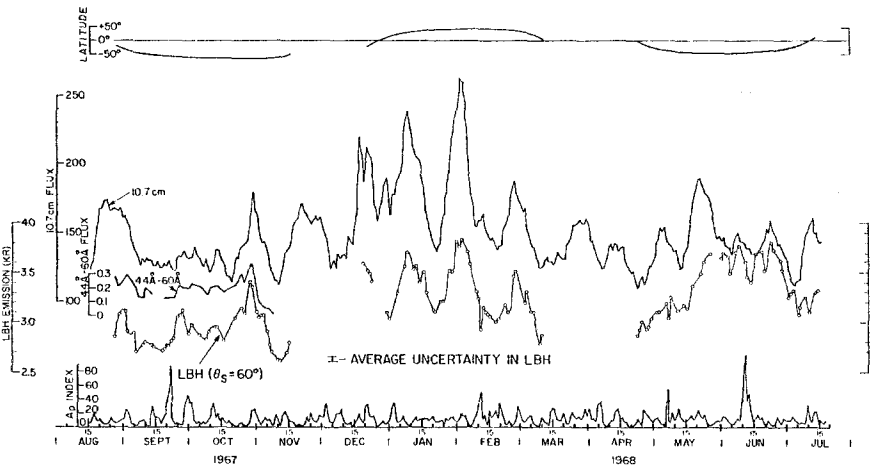

Fig. 14. N_2 LBH total band emission rate in the nadir at 60 deg solar zenith angle vs day of year in 1967 and 1968 for orbits of OGO-4 near noon GMT (Prinz and Meier, 1971). Also plotted are the solar 10.7 cm and X-ray fluxes, the A_p geomagnetic index, and the latitude of the spacecraft for the LBH observations. Gaps in the data are periods when the precessing orbit did not satisfy the prescribed 60 deg solar zenith angle.

The solar zenith angle and temporal dependences of the O I 1304 Å triplet lines measured from OGO-4 by Meier and Prinz (1971) were found to be similar to those of the LBH-bands even though the atomic oxygen atmosphere is very optically thick to the line radiation. More recent spectroscopic data from STP 78-1 verify the earlier OGO-4 results (Link *et al.*, 1988a). Figure 15 shows the STP 78-1 near-zenith and nadir-column emission rates of the three bright O I lines at 989, 1304, and 1356 Å, as functions of orbital position at 600 km altitude (Link *et al.*, 1988a). The Sun was on the equator for Orbit 373, so that away from the poles, the solar zenith angle nearly equals the absolute value of latitude. Strong multiple scattering occurs for O I 1304 and 989 Å, the latter suffering significant loss through branching (Meier and Lee, 1982; Meier, 1982; Link *et al.*, 1988a; Morrison and Meier, 1988). There is weak multiple scattering of O I 1356 Å near 100 km, where molecular absorption by O_2 sets in. The O I 989 Å variation with latitude at mid-latitudes is less than the other two lines.

A weaker O I line at 1641 Å due to an occasional transition from the parent state of 1304 Å, $O(^3S)$, to $O(^1D)$ was discovered by Meier and Conway (1985) in the S3-4 satellite data of Huffman *et al.* (1980). Figure 16 taken from Conway *et al.* (1988) shows the latitudinal variation of O I 1304, 1356, and 1641 Å for several orbits in April 1978. The Sun was about 23 deg out of the orbital plane. The data are skewed in latitude due to the varying altitude of the spacecraft (260–160 km). The 1304 Å emission rate is larger than seen in Figure 15, since S3-4 is at a lower altitude where the enhancement in the radiation field due to multiple scattering is much greater; STP 78-1 is mostly outside of the atmosphere and thus sees photons escaping to space. The 1641 Å line has a mean brightness of about 50 *R* in the vertical. During geomagnetically active periods (Orbit 425), all three lines show large depletions in the atomic oxygen airglow

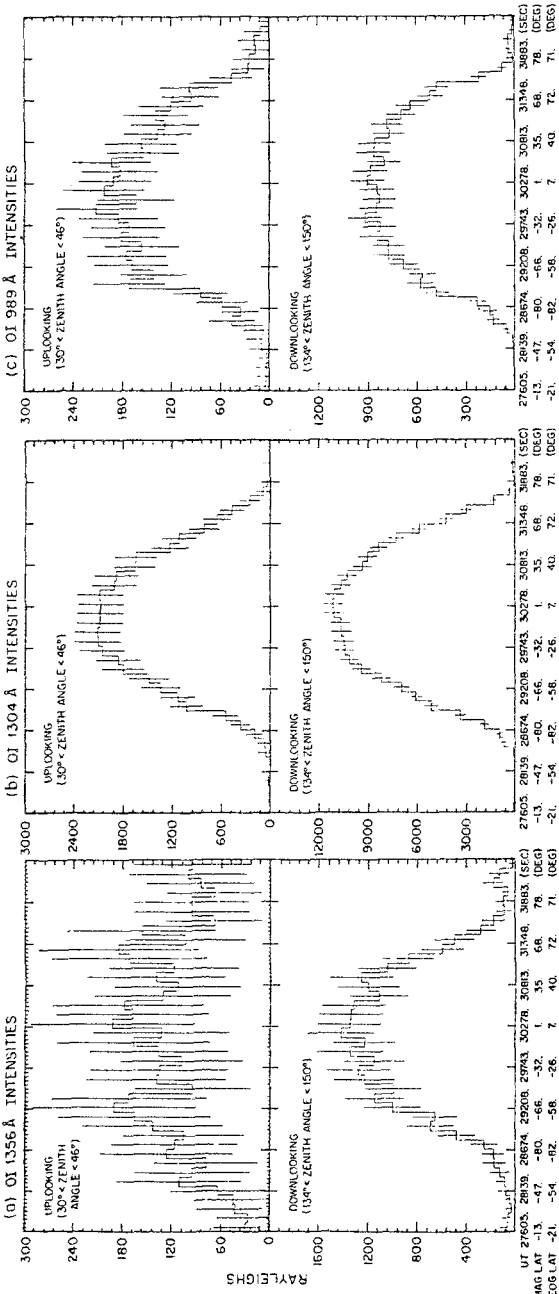

Fig. 15. O I 1356, 1304, and 989 Å dayglow emission rates for Orbit 373 of STP 78-1 on 21 March, 1979 (Link *et al.*, 1988a). Uplooking (*upper panels*) and downlooking (*lower panels*) data are plotted vs universal time (UT). Since the Sun was in both the equatorial and orbital planes, absolute values of latitude are nearly equal to solar zenith angle away from the poles. Statistical error bars are indicated by vertical lines.

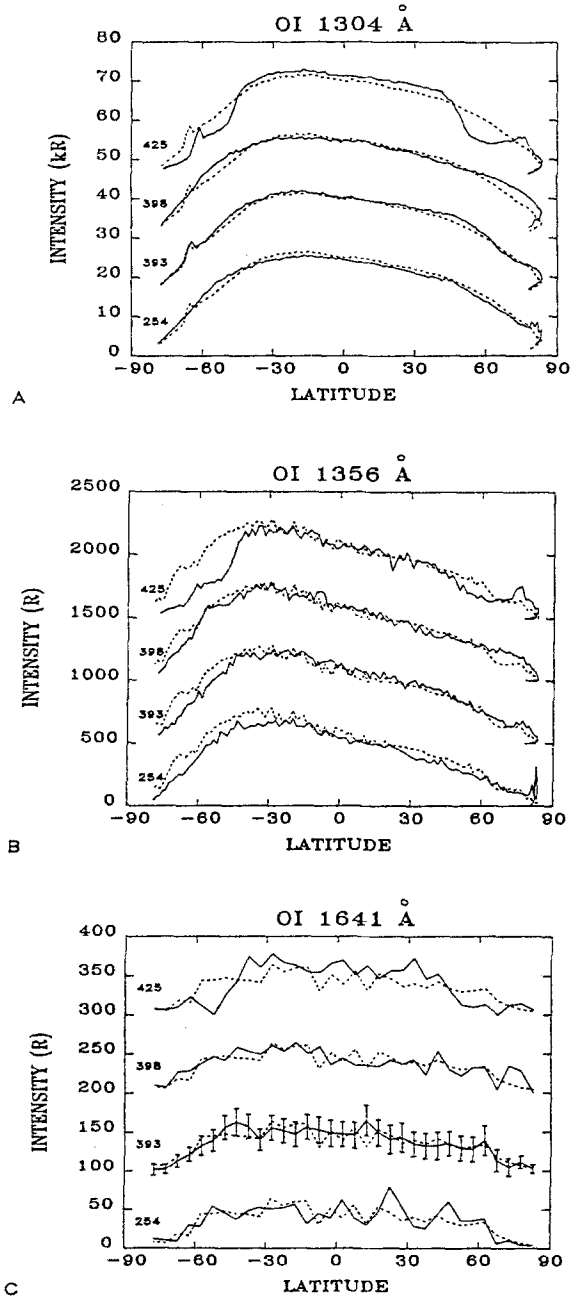

Fig. 16. Five orbits of S3-4 nadir viewing O I emission rates taken from Conway *et al.* (1988). The underlying dotted data are from Pass 360 for comparison with the others, which have successively been offset by 15 kR (A), 500 *R* (B), and 100 *R* (C) for easier viewing. Passes 254, 360, 393, 398, and 425 are for days 91, 97, 99, 100, and 101 of 1978, respectively. One sigma error bars are indicated for the 1641 Å data. The altitude of the spacecraft was 240 km at −60 deg latitude, 180 km at 0 deg, and 168 km at +60 deg. This altitude variation accounts for the skewing of the emission rates. The minimum solar zenith angle was 23 deg at about 10 deg latitude. Notice the high latitude airglow depletions in Pass 425, when A_p reached 64.

below the spacecraft at high latitudes compared with the quiet Orbit 360, plotted for reference as the dashed curve. Such reductions appear to be related to regions of localized heating where the atomic oxygen concentration is low. Note that at low latitudes, the brightness is larger under disturbed conditions, indicating transport of oxygen from high latitudes.

At night, the strongest O I radiative recombination emissions in the UV are at 911, 1304, and 1356 Å (Figure 12). Since these ionospheric emissions are proportional to the product of the electron and O^+ concentrations, or equivalently the square of the electron concentration in the *F*-region, they are brightest in the Appleton Anomaly regions on either side of the dip equator. Figures 17(a) and 17(b) show the nadir-viewed radiance

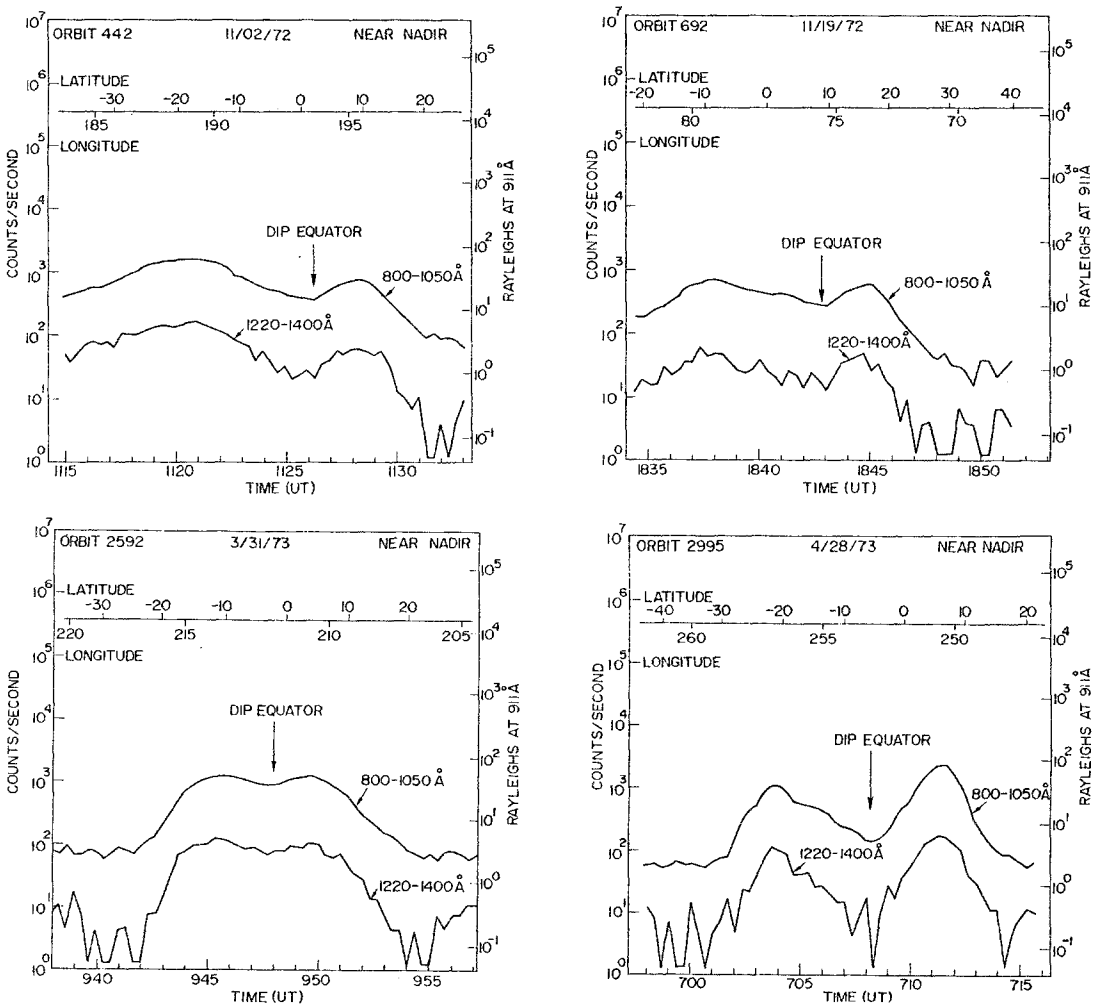

Fig. 17a. Near-nadir (155 deg zenith angle) emission rates observed during four orbits of the STP 72-1 spacecraft at 740 km in the equatorial ionosphere at midnight (Anderson *et al.*, 1976). Signals from two photometric channels are shown, one including both O I 1304 and 1356 Å lines, and the other, the O I 911 Å continuum. The conversion to Rayleighs is shown on the right for the 800–1050 Å photometer.

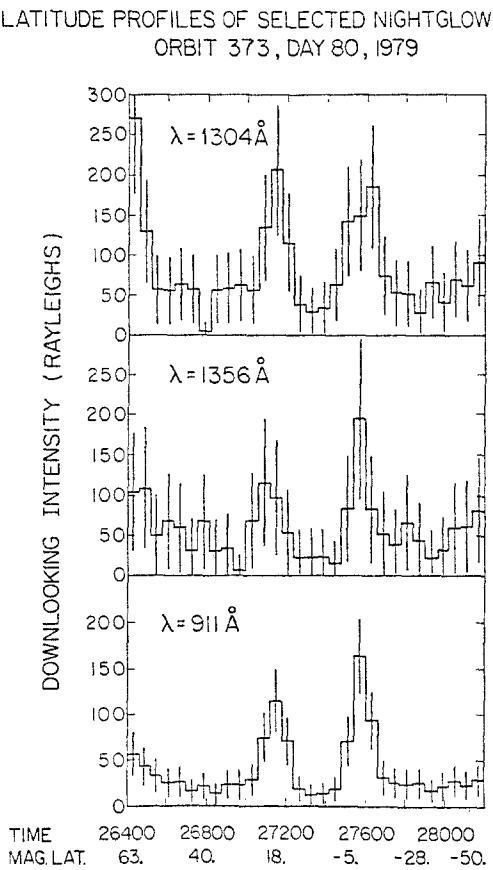

Fig. 17b. Variation of spectrally resolved O I nightglow emission features with magnetic latitude as observed from 600 km by the STP 78-1 spectrograph. Taken from Chakrabarti (1984).

as a function of latitude. Figure 17(a) contains data from the STP 72-1 spacecraft (740 km altitude) in two bands, one containing the 911 Å continuum, and the other including both 1304 and 1356 Å lines (Anderson *et al.*, 1976). Figure 18 shows the seasonal variation of the STP 72-1 emission rate at 911 Å from Fall, 1972 through Spring, 1974. The emission rate can exceed 100 *R* when the peak *F*-region electron concentration is large, but can also be quite weak during certain seasons. Zonal discrimination was not attempted. Figure 17(b) shows spectrally resolved oxygen emissions from the STP 78-1 spacecraft (600 km altitude) published by Chakrabarti (1984). Abreu *et al.* (1984, 1986) also discussed various aspects of these and other O I emissions in the nocturnal tropical airglow.

The atomic hydrogen Lα line at 1216 Å is detectable throughout the geocorona. Column emission rates observed in the zenith and nadir from three low orbiting satellite experiments are compared in Figure 19. The OGO-4 and Orbiting Solar Observatory (OSO-4) data for October 1967 were taken from Meier and Mange (1973) and the STP 78-1 observations in March 1979, from Anderson *et al.* (1987a). (Note that in the

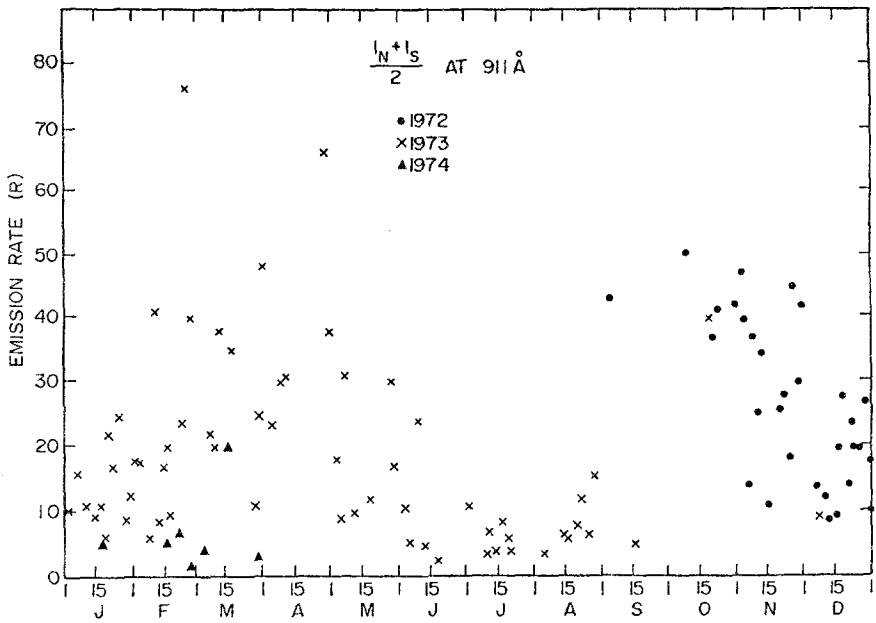

Fig. 18. Seasonal variation of the tropical ionospheric emission at 911 Å measured from the STP 72-1 spacecraft (Anderson *et al.*, 1976). The mean of the north and south Appleton Anomaly peak emission rates is plotted for each orbit when measurements were made.

labelling of Figure 2 of Anderson *et al.*, the symbols for zenith and nadir were inadvertently interchanged.) The differences in the emission rates from the 1967 and 1979 missions are principally the result of differences in atmospheric conditions: the change in the geocoronal hydrogen concentration due to the hotter atmosphere in 1979 produces a weaker dependence of the emission rate on solar zenith angle during the day (see Figure 12 of Meier and Mange, 1970). Theoretical computations of the column emission rate were made by Meier and Mange (1973) for a circular orbit at 650 km (solid line) and one which reproduced the altitude of OGO-4 (dashed line). As can be seen in Figure 19, the altitude variation of the computed emission rate is slight from 400 to 800 km. The agreement between the 1967 data and the theory is good. Using the appropriate geocoronal hydrogen model, Anderson *et al.* (1987a) found equally good agreement with the 1979 data. The zenith emission rate contains a contribution of several hundred Rayleighs from the interplanetary background (see Ajello *et al.*, 1987, and their references for various observations of the interplanetary background); this accounts for at least part of the difference between the model and data near midnight.

The Lα emission rate displays a temporal variation which depends on solar activity, being directly proportional to the solar Lα line-center irradiance. This can be seen in Figure 20, a plot of the near-zenith emission rate at 110 deg solar zenith angle observed from OGO-4 for seven months (Meier and Mange, 1970). The solar 10.7 cm radio emission is also plotted in Figure 20 as a proxy for the Lα irradiance. The airglow does not follow the 10.7 cm radio flux exactly because the geocoronal hydrogen concentration

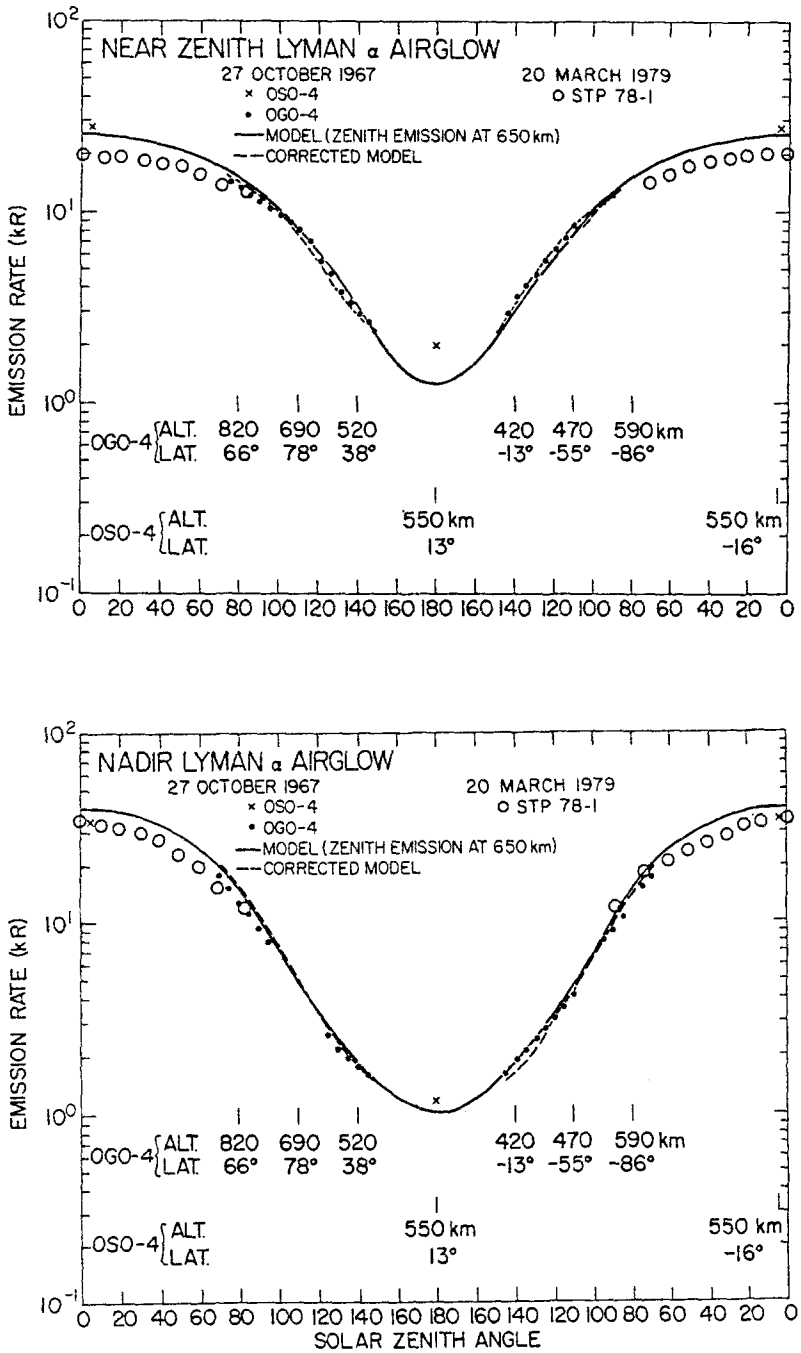

Fig. 19. Comparison of near zenith (15° OZA) and nadir (180° OZA) hydrogen Lα emission rates observed from the OGO-4, OSO-4 (Meier and Mange, 1983), and STP 78-1 (Anderson *et al.*, 1987a) spacecraft. The solid line is a model computation for a spherically-symmetric geocorona, observed from 650 km; the dashed curve is the same model corrected for the altitude variation of OGO-4. Part of the discrepancy between the model and OSO-4 zenith data at night is due to the interplanetary Lα emission.

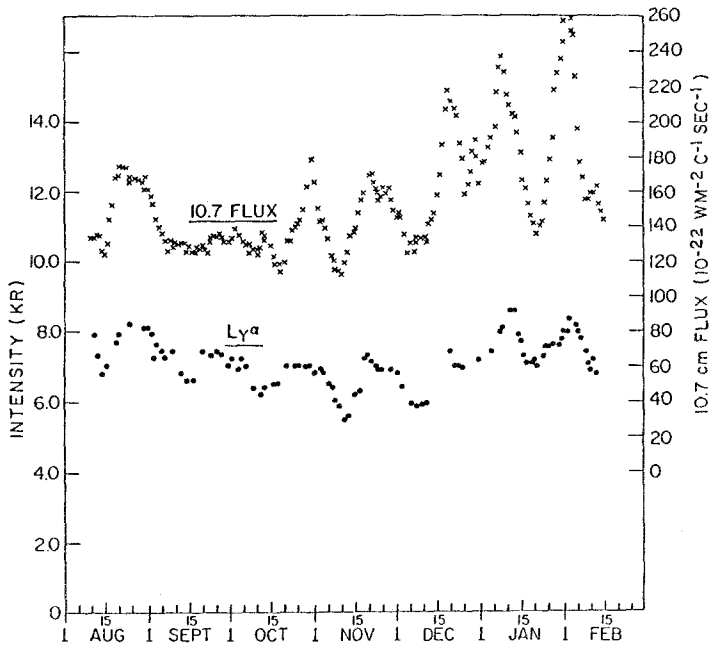

Fig. 20. Near-zenith (15 deg) Lα emission rates at 110 deg solar zenith angle observed from OGO-4 and the solar 10.7 cm flux from August 1967 through February 1968 (Meier and Menge, 1970).

varies with solar energy input and because the 10.7 emission is not an exact substitute for the solar Lα line center irradiance (Meier and Mange, 1973; Thomas and Anderson, 1976; Lean, 1987).

It has long been recognized that the O I radiative recombination emissions in the night airglow provide a means of monitoring the ionospheric electron density profile in the *F*-region (Chandra *et al.*, 1975; Tinsley and Bittencourt, 1975). However, during the day the weak recombination emissions are overwhelmed by solar induced emissions. An alternative candidate for remote sensing of the *F*-region during the day has been found in the O II triplet at 834 Å (Feldman *et al.*, 1981; Kumar *et al.*, 1983; Anderson and Meier, 1985; McCoy *et al.*, 1985). The O II emission rate in the *F*-region is due ultimately to photoionization of atomic oxygen at lower altitudes. Some of these O^+ ions are produced in the ^4P state, spontaneously emitting an 834 Å photon. Ambient ground state O^+ (^4S) in the *F*-region is illuminated from below by this photoionization radiation, and multiply scatters the 834 Å photons several times before they are lost from the atmosphere. In the multiple scattering process, the 834 Å radiation field takes on the character of the *F*-region. The zenith and nadir 834 Å emission rate for a daytime pass of the STP 78-1 satellite at 600 km is shown in Figure 21 (Kumar *et al.*, 1983). The zenith airglow reflects the upwelling of the equatorial *F*-region resulting from $\mathbf{E} \times \mathbf{B}$ vertical plasma drift. The nadir shows additional structure below the spacecraft, reflecting the dynamic behavior of the equatorial ionosphere.

The helium 584 Å dayglow is produced by resonant scattering of the solar He I line.

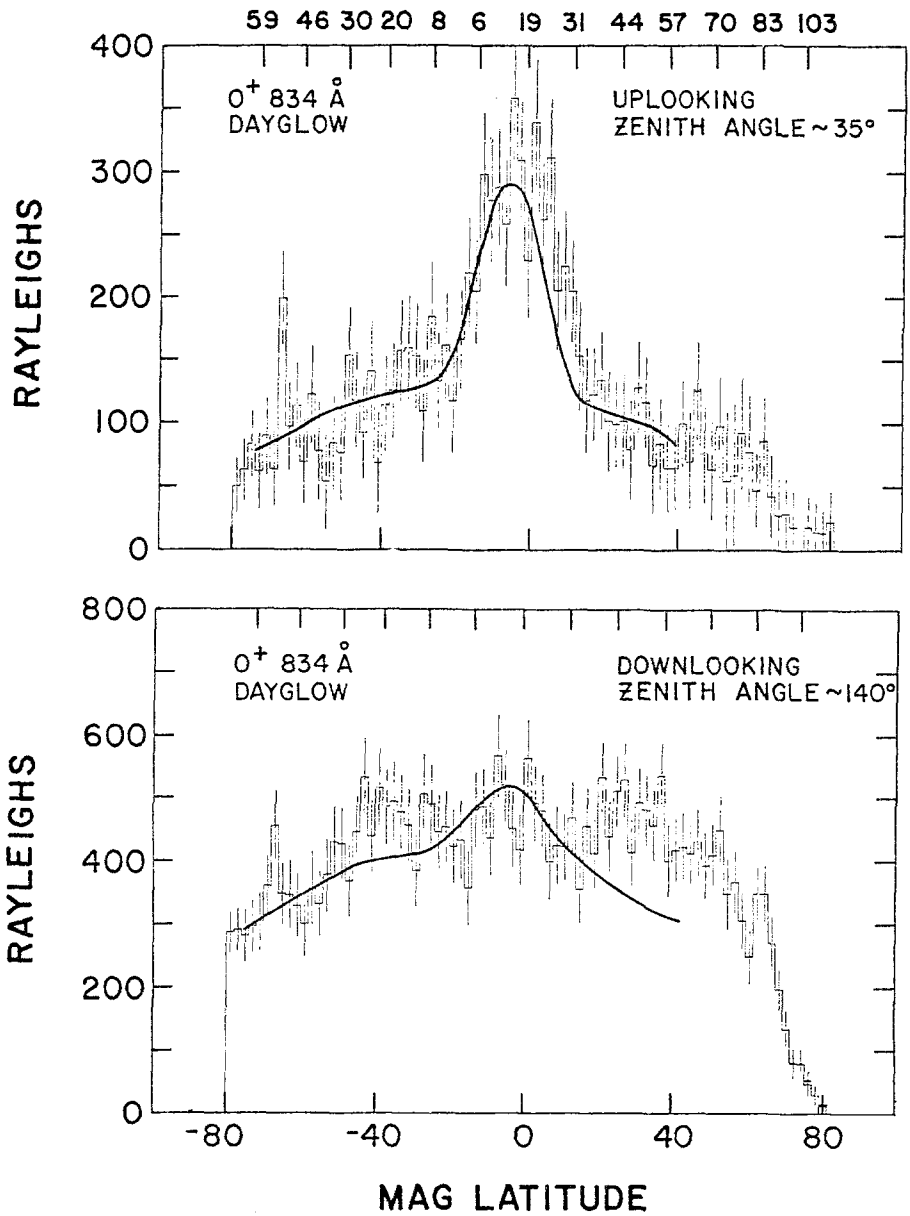

Fig. 21. Upviewing and downviewing O II 834 Å column emission rates observed during orbit 409 of the STP 78-1 satellite on 23 March, 1979 (Kumar *et al.*, 1983). The data are given by histograms, 1σ error bars by the vertical lines, and the dark solid line is a model calculation. Courtesy of S. Chakrabarti.

Meier and Weller (1974) and Anderson *et al.* (1979) analyzed observations from the STP 72-1 satellite from 740 km, showing that the airglow is quite sensitive to the atomic helium concentration. Figure 22 displays observations near zenith and near nadir for

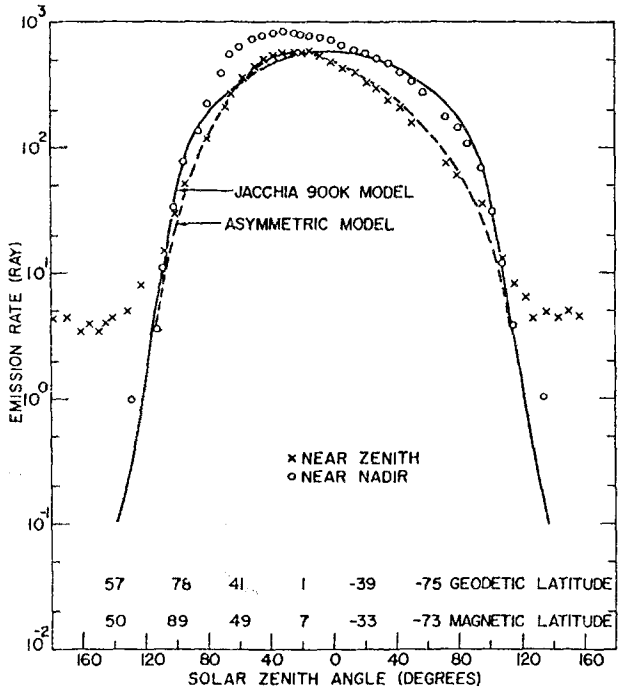

Fig. 22. He I 584 Å upviewing and downviewing airglow for one orbit of the STP 72-1 satellite on 16 November, 1972. The solid line is a theoretical model calculation of the zenith emission rate using a spherically-symmetric helium atmospheric model and the dashed curve uses a model which accounts for the winter helium bulge. The excess signal in the zenith at night is due to the interplanetary He 584 Å emission. Nadir data are contaminated by other emissions within the photometric passband. Taken from Meier and Weller (1974).

a single orbit of STP 72-1 (taken from Meier and Weller). The dayglow is brighter in the northern hemisphere, responding to the well-known winter helium bulge. The theoretical curves in the figure contrast the airglow computed with spherically-symmetric and asymmetric models of the helium concentration. At night the airglow is expected to decrease to low levels since, in contrast to hydrogen, the scale height of helium is too small to allow significant scattering of 584 Å photons into the night sector. Anderson *et al.* (1979) have published additional STP 72-1 data which exhibit a significant decrease in magnitude and a shift of the dayglow maximum to the northern hemisphere in August.

The He^+ Lα line at 304 Å displays a much different global variation than the photoelectron or resonant scattered emissions discussed so far. Helium ions trapped within the plasmasphere resonantly scatter the solar 304 Å line, providing the opportunity to image the plasmasphere out to several earth radii. (See Figure 6 of Meier and Weller (1972) for a sketch of the plasmasphere scattering geometry.) Figure 23, taken from Weller and Meier (1974), contains a plot of observations made near zenith from the STP 72-1 satellite at 740 km. During the day, the plasmasphere is uniformly illumi-

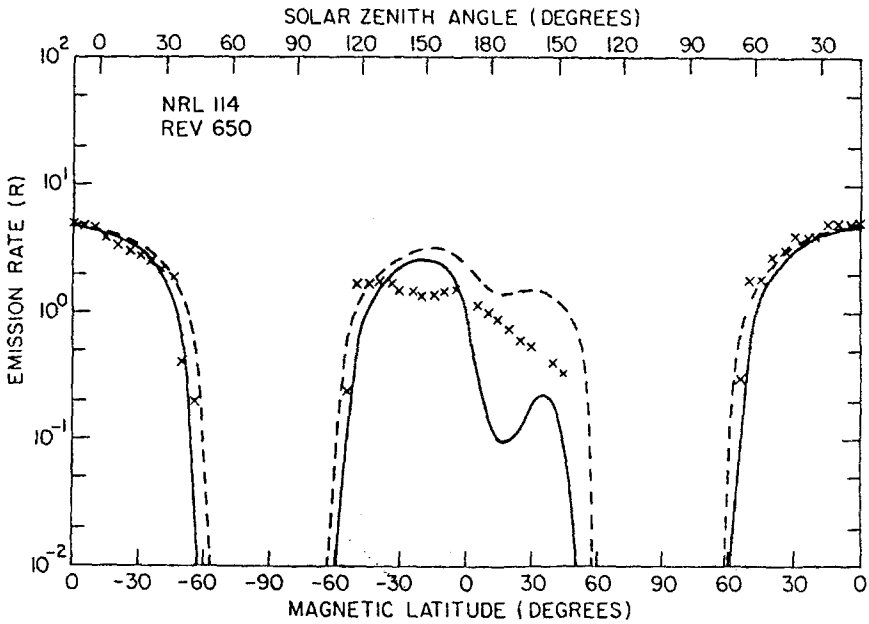

Fig. 23. He II 304 Å near-zenith column emission rate for Pass 650 of STP 72-1 on 16 November, 1972. The data are given by Xs, and the solid and dashed lines are model calculations of resonant scattering from plasmaspheres with boundaries of 3 and 4.25 earth radii at the equator. The emission rate is low over the poles because helium ions are not populous where the geomagnetic field lines are open. Taken from Weller and Meier (1974).

nated under optically thin conditions, and not much structure is evident. Over the poles, no trapped He^+ is present due to the open magnetic field lines. At night the occulting Earth shadows part of the plasmasphere, the geometric extent depending on the orientation of the plasmasphere to the Sun and the location of the plasmapause (the boundary between closed and open field lines). Two theoretical models are shown for plasmapause values of $L = 3$ and 4.25 earth radii at the magnetic equator. The actual variation throughout the night depends sensitively on the details of the viewing geometry and the field-of-view of the instrument. Other satellite observations of He II 304 Å airglow were made during the Apollo–Soyuz mission (Chakrabarti *et al.*, 1982).

EUV emissions associated with ring-current neutral helium precipitation have been observed by Meier and Weller (1975) and Paresce (1979). Broadband filter photometer data indicate that the emission occurs at 304 Å and below, probably due to recombination radiation from quasi-trapped He^{++} (Meier and Weller, 1975). Independent support for this view is from energetic particle detections by Hovestadt *et al.* (1972) and Scholer *et al.* (1975). A comparison of the helum ion observations of Hovestadt and the optical data of Meier and Weller, as well as hydrogen Balmer alpha emissions from Levasseur (1976), was made by Tinsley (1981). His comparison is reproduced in Figure 24, showing the strong latitudinal similarity between the helium ion and photon data. The hydrogen emission shows a much different structure. The helium emission varies strongly in intensity and latitudinal extent with ring-current indices and apparently

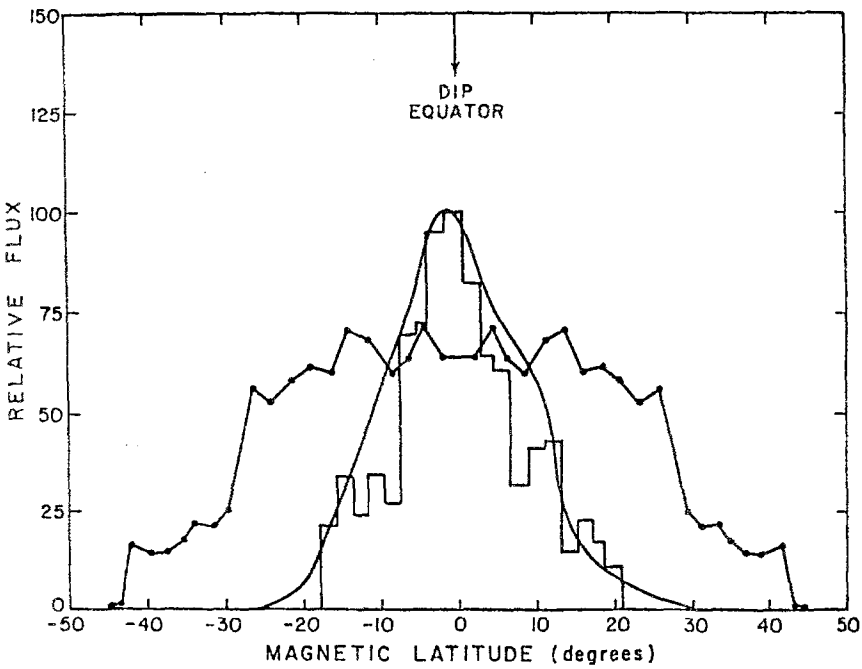

Fig. 24. Comparison of equatorial passes of satellite observations of MeV low altitude trapped particles (histogram, taken from Hovestadt *et al.*, 1972), EUV optical radiation at 304 Å and below (smooth curve, taken from Meier and Weller, 1975) and H Balmer α emission observed by Levasseur (1976) (connected points, with the points for northern latitudes reflected into the southern hemisphere). Taken from Tinsley (1981).

are associated with particles having energies in the 100's of keV or MeV regimes (Meier and Weller, 1975).

2.4. Global Images

The first actual global images of the Earth in the FUV were obtained from the lunar surface during the Apollo-16 mission (Carruthers and Page, 1972, 1976b). This investigation produced truly dramatic pictures of the hydrogen geocorona, polar auroras, tropical airglow belts, and general airglow, as well as EUV and FUV spectra (Carruthers and Page, 1976a). Later experiments which provided FUV images of the Earth were flown by Bertaux (1978) on OGO-5; Kaneda *et al.* (1981) on the KYOKKO satellite; Frank and Craven (1988a) (and their many references) on the Dynamics Explorer DE-1; Meng and Huffman (1984) on HILAT; Meng and Huffman (1987) on POLAR BEAR; and Anger *et al.* (1987) on VIKING. Most of the analysis efforts on these programs have been directed at high latitude phenomena. For the present review, examples of global images from two missions have been chosen: Apollo-16 and DE-1. Observation conditions are given in Table I.

Three images taken while the Apollo-16 lander was on the Moon are shown in Figure 25. These images were taken with an electrographic camera and have been

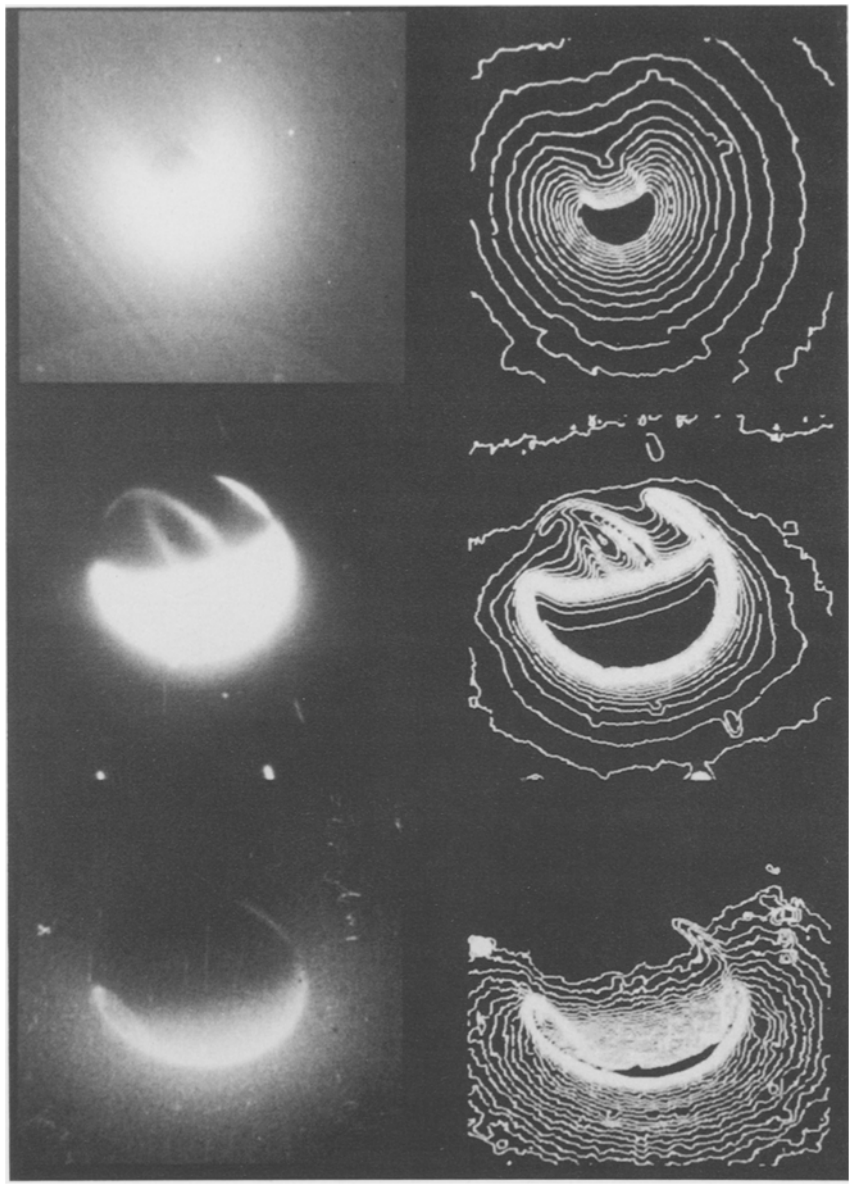

Fig. 25. Three FUV images of the Earth taken from the lunar surface during the Apollo 16 mission on 21 April, 1972 (Carruthers and Page, 1976b). The solar direction is to the lower left and north is at the upper left. The upper left (5 s exposure) and right (15 s) images covered the wavelength range of 1050–1600 Å, including H I Lα and thermospheric emissions. Polar aurora can be seen at the top and bottom. The center image is a 10 min exposure covering the 1250–1600 Å range. The day airglow on the disk is overexposed, but the ionospheric tropical arcs are clearly seen at night. Stars can be seen in the background. Isophotes for each image are shown in the panels below each image.

reproduced from Carruthers and Page (1976b). The upper left image in Figure 25 is a short exposure covering the 1050–1600 Å band. A densitometry trace is shown in the lower left. The solar direction is from the lower left, north is to the upper left, and the terminator produces a crescent shape for the dayglow since the Sun–Earth–Moon angle was 105 deg. The emission rate on the planetary disk is mostly due to H I 1216 Å and O I 1304 Å. Lα can be seen extending above the Earth limb. The auroral oval and polar cap can be seen in the north, but the southern aurora can only be seen edge-on. The auroral emission is due to O I and N_2 radiation.

The upper central image in Figure 25 is a long exposure electrograph taken with a CaF_2 filter which limits the wavelength band to 1250–1600 Å, thereby excluding Lα. The dayglow, which is mostly O I 1304 Å emission in this passband, and the auroras are overexposed, but the weaker nightglow due to O I 1304 and 1356 Å radiation can be clearly seen as arcs straddling the magnetic dip equator. As discussed above, these are manifestations of the recombination of O^+ in the *F*-region at night. Weaker recombination radiation can be seen at mid-latitudes in the densitometer trace in the lower central image. This image illustrates that it is indeed possible to make a global 'weather map' of the inosphere.

The upper right panel of Figure 25 is a long exposure image taken without the CaF_2 filter, showing the extension of the geocorona out to several earth radii. Other images show Lα scattering by the geocorona to beyond 100 000 km (Carruthers *et al.*, 1976; see also Mange and Meier, 1970; Wallace *et al.*, 1970; Thomas and Bohlin, 1972). Shadowing by the Earth reduces the emission rate in the direction away from the Sun, but significant foreground illumination from sunlit hydrogen, as well as multiply scattered radiation within the shadow, are present in the image. The Apollo-16 data show evidence for a 'geotail', or extension of the geocorona in the antisolar direction, consistent with earlier detections (Thomas and Bohlin, 1972; Bertaux and Blamont, 1973; see also Rairden *et al.*, 1986).

The University of Iowa experiment on the DE-1 satellite has been amazingly successful, returning more than 500 000 images of the Earth. Frank and Craven (1988a) review some of the more important results obtained so far from the experiment and show many examples of images. Their paper references the various investigations using DE-1 imaging data. Particularly illustrative examples of the ultraviolet Earth are shown in Figure 46 of Frank and Craven (1988a), reproduced here in Figure 26. Both images include hydrogen Lα and O I 1304 Å emissions. The left image is a polar view with the Sun direction from the upper left. In the right image the Sun is eclipsed by the Earth. North is up. In both images, the emission is entirely Lα above the limb, while on the disk, oxygen and some N_2 emissions are present in the dayglow and auroras. Recombination radiation in the tropical arcs can be seen in both images. The arcs do not converge toward the equator near midnight as they do in the Apollo-16 image. This is undoubtedly the result of different electric fields in the ionosphere for the two observations.

Other images so far unpublished show dramatic changes in the O I 1304 Å emission following geomagnetic storms (Craven and Frank, 1988). The emission is significantly depleted at high latitudes, showing regions of localized heating which are similar to the

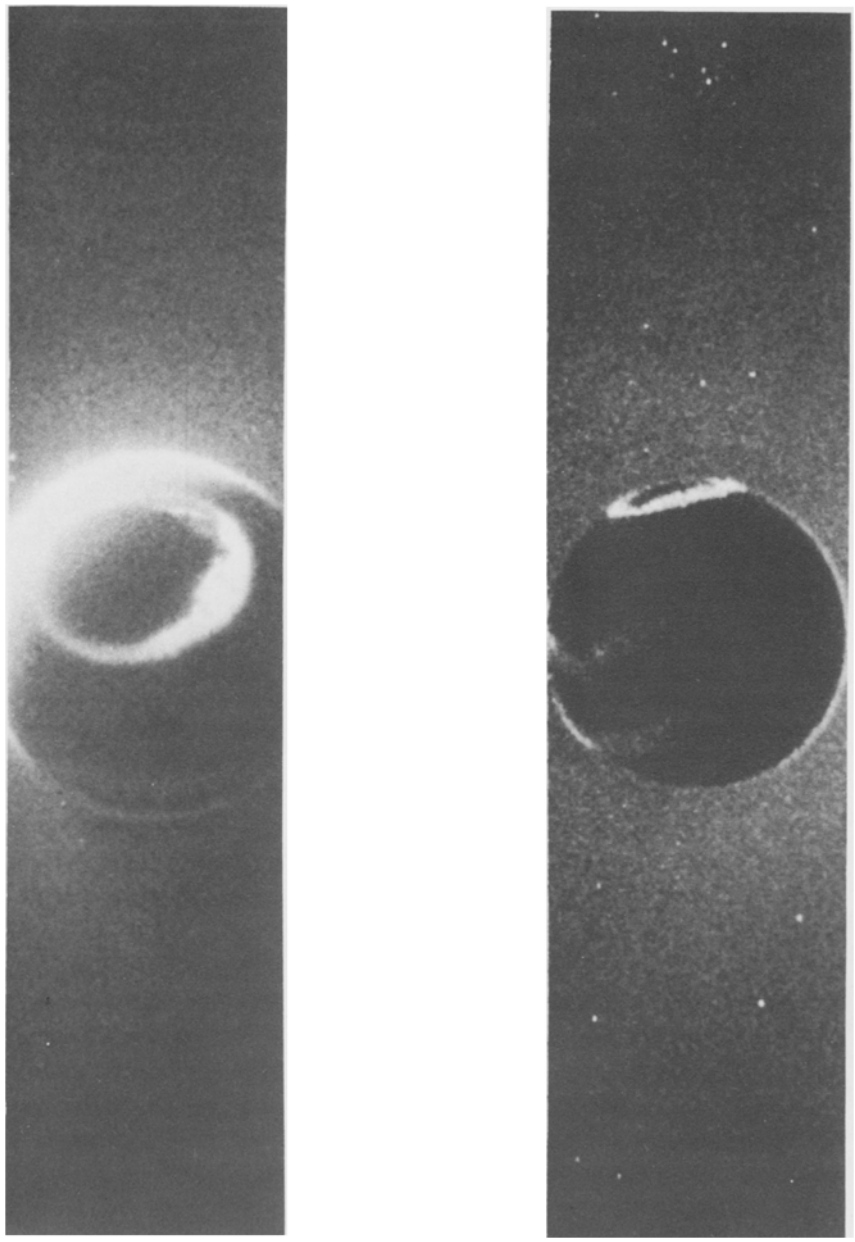

Fig. 26. Two FUV images of the thermosphere and hydrogen geocorona. The left image taken at 20 : 17 UT on 14 October, 1981 shows the northern hemisphere dayglow at the top, the auroral oval, and the projection of the ionospheric tropical arcs at night. The Sun is to the upper left. The right image taken at 02 : 22 UT on 16 February, 1982 shows the nightglow and aurora as the Earth eclipses the Sun. The emission above the Earth disk is due to H I Lα. Taken from Frank and Craven (1988).

depletions seen in S3-4 data (Figure 16). Study of these images as well as the spectroscopic data from the S3-4 experiment will likely lead to new ways of monitoring global heating during geomagnetically active periods.

A stunning and controversial result from the DE-1 imaging experiment is the report of 'hole-like' depletions in the O I 1304 Å dayglow, usually taking place over about a 0.32 deg pixel (Frank *et al.*, 1986a, b). The holes are dark, having a contrast of 5 to 29% of the surrounding airglow. On the average, they cover an area of 2000 km^2, last a few minutes, and have an occurrence frequency of 10 per minute on the day side of the Earth. Frank *et al.* (1986b) interpret these events as the result of small comet-like objects with a mass near 100 tons, and a speed of about 20 km s^{-1}. The objects are hypothesized to fragment in the vicinity of 2000 km altitude, producing a cloud of UV-absorbing water molecules between the spacecraft and the airglow. The cloud size is predicted to cover about a pixel when DE-1 is at apogee. As might be expected, there are profound implications of this interpretation. Many formal objections have been raised to the Frank *et al.* interpretation and have been countered by Frank *et al.* (see the 'Replys' in the references of Frank and Craven, 1988a). Undoubtedly, this controversy will continue into the foreseeable future.

3. Emission, Absorption, and Excitation Processes

In order to interpret the emissions described in Section 2 it is necessary to review the formal relationships between optical observables and atmospheric composition, dynamics, and energy inputs, and the assumptions routinely made in their applications. In this section, derivations of the appropriate formalism from basic principles are described. The theory of spectral line formation, which includes frequency changes in the scattering process, is discussed for both optically thick and thin atmospheres. Approximations which simplify the practical application to airglow problems are also discussed. Finally, the various energy sources responsible for excitation of the UV dayglow and nightglow are summarized and illustrated with selected examples. Only absorption and emission of resonance radiation are considered. Monochromatic scattering theory (e.g., Rayleigh scattering) using a similar approach has been developed by Meier *et al.* (1982a).

3.1. Radiation Emission and Scattering Theory

3.1.1. *General Formalism*

The approach reviewed here is to begin from first principles with the non-local thermodynamic equilibrium form of photon-scattering theory using the frequency redistribution function developed by Hummer (1962, 1969). Hummer's formalism is also presented in the textbook by Mihalas (1978). A less rigorous description worked out by Holstein (1947, 1951) is a natural consequence of that approach, assuming that the opacity of the scattering medium is not high. As has been shown by many authors, Holstein's theory has many practical advantages for interpreting large bodies of data. Donahue and

co-workers have expanded upon Holstein's work and applied it to a variety of airglow problems (Donahue and Foderaro, 1955; Thomas, 1963; Donahue, 1965; Donahue and Meier, 1967; Strickland and Donahue, 1970; Doschek and Donahue, 1970; Donahue and Kumer, 1971).

The basic equations of radiative transfer are described herein assuming a Maxwell–Boltzmann distribution of velocities for atoms possessing two electronic states; the lowest state is discrete, but the upper state may be broadened due to its natural lifetime. For most applications in planetary atmospheres, the vast majority of atoms reside in the ground state; consequently, stimulated emission, collisional broadening and other redistribution processes affecting atoms in upper states can be ignored. For simplification of the radiative transport theory, loss of photons due to absorption by other species, multi-level atomic states (which involve branching to intermediate states or atomic fine structure), polarization, atmospheric temperature gradients, and geometric considerations are not included explicitly, but implementation of these features is indicated where appropriate. The theory allows for both external energy sources (resonant scattering of sunlight) and internal sources (i.e., energetic electron impact excitation or radiative recombination). Steady-state and stationary (no bulk flow) conditions are assumed for the scattering atmosphere. Anderson *et al.* (1987b) include the effects of motional perturbations in treating the geocoronal hydrogen scattering problem.

The fundamental quantity describing the radiation field is the spectral radiance, I (photon $\mathrm{cm}^{-2}\,\mathrm{s}^{-1}\,\mathrm{hz}^{-1}\,\mathrm{ster}^{-1}$), otherwise known by the radiative transfer community as the 'specific intensity'. The change of I at position $\mathbf{r}$ along a pathlength $\mathrm{d}s$ is given by the following differential equation,

$$\frac{\mathrm{d}I}{\mathrm{d}s} = -\chi I + \varepsilon\,, \tag{1}$$

where χ is the probability per cm at a given frequency of a photon being scattered out of the beam of radiation (sometimes called the extinction coefficient), and ε is the volume emissivity, or number of photons $\mathrm{cm}^{-3}\,\mathrm{s}^{-1}\,\mathrm{hz}^{-1}\,\mathrm{ster}^{-1}$ being emitted into the beam. This equation has the formal solution,

$$I[\mathbf{r}, \hat{n}, \nu] = I[\infty, \hat{n}, \nu] \exp[-\tau[\infty, \mathbf{r}, \nu] - t_a[\infty, \mathbf{r}]] + \\ + \int \varepsilon[\mathbf{r}, \hat{n}, \nu] \exp[-\tau[\mathbf{r}, \nu] - t_a[\mathbf{r}, \mathbf{r}']]\,\mathrm{d}s\,, \tag{2}$$

where ∞ symbolizes an external radiation source and $\mathbf{r}'$ is the position along the path where emission occurs; $\mathrm{d}s = \mathrm{d}|\mathbf{r} - \mathbf{r}'|$. The optical depth, τ, is defined as

$$\tau[\mathbf{r}', \mathbf{r}, \nu] = \int_{s[\mathbf{r}']}^{s[\mathbf{r}]} \sigma[\nu]\rho[\mathbf{r}]\,\mathrm{d}s = \tau_0[\mathbf{r}', \mathbf{r}]\phi[\nu]\,, \tag{3}$$

where σ is the resonant scattering cross section at frequency ν, and ρ is the concentration (atoms cm^{-3}) of atomic scatterers. In Equation (3), τ_0 is the optical depth at the center of the absorption line (the product of the absorption cross section at line center and the column concentration of atoms in an isothermal, Maxwellian medium), and ϕ is the frequency dependence of the absorption cross section, which will be derived below (Equations (14) or (18)). Strickland (1979) has shown how to include temperature gradients in the theory. The optical depth due to pure absorption (absorptive loss of photons along the path) is t_a. Often, t_a is independent of frequency over the range of the emission line and is given by the product of the absorption cross section and the column concentration of absorbers. For the remainder of this section, pure absorption is not included explicitly.

The volume emissivity is described by the sum of two terms, one related to the internal generation of radiation (via, say, collisional excitation), ε_0, and the other to the rate of scattering:

$$\varepsilon[\mathbf{r}, \hat{n}, \nu] = \varepsilon_0[\mathbf{r}, \hat{n}, \nu] + \int\int k[\mathbf{r}', \hat{n}', \nu', \hat{n}, \nu] I[\mathbf{r}', \hat{n}', \nu'] \, d\nu' \, d\Omega'/4\pi \,. \quad (4)$$

In Equation (4), the scattering coefficient, k, is defined as the probability per cm per unit frequency that a photon of frequency ν' incident on a volume of atoms at $\mathbf{r}'$ from direction $\hat{n}'$ will be scattered into direction $\hat{n}$ at frequency ν. For resonant scattering of sunlight, I in Equation (4) is the sum of two terms, one representing the multiply scattered radiation field and one due to unscattered solar photons, if any (see Section 3.1.3).

The scattering coefficient for an ensemble of atoms with velocity distribution $\rho[\mathbf{r}, \mathbf{v}]$ is given by

$$k[\mathbf{r}, \hat{n}, \nu] = \frac{h\nu_0}{4\pi} B_{12} \int R[\hat{n}', \nu', \hat{n}, \nu, \mathbf{v}] \rho[\mathbf{r}, \mathbf{v}] \, d\mathbf{v} \,, \quad (5)$$

where ν_0 is the frequency at the center of the resonance line, B_{12} is the Einstein absorption coefficient from level 1 to 2. R is Hummer's (1962, 1969) redistribution function, which describes the change in frequency of a photon undergoing a scattering. $R \, d\nu \, d\nu' \, d\Omega \, d\Omega'/(4\pi)^2$ is the total probability per atom with velocity $\mathbf{v}$, that a photon from direction $\hat{n}'$ in the solid angle $d\Omega'$ and in the frequency interval ν' to $\nu' + d\nu'$ will be scattered into direction $\hat{n}$ in the solid angle Ω and in the frequency range ν and $\nu + d\nu$. Integration of R over the independent variables yields unity. The factors in front of the integral in Equation (5) equal the integral of the absorption cross section over frequency, σ_T (Mitchell and Zemansky, 1961). They are also related to the oscillator strength (or ratio of the strength of the electronic transition in the atom to that of an electric dipole transition between two states of a simple harmonic electron oscillator) in the following way:

$$\sigma_T = \int \sigma[\nu] \, d\nu = \frac{\pi e^2}{mc} f_{12} = \frac{h\nu_0}{4\pi} B_{12} \,.$$

The velocity distribution $\rho[\mathbf{r}, \mathbf{v}]$ can be expressed as the product of the total concentration $\rho[\mathbf{r}]$ and the velocity distribution $P(\mathbf{v})$. Equation (5) can now be written more compactly as

$$k = \sigma_T \rho[\mathbf{r}] R[\hat{n}', v', \hat{n}, v] \tag{6}$$

and

$$R[\hat{n}', v', \hat{n}, v] = \int R[\hat{n}', v', \hat{n}, v, \mathbf{v}] P[\mathbf{v}] \, d\mathbf{v} . \tag{7}$$

The Maxwell–Boltzmann velocity distribution is given by

$$P(\mathbf{v}) = \frac{1}{(\sqrt{\pi}\,\bar{v})^3} \exp[-v^2/\bar{v}^2] ,$$

where $\bar{v} = \sqrt{(2kT/M)}$ is the thermal velocity, T is the temperature of the scattering medium, and M is the atomic mass.

Substitution of Equations (2) and (6) into Equation (4) gives an integral equation for the volume emissivity which completely describes the frequency distribution of the radiation field, including changes in frequency in the scattering process:

$$\varepsilon[\mathbf{r}, \hat{n}, v] = \varepsilon_0[\mathbf{r}, \hat{n}, v] + \sigma_T \rho[\mathbf{r}] \int\int I[\mathbf{r}', \hat{n}', v'] R[\hat{n}', v', \hat{n}, v] \, dv' \, d\Omega'/4\pi . \tag{8}$$

In general the solution of Equation (8) is formidable because the volume emissivity is a function of frequency, direction, and location in the atmosphere and algebraic forms of the redistribution function are complex. Even for resonant scattering of sunlight under optically thin conditions, the functional form of the emissivity is complicated if the solar irradiance varies with frequency or if the velocity distribution is non-Maxwellian (see Meier (1975, 1977) for examples of these situations). It remains to complete the description of the redistribution function, the absorption coefficient, and to discuss tractable forms for the volume emissivity and the radiance.

3.1.2. *Frequency Redistribution and the Absorption Cross Section*

Following Hummer (1962), the redistribution function is defined as the product of three probabilities:

$$R = f[\xi'] p[\xi', \xi] \Phi[\hat{n}', \hat{n}] , \tag{9}$$

where $f[\xi']$ (using the same symbolism as Hummer, 1962, 1969) is the (absorption) probability of a transition from the lower level of the atom to the upper level at frequency ξ' in the rest frame of the atom, $p[\xi', \xi]$ is the probability of emission at rest frame frequency ξ following an absorption at frequency ξ', and Φ is the angular scattering probability (phase function). $\Phi = 1$ for isotropic scattering. The relationships between the atomic rest frame and observer frame frequencies are given by the usual Doppler

shift conditions:

$$\nu' = \xi' + \nu_0 \frac{\hat{n}' \cdot \mathbf{v}}{c}$$

and

$$\nu = \xi + \nu_0 \frac{\hat{n} \cdot \mathbf{v}}{c} . \tag{10}$$

Hummer (1962) and Mihalas (1978) describe four forms of the redistribution function probabilities. Two are applicable to UV airglow emission line problems, and are discussed next.

Case I: Discrete upper and lower states, and coherent scattering in the rest frame of the atom

This case applies to those scattering problems where the natural wings of the emission line can be ignored. Experience has shown that for UV emission lines in the airglow, Case I is appropriate if the optical depth at the center of the line is low to moderate (of the order of or less than several hundred, the exact value depending on the problem). While the derivation of the redistribution function needed to obtain the volume emissivity is presented here, in practice it is unnecessary to undertake the laborious task of solving Equation (8). A much simpler form for the radiative transport equation is described in Section 3.1.4.

In Case I, photon absorption can only take place at the line center frequency in the rest frame of the atom, ν_0, which corresponds to the energy difference between the two levels. The absorption probability has the following form:

$$f[\xi'] = \delta[\xi' - \nu_0] , \tag{11}$$

where δ is the Dirac delta function. Equation (11) is a statement of the fact that photons can only be absorbed at line center in the rest frame of the atom since the lower and upper states are discrete. The emission probability is given by

$$p[\xi', \xi] = \delta[\xi' - \xi] . \tag{12}$$

The frequency coherence required by Equation (12) is simply a statement of conservation of energy. Substituting Equations (10) into (11) and (12), substituting these into Equation (9), and integrating (Equation (7)) over the Maxwell–Boltzmann velocity distribution, yields the following analytic form for the redistribution function (Hummer, 1962; Mihalas, 1978):

$$R = \frac{\Phi[\hat{n}]}{\pi \sin\theta} \exp[-x^2 - (x' - x\cos\theta)^2 \operatorname{cosec}^2\theta] , \tag{13}$$

where θ is the angle between the incoming and outgoing photons, x is the frequency

measured from line center in units of the Doppler width, and $\Delta\nu_D$ is the Doppler width:

$$\cos\theta = \hat{n}' \cdot \hat{n}\,, \qquad x = (\nu - \nu_0)/\Delta\nu_0\,, \qquad \Delta\nu_D = \nu_0\bar{v}/c\,.$$

R is symmetric in x and x'.

It is important to note that even though the scattering process is assumed to be coherent in the rest frame of the atom, frequency redistribution in the observer's frame occurs due to Doppler shifts from atoms moving with a distribution of velocities. In spite of this frequency coherence in the observer's frame, in those situations where Case I applies (negligible photon transport in the wings of the line), it can be shown (Thomas, 1967; Mihalas, 1978) that very little error is introduced when complete incoherence is assumed. Thus for those airglow problems in which the atmospheric optical depth is low to moderate (less than a few hundred optical depths), it is unnecessary to solve the full transport equation (Equation (8)) with the redistribution function given by Equation (13). The much simpler approximation of complete incoherence in the scattering process, known as complete frequency redistribution (CFR), can be used. It is discussed in Section 3.1.4.

The absorption cross section in the rest frame of an atom is given by

$$\sigma[\xi'] = \frac{\pi e^2}{mc} f_{12}\delta[\xi' - \nu_0]\,. \tag{14a}$$

Integrating this over the velocity distribution of the atoms yields the absorption cross section in the observer's frame:

$$\sigma[\nu] = \sigma_0 \exp[-x^2]\,, \tag{14b}$$

where $\sigma_0 = \sigma_T/\sqrt{\pi}\,\Delta\nu_D$ is the cross section at the center of the absorption line ($x = 0$). Equation (14b) is the usual Gaussian-shaped form of an absorption cross section when the natural wings of the line can be ignored; that is, when only the Doppler core of the line ($|x| < 3$) is important.

Case II: Discrete lower state, diffuse upper state, and coherent scattering in the atomic rest frame

This case is appropriate for atmospheric spectroscopy problems where the optical depth at the center of the line is of the order of or greater than 500 to 1000. There the optical depth in the natural wings of the line is large enough that photons with frequencies of several Doppler widths from line center can still be scattered. It has been shown by many authors (e.g., see references given in Mihalas, 1978) that when scattering occurs outside the Doppler core of the line, complete incoherence cannot be assumed; the photons retain a memory of their pre-scattered frequency. This is often called partial frequency redistribution (PFR).

In Case II, the upper state of the atom is broadened in energy due to its finite lifetime against radiative decay. Thus an atom can absorb photons not only at the line center frequency, but also in the natural wings of the line. The absorption probability in the

rest frame of the atom has a Lorentz profile:

$$f[\xi'] = \frac{\gamma}{\pi((\xi' - v_0)^2 + \gamma^2)} , \tag{15}$$

where $\gamma = A/4\pi$ and A is the transition probability (inverse of natural lifetime) of the upper state. The emission probability is still given by Equation (12). Again, going through the various substitutions and integrating Equation (7),

$$R = \frac{\Phi[\hat{n}', \hat{n}]}{\pi \sin\theta} \exp[-((x - x')/2)^2 \operatorname{cosec}^2[\theta/2]] \times$$

$$\times \phi[a \sec[\theta/2], ((x + x')/2) \sec[\theta/2]] , \tag{16}$$

where $a = \gamma/\Delta v_D$, and ϕ is the unnormalized Voigt function:

$$\phi[a, x] = \frac{a}{\pi} \int \frac{\exp[-y^2]\, dy}{(x - y)^2 + a^2} . \tag{17}$$

The numerical solution of the transport equation (8) with this redistribution function is exceedingly difficult. One method of simulating the full frequency redistribution function using probability theory with the Monte-Carlo method was derived by Lee (1974a, b, 1977). Following this pioneering work, Lee and Meier (1980) and Meier and Lee (1981) developed a radiation transport model which incorporated the Monte-Carlo simulation of R (Equation (16)) in the numerical solution of Equation (8). Other authors (see the references of Mihalas, 1978; Gladstone, 1982; Yelle and Wallace, 1989) have used a less accurate form of R, derived by assuming that when photon scattering occurs, the frequency dependence of R on scattering angle is not significant. Physically, this can be justified if the radiation field is isotropic. Then R can be integrated over all angles, yielding a less complex functional form. However, Meier and Lee (1981) found that the angle-averaged case can lead to inaccuracies (albeit they are not large for realistic scattering problems), and that care must be exercised when applying this approximation. Meier and Lee (1982) used the Monte-Carlo approach to solve the O I 1304 Å problem in the UV dayglow. Other applications of this model will be discussed in later sections of the review. Gladstone *et al.* (1987) and Link *et al.* (1988a) also modelled the O I optically thick airglow, but used the angle-averaged approximation.

The absorption cross section in the rest frame of a Lorentzian atom is given by

$$\sigma[\xi'] = \frac{\pi e^2}{mc} f_{12} \frac{\gamma}{\pi((\xi' - v_0)^2 + \gamma^2)} .$$

Integrating this over the Maxwell–Boltzmann velocity distribution gives

$$\sigma[v'] = \sigma_0 \phi[a, x'] . \tag{18}$$

If the natural wings of the line are ignored ($a = 0$), this reduces to the form given by Equation (14).

The reader is referred to the citations given in this section for more details on the solution of the equations of transport under high opacity conditions. The remainder of Section 3.1 discusses the more tractable forms of the solution.

3.1.3. *Single Scattering*

If the atmospheric opacity is small, the radiance given by Equation (2) reduces to the integration of the emissivity along a line-of-sight (assuming that the Sun is not along this line). Two excitation sources are considered in this section: photoelectron excitation and resonant scattering of sunlight.

In photoelectron impact excitation of an atom, the upper state is populated at a rate $g[\mathbf{r}]$ (excitations per second per atom); g will be defined physically in Section 3.2. The total volume excitation rate ($\mathrm{cm}^{-3}\ \mathrm{s}^{-1}$) is $g[\mathbf{r}]\rho(\mathbf{r})$. The frequency dependence of the emission probability, $p[\xi]$, depends on the number of substates populated in the upper level, and hence is described by the Lorentz function (or delta function if a discrete upper state is assumed) in the rest frame of the atom. When p is integrated over the velocity distribution of atoms (assumed to be unperturbed by the electron collisions), the emission profile in the observer's frame of reference is given by the Voigt function. Assuming the emission rate to be isotropic, the emissivity is given by

$$\varepsilon_0[\mathbf{r}, \nu] = \frac{g[\mathbf{r}]\rho[\mathbf{r}]}{4\pi} \frac{\phi[a, x]}{\sqrt{\pi}\,\Delta\nu_{\mathrm{D}}} . \tag{19}$$

The specific intensity or spectral radiance is

$$I[\mathbf{r}, \hat{n}, \nu] = \frac{1}{4\pi} \frac{\phi[a, x]}{\sqrt{\pi}\,\Delta\nu_{\mathrm{D}}} \int g[\mathbf{r}]\rho[\mathbf{r}]\,\mathrm{d}s , \tag{20}$$

where the path $\mathrm{d}s$ is along the direction $\hat{n}$. Since there is usually little emission in the wings of the line, the Doppler profile (Equation (14)) can be used in Equation (20). By measuring the profile of the emission line, the temperature of the atmosphere can be obtained from the Doppler width. The frequency dependence must be included in the integral if the region of the atmosphere is not isothermal.

Integration of I over frequency yields the usual expression

$$I[\mathbf{r}, \hat{n}] = \frac{1}{4\pi} \int g[\mathbf{r}]\rho[\mathbf{r}]\,\mathrm{d}s . \tag{21}$$

The above comments on the line profile do not apply if the excited atom is produced in a molecular dissociation process because excess energy is carried by the kinetically fast fragments, leading to an emission profile which is much broader than the thermal Doppler width (e.g., Erdman and Zipf, 1987). Non-Doppler profiles are also produced from heavy atom impact excitation, from dissociative recombination of molecular ions, and from charge exchange with fast moving (precipitating) ions.

For resonant scattering of sunlight under optically thin conditions, I in Equation (8)

is given symbolically by $\pi F\,\delta[\Omega - \Omega_s]$ where Ω_s is a solid angle in the direction of the Sun and πF is the solar spectral irradiance (photons $\mathrm{cm}^{-2}\,\mathrm{s}^{-1}\,\mathrm{hz}^{-1}$). Since solar emission lines are much broader than the terrestrial Doppler width, πF can usually be assumed constant. Substituting the redistribution function into Equation (8), and integrating over direction and over the incoming (solar) frequency yields the following expression for the emissivity after the first scattering of solar photons:

$$\varepsilon_s[\mathbf{r}, \hat{n}, \nu] = \Phi[\hat{n}, \hat{n}]\,(\pi F \sqrt{\pi}\,\Delta\nu_{\mathrm{D}})\sigma_0 \rho[\mathbf{r}]\,\frac{\phi[x]}{\sqrt{\pi}\,\Delta\nu_{\mathrm{D}}}\,. \tag{22}$$

Thus for a continuum excitation source, the emission profile is also characteristic of the velocity distribution of scatterers. The quantity

$$g_s = (\pi F \sqrt{\pi}\,\Delta\nu_{\mathrm{D}})\sigma_0 = \frac{\pi e^2}{mc} f_{12}\pi F \tag{23}$$

is the usual form of the solar g-factor (photons scattered per sec per atom). Thus Equations (20) and (21) for photoelectron excitation apply to solar resonance scattering as well, wherever the solar source is a continuum. For a monochromatic external source, Meier (1981) examined the complex behavior of the single-scattered spectral radiance as a function of incident frequency.

3.1.4. *Complete Frequency Redistribution*

In Section 3.1.3, the general expressions for the volume emissivity and the radiance were seen to reduce to familiar relationships when single scattering applies. In previous sections the difficulty of solving the transport equation (8) was alluded to, but it was noted that if the opacity of the scattering atmosphere (usually defined as the vertical optical depth from the top of the atmosphere down to an altitude where scattering is no longer important or where extinction dominates) is less than a few hundred, the redistribution function could be simplified by assuming that there is complete incoherence of frequency in the scattering process. This is known as complete frequency redistribution (CFR).

The physical justification for CFR is that incident photons with frequencies in the Doppler core of the line are mostly scattered by atoms with velocities near the thermal speed. The scattered photon also has a frequency within the Doppler core since the atomic velocity does not permit a greater frequency shift relative to line center ($-x' \leq x \leq x'$). It can be shown that there is nearly equal probability of the emitted frequency lying in this range (Jefferies and White, 1960), demonstrating the independence of the absorption and emission frequencies. On the other hand, if the incident photon has a frequency well outside the Doppler core, there are a few atoms moving fast enough to absorb the photon at line center in their rest frames; it is more likely that the photon will be absorbed in the natural wings. Because the atoms are effectively at rest for scattering large frequency photons, there is little frequency redistribution. For an atmospheric optical depth of 200 at line center, unit optical depth occurs near $x = 2.3$

Doppler widths from line center for typical values of the Voigt parameter, a. When the optical depth is greater than approximately 200, scattering in the wings of the line becomes important and allowance must be made for partial redistribution in frequency (PFR). The term PFR is used to describe the combination of incoherent scattering in the Doppler core and approximately coherent scattering in the natural wings. Experience has shown PFR becomes important when the line center optical depth reaches the range 200–1000, the precise value depending on details of the problem. More detailed discussions of these points are given by Mihalas (1978), Strickland and Donahue (1970), Jefferies (1968), Jefferies and White (1960), Thomas (1957), and their references.

CFR means that the absorption and emission parts of the redistribution function are separable, and have the same functional form:

$$R[x', x] = \Phi[\hat{n}', \hat{n}] \frac{\phi[x']}{\sqrt{\pi}\,\Delta\nu_D} \frac{\phi[x]}{\sqrt{\pi}\,\Delta\nu_D} . \tag{24}$$

As will be seen next, a tremendous simplification of the transport equation occurs with this form of R, namely, that the frequency dependences can now be factored and frequency-independent emissivities and radiances can be obtained.

Substitution of Equation (24) into (8) yields the following form of the transport equation:

$$\varepsilon[\mathbf{r}, \hat{n}, x] = \varepsilon_0[\mathbf{r}, x] + \sigma_T \rho[\mathbf{r}] \Phi[\hat{n}', \hat{n}] \frac{\phi[\mathbf{x}]}{\sqrt{\pi}\,\Delta\nu_D} \times$$

$$\times \int\int I[\mathbf{r}', \hat{n}', x'] \frac{\phi[x']}{\sqrt{\pi}\,\Delta\nu_D} \, dx' \, d\Omega' . \tag{25}$$

All of the terms in Equation (25) have the common factor $\phi(x)/\sqrt{\pi}\,\Delta\nu_D$, which can be eliminated, leaving frequency-independent emissivities. Equation (25) can now be cast into an integral equation for ε by substituting I from Equation (2). Assuming isotropic scattering, the emissivity is given by

$$\varepsilon[\mathbf{r}] = \varepsilon_0[\mathbf{r}] + \varepsilon_s[\mathbf{r}] + \frac{\sigma_0 \rho[\mathbf{r}]}{4\pi} \frac{d\Omega'}{4\pi} \int \varepsilon[\mathbf{r}'] G[\mathbf{r}', \mathbf{r}] \, ds , \tag{26}$$

$\varepsilon[\mathbf{r}]$ now has units of photon cm^{-3} s^{-1} $ster^{-1}$. $G\,d\mathbf{r}'\,d\mathbf{r}$ is the Holstein (1947) probability that a photon emitted in $d\mathbf{r}'$ at $\mathbf{r}'$ will be absorbed in a volume element $d\mathbf{r}$ at $\mathbf{r}$:

$$G[\mathbf{r}', \mathbf{r}] = \frac{1}{\sqrt{\pi}} \int \phi^2[x'] \exp[-\tau_0[\mathbf{r}', \mathbf{r}] \phi[x']] \, dx' , \tag{27}$$

where τ_0 is the optical depth at line center between $\mathbf{r}'$ and $\mathbf{r}$. The expression for the solar resonant scattering excitation source is determined as in Section 3.1.3, with the Dirac delta function applied to the first term in Equation (2). However, account must now be

taken of the attenuation of the sunlight:

$$\varepsilon_s[\mathbf{r}] = \frac{\sigma_0 \rho[\mathbf{r}]}{4\pi} (\pi F \sqrt{\pi}\, \Delta\nu_D) T[\tau_s], \tag{28}$$

where T is the Holstein (1947) probability that a photon will traverse a path with optical depth τ and be scattered at $\mathbf{r}$:

$$T[\mathbf{r}', \mathbf{r}] = \frac{1}{\sqrt{\pi}} \int \phi[x'] \exp[-\tau[\mathbf{r}', \mathbf{r}]\phi[x']]\, dx' . \tag{29}$$

Equation (26) for the emissivity can be cast into matrix form and solved for both plane parallel (e.g., Strickland and Donahue, 1970) and spherical (Anderson and Hord, 1977) geometries.

Phase functions and polarization effects can be included to first order by assuming that the multiply scattered part of the emissivity is isotropic and unpolarized. The appropriate functions can then be applied to ε_0 alone. A more complete treatment of polarization using this approach is given by Kumer (1974).

The advantage of solving the integral equation (26) for the emissivity, rather than the differential equation (1) for the radiance is now apparent. To analyze a body of data containing many viewing directions, the equation of transfer has to be solved only once. The radiance can then be computed for any location and viewing direction with a single integral:

$$I[\mathbf{r}, \hat{n}] = \int \varepsilon[\mathbf{r}'] T[\mathbf{r}', \mathbf{r}]\, ds . \tag{30}$$

Transformation to optical depth as the independent variable is often done to facilitate the numerical solutions. The equation for the emissivity becomes an equation for the source function, normalized to the strength of the excitation source:

$$S[\tau] = S_0[\tau] + \int \frac{d\Omega'}{4\pi} \int S[\tau'] G[\tau', \tau]\, d\tau' , \tag{31}$$

where

$$S_0 = \frac{4\pi\varepsilon_0[\mathbf{r}]}{\sigma_0 \rho[\mathbf{r}]} = \frac{g[\mathbf{r}]}{\sigma_0} \quad \text{for photoelectron excitation},$$
$$S_0 = \frac{4\pi\varepsilon_s[\mathbf{r}]}{\sigma_0 \rho[\mathbf{r}]} = (\pi F \sqrt{\pi}\, \Delta\nu_D) T[\tau_s] \quad \text{for solar excitation}. \tag{32}$$

The radiance is then given by

$$I[\mathbf{r}, \hat{n}] = \frac{1}{4\pi} \int S[\tau'] T[\tau']\, d\tau' . \tag{33}$$

The transport equation reduces to a one-dimensional equation when plane-parallel geometry is used. The optical depth is related to the vertical optical depth by $\tau = \tau_v \cos\theta$, where θ is the angle from local vertical, and the equation for the source function becomes

$$S[\tau] = S_0[\tau] + \int S[\tau']H[\tau', \tau]\,d\tau' , \tag{34}$$

where

$$H[\tau', \tau] = \frac{1}{2\sqrt{\pi}} \int \phi^2[x']E_1[|\tau' - \tau|\,\phi[x']]\,dx'$$

is the Holstein G probability for planar geometry and E_1 is the first exponential integral. As long as the atomic level populations are not affected significantly by scattering, the transport equation can be solved independently for either the solar or the photoelectron sources. The emissivities and radiances can be combined linearly.

The transport equation (34) is sometimes cast into the following form (Donahue and Fastie, 1964):

$$S[\tau] = \frac{S_0[\tau]}{E[\tau]} + \frac{1}{E[\tau]} \int (S[\tau'] - S[\tau])H[\tau', \tau]\,d\tau' , \tag{35}$$

where

$$E[\tau] = 1 - \int H[\tau', \tau]\,d\tau'$$

is the probability of a photon at level τ escaping from the medium. E^{-1} is approximately the mean number of scatterings before escape, $\langle N \rangle$. Equation (35) is a useful form of the transport equation, since the first term often is a reasonable first approximation to the source function:

$$S[\tau] \approx S_0[\tau]/E[\tau] \approx S_0[\tau]\,\langle N \rangle . \tag{36}$$

That is, the initial excitation rate times the mean number of scatterings approximates the final excitation rate. This approximation amounts to requiring a slow variation of the source function with optical depth, so that the integrand in Equation (35) is small. It breaks down when the initial excitation source consists of a narrow layer. In that case, S_0 is essentially zero throughout most of the atmosphere, but S may not be small because of higher-order scattering.

3.1.5. *Multi-level Atoms and Molecules*

The emission concepts in the previous section considered only idealized two-level atoms. If an intermediate third state exists, simple modification can be made to the emissivity and radiance to include what is essentially non-conservative scattering (Meier, 1969, 1982). If fine structure is present in the upper state of the atom, often the problem can be treated as the sum of several independent transitions. An example of

this is the O II 834 Å problem which has a single lower level and a triplet upper level (Anderson and Meier, 1985). However, if the energy differences of the split levels are close, mixing of the levels can take place (Meier *et al.*, 1987). Fine structure in the ground state can also be accomodated by allowing for the coupling among states (Strickland and Donahue, 1970; Meier and Lee, 1982).

Molecular emission processes are complicated by the necessity of including vibrational-rotational phenomena. For photoelectron excitation, g-factors can be defined in the same way as for atoms. In some cases cross sections have been measured for excitation to the individual vibrational levels of the excited electronic state (e.g., Ajello and Shemansky, 1985). A synthetic spectrum of the molecule is required to partition the resulting emission rate into rotational lines and vibrational bands. For resonant scattering of sunlight, Barth (1964, 1966) has defined a fluorescence g-factor which accounts for excitation from the ground vibrational level $v'' = 0$ to an excited vibrational v', followed by re-emission to another ground vibrational level, v'':

$$g_{v'v''} = \frac{\pi e^2}{mc} f_{12} \pi F_{0v'} q_{0v'} B_{v'v''} , \tag{37}$$

where f_{12} is the oscillator strength for the electronic transition (sum of the oscillator strengths for the individual band oscillator strengths between the $v'' = 0$ level of the ground state and all v' levels of the upper state), q is the Franck–Condon factor, and $B_{v'v''}$ is the branching ratio for the band of interest. For optically thin conditions, the product of the g-factor and the molecular column concentration gives the column emission rate.

Multiple scattering of rotational lines of molecules is more difficult to deal with because account must be taken of the coupling among the many levels. Kumer and James (1974) and Conway (1982, 1983) have worked out the formalism using CFR theory. Self-absorption has also been discussed by Cravens (1977). Even if the atmospheric optical depth is large for a given rotational line, the molecular scattering problem is often 'effectively thin': that is, when there is a large branching probability to other rotational levels for which the opacity is small, the photon is lost from the system after only a few scatterings.

3.1.6. *Some Emission Line Parameters*

Numerical values of parameters discussed in Section 3.1 are listed in Table IV for some important airglow features which undergo multiple scattering in the upper atmosphere. An atmospheric temperature of 1000 K was chosen for the computations. Listed are the emission line, the oscillator strength, the transition probability (natural damping coefficient), Doppler width, a value, solar irradiance and solar g-factor. The latter two quantities are discussed in Section 3.2.1.2. For more details, see Section 4.

3.2. Excitation Processes

In this section the various physical processes responsible for the production of the UV airglow are reviewed. Examples of excitation rates and related quantities have been

TABLE IV

Atomic absorption and emission line parameters at 1000 K

	λ[b] (Å)	f_{12}	A (s^{-1})	$\Delta\lambda_D$ (Å)	σ_0 (cm^2)	a	πF ($cm^{-2}\,s^{-1}\,Å^{-1}$)	g_s ($s^{-1}\,atom^{-1}$)	Ref.
H I	1215.67	4.162 – 01	4.699 + 08	1.647 – 02	1.865 – 13	1.119–03	2.200 + 11	1.198 – 03[c]	1
H I	1025.722	7.910 – 02	5.575 + 07	1.390 – 02	2.991 – 14	1.120 – 04	3.700 + 09	2.726 – 06	1
He I	584.334	2.762 – 01	1.799 + 09	3.959 – 03	1.190 – 13	4.119 – 03	1.360 + 10	1.135 – 05	1
He II	303.78	4.162 – 01	4.699 + 08	2.058 – 03	9.321 – 14	5.593 – 04	2.700 + 10	9.180 – 06	1
N I	1200.7098	4.600 – 02	4.240 + 08	4.348 – 03	7.618 – 14	3.732 – 03	[a]	[a]	2
	1200.2233	8.500 – 02	4.090 + 08	4.346 – 03	1.407 – 13	3.598 – 03	[a]	[a]	
	1199.5496	1.390 – 01	4.240 + 08	4.344 – 03	2.300 – 13	3.728 – 03	[a]	[a]	
O I	1358.5123	6.200 – 07	1.207 + 03	4.602 – 03	1.242 – 18	6.251 – 08	[a]	[a]	3
	1355.5977	1.250 – 06	4.575 + 03	4.592 – 03	2.499 – 18	6.251 – 08	[a]	[a]	
O I	1306.0286	4.850 – 02	6.400 + 07	4.424 – 03	9.340 – 14	6.027 – 03	2.600 + 09	1.900 – 06	3, 4, 5
	1304.8575	4.850 – 02	1.970 + 08	4.420 – 03	9.331 – 14	6.027 – 03	2.600 + 09	1.900 – 06	
	1302.1685	4.860 – 02	3.290 + 08	4.411 – 03	9.331 – 14	6.027 – 03	2.600 + 09	1.900 – 06	
O I	1028.1571	1.900 – 02	3.800 + 07	3.485 – 03	2.882 – 14	5.678 – 04	[a]	[a]	5
	1027.4313	4.800 – 03	3.040 + 07	3.483 – 03	7.277 – 15	5.678 – 04	[a]	[a]	
	1027.4307	1.500 – 02	5.510 + 07	3.483 – 03	2.274 – 14	5.915 – 04	[a]	[a]	
	1025.7633	1.900 – 04	2.100 + 06	3.480 – 03	2.878 – 16	5.678 – 04	3.700 + 09	5.514 – 07	
	1025.7626	2.850 – 03	1.840 + 07	3.477 – 03	4.314 – 15	5.915 – 04	3.700 + 09	5.514 – 07	
	1025.7618	1.600 – 02	7.400 + 07	3.475 – 03	2.420 – 14	5.948 – 04	3.700 + 09	5.514 – 07	
O I	990.8010	5.900 – 02	1.310 + 08	3.356 – 03	8.619 – 14	1.849 – 03	[a]	[a]	5
	990.2043	4.600 – 02	1.850 + 08	3.354 – 03	6.716 – 14	1.924 – 03	[a]	[a]	
	990.1269	1.500 – 02	1.000 + 08	3.354 – 03	2.190 – 14	1.849 – 03	[a]	[a]	
	988.7734	5.100 – 02	2.500 + 08	3.349 – 03	7.435 – 14	1.937 – 03	[a]	[a]	
	988.6549	9.300 – 03	6.300 + 07	3.349 – 03	1.356 – 14	1.924 – 03	[a]	[a]	
	988.5778	6.300 – 04	7.200 + 06	3.349 – 03	9.183 – 16	1.849 – 03	[a]	[a]	
O II	834.462	1.220 – 01	7.600 + 08	2.827 – 03	1.501 – 13	4.970 – 03	1.300 + 09	9.400 – 07	6
	833.332	8.700 – 02	8.200 + 08	2.823 – 03	1.069 – 13	5.355 – 03	8.400 + 08	4.600 – 07	
	832.762	4.100 – 02	8.200 + 08	2.821 – 03	5.034 – 14	5.351 – 03	4.200 + 08	1.000 – 07	

[a] No significant solar contribution.
[b] Wavelengths from Kelly (1987) and recent NIST compilations.
[c] $-03 = 10^{-3}$.

References

1. Wiese *et al.* (1966). 2. Brooks *et al.* (1977). 3. Zeippen *et al.* (1977). 4. Tayal and Henry (1989). 5. Doering *et al.* (1985). 6. Ho and Henry (1983).

selected to illustrate behavioral patterns. Emission rates and issues concerning individual features are reviewed in Section 4.

3.2.1. *Dayglow*

3.2.1.1. *Photoelectron Excitation.* As described earlier, much of the dayglow is produced by energetic photoelectron impact excitation of the neutral atmosphere. Much work was done in the 1970's and early 1980's, in trying to model theoretically the steady-state photoelectron flux observed from rockets and satellites (e.g., Oran and Strickland, 1978; Hernandez *et al.*, 1983; Richards and Torr, 1985; and their many references). The most complete set of observations are those made from the Atmospheric Explorer satellites, published by J. Doering and colleagues (Lee *et al.*, 1980a, b; Hernandez *et al.*, 1983). Comparison of the observations with theory and with simultaneous airglow measurements suggests that absolute values of the measured photoelectron flux may be uncertain by as much as a factor of two (e.g., see Conway, 1983b). There are additional uncertainties associated with the solar EUV spectral irradiance (Ogawa and Judge, 1986; Lean, 1988) and its consistency with the photoelectron flux (Richards and Torr, 1984). It has been a decade or more since photoelectron flux measurements were obtained from the Atmospheric Explorer program; there is a strong need for new measurements.

Since photoelectron observations are not available for all geophysical and temporal conditions, photoelectron models will be used of necessity to calculate airglow excitation rates. The modelling process begins by (1) selecting a model atmosphere for the desired geophysical conditions, (2) characterizing the solar spectral irradiance, and (3) selecting the appropriate electron energy loss cross sections. These are inputs to a model which computes the initial ionization rate (photoelectron production rate) and the resulting steady-state photoelectron flux. The next step involves combining the photoelectron flux with the atmospheric composition and relevant electron impact excitation cross sections to provide the volume excitation rates of the desired species. The modelling process is described in this section and examples of cross sections, model atmospheres and photoelectron fluxes are given.

To illustrate the process of obtaining airglow excitation rates from photoelectrons, the model of Strickland and Meier (1982) is used, but with several important improvements. The incident solar irradiance was changed from the coarse band model of Torr *et al.* (1979) to the much more detailed spectrum of Hinteregger *et al.* (1981) (Figure 1), with allowance for higher solar activity using Hinteregger's algorithms, provided by the National Space Science Data Center magnetic tape containing SC No. 21REF. Users should be aware that the algorithms should be modified to ensure that the solar spectrum reduces to the SC No. 21REF irradiances at solar min; otherwise occasional negative values of the irradiance may occur. A new compilation by Conway (1988) of the absorption cross sections used for attenuating the solar irradiance through the atmosphere was incorporated into the code. As discussed by Conway, an earlier compilation by Kirby *et al.* (1979) contained important discrepancies with recent laboratory measurements. Current energy loss and excitation cross sections have been included.

Finally, a variety of model atmospheres are now selectable: Jacchia (1971, 1977), MSIS-83 (Hedin, 1983), and MSIS-86 (Hedin, 1987).

Figure 27, taken from Strickland *et al.* (1989) is a plot of the total inelastic scattering cross sections for electrons on N_2, O_2, and O. Twenty-five individual cross sections

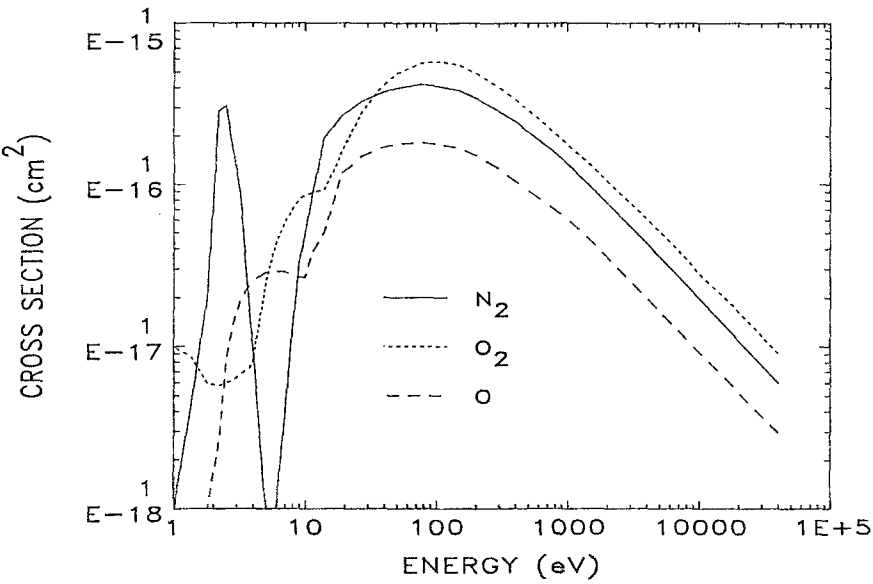

Fig. 27. Sum of cross sections for inelastic scattering of electrons by N_2, O_2, and O.

have been summed for N_2, nine for O_2, and nine for O. Table V lists the peak value of UV emission cross sections and the energy at which the peak occurs. A number of the cross sections have been scaled downward by a factor of 0.7 to account for re-measurement of the $e + H_2 \rightarrow L\alpha$ cross section, which was used in many instances as a secondary reference standard (e.g., Shemansky *et al.*, 1985). Other factors used to scale the original measurements of emission cross sections in Table V are discussed in the next section, under the individual features. *The cross sections in Table V include the scaling factors.* The energy functions of selected emission cross sections are shown in Figure 28. The N_2-band cross sections are for excitation to the molecular state and must be multiplied by the branching ratio into the band of interest.

Photoelectrons are only a small portion of the total electron population in the ionosphere. This perspective is illustrated in Figure 29, provided by J. Jasperse (private communication, 1988); also see Jasperse (1977). The isotropic electron energy distribution function has been normalized to the total electron concentration at 170 km for mid-latitude average daytime conditions and moderate solar activity (solar 10 cm flux of 120). The main population below 1 eV consists of thermal electrons, but photoelectrons dominate at larger energies. The valley between 2 and 3 eV is due to collisional energy loss to vibrational states of N_2. The large loss cross section for this process can be seen at the same energies in Figure 27. The structure in the spectrum between 20 and

TABLE V

UV emission cross sections for electron impact excitation

Feature/system	E_{max} (eV)	Scaled cross section at E_{max} (10^{-18} cm^2)	Scaling factor applied	Reference for original cross section
Bands				
N_2^+ 1 NG	100	26.0	1.00	Borst and Zipf (1970)
N_2 LBH	18	30.0	1.00	Ajello and Shemansky (1985)
N_2 BH	32	47.0	1.00	Zipf and McLaughlin (1978)
N_2 2 PG	14	41.0	1.00	Cartwright *et al.* (1977)
N_2 1 PG	14	113.0	1.00	Cartwright *et al.* (1977)
N_2 c_4' (0, 0)	75	7.9	1.00	Ajello *et al.* (1989)
N_2 c_4' (0, 1)	75	1.3	1.00	Ajello *et al.* (1989)
Lines				
N I 1200 (*e* on N)	35	175.0	0.70	Stone and Zipf (1973)
N I 1200 (*e* on N_2)	90	4.5	0.70	Ajello and Shemansky (1985)
N I 1134 (*e* on N)	20	140.0	0.70	Stone and Zipf (1973)
N I 1134 (*e* on N_2)	60	0.9	0.70	Stone and Zipf (1973)
N I 1493 (*e* on N)	18	25.4	0.70	Stone and Zipf (1973)
N I 1493 (*e* on N_2)	80	1.9	0.70	Mumma and Zipf (1973)
N I 1743 (*e* on N)	17	9.1	0.70	Stone and Zipf (1973)
N I 1743 (*e* on N_2)	80	0.66	0.70	Mumma and Zipf (1971a)
N II 1085 (*e* on N_2)	130	2.9	0.70	McLaughlin (1977)
N II 916 (*e* on N_2)	150	1.0	0.70	McLaughlin (1977)
O I 1356 (*e* on O)	16	9.0	0.36	Stone and Zipf (1974)
O I 1356 (*e* on O_2)	110	8.8	1.26	Wells *et al.* (1971)
O I 1304 (*e* on O)	18	24.0	1.42	Zipf and Erdman (1985)
O I 1304 (*e* on O_2)	80	3.2	0.70	Zipf *et al.* (1979)
O I 989 (*e* on O)	50	7.3	0.50	Zipf and Erdman (1985)
O I 989 (*e* on O_2)	90	1.3	0.70	Zipf *et al.* (1979)
O I 1026 (*e* on O)	50	2.74	1.00	Zipf and Erdman (1985)
O I 1026 (*e* on O_2)	90	0.86	1.00	Ajello and Franklin (1985)
O II 834 (*e* on O)	140	2.0	1.00	Zipf *et al.* (1985)
O II 834 (*e* on O_2)	170	2.26	1.0	Ajello and Franklin (1985)

30 eV is due to photoionization into various ion states by the bright solar He II 304 Å line (Jasperse, 1981). Greater detail can be seen in the insert panel of Figure 29.

To study systematically the energetic portion of the electron population in Figure 29, and its relationship to the dayglow, the atmospheric composition is needed in the photoelectron model along with the solar flux, the energy loss processes and excitation rates. For the purpose of the review paper, the MSIS-86 empirical model (Hedin, 1987) is used for two cases of atmospheric conditions; low and moderately high solar activity, at mid-latitude, mid-morning, spring equinox. The MSIS parameters are listed in Table VI. Atmospheric composition is shown in Figure 30 for both models.

Photoelectron fluxes using the updated Strickland and Meier (1982) model are shown in Figure 31 for the two model atmospheres. The energy resolution chosen for these

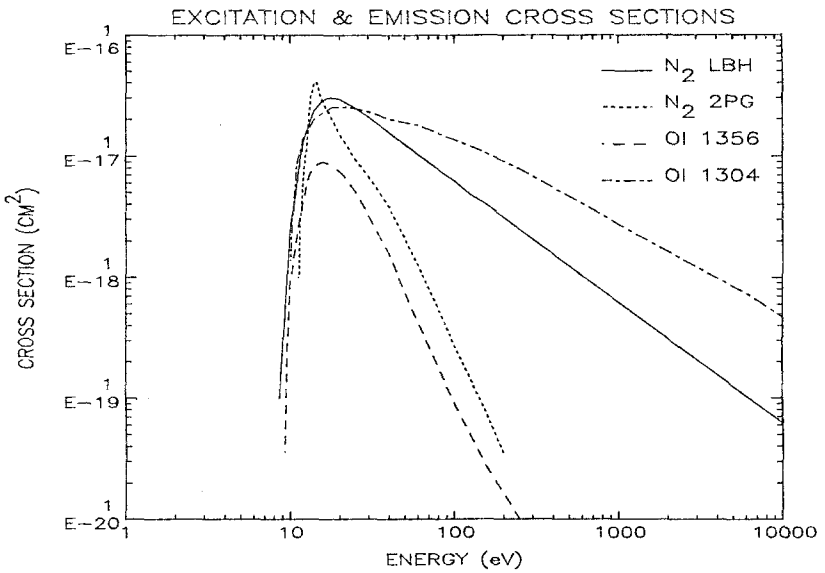

Fig. 28. Selected excitation and emission cross sections. The N_2 cross sections are for total excitation to the upper state of the indicated band; the excitation must be partitioned among the vibration levels of the upper state and multiplied by branching ratios to obtain emissions in the bands of interest. The O cross sections are for emission, including cascade from upper states under optically thin conditions. See Table V for references.

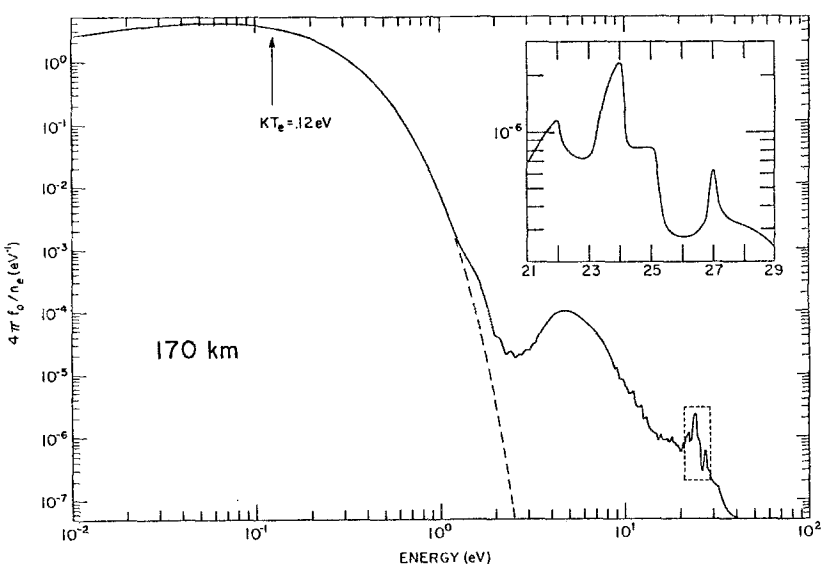

Fig. 29. Isotropic energy distribution function for ionospheric electrons at 170 km, normalized to the total electron number density. The calculated thermal distribution is indicated by the dashed curve; the photoelectron population is seen at energies above 1 eV. The insert panel shows the structure due to photoionization by the solar He II 304 Å line (J. Jasperse, private communication, 1989).

TABLE VI

MSIS-86 model atmosphere parameters

Parameter	Solar min	Solar max
Date	21 March, 1976	21 March, 1980
Latitude	32°	32°
Longitude	254°	254°
Local solar time	10:00	10:00
Solar 10.7 cm flux		
– 81 day average	71	188
– Prior day	86	163
A_p	6	18
T_{exo}	816 K	1191 K
Solar 1304 Å flux	6×10^9 ph cm^{-2} s^{-1}	10×10^9 ph cm^{-2} s^{-1}

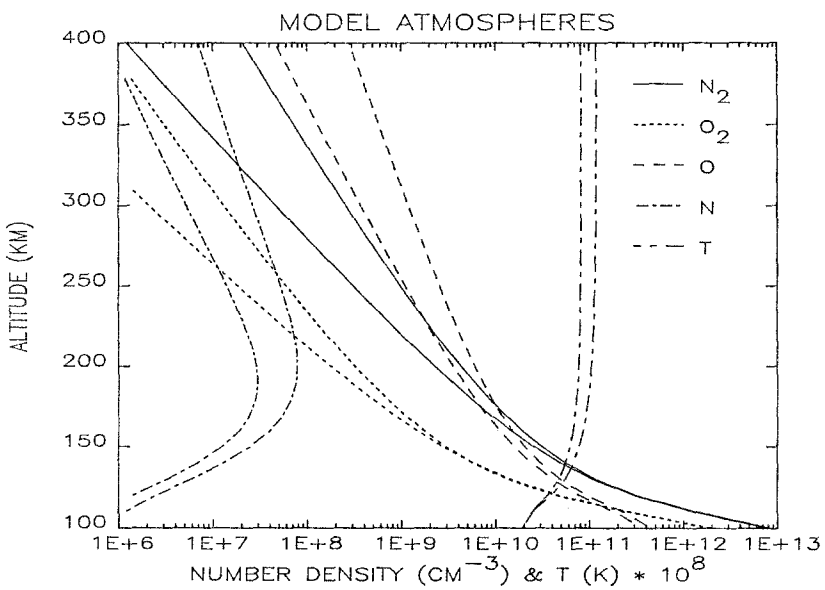

Fig. 30. Atmospheric composition from the MSIS-86 model at solar min (left curves) and max (right curves). The conditions chosen to represent min and max are given in Table VI. Temperature has been multiplied by 10^8 to be on scale.

calculations is not sufficient to separate the fine structure seen in Figure 29. Except at the highest altitudes, the flux decreases monotonically with decreasing altitude. The altitude distribution of the photoelectron flux mainly depends on the atmospheric column concentration in the direction of the Sun through extinction (Stewart, 1970; Richards and Torr, 1985). Thus the altitude of the peak of the emission rate rises with increasing column concentration. This effect also occurs throughout the day as the column concentration increases with increasing solar zenith angle. (See below and Meier and Anderson, 1983.)

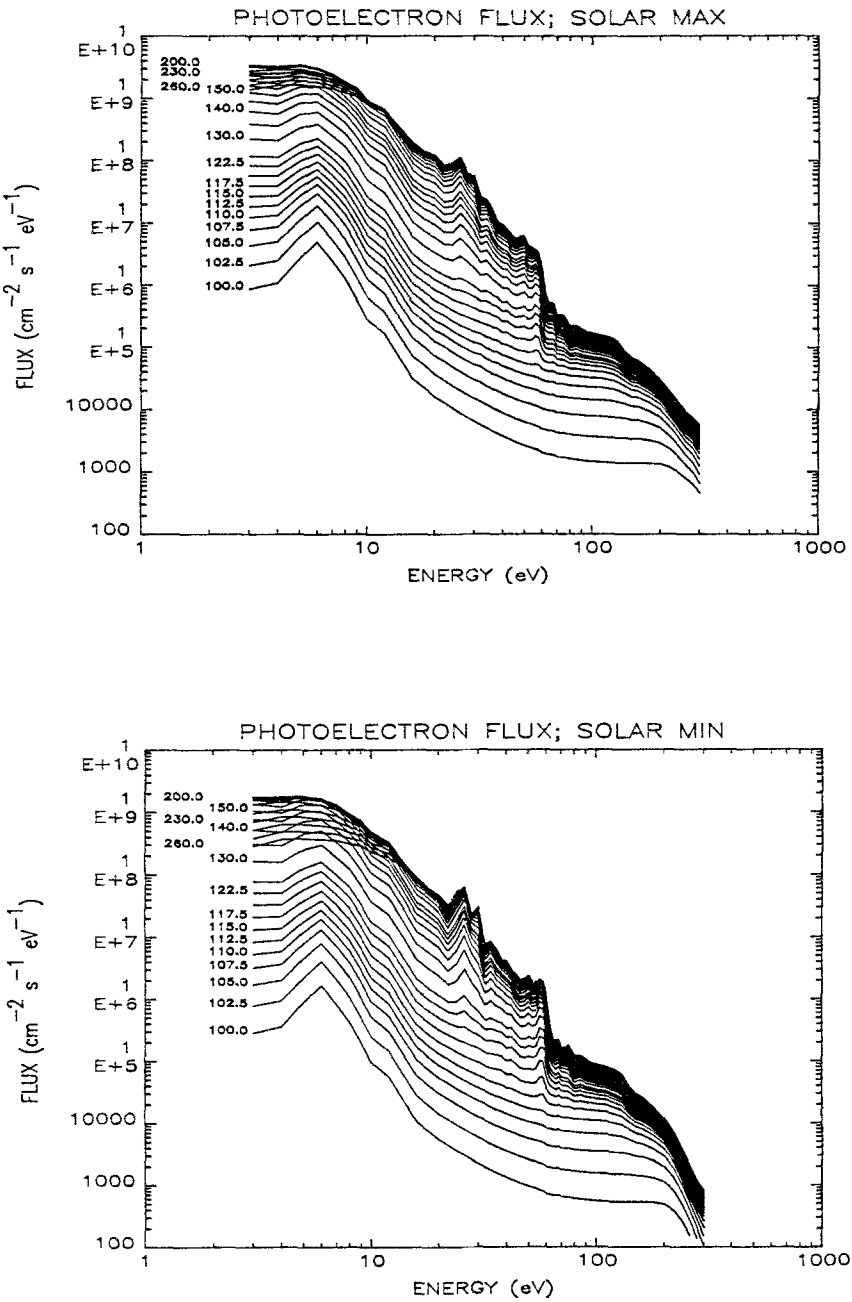

Fig. 31. Isotropic photoelectron fluxes vs energy for the altitudes indicated. The fluxes were computed using the Strickland and Meier (1982) model, updated as discussed in the text. The non-monotonic behavior at lower energies is a consequence of the photoelectron initial production rate increasing with decreasing altitude in proportion to the increase in atmospheric concentration until attenuation of ionizing sunlight causes the production rate to decrease. At higher energies, the loss rate compensates for the production rate, so the photoelectron flux does not exhibit the same behavior there. The solar zenith angle is 30 deg. The atmospheric models are given in Figure 30.

The excitation rate of atmospheric species can now be computed using the photoelectron fluxes in Figure 31 and the model atmospheres in Figure 30. The volume rate of excitation to some atomic or molecular state by photoelectron impact, j ($cm^{-3}\ s^{-1}$), is given by

$$j[\mathbf{r}] = \rho[\mathbf{r}] \int_{E_0}^{\infty} \sigma[E]F[\mathbf{r}, E]\, dE = \rho[\mathbf{r}]g[\mathbf{r}]\,, \tag{38}$$

where $\sigma[E]$ is the electron impact excitation cross section (Figure 28), $F[\mathbf{r}, E]$ is the photoelectron flux ($cm^{-2}\ s^{-1}\ eV^{-1}$) at location $\mathbf{r}$, and g is the excitation rate per sec per atom described in Section 3.1.3. The integral is carried out beginning at the threshold for excitation to the upper state, E_0. The volume emissivity is then

$$\varepsilon[\mathbf{r}] = \frac{Bj[\mathbf{r}]}{4\pi}\,, \tag{39}$$

where B is the branching ratio. If the only loss from the excited state is radiative in the emission feature of interest, then $B = 1$.

Some typical values of a variety of excitation rates $j(\mathbf{r})$ are shown in Figures 32 and 33. Examples are presented in Figure 32 for optically thin ($N_2\ a\ ^1\Pi_g$), small opacity (optical depth near unity: $O(^5S)$) and in Figure 33 for large opacity ($O(^3S)$) conditions. The N_2 and O excitation rates are shown in Figure 32 as functions of altitude for various solar zenith angles by evaluating the photoelectron model for conditions of maximum and minimum solar activity. (Strictly speaking, the atmospheric composition varies with geographic position and local time. Since Figure 32 is intended to illustrate the variation with solar zenith angle, fixed atmospheric models were used.) The dotted lines are the excitation rates of $O(^5S)$, including multiple scattering of the O I 1356 Å lines, and are discussed in Section 4. The secondary peaks in the excitation rates at low altitudes are due to ionization where the atmospheric column density becomes large enough to stop solar X-rays. At solar max the magnitude of the excitation rate is larger than at solar min, and the emission peaks are broader in altitude due to the increase in atmospheric scale height.

By integrating excitation rates such as those in Figure 32 along the chosen line-of-sight (Equation (21)), LBH-band radiances are obtained after multiplying by the appropriate branching ratios (discussed in Section 4). Attenuation by O_2 Schumann–Runge continuum absorption must be taken into account if altitudes below about 150 km are reached. O I 1356 Å radiances are more difficult to compute since multiple scattering and self-absorption, as well as O_2 absorption must be included (Equation (30)). Details of the computation are given in Section 4.

Volume excitation rates under extremely thick conditions are shown in Figure 33 for the O I 1304 Å triplet at 30 deg solar zenith angle. The initial excitation rate computed with the Strickland and Meier photoelectron model is shown as the solid lines. The excitation rate after multiple scattering is taken into account is given by the histograms. The excitation rates including multiple scattering were computed using the model of

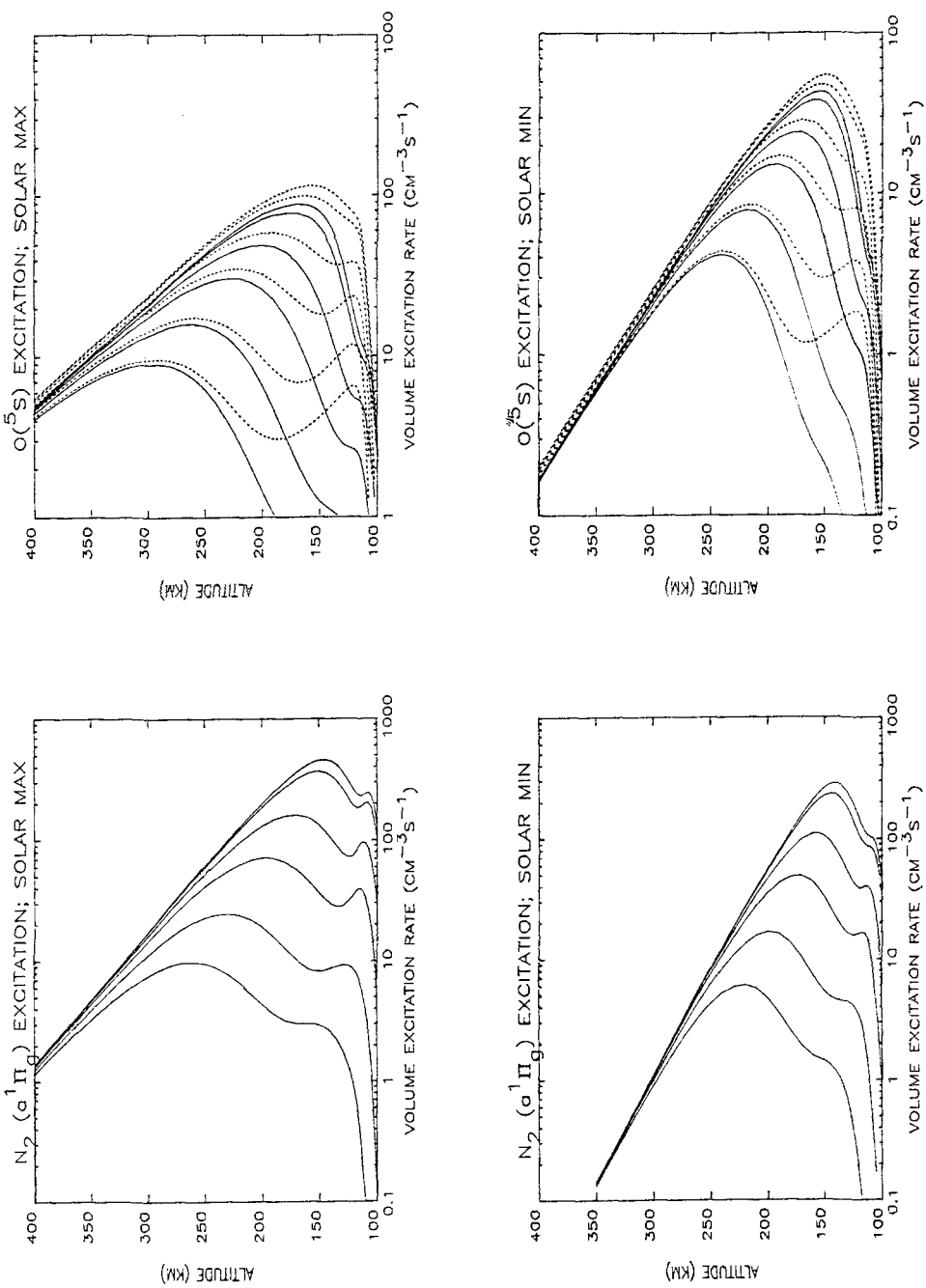

Fig. 32. Volume excitation rate for the upper states of N_2 LBH bands and O I 1356 Å. The families of curves are for solar zenith angles of 0, 30, 60, 75, 85, and 90 deg, from right to left within each panel. The solid lines are the initial excitation rates due to photoelectron impact excitation and the dotted lines include multiple scattering. The radiance itself does not increase in proportion to the enhanced multiple scattering because of attenuation due to self-absorption (see text). The atmospheric models are given in Figure 30.

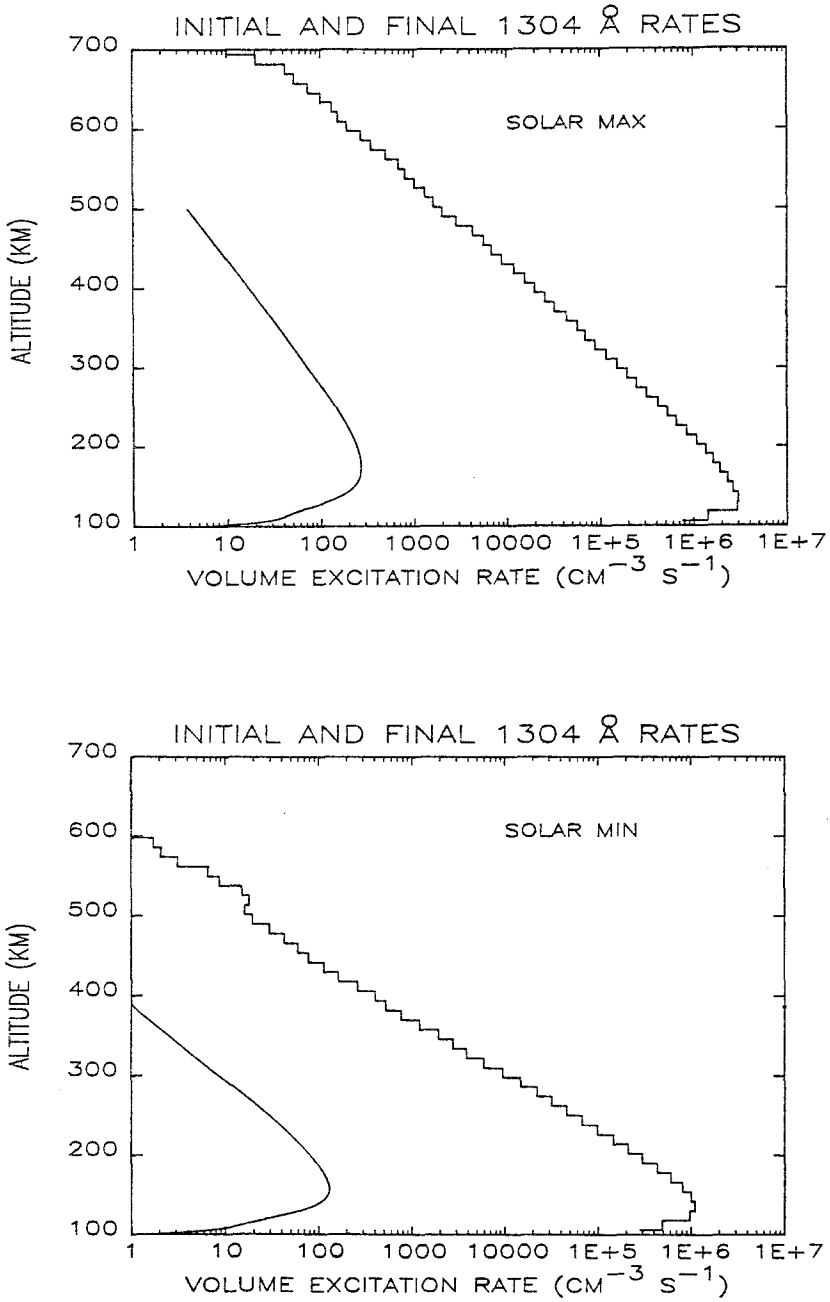

Fig. 33. Photoelectron excitation rates for O(^3S) leading to emission of 1304 Å photons. Solid lines are the initial excitation rate, including cascade from upper states. Histograms include enhanced excitation from multiple scattering, computed using the Monte-Carlo model of Meier and Lee (1982). Point-to-point variations indicate the statistical noise level. All rates have been integrated over frequency. Note that the radiance does not increase in proportion to the enhanced multiple scattering because of attenuation due to self-absorption (see text). The atmospheric models are given in Figure 30. The solar zenith angle is 30 deg.

Meier and Lee (1982). Multiple scattering greatly amplifies the excitation rate because the average photon scatters from 5000–10 000 times before escape to space or absorption by O_2. The radiance does not, however, increase in linear proportion to the excitation rate. Photons which are created within the scattering atmosphere and which have an initial emission profile which peaks at line-center are imprisoned locally because of the large opacity. Many scatterings occur, causing the large buildup in the volume excitation rate. Ultimately, when a frequency shift occurs into the optically thin wings of the line, the photon is able to move large distances spatially. The actual enhancement of the radiance often is only a factor of 2 or 3, depending on observing conditions. Details of the transport physics are given in Meier and Lee (1982). See also Section 4 for discussion of emission processes.

3.2.1.2. *Resonant Scattering of Sunlight.* A number of strong emission lines and bands in the dayglow are produced by resonant scattering of solar lines and continuum. The strongest atomic lines are listed in Table IV. High-resolution solar line profiles which are the source of these airglow features are shown in Figure 34. Only one line of the O I 1304 Å triplet is shown. References for the solar observations are given in the figure caption. The solar hydrogen and oxygen lines exhibit significant self-reversal. Additional self-absorption by geocoronal hydrogen is seen as the narrow, deep feature at the center of the line profile. Terrestrial absorption is also present in the Lβ and 584 Å profiles which were observed at a resolution too poor to resolve the narrow features: both line-center irradiances should be raised by about 15% to correct for this.

All irradiances in Figure 34 have been scaled to solar minimum values. The variation in the irradiances over a solar cycle is typically of the order of a factor of two, with a lesser amount of rotation modulation superimposed. This variability is typical of chromospheric emission lines; variation of coronal EUV lines is somewhat larger. Lean (1987) discusses the variability of the solar lines.

In the vicinity of most airglow lines, which are narrow compared with their solar counterparts, the solar line-center irradiance can be assumed to be independent of frequency. Then the g-factor can be calculated using Equation (23). Table IV lists the line-center irradiances for the lines and the resulting g-factors at the top of the atmosphere. As long as the atmospheric optical depth is less than a few hundred, CFR can be assumed. The initial excitation rate throughout the atmosphere can be calculated from Equation (28), and the final excitation rate including multiple scattering, from Equation (26). The hydrogen Lα and Lβ, and helium 584 Å problems can be treated with CFR, but spherical geometry must be employed because of the large-scale heights of these light elements.

If the line center optical depth is very large, absorption in the wings of the line becomes important and CFR cannot be used. This is the case for resonant scattering of the solar O I 1304 Å lines. The volume excitation rate must be calculated by including the solar spectral shape in the T function frequency integral (Equations (28) and (29)). If the frequency dependence of the subsequent emission rate were desired, the redistribution function would have to be included in the integral. Figure 35 illustrates examples of the

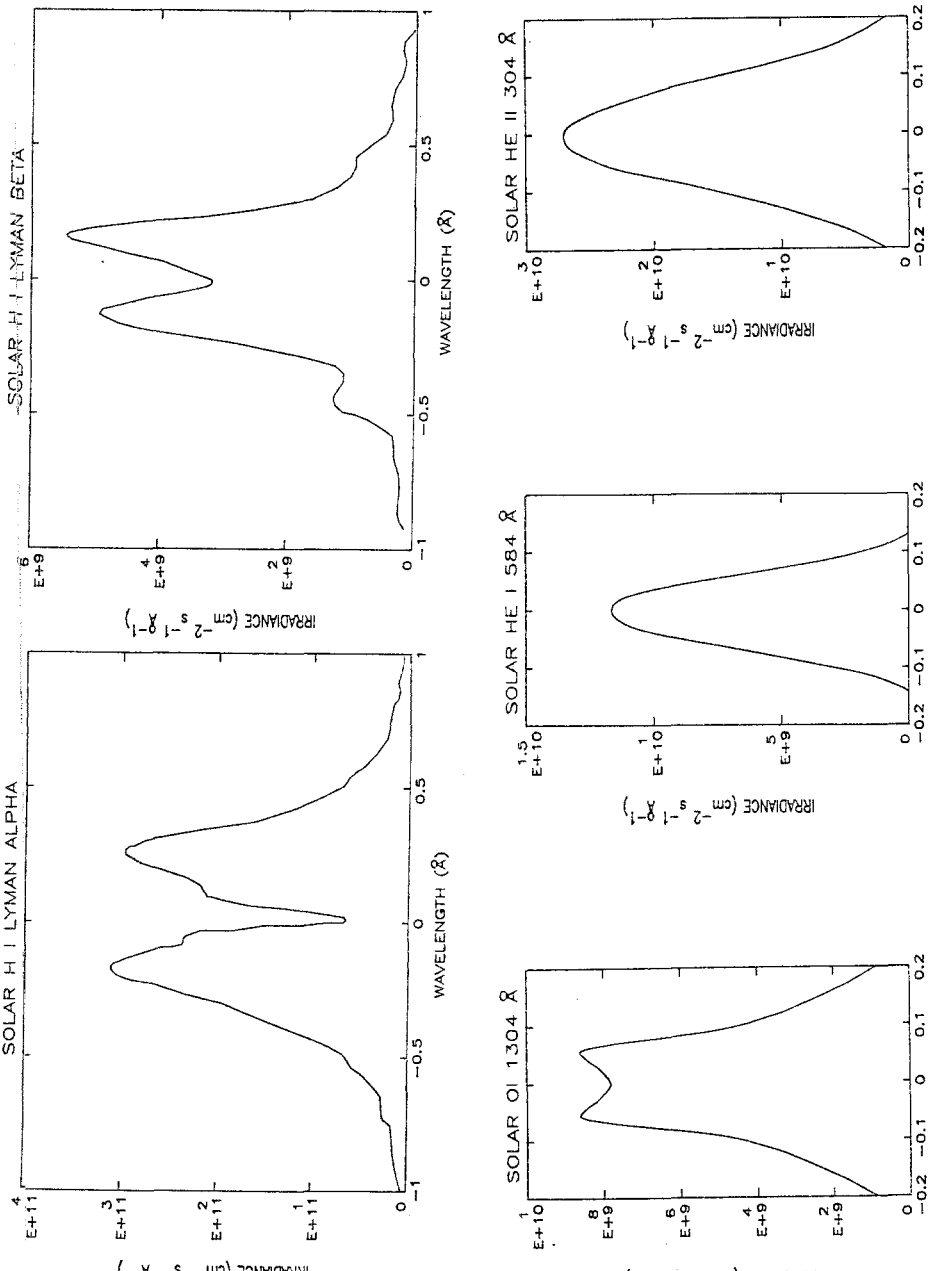

Fig. 34. Observed high-resolution profiles for important solar (full-disk) emission lines which are resonantly scattered in the terrestrial atmosphere. Absolute values have been adjusted to solar min conditions, with values of 2.2×10^{11}, 3×10^{9}, 2×10^{9} (for a single line of the triplet, as shown), 1.58×10^{9}, and 6×10^{9} photons $cm^{-2}\,s^{-1}$ integrated irradiances for Lα, Lβ, 1304, 584, and 304 Å, respectively. Terrestrial self-absorption can be seen at the center of the Lα line, but the resolution is insufficient to detect absorption at Lβ, 1304 and 584 Å. Line center irradiances should be increased by about 15% for both Lβ and 584 Å to account for terrestrial absorption. The profiles were adapted from Lemaire *et al.* (1978): Lα and Lβ; Bruner *et al.* (1970): O I 1304 Å; Doschek *et al.* (1974): 584 and 304 Å.

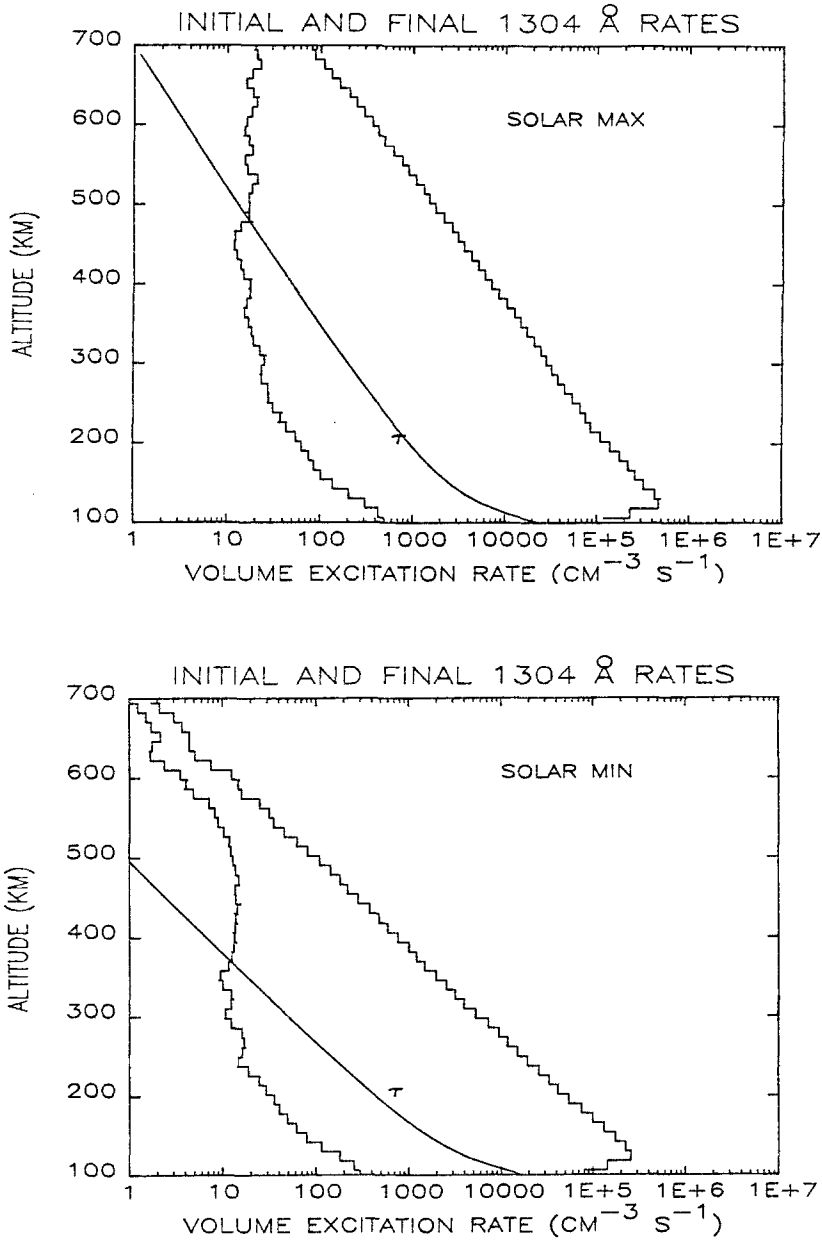

Fig. 35. Solar resonant scattering excitation rates of O(^3S) leading to emission of 1304 Å photons. The vertical optical depth at line center for the $^3P_1 - {}^3S_0$ transition at 1304.8575 Å is shown as solid lines for comparison. See Figure 33 caption.

frequency-integrated O I 1304 Å excitation rates for solar max and min conditions, calculated with the Meier and Lee (1982) Monte-Carlo model. The lower histograms are the initial scattering rate of the solar lines. The unusual shape of the curves is due

to the fact that at high altitudes where the opacity is smaller, the exponential increase of O concentration with decreasing altitude is greater than the rate of scattering of photons out of the solar beam. As the optical depth increases with decreasing altitude, the transmission function decreases more rapidly, overtaking the increase of concentration and a high altitude peak occurs. At lower altitudes, solar photons are depleted in the Doppler core of the line and the optical depth becomes large enough that significant resonant absorption takes place in the wings of the line. The decrease in the transmission function with altitude is slower for absorption in the wings of the line and the increase in concentration begins to dominate. The excitation rate again rises with decreasing altitude, until pure O_2 absorption extinguishes the solar line at about 100 km. The line-center optical depth in the 1304.9 Å line of the triplet is shown in Figure 35 for general interest.

The upper histograms in Figure 35 show the excitation rate including multiple scattering. The degree of amplification is not as large as for photoelectron excitation (Figure 33) because much of the solar scattering, especially at lower altitudes, takes place in the wings of the line where the opacity is smaller. Furthermore, photons scattered at wing frequencies tend not to shift frequency significantly because of the nearly monochromatic nature of the frequency redistribution probability there (Section 3.1.2). Thus the solar resonant scattering excitation process is 'effectively' thinner than for photoelectron excitation which creates photons within the Doppler core of the line. As in the case of photoelectron excitation, the radiance does not exhibit the same degree of amplification as the volume excitation rate. More details are given in Section 4.

There are two important cases of molecular resonant fluorescence stimulated by continuum sunlight in the UV: the nitric oxide γ-bands and the N_2^+ first negative bands. Emission rate g-factors calculated with Equation (37) for the NO γ-bands have been tabulated by several authors: Cravens (1977) compares several published sets. Those of D. Albritton (private communication to Cravens, 1976) are listed in Table VII for a temperature of 200 K. N_2^+ 1 NG g-factors taken from Barth (1965, 1966) are also listed in Table VII.

Examples of volume emission rates for the NO (0, 0) γ-band at 2262 Å are shown in Figure 36 for different local times. The emission rates were computed using the g-factor in Table VII along with NO concentrations taken from the model of McCoy (1983b). The strong variability is indicative of the odd nitrogen chemistry in the thermosphere. More details on the emission rates are given by McCoy and in Section 4.

3.2.1.3. *Photoionization/Photodissociation Excitation.* Ionization and dissociation of atmospheric molecular and atoms by solar radiation initiates (internal) excitation processes that are analogous in functional form to energetic electron impact excitation, except that the excitation rate per sec per atom (or molecule) is computed by substituting the solar flux, after attenuation through the atmosphere, into Equation (38). The appropriate partial cross section for the process in question is used in the integral. Some examples of these excitation processes are:

TABLE VII

Molecular emission rate g-factors for solar excitation

Band	Wavelength (Å)	(v', v'')	g-factor (s^{-1} molecule^{-1})
NO γ	2262	(0, 0)	2.72 – 6[a]
	2363	(0, 1)	3.79 – 6
	2149	(1, 0)	7.72 – 6
	2239	(1, 1)	2.11 – 6
	2047	(2, 0)	2.02 – 6
	2216	(2, 2)	8.48 – 7
	2030	(3, 1)	3.00 – 7
N_2^+ 1 NG	3914	(0, 0)	1.43 0
	4278	(0, 1)	4.37 – 1
	3579	(1, 0)	2.95 – 1
	3881	(1, 1)	1.71 – 1
	4233	(1, 2)	1.69 – 1

[a] $-6 = 10^{-6}$.

$$O(^3P) + h\nu \rightarrow O^+(^4P) + e \rightarrow (834\ \text{Å}),$$

$$N_2(X\,^1\Sigma_g^+) + h\nu \rightarrow N(^4S) + N(^4P) \rightarrow (1200\ \text{Å}),$$

$$N_2(X\,^1\Sigma_g^+) + h\nu \rightarrow N(^4S) + N^+(^3D) + e \rightarrow (1085\ \text{Å}),$$

$$N_2(X\,^1\Sigma_g^+) + h\nu \rightarrow N + N^+(^5S) + e \rightarrow (2143\ \text{Å}).$$

Since it takes of order 20–30 eV to produce an excited fragment atom or ion these processes require energetic photons. Thus solar photons above 400–500 Å do not participate. Also, some states of the excited species are not accessible from the ground state of the parent atom or ion because they are forbidden by dipole selection laws.

An important consideration for molecular dissociation is that the fragment excited species are kinetically hot, having emission temperatures which are much larger than the ambient atmospheric temperature. Consequently they have a much broader spectral signature than direct excitation. Furthermore, they should not play a significant role in multiple scattering because little of the emitted radiation is within the Doppler core of the ambient scatterers. The relevance of these issues to particular emissions is discussed in Section 4.

3.2.2. *Nightglow*

3.2.2.1. *Radiative Recombination.* FUV radiation from the nighttime ionosphere was discovered by experiments onboard the OGO-4 satellite (Hicks and Chubb, 1970; Barth and Shaffner, 1970). Subsequently, many experiments have shown that radiative recombination as proposed by Hanson (1969) is the principal source mechanism:

$$O^+ + e \rightarrow O^*. \tag{40}$$

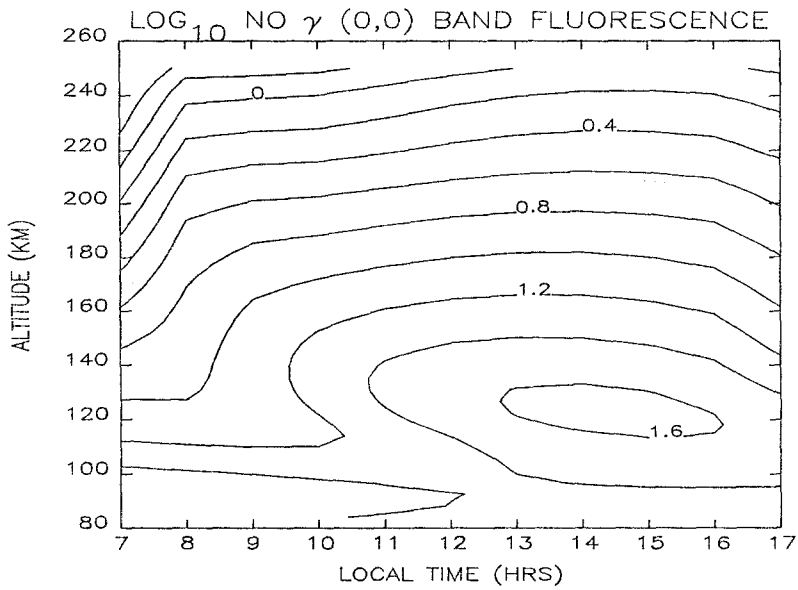

Fig. 36. Volume emission rates of the NO (0, 0) γ band at 2262 Å from resonant scattering of sunlight calculated using the product of the NO concentrations of McCoy (1983b) at the indicated local times, and the g-factor in Table VII. The atmospheric conditions are for the solar max model of McCoy. The model NO values below 130 km may be low due to underestimates of the effect solar X-rays (Barth *et al.*, 1988; R. McCoy, private communication, 1989).

The resulting excited O atom can emit line radiation at 1356, 1304, 1027, and 989 Å (Figures 9 and 12), as well as at a variety of visible and infrared wavelengths. If the recombination to the ^3P ground state of O takes place, a narrow continuum shortward of 911 Å is produced, whose shape is characteristic of the electron temperature.

A weak contribution to the line radiation is possible from ion-ion mutual neutralization:

$$O^+ + O^- \rightarrow 2O^*,$$

but the 911 Å continuum is not produced with this mechanism. This source will contribute less than 10% to the total column emission rate (Tinsley *et al.*, 1973).

The volume excitation rate from radiative recombination is given by

$$j = \alpha\rho[O]\rho[e], \tag{41}$$

where the ρ denotes the number density of the indicated species; α is the partial recombination rate into the electronic state of interest. In the F-region, atomic oxygen ions are the dominant species, so the volume excitation rate is nearly equal to the square of the electron concentration. For recombination into the ground state of oxygen, the recombination rate for the production of 911 Å radiation is 4.4×10^{-13} cm^3 s^{-1} for an electron temperature of 1160 K (0.1 eV), according to Julienne *et al.* (1974). Figure 37 shows an example of the 911 Å volume emission rate computed with the International

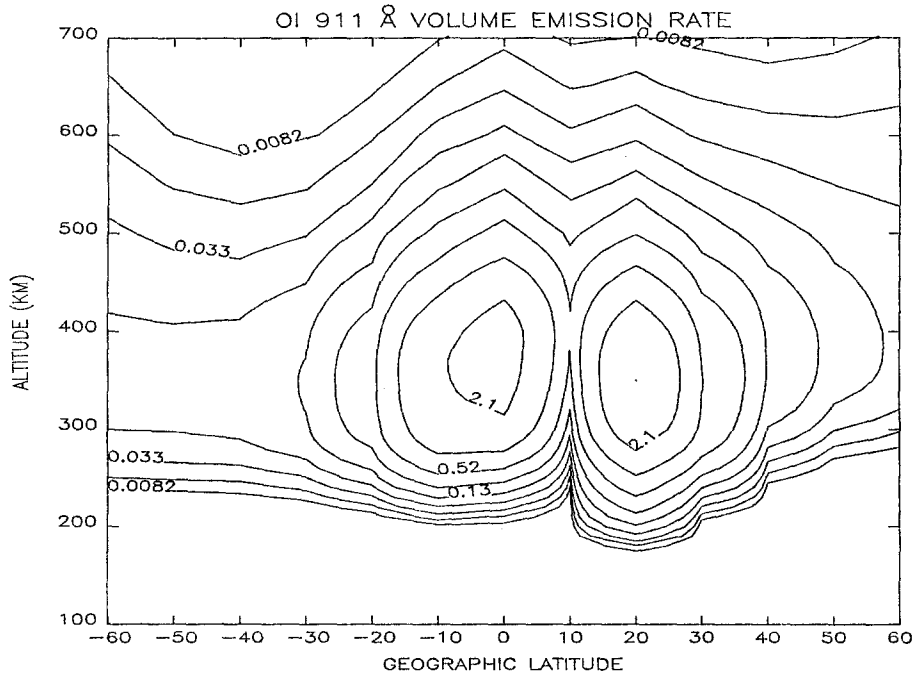

Fig. 37. Volume emission rates of the O I 911 Å continuum due to *F*-region radiative recombination. The units of the contours are photon cm^{-3} s^{-1}. The International Reference Ionosphere (IRI) model was used for the electron concentration. The atmospheric conditions corresponded to solar max (Table VI) at 22 : 00 local time and 0 deg longitude.

Reference Ionosphere (IRI) model of ionospheric composition. (The O^+ concentration was set equal to the electron concentration since IRI contains a poor description of the latitudinal variation of O^+.) The conditions are for solar max. The figure shows contour plots of volume emission rate vs latitude and altitude for 22 : 00 local time. The strong emission from the Appleton Anomaly electron density peaks on either side of the magnetic dip equator are obvious. These are the same bright emission regions seen in Figures 17, 18, 25, and 26. Radiative recombination emissions offer a unique means of remote sensing of the *F*-region ionosphere at night (Chandra *et al.*, 1975; Tinsley and Bittencourt, 1975). The initial volume excitation rates for $O(^3S.\ ^5S)$ have the same spatial distribution as the 911 Å emission rates (except for the minor ion-ion recombination), but have different recombination rates (Julienne *et al.*, 1974). However, in contrast to the optically thin 911 Å continuum, there are, respectively, slight and strong radiative transport effects for 1356 and 1304 Å line radiation (Paxton *et al.*, 1991).

3.2.2.2. *Chemiluminescence.* The nitric oxide and molecular oxygen bands in the nightglow (Figures 9–11) are produced by chemiluminescence. The NO γ- and δ-bands (identified later in the energy level diagram in Figure 64) are produced via two-body

association followed by radiative relaxation:

$$\begin{aligned} &N(^4S) + O(^3P) \leftrightarrow NO(C\,^2\Pi)\,(v' = 0)\,, \\ &NO(C\,^2\Pi) \rightarrow NO(X\,^2\Pi) + \delta\text{-bands}\,, \\ &NO(C\,^2\Pi) \rightarrow NO(A\,^2\Sigma^+)\,(v' = 0) + 1.22\ \mu\text{m}\,, \\ &NO(A\,^2\Sigma^+) \rightarrow NO(X\,^2\Pi) + \gamma\text{-bands}\,. \end{aligned} \tag{42}$$

The volume rate of emission of the δ-bands is

$$j = k\rho[O]\rho[N]\,, \tag{43}$$

where $k = 1.5 \times 10^{-17}\,(300/T)^{0.35}$ cm^3 s^{-1} is the partial rate coefficient for the production of C state NO followed by δ-band radiation (combining the rate coefficient of Mandelman *et al.* (1973) and the temperature dependence of Gross and Cohen (1968)). (Pre-dissociation is actually the dominant loss process for NO(C) molecules; k is the equilibrium rate coefficient.) Since the γ-bands are produced by cascade from the C state through the A state, the volume emission rate for the γ-bands is given by

$$j = R_{C-A}k\rho[N]\rho[O]\,, \tag{44}$$

where $R_{C-A} = 0.3$ is the ratio of $C-A$ to $C-X$ transition rates, calculated using the C to A state branching ratio of 0.23 (Sharp and Rusch, 1981; McCoy, 1983a).

Since the chemiluminescent airglow is proportional to the product of O and N, it is expected to be quite variable throughout the day. Figure 38, taken from McCoy (1983), illustrates the large variation in the volume excitation rate of NO(C) under solar max conditions at mid-latitude. The rates in Figure 38 were computed from Equation (43), but adjusting k upward by 1.3 to obtain the total C-state production. The O and N concentrations were obtained from the MSIS-86 model appropriate for the rocket flight of McCoy (1983a, b).

The O_2 Herzberg I-bands (see identifications in Figure 45) in the nightglow are produced by three-body recombination of ground state O atoms:

$$O + O + M \rightarrow O_2(A\,^3\Sigma_u^+) + M\,, \tag{45a}$$

followed by

$$O_2(A\,^3\Sigma_u^+) \rightarrow O_2(X\,^3\Sigma_g^-) + \text{Herzberg I bands} \tag{45b}$$

or

$$O_2(A\,^3\Sigma_u^+) + M_i \rightarrow O_2(X\,^3\Sigma_g^-) + M_i\,, \tag{45c}$$

where M represents the third body, mainly N_2. The volume emission rate of the Herzberg I-bands is

$$4\pi\varepsilon = \frac{k_H\rho[O]^2\rho[M]}{1 + Q/A_H}\,, \tag{46}$$

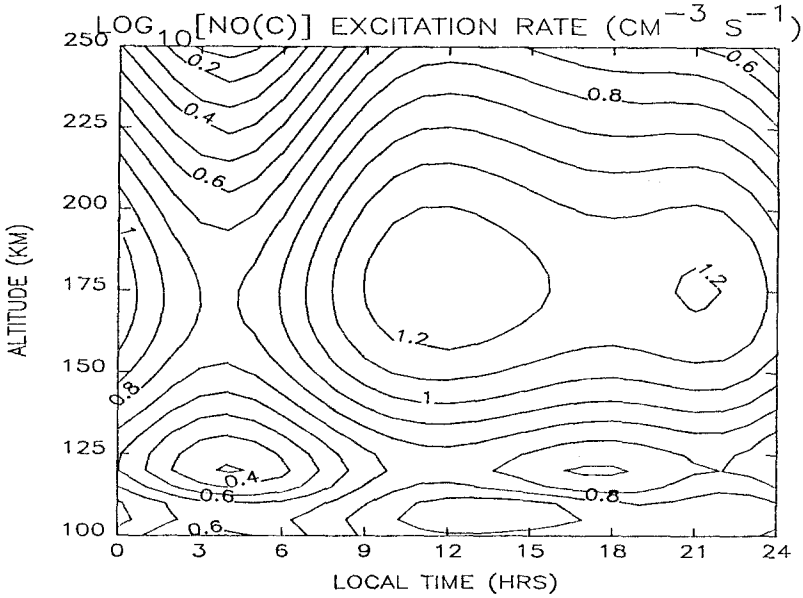

Fig. 38. Volume production rates of the NO (C) state from chemiluminescence vs altitude and local time, for mid-latitude, solar max conditions appropriate to the rocket flight of McCoy (1983a) on 7 November, 1979. The production rates were computed using MSIS-86 concentrations of O and N, and a reaction rate value described in the text.

where k_H is the rate of reaction (45a), A_H is the radiative transition probability for (45b) and $Q = \Sigma q_i \rho[M_i]$ is the quenching rate of reaction (45c) summed over all quenching species. Equation (46) must be modified if emission into individual vibrational bands is desired. Rate constants and quenching coefficients, q_i, and other issues are discussed in Section 4.1.2.1.

To obtain volume emission rates for individual NO or O_2 vibrational bands, Equations (44) and (46) must be further multiplied by individual branching ratios, $B_{v'v''}$, as in Equation (37).

3.2.2.3. *Resonant Scattering of Sunlight.* Light atmospheric constituents with large-scale heights can resonantly scatter solar lines into the night sector. Hydrogen Lα and Lβ are the best known examples. To compute the excitation rate at night, multiple scattering in a spherical atmospheric model must be used (Anderson and Hord, 1977; Anderson *et al.*, 1987b). Neutral helium does not reach altitudes high enough to scatter solar 584 Å photons very far beyond the terminator (Figure 22). Helium ions, on the other hand, extend to several earth radii in the equatorial plasmasphere. Ions above the Earth shadow can scatter the solar 304 Å line and be seen at night when viewing away from the Earth (see Figure 23). Since the plasmasphere is optically thin, no significant resonant backscattering of 304 Å photons from the ionosphere occurs at night. Models of He^+ resonant scattering in the plasmasphere have been developed by Meier and Weller (1972) and Paresce *et al.* (1973).

3.2.2.4. *Energetic Heavy Particle Excitation.* An important loss process for ring-current ions is charge exchange with geocoronal hydrogen atoms, producing energetic neutrals which can then be lost to space or move downward, impacting the thermosphere. The downward moving atoms quickly set up a charge state equilibrium through electron stripping by the ambient gas and charge capture. A quasi-trapped population of energetic ions is present at low altitudes. The proportion of ions in various charge states depends upon the energy of the primary neutrals (10's of keV to the MeV range). These energetic species undergo elastic scattering, and inelastic collisions which can produce airglow emissions. A review by Tinsley (1981) describes mechanisms leading to optical emissions. Evidence has been reported for precipitation of hydrogen (Levasseur and Blamont, 1973; Cazes and Emerich, 1980; Rohrbaugh *et al.*, 1983), helium (Meier and Weller, 1975; Tinsley, 1976a, b; Paresce, 1979), and oxygen (Tinsley *et al.*, 1982; Rohrbaugh *et al.*, 1983; Ishimoto *et al.*, 1986).

Some modelling of excitation rates has been reported by Meier and Weller (1975), Tinsley (1979), and Ishimoto *et al.* (1986). The principal difficulties are ignorance of emission cross sections for inelastic collisions of heavy ions and atoms and details of the flux distribution with energy and pitch angle.

4. Discussion of Important Airglow Emissions

In this section, the current understanding of important airglow features is reviewed. The topics are ordered by emitting species, with major species first, followed by minor species, and then ion emitters. The main ingredients which make up the excitation and emission processes for each feature are discussed, along with relevant issues and selected examples of radiances. Energy level diagrams are provided for orientation. Additional examples of radiances and remote sensing issues are covered in Section 5.

4.1. Major species

4.1.1. *Molecular Nitrogen*

4.1.1.1. *Second Postive Bands* ($C\,^3\Pi_u - B\,^3\Pi_g$). The strongest emission bands of the 2 PG system are in the vicinity of 3000 Å (see Figure 5). Since optical transitions from the X ground state of N_2 to the upper C state are spin forbidden, the main excitation source is by energetic electron impact. (See Figure 39 for a partial energy level diagram of N_2.) But the $C \rightarrow B$ transition is allowed, and proceeds rapidly. (See Figure 40(a) for plots of transition probabilities from Cartwright, 1978.) Cascades from the D and E (not shown in Figure 39; see Cartwright, 1978) states do not contribute significantly to the population of the C state because their excitation cross sections are small. The C level excitation cross section (Figure 28 and Table V), is sharply peaked near 14 eV, dropping rapidly with increasing energy, as is usual for forbidden transitions. Thus, the 2 PG emission is sensitive to the lower-energy component of the photoelectron flux. The emission rate can be computed using Equations (21) and (37), since there are no opacity effects. Pre-dissociation occurs for C state vibrational levels greater than $v' = 1$. The

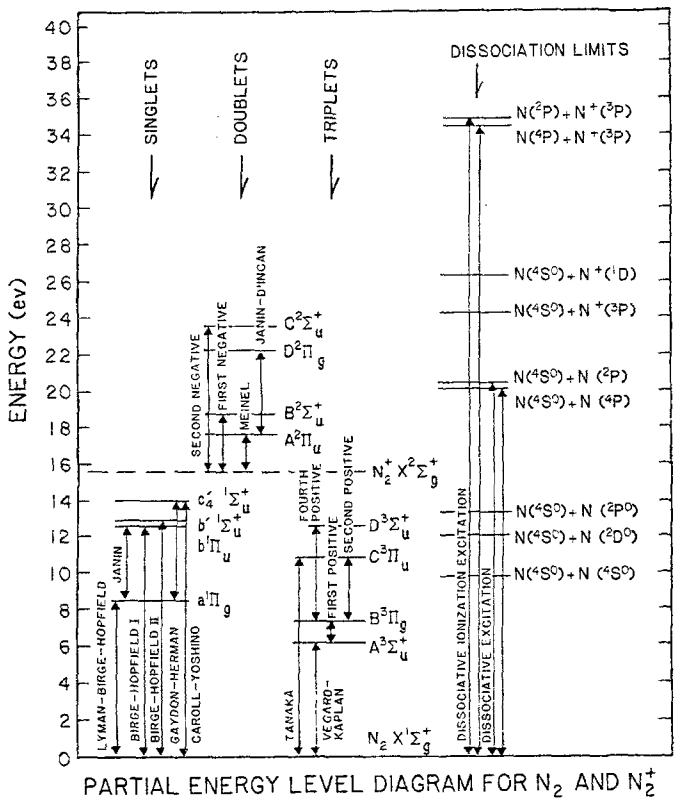

Fig. 39. Partial energy level diagram for N_2 and N_2^+. Adapted from Ajello (1969).

total pre-dissociation branching ratio for all vibrational levels is 0.5 as calculated by Porter *et al.* (1976).

The vibrational population of the *C* state in an aurora has been computed by Cartwright (1978). His results are shown in Figure 40(b), where the relative number densities of various excited N_2 molecules under auroral conditions are plotted as functions of the vibrational quantum number. The population rates should be similar in the dayglow, except that quenching of some of the metastable states would not be as strong. The *C* state population is seen to peak at $v' = 0$. Apparently no deductions of the vibrational population in the dayglow have been reported.

The strong emission in the (0, 0)-band at 3371 Å has been used as a monitor of the photoelectron flux as well as the altitude profile of molecular nitrogen (e.g., Doering *et al.*, 1970; Kopp *et al.*, 1977; Conway and Christensen, 1985). Comparison of 3371 Å emission rates measured with the Visible Airglow Experiment (VAE) on the Atmospheric Explorer *AE – C* with photoelectron flux measurements on both *AE – C* and *– E* and with a theoretical model indicated that the measured *AE – E* photoelectron fluxes were high by 20–30% (Hernandez *et al.*, 1983). However, Conway (1983b) pointed out that the N_2 VK system has emissions within the VAE instrument passband, thereby reducing

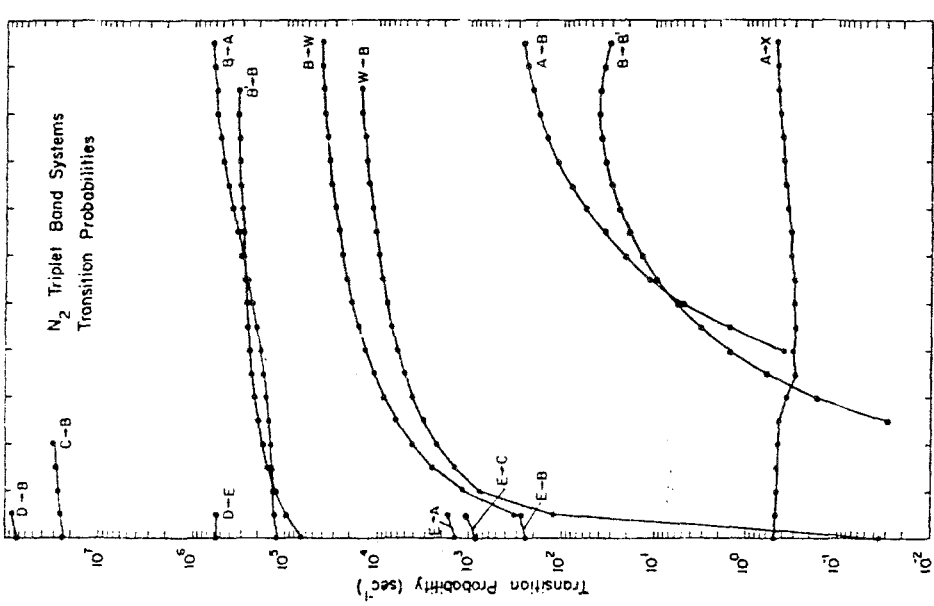

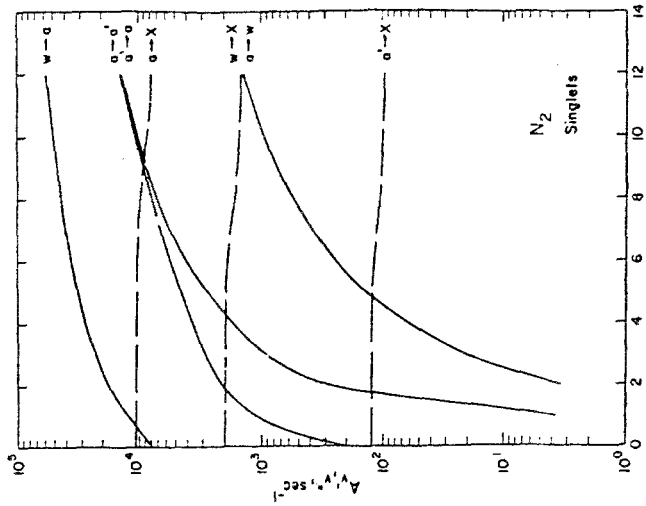

Fig. 40a. Transition probabilities for triplet (*left*) and singlet (*right*) states of N_2 as functions of vibrational quantum number. Taken from Cartwright (1978).

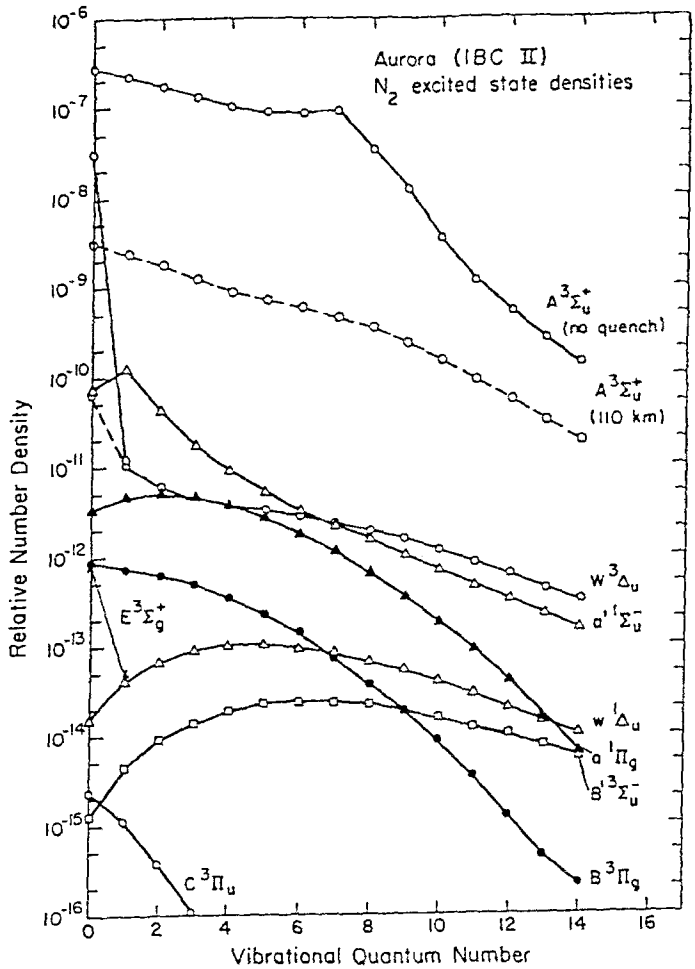

Fig. 40b. Relative number densities for various excited states of N_2 vs vibrational quantum number. The results are appropriate for an IBC II aurora. Taken from Cartwright (1978).

the portion of the measured signal attributable to the 3371 Å (0, 0)-band by 20–30%, and increasing the discrepancy between the airglow and the photoelectron fluxes to 45–70%. This issue has not yet been resolved, although other airglow analyses are consistent with lower photoelectron fluxes (Meier *et al.*, 1985). In addition, concerns about the consistency among the solar EUV irradiance and the photoelectron flux have been raised by Richards and Torr (1984).

As noted above, the scale height of N_2 and consequently the exospheric temperature can be deduced from measurements of the topside of the 3371 Å airglow layer. This is discussed in more detail in Section 5, and by Meier and Anderson (1983) and Conway and Christensen (1985). Also the rotational structure of the (0, 0)-band is sensitive to temperature, so that its measurement can give information on the thermal structure of

the atmosphere. Figure 41 taken from Conway and Christensen (1985) shows the strong change in the intensity distribution of the (0, 0)-band for two rotational temperatures.

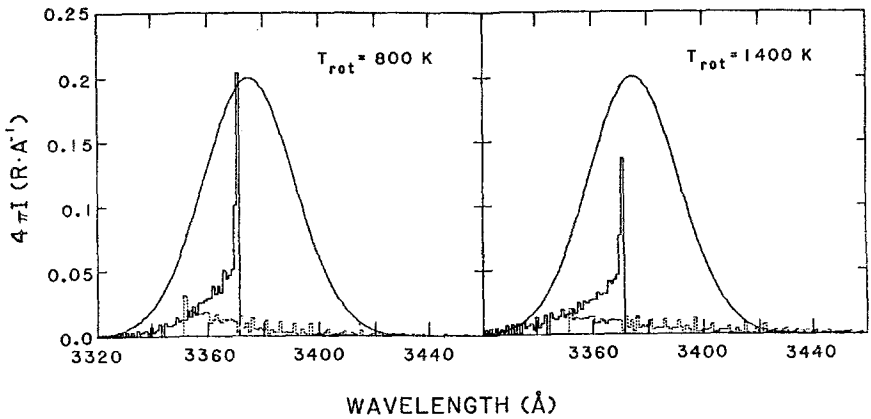

Fig. 41. Partial spectra for N_2 2 PG (0, 0) (solid histogram) and VK (dotted histogram) (0, 9) bands for two rotational temperatures. The smooth solid curve indicates the relative response function of a photometer with a 38 Å FWHM filter. Taken from Conway and Christensen (1985).

The underlying VK (0, 9)-band is represented by the dotted lines. Figure 41 illustrates the need to resolve spectrally the rotational structure if temperature information is desired. If a broadband filter photometer was used, not only would the signal be a blend of the two bands, but also the response of the photometer would be dependent on the assumed temperature. Conway and Christensen showed that the response of a 38 Å FWHM filter photometer (as given by the smooth solid line in Figure 41) to the 2 PG (0, 0)-band decreases by 35% from 800 to 1400 K.

As discussed in Section 3.2.1.1 and by Meier and Anderson (1983), the altitude of the peak production rate of 2 PG (as well as other photoelectron excited allowed transitions) depends on the total atmospheric column concentration in the direction of the Sun. Consequently, measurement of the altitude profile of 2 PG bands provides information on total atmospheric concentration as well as exospheric temperature.

4.1.1.2. *Vegard–Kaplan Bands* ($A\,^3\Sigma_u^+ - X\,^1\Sigma_g^+$). The VK bands are important contributors to the middle- and near-UV spectral regions in the dayglow (see Figure 5). Transitions from the ground state of N_2 to the A state are forbidden, so photoelectron impact is the excitation source. In addition to direct excitation from the ground state, cascade from the C, B, and W states occurs and is important. The A state population rate can be estimated using the sum of the direct plus the B, W, and half of the C state (since half of $N_2(C)$ excitations are lost though pre-dissociation) excitation cross sections (Conway and Christensen, 1985; Daniell and Strickland, 1986). Cartwright *et al.* (1977) have measured the cross sections. The lifetime of the A state is about 2 s (Shemansky, 1969; Shemansky *et al.*, 1971). Transition probabilities from the various vibrational levels are shown in Figure 40(a) (Cartwright, 1978).

The principal loss processes for $N_2(A)$ state are radiative to the ground state resulting in the VK-bands and quenching by atomic oxygen (and by molecular oxygen below 120 km). The magnitude of the quenching coefficient for $N_2(A) + O(^3P)$ has been disputed in the literature. Several laboratory measurements have now been made, which yield rate coefficients much lower than earlier deductions from altitude profiles of VK emissions in auroras. Table VIII lists various determinations of the rate coefficients. See

TABLE VIII

$N_2(A)$ + O quenching coefficients (10^{-11} cm^3 s^{-1})

$v' = 0$	1	Source	Observation	Reference
9	11	Aurora	Rocket	Sharp (1971)
2–13	–	Aurora	Ground	Vallance Jones and Gattinger (1976)
20	20	Aurora	Rocket	Beiting and Feldman (1979)
–	20	Aurora	Rocket	Torr and Sharp (1979)
2	2	Artificial aurora	Rocket	O'Neil *et al.* (1979)
2.8 ± 0.4	3.4 ± 0.6	–	Laboratory	Piper *et al.* (1981)
3.5 ± 0.6	4.1 ± 0.5	–	Laboratory	Thomas and Kaufman (1985)
2.8	3.3	–	Laboratory	De Souza *et al.* (1985)

the review by Torr and Torr (1982) for references to earlier work. Possible sources of the discrepancies may be incorrect auroral atomic oxygen concentrations used to deduce the quenching coefficient or an unknown quencher in the atmosphere. The former seems to be the likely source of error since it has been a matter of vigorous dispute itself. Production and loss for the A state are also reviewed by Torr and Torr.

The total (isotropic) volume emission rate for the VK-bands is given by

$$4\pi\varepsilon = \frac{g\rho[N_2]}{1 + Q/A}\,, \tag{47}$$

where the g-factor includes cascade contributions, $Q = q_O\rho[O] + q_{O_2}[O_2]$ is the quenching rate, and A is the radiative lifetime. If individual vibrational bands are desired, modification of Equation (47) in the manner of Equation (37) is required. Also the A value and quenching rate for each vibrational level must be included individually. Self-absorption is not important for computation of column emission rates, but extinction by O_3 and O_2 may be important at the shorter wavelengths, depending on observation conditions.

The relative number densities for the A state in an aurora are plotted in Figure 40(b) without quenching, and with quenching for excitation at 110 km (Cartwright, 1978). The population rates have been determined by allowing for the various cascade processes in addition to the direct population of the A state. Comparison of auroral observations of the vibrational populations with theory were published by Eastes and Sharp (1987). Their results implied an underpopulation for $v' > 3$, but their normalization to the observations of Vallance Jones and Gattinger (1976) was somewhat arbitrary and

perhaps low. Furthermore, their comparison with the theory of Cartwright (1978) used the solid curve for the A state in Figure 40(b) (no quenching), whereas the dashed curve with quenching is more appropriate for the observation conditions of their rocket flight, and improves the agreement between theory and data. Figure 4 of Eastes and Sharp (1987) which compared their vibrational populations with other results, is reproduced in Figure 42, but Cartwright's A state population for quenching at 110 km (taken from

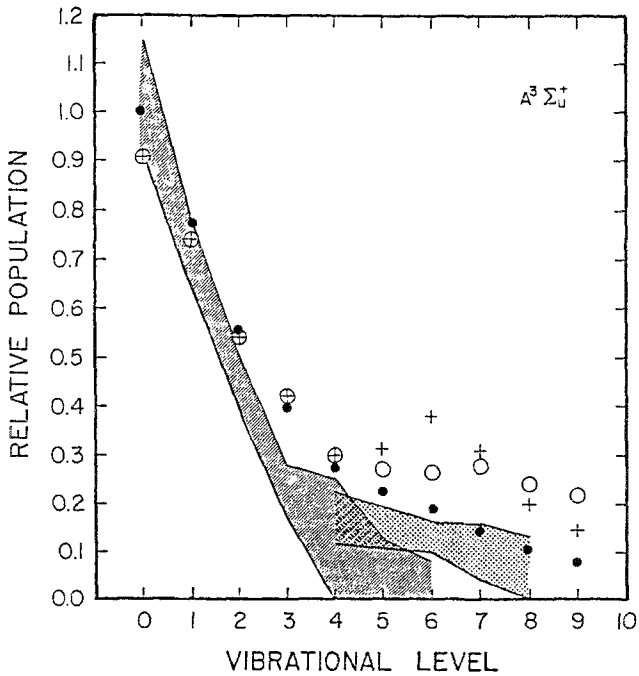

Fig. 42. Relative populations of N_2 (A) vs vibrational quantum number. The shaded area for v' between 0 and 6 gives the range of populations measured by Vallance Jones and Gattinger (1976). The shaded area from $v' = 4$ to 8 is the range measured by Eastes and Sharp (1987), normalized as shown. The plus symbols give the results of Degen (1982), the circles are from Cartwright (1978): open, no quenching; closed, quenching at 110 km altitude replotted from Figure 40(b). Adapted from Eastes and Sharp (1987).

Figure 40(b)) has also been plotted as large dots. As expected, the agreement between the population with quenching and the data is improved. Apparently no such analyses are available for the dayglow.

Assuming that the uncertainty in the laboratory values of the quenching rate of $N_2(A)$ by O is small, the ratio of emission rates of VK to 2 PG-bands can be used to obtain the atomic oxygen concentration in the atmosphere. This has been attempted on numerous occasions in auroras, but with mixed results due to the issues about the magnitude of the quenching rate (e.g., Sharp *et al.*, 1979; McDade and Llewellyn, 1984; Shepherd, 1984; Meier *et al.*, 1989).

The long lifetime of the A states means that it is an important carrier of chemical

energy. For example, quenching by atomic oxygen is likely to be an important, if not the main source of the green line (O I 5577 Å) in auroras (see the review by Hendriksen and Egeland, 1988). The yield for production of $O(^1S)$ from $N_2(A)$ quenching, however, is also controversial, ranging from 75–80% for $v' = 0$ in laboratory experiments (Piper, 1982; De Souza *et al.*, 1985) to much lower values derived from field measurements (Gattinger *et al.*, 1985; McDade and Llewellyn, 1984; O'Neil *et al.*, 1979). Quenching of higher v' levels apparently has not been measured.

4.1.1.3. *Lyman–Birge–Hopfield Bands* ($a\,^1\Pi_g - X\,^1\Sigma_g^+$). The $X - a$ transition is electric-dipole-forbidden, but is allowed for both magnetic dipole and electric quadrupole transitions. The a state is excited in the dayglow by photoelectron impact excitation. Recent measurements of the cross section made with fine-energy resolution, show the different cross section onsets as successive vibrational levels of the upper state are populated (Ajello and Shemansky, 1985). The peak value of the total cross section is given in Table V. Cascade from c_4' to a in the near-ultraviolet Gaydon–Herman bands (see Figure 39) has been observed as weak emission features in auroras (Dick, 1970; Slanger, 1983, 1986), but the branching ratio is perhaps only about 1% (Ajello *et al.*, 1989; see Section 4.1.1.5). Ajello and Shemansky (1985) place an upper limit of 5% for cascade of any type to the a state. The lifetime of the a state was found to be 80 μs by Holland (1969) and Shemansky (1969) (also see Ajello and Shemansky, 1985), 94 μs by Freund (1972), 115 μs by Borst and Zipf (1971) and Mason and Newell (1987); but a new measurement by Marinelli *et al.* (1989) gives 56 μs in excellent agreement with the theoretical calculations of Dahl and Oddershede (1986). There is little dependence of the transition probability on vibrational number (Figure 40(a) and Marinelli *et al.*, 1989). Quenching is not important above 95 km (Vallance Jones, 1974). The energy dependence of the LBH excitation cross section of Mason and Newell agrees quite well with the emission cross section of Ajello and Shemansky (Table V).

The vibrational population of the a state in the dayglow should follow Franck–Condon theory with slight enhancements of the lower vibrational levels due to the cross-section thresholds occurring at lower energies where the photoelectron fluxes are increasing (Meier *et al.*, 1985; Ajello and Shemansky, 1985). Pre-dissociation occurs above the $v' = 6, J' = 13$ rotational level (Douglas and Herzberg, 1951), apparently via the $^5\Sigma$-state. (See Gilmore (1965) for potential energy curves.) Rocket observations of the aurora (Meier *et al.*, 1982b) and dayglow at low solar activity (Meier *et al.*, 1980; Conway, 1982) have both supported direct excitation populations. Occasionally however, a depletion at $v' = 3$ has been observed (Meier *et al.*, 1985; Eastes and Sharp, 1987). Figure 43 taken from Meier *et al.* (1985) compares (1) vibrational populations from the 1978 auroral rocket (Meier *et al.*, 1982b; the 1987 dayglow gave essentially the same populations), (2) the direct theory, using Franck–Condon factors, (3) the 'threshold' theory which uses individual excitation cross sections for direct excitation to each vibrational level allowing for their different energy thresholds (Ajello and Shemansky, 1985), and (4) the 1980 dayglow results. The depletion in the 1980 dayglow population at $v' = 3$ is evident. However, a dayglow measurement in 1985 at solar

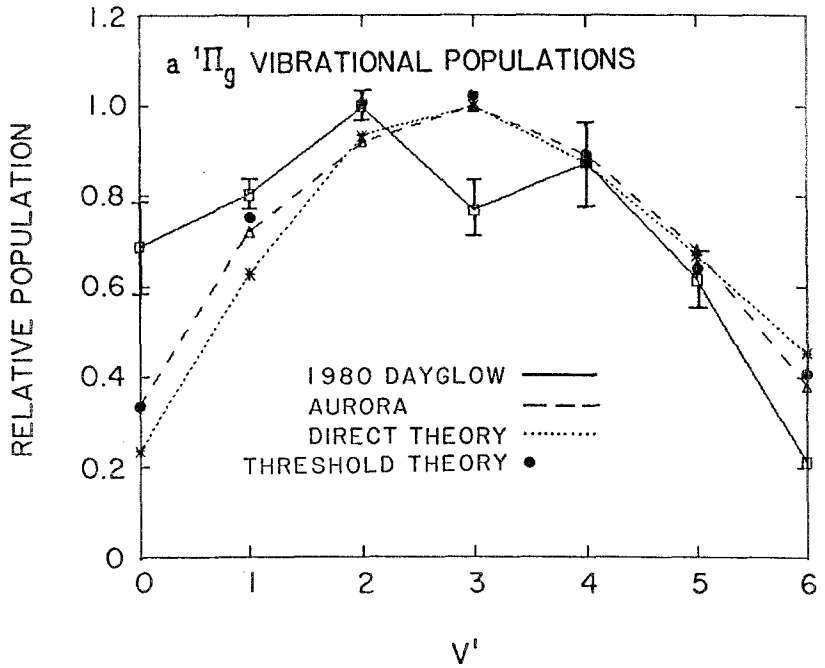

Fig. 43. Relative populations of N_2 (a) state vs vibrational quantum number. The solid lines with open squares are from the 1980 rocket data (see Table I); dashed with triangles, 1978 aurora (Meier *et al.*, 1982b); dotted with asterisk, Franck–Condon theory; closed circles, direct population using cross sections for individual vibrational transitions as measured by Ajello and Shemansky (1985). Taken from Meier *et al.* (1985).

minimum actually found a marginal *enhancement* at $v' = 3$, but it may not be statistically significant (Morrison *et al.*, 1990). The $v' = 3$ issues are not resolved.

The second peculiarity of the 1980 data is the overpopulation at lower v'. The relative densities for the a state given by Cartwright (1978) in Figure 40(b) include cascade from the a' and w states. The a'-state population peaks at $v' = 1$. The high population in the 1980 dayglow data at $v' = 0$ might be evidence for cascade from $a' \rightarrow a$, but this is not seen in the 1978 dayglow, the 1978 aurora, the 1985 dayglow, nor in the laboratory. The reasons for these departures are not understood, but perhaps quenching of the a' state may play a role (Cartwright, 1978). The percentages of $a\ ^1\Pi_g$ excitation which results in LBH emission are given in Table IX for selected bands (taken from Meier *et al.*, 1985).

Vibrational populations peaking at low vibrational levels have actually been observed in S3-4 satellite data (Meier and Conway, 1983) and from the Shuttle (Torr *et al.*, 1985). It now appears as though these observations are of interactions of the spacecraft with the atmosphere (Conway *et al.*, 1987). (The differences in Figure 6(a) between the solid line spectra (S3-4 observations) and the dotted line (dayglow theory) are attributed to spacecraft glow.) While earlier proposed explanations involving N + N association (Kofsky, 1988; Swensen and Meyerott, 1988) did not count for the vibrational distribu-

TABLE IX

Percentage of $N_2(a\ ^1\Pi_g)$ excitation resulting in LBH band emission

Band	Band origin, Å	Emission, %		
		1980 airglow	1978 aurora/airglow	Franck–Condon theory
(6, 5), (3, 3)	1488.8, 1493.4	1.8	2.3	2.4
(2, 0), (5, 2)	1384.0, 1381.7	6.5	5.7	5.8
(3, 0)	1353.8	4.9	5.9	6.0
(4, 0)	1325.4	5.3	4.8	4.9
(6, 0)	1273.4	0.8	1.5	1.5

tion, a recent report by Myerott and Swensen (1990) suggest that cascading from higher levels could. Marinelli *et al.* (1988) have observed rapid vibrational relaxation of the *a* state in the laboratory, which could play a role in redistributing the populations in a collisional environment. Thus while there are at least some processes which result in vibration populations different from Franck–Condon theory, their relevance to the airglow awaits a complete understanding of the processes themselves.

As with the 2 PG bands, the LBH-band radiances can be computed using Equations (21) and (37), but with modification for extinction by O_2. Self-absorption is weak, except for the (6, 0)-band at 1275 Å, whose low altitude radiance can be reduced by as much as 20% (Conway, 1982). Conway derived a band transmission function by taking the molecular rotational structure into account in the Holstein function (Equation (29)). He then applied this band transmission function to the multiple scattering of LBH and Birge–Hopfield (BH) emissions, assuming complete frequency redistribution (Conway, 1983a). Even in an energetic aurora where the excitation rate peaks below 110 km, enhancement of the LBH volume emission rate due to multiple scattering is limited to 7% because O_2 absorption rapidly removes LBH photons at these low altitudes where radiation entrapment would take place.

The N_2 scale height and, therefore, the exospheric temperature can be found from a measurement of the altitude profile of the emission rate above the peak (Meier and Anderson, 1983). The LBH-bands, like the 2 PG-bands, can provide information about the photoelectron flux, especially in the vicinity of 10–50 eV. The altitude of peak emission rate depends on the total atmospheric column through absorption of sunlight. These concepts are illustrated in the plots displayed in Figure 44, which show column emission rates for selected LBH-bands as functions of observation altitude, when viewing at 0 and 180° observation zenith angle (OZA). The upper and lower panels display solar max and min conditions. The column emission rates were obtained by integrating the volume emission rates at each of the six solar zenith angles in Figure 32, from the observing altitude to the atmospheric boundaries. Extinction by the O_2 Shumann–Runge continuum is included; the absorption cross section is shown in

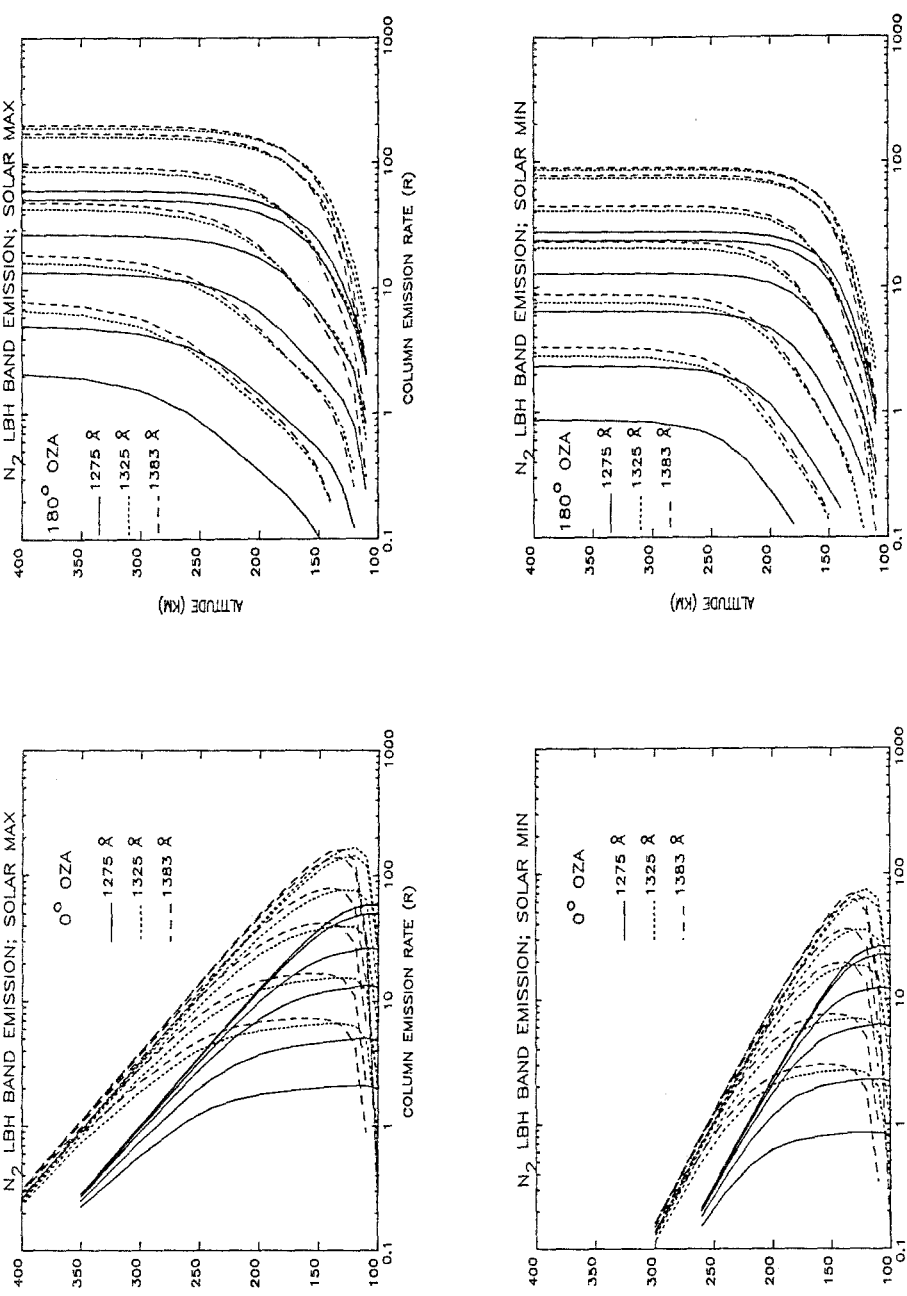

Fig. 44. Zenith (0 deg observation zenith angle) and nadir (180 deg) column emission rates for three LBH bands vs observing altitude at solar max (*upper panels*) and min (*lower panels*). The solar zenith angles are from right to left within each panel: 0, 30, 60, 75, 85, 90 deg, as in Figure 32. Branching ratios are from Franck–Condon theory and given in Table IX. The differences in slope at lower altitudes are due to O_2 absorption; the absorption cross section is given in Figure 47.

Figure 47. The branching ratios for the selected bands are from Table IX, using the Franck–Condon theory.

For zenith observations (0° OZA), the radiances from each of the bands converge at high altitude to the slope given by the altitude distribution of the N_2 concentration (determined by the exospheric temperature). The differences between solar min and max are obvious. At lower altitudes, the different behavior of the various bands is a consequence of pure absorption. The (6, 0)-band at 1273 Å suffers much less extinction, and its profile is less peaked. (The weak effects of self-absorption and pre-dissociation in the (6, 0)-band have not been included.) The other bands have significantly more absorption in the vicinity of the Shumann–Runge continuum. Consequently, the O_2 concentration can in principle be extracted from such observations. The utility of these emissions for remote sensing of thermospheric N_2 and O_2 is discussed more fully in Section 5.

As this review is going to press, R. Link pointed out a new measurement of the LBH-band electron impact excitation cross section by Brunger and Teubner (1990). Their peak value of 4.2×10^{-17} cm^2 is 40% larger than Ajello and Shemansky (1985). After accounting for pre-dissociation, the discrepancy is about 25%. If this new value is correct, modification of the airglow studies must be made.

4.1.1.4. *Birge–Hopfield I Bands* ($b\,^1\Pi_u - X\,^1\Sigma_g^+$). BH transitions have been identified in the dayglow by Chakrabarti *et al.* (1983) (Table II) and Eastes *et al.* (1985). Unfortunately, the bands are blended with other lines and are difficult to quantify. The bands have also been observed in the aurora (Feldman and Gentieu, 1982; see also Fischer and Schmidke, 1980) and in the atmosphere of Titan (Strobel and Shemansky, 1982). As will be seen below, the BH bands are a sensitive indicator of the vibrational population of ground state N_2.

The BH transition is dipole-allowed, but the solar EUV irradiance is weak at the locations of the vibrational bands, so photoelectron impact is the excitation source in the dayglow. As discussed by Zipf and Gorman (1980), most of the vibrational levels of the b state pre-dissociate, except for $v' = 1$, whose branching ratio for pre-dissociation is less than 10%. Table X lists the band origins and transition probabilities for some members of the $v' = 1$ progression (Conway, 1983a).

TABLE X

Band origins and transition probabilities for the N_2 Birge–Hopfield system

(v', v'')	$\lambda_{v'v''}$ Å	$A_{v'v''}$ s^{-1}
(1, 0)	985.7	4.77 + 7[a]
(1, 1)	1008.8	9.39 + 7
(1, 2)	1032.8	9.34 + 7
(1, 3)	1057.6	5.97 + 7
(1, 10)	1258.7	1.13 + 7

[a] $+7 = 10^7$.

The optical depth at line center for the thickest rotational line in the (1, 0) BH-band is 12000 above 100 km. Consequently, multiple scattering must be taken into account when computing the excitation rates and radiances. Conway (1983a) has described the radiative transport problem, assuming that the population of N_2 molecules in the ground state vibrational levels can be characterized by a vibrational temperature. When a molecule is excited to the b level by an electron collision, there is only a 4% probability of populating the $v' = 1$ level. Therefore the emission is expected to be weak. The transition probabilities to the various vibrational levels of the ground state are given in Table X. Because of the large optical depth in the (1, 0)-band, even if the population of $v'' > 0$ states is small, multiple scattering can ensue. The photons will continue to resonantly scatter, eventually working their way out through successive branches to optically thin v'' levels, from which they will escape the atmosphere or be absorbed by O_2. As a result, the emission rates of the (1, v'')-bands depend sensitively on the v'' populations. For calculations of multiple scattering of BH-bands in an aurora, Conway (1983a) has shown that in spite of the very large optical depth for $v'' = 0$, the rapid loss of photons through migration to larger v'' transitions limits the number of scatterings to fewer than three. To calculate the radiance, it is necessary to use a band-averaged version of the transmission function in Equation (29), which takes into account the detailed rotational structure (Conway, 1982). Because enhancement of the volume emission rate due to multiple scattering is weak in the thickest bands, while self-absorption is strong, the radiance of these bands is substantially less than would be computed under optically thin conditions.

Conway's calculations of the radiance in a 2 keV aurora were about a factor of two larger than the observations of Feldman and Gentieu (1982) (actually now only 70% larger, due to a change in the H_2 Lα emission cross section, which had been used as a calibration standard for measurements of many other emission cross sections (Shemansky *et al.*, 1985)). The (1, 10) features observed by Feldman and Gentieu suggested a vibrational temperature of 1000 K. No calculations have been made for BH-bands in the dayglow, but the degree of multiple scattering should be less than for a 2 keV aurora.

4.1.1.5. *Birge–Hopfield II Bands* ($b'\,{}^1\Sigma_u^+ - X\,{}^1\Sigma_g^+$). Emissions from the b'-state have been identified in the airglow by Gentieu *et al.* (1981), Chakrabarti *et al.* (1983), and Morrison *et al.* (1990). In most cases the bands were blended with other emissions, so precise magnitudes are difficult to determine. The $X \rightarrow b'$ transition is allowed, but at the resonant wavelengths weak solar irradiance dictates that photoelectron impact is the excitation source. The excitation cross sections have been measured in the laboratory by Zipf and McLaughlin (1978) and recently at higher resolution by Ajello *et al.* (1989). Both groups find that pre-dissociation of the b' state is of order 84%. That coupled with fairly small emission cross sections for individual bands implies weak airglow radiances. No modelling of these bands has been undertaken.

4.1.1.6. *Caroll–Yoshino (CY) Bands* ($c_4'\,^1\Sigma_u^+ - X\,^1\Sigma_g^+$). The transition of N_2 from the ground state to the c_4' Rydberg level is allowed, but, as in the case of the BH-band excitation, photoelectron impact is the source due to the lack of EUV sunlight. Laboratory work by Zipf and McLaughlin (1978) and Ajello *et al.* (1989) has shown relatively strong emission cross sections for the (0, 0) and (0, 1)-bands at 958 and 980 Å, respectively (Table V). Yet only weak emission is seen in the aurora (Park *et al.*, 1977; Feldman and Gentieu, 1982; Fischer and Schmidke, 1980) and dayglow (Gentieu *et al.*, 1981, see Figure 7; Chakrabarti *et al.*, 1983, see Table II). This missing radiation has been the subject of serious concern, especially for the energy budget in auroras. Zipf and MacLaughlin review the issues through 1978. More recently, Slanger (1986) estimated that as much as 1 *MR* is unaccounted for (although below it is found that Slanger's conclusions should be modified based on new data).

N_2 molecules excited to the c_4' state can suffer any of several fates. They can: (1) relax to the X ground state, re-emitting in the CY-bands; (2) pre-dissociate; (3) branch to the a state, emitting in the Gaydon–Herman bands (Figure 39); (4) mix with the b' state, followed by emission or loss via b' pre-dissociation. Zipf and McLaughlin (1978) and Ajello *et al.* (1989) have reviewed many of the issues regarding these processes.

Zipf and McLaughlin argued that while pre-dissociation is weak (they found $< 15\%$ for $v' = 0$ and 3), multiple scattering within the CY-bands effectively increases the pre-dissociation probability to the extent that little EUV radiation is left. Ajello *et al.* put the upper limit to pre-dissociation at 10%, citing the close agreement between their CY-band emission cross sections and the energy loss cross sections of Geiger and Schroder (1969), as well as the lack of diffuseness in absorption lines measured at 5 mÅ resolution by Yoshino and Tanaka (1977).

Ajello *et al.* calculated the branching ratio to the a state from $v' = 0$ of the c_4' state by comparing their total $c_4'(O) - X$ emission cross section of 88.5×10^{-19} cm^2 to the $c_4'(O) - a$ emission cross section of Filippelli *et al.* (1984) of 9.7×10^{-20} cm^2. This yields a branching ratio of 1.1% to the a level.

The optical depths of the rotational lines of the CY-bands reach tens of thousands. The multiple scattering problem is similar to the BH problem, except that $v' > 0$ vibrational levels should be taken into account. If no other loss process were at work, there would be a trend for photons to migrate from the thickest to the thinnest bands by branching to higher v' levels, followed by escape or by O_2 absorption. A difficulty in modelling the radiative transport problem, is that if pre-dissociation occurs, the absorption line width is not determined by the natural lifetime, but by broadening caused by the perturbation leading to dissociation. As with the BH problem, the vibrational population of the ground state is a crucial parameter; the greater the numbers of molecules in $v'' > 0$, the greater the degree of multiple scattering.

In order for the Zipf and McLaughlin mechanism of enhanced pre-dissociation under optically thick conditions to work, the probability of pre-dissociation would have to be greater than the $c_4' - a$ branching probability. Otherwise $c_4' - a$ branching would dominate the loss of CY radiation and copious emission would be present in the Gaydon–Herman bands between 2800–3700 Å. Weak emissions seen in auroras (Dick,

1970 and Sivjee, 1983) have led Slanger (1983, 1986) to estimate that 1 *MR* of $c_4' - X$ emission is missing in an IBC III aurora. Slanger's estimate of the $c_4' - X$ is based on the ratio of the N_2 2 PG (3, 5)-band to the $c_4'(0) - a(5)$ (= 1.33) reported by Vallance Jones (1971) and Sivjee (1983). Assuming that 0.5% of the 2 PG emission resides in the (3, 5)-band and that the $c_4'(0) - a(v'')$ to $c_4'(0) - X(v'')$ ratio is 0.006 (Fillipelli *et al.*'s (1984) upper limit), Slanger found a ratio of 0.12 for the total 2 PG to $c_4'(0) - X(v'')$ which implies more than a *MR* for the Caroll–Yoshino bands in an IBC III aurora (110 kR of 2 PG). Slanger's ratio of 0.12 becomes 0.3 if the 2 PG (3, 5)-band consists of 0.28% (instead of 0.5%) of the total (Vallance Jones, 1974) and if the $c_4'(0) - a(v'')$ branching ratio is computed using the ratios of the Fillipelli *et al.*'s $c_4' - a$ and Ajello *et al.*'s (1989) $X - c_4'$ cross sections (yielding 0.011 instead of 0.006).

An alternative way to estimate the amount of $c_4' - X$ excitation is to use the Strickland *et al.*'s (1989) model to compute the ratio of 2 PG to $c_4' - X$ excitation rates. The model gives a ratio of 1.9, a factor of 6 larger than the revised Slanger number. The resolution of this apparent discrepancy can be found by considering multiple scattering effects. The $X(0) - c_4'(0)$-band (at least) is optically thick. Multiple scattering will increase the $c_4' - a$ branching ratio considerably over the optically thin value of 0.011. Preliminary computations indicate that a factor of 6 enhancement in the $c_4' - a$ emission rate is certainly attainable. Therefore, using the ratio of 1.9 for 2 PG to CY-band excitation, an IBC III aurora should produce 56 kR initially, rather than a *MR* inferred from the observed $c_4' - a$ emission rate. This is still a formidable amount to explain away.

Since no observation of the Caroll–Yoshino bands has been reported for an IBC III aurora, perhaps a better estimate of the missing radiation can be made using the EUV data obtained by Feldman and Gentieu (1982) in a well-characterized aurora. During that flight, the 3914 Å emission rate observed horizontally at 180 km (where O_2 atmospheric extinction is low) was about 4 kR (Meier *et al.*, 1982). The ratio of 958 to 3914 from the Strickland *et al.* (1989) model is 0.48, for optically thin conditions. Thus about 2 kR of 958 Å emission should have been produced initially in that horizontal column. The 958 Å intensity actually observed by Feldman and Gentieu is difficult to determine due to contamination by an N I line, but is less than 200 *R* at 180 km. Thus the predicted column excitation rate at 958 Å is about an order of magnitude larger than the observed upper limit to the emission rate. There is still a problem in accounting for missing CY-bands, but it is not as serious as previously thought.

Perhaps the best observational information is the recent measurement of the EUV dayglow spectrum at 2 Å resolution from a rocket at 80 deg solar zenith angle reported by Morrison *et al.* (1990). They were able to separate the (0, 0), (0, 1), and (0, 2) bands, albeit with some lack of precision in the magnitudes of the radiances. The measured emission rates at 958, 980, and 1003 Å were 3.9 ± 2, 9 ± 5, and $0.9 \pm ?$ *R*, respectively. The values calculated with the Strickland and Meier (1982) photoelectron code under optically thin conditions were 37, 6, and 0.6 *R* for the three bands. The observed emission rates peak in the (0, 1)-band, rather than at (0, 0) as computed, supporting the contention that multiple scattering is shifting photons to higher, but thinner v'' levels. Furthermore, the ratio of the calculated column emission in the three bands to the measured was 3, implying that multiple scattering enhances any loss process.

Ajello *et al.* (1989) suggested on the basis of work by Stahel *et al.* (1983) that the weak interaction between the c_4' and b' states may be a loss process for CY-band radiation. This has not been investigated quantitatively. Clearly, detailed modelling of the c_4'-band system is required to assess this loss process as well as the other issues discussed above.

4.1.2. *Molecular Oxygen*

4.1.2.1. *Herzberg I Bands* ($A\,^3\Sigma_u^+ - X\,^3\Sigma_g^-$). The Herzberg I transition is shown in the energy level diagram for O_2 in Figure 45. The study of these nightglow bands

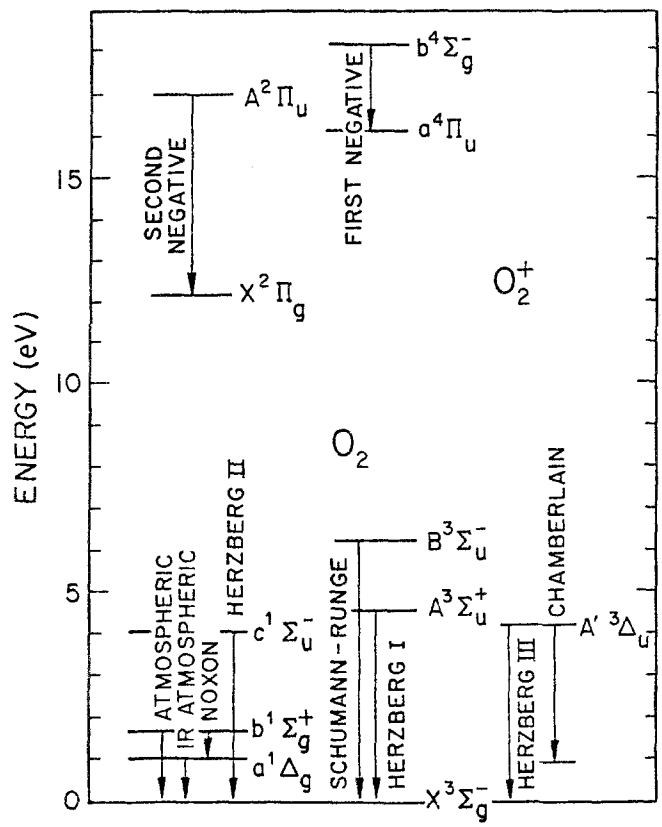

Fig. 45. Partial energy level diagram for O_2 and O_2^+.

(Figures 9 and 10) has had a long history. Reviews of the Herzberg I and II, and Chamberlain bands were published by McDade and Llewellyn (1986) and Bates (1988a, b). See also Parisot (1986). The photochemistry leading to the Herzberg I-band excitation is discussed as an example of chemiluminescence in Section 3.2.2.2. The volume emission rate for the bands is given by Equation (46). Transition rates for the forbidden Herzberg and Chamberlain systems of O_2 were given recently by Bates (1988a) (see Bates, 1989, for an update). Transition rates for Herzberg I range from 10.5–2.0 s^{-1} for v' between 0 and 11. Rocket observations have shown that the volume

emission rate at night peaks in the vicinity of 95–100 km (Thomas, 1981; McCoy, 1983a; Murtagh *et al.*, 1986). Quenching coefficients measured in the laboratory for N_2 and O_2 (Kenner and Ogryzlo, 1984) are much lower than deduced from rocket experiments (Thomas, 1981). Apparently there is little quenching by O. Bates (1988a, b) has argued that quenching of various states of O_2 collision-induced transitions were not taken into account in the laboratory work and that severe quenching of the A state can explain the nightglow.

Vibrational populations of the A level peak at $v' = 5$ and 6 in the terrestrial nightglow. Figure 46, taken from Stegman and Murtagh (1988), compares relative populations

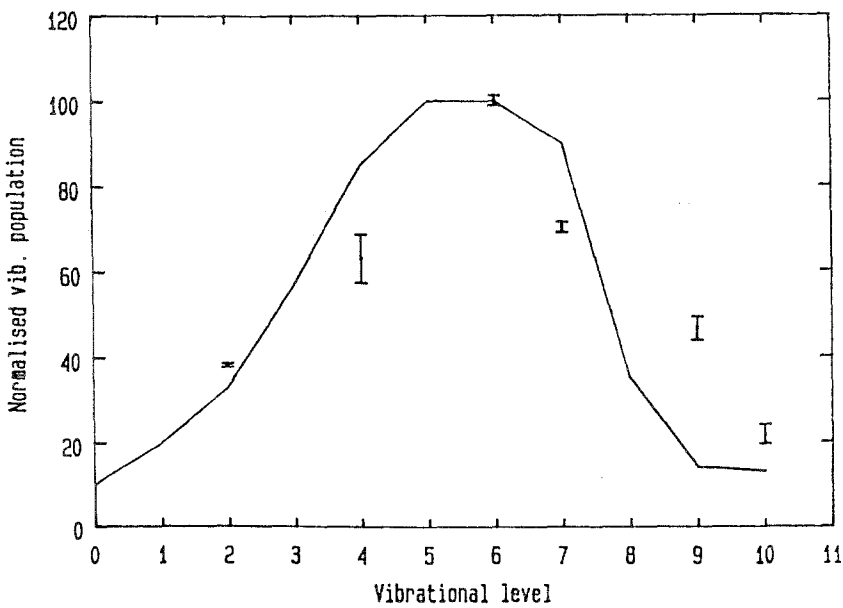

Fig. 46. Relative populations of the O_2 (A) state vs vibrational quantum number. The solid line is the population distribution deduced by Slanger and Huestis (1981) and the points with error bars are the measurements of Stegman and Murtagh (1988). Taken from Stegman and Murtagh (1988).

obtained from their ground-based observations with those deduced by Slanger and Huestis (1981) (also see Figure 10). The agreement between the two is fair. Further complicating the situation are peculiar changes which have been seen in the altitude dependence of the vibrational poulations, but which are not explained satisfactorily by selective quenching (Murtagh *et al.*, 1986). The various issues are discussed in detail by McDade and Llewellyn (1986) and Bates (1988a, b).

For altitudes somewhat above the peak of the volume emission rate (on the Earth), quenching is not important. The O concentration there can be obtained from the volume emission rate (found by differentiating the column emission rate with respect to altitude).

There is a weak Herzberg I absorption continuum from 1850 to 2600 Å, which results in dissociation of O_2. This is an especially important process for middle atmosphere problems where it is necessary to include absorption in the vicinity of 2000 Å, i.e., the

region from the O_2 Schumann–Runge bands to the longer wavelength Hartley bands and continuum of O_3. Yoshino *et al.* (1988) have re-analyzed and assessed various observations of the absorption cross-section, which peaks near 2000 Å with a value of 7×10^{-24} cm^2.

4.1.2.2. *Schumann–Runge Absorption* ($B\,^3\Sigma_u^- - X\,^3\Sigma_g^-$). The SR absorption bands (1750–2050 Å) are important absorbers of solar FUV radiation in the middle atmosphere. High-resolution spectroscopic observations in the laboratory have been made over the years (e.g., see Lewis *et al.*, 1986; Cheung *et al.*, 1986; Yoshino *et al.*, 1987). Recent theoretical studies include work by Nicolet *et al.* (1988), Nicolet and Kennes (1988a, b) and Murtagh (1988).

The SR continuum between 1250 and 1750 Å causes differential absorption of the N_2 LBH-bands in the lower thermosphere. Consequently, the ratios of different LBH-bands provide information on the absolute concentration of O_2. This effect is illustrated in Figure 47, which shows an LBH spectrum (albeit for an aurora), as well as the O_2

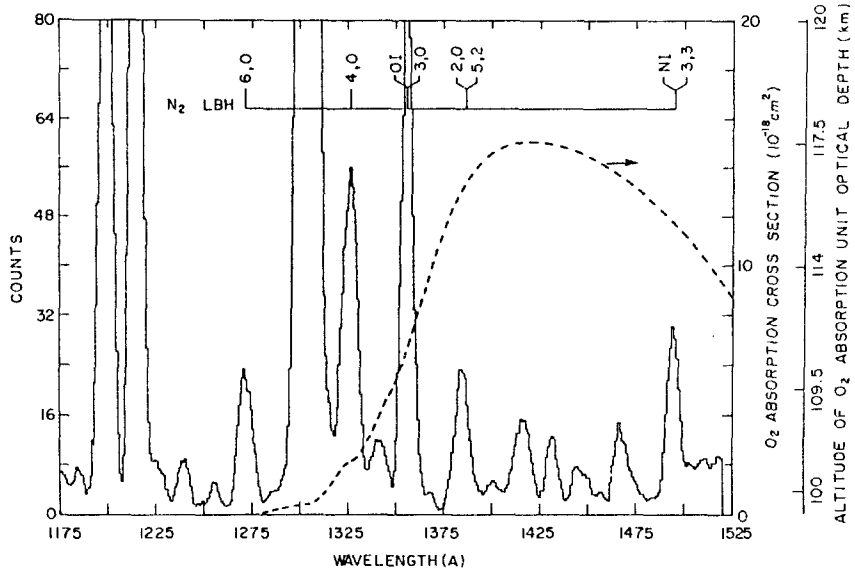

Fig. 47. Comparison of FUV nadir viewing auroral spectrum (solid line) and O_2 absorption cross section (dashed line). The scales on the right give the magnitude of the cross section and the altitude of unit optical depth in the vertical for extinction. Taken from Strickland *et al.* (1983).

absorption cross section and the altitude corresponding to unit vertical optical depth (taken from Strickland *et al.*, 1983). As an example, the (6, 0) LBH-band at 1275 Å suffers little O_2 extinction in the thermosphere, so the entire emitting column can be observed. But for the (2, 0)-band at 1384 Å, Figure 47 shows that only emission above about 116 km can be detected. Thus the ratio of these two bands is sensitive to extinction by O_2. In principle, an altitude profile of the LBH-bands can yield the O_2 concentration.

When viewing the limb, the O_2 'filtering' altitude increases by several tens of km. Detailed examples are given in Section 5.

4.1.3. *Atomic Oxygen*

The figures presented in Section 2 showed the emission lines of atomic oxygen to be among the brightest in the UV airglow. Remote sensing of these lines offers an attractive technique for measuring the global variation of atomic oxygen, a feat which has been notoriously difficult using alternative methods. In this section, the relative merits of several spectroscopic approaches are discussed, focussing on the FUV and EUV emissions. Most of the transitions can be seen in the energy level diagram in Figure 48.

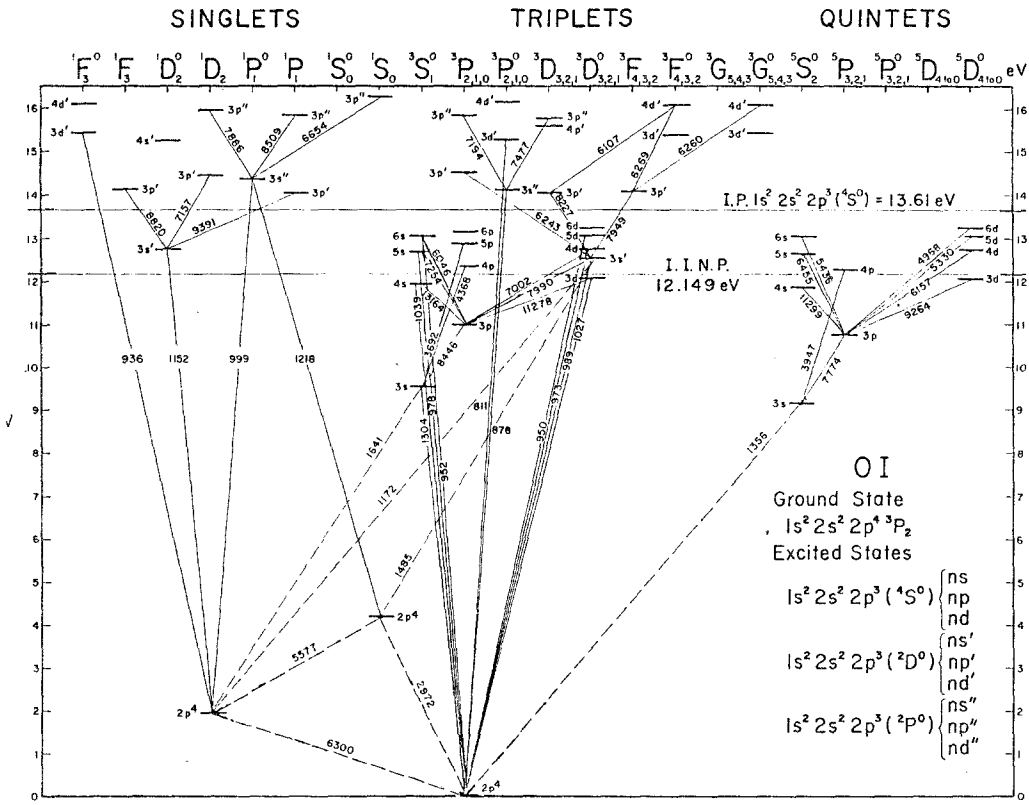

Fig. 48. Partial energy level diagram of atomic oxygen. Forbidden transitions are indicated by dashed lines. Adapted from Tinsley (1972).

The emission line at 2972 Å will not be discussed here; it originates at the same level as the green line at 5577 Å, and is subject to the same controversial issues (see reviews by Hays *et al.*, 1988; and Bates, 1988c; and their references).

4.1.3.1. *1356 Å* ($2p^4\ ^3P - 3s\ ^5S$). This spin-forbidden transition is a prominent feature of the dayglow. The emission consists of a doublet ($^3P_2 - {}^5S_2$) and ($^3P_1 - {}^5S_2$), with wavelengths, oscillator strengths, and transition probabilities given in Table IV. The traditional designation '1356 Å' is meant to indicate the sum of the emission in both lines of the doublet. The transition is shown in more detail in the partial energy level

diagram of Figure 49. Solar fluorescence at these wavelengths is weak compared with photoelectron impact excitation in the dayglow. Even though the energy dependence of

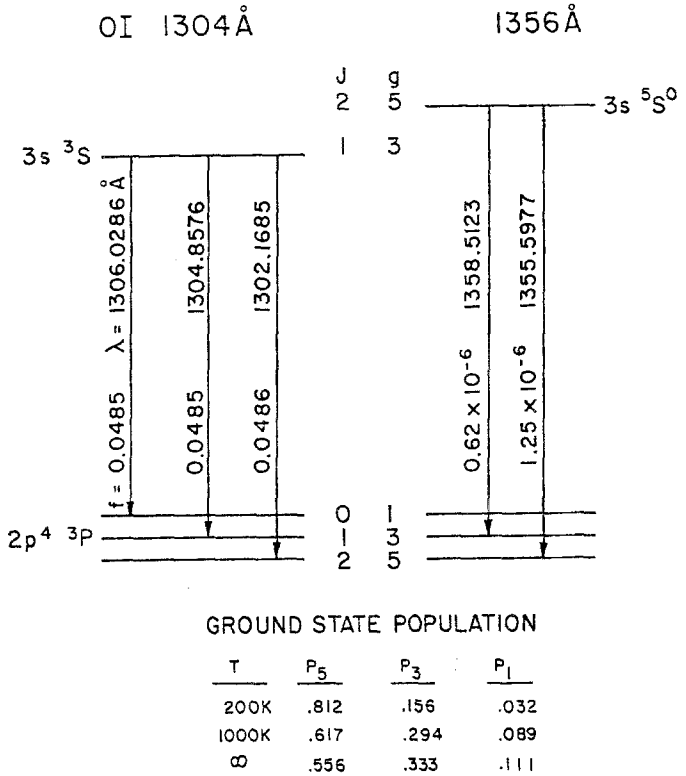

Fig. 49. Qualitative energy level diagram for the 1304 and 1356 Å transitions of atomic oxygen, giving fine structure wavelengths and oscillator strengths. Populations of ground state levels are tabulated for different temperatures.

the electron inelastic scattering cross section is narrow, the magnitude of the peak is appreciable (Figure 28 and Table V), and the excitation rate is significant (Figure 32). The resonant optical depth above the O_2 absorption level (about 110 km; Figure 47) is near unity at line center due to the large abundance of atomic oxygen. Therefore multiple scattering should be taken into account for precise modelling.

The total cross section plotted in Figure 28 consists of direct population of the ^5S state as well as cascade from higher states. The cross section for direct excitation was recently measured by Doering and Gulcicek (1989); the peak value is 3.1×10^{-18} cm^2 near 15 eV, in excellent agreement with the theoretical calculations of Julienne and Davis (1976). However, the observed energy function is more sharply peaked than the Julienne and Davis theory. Further complicating the situation is the theoretical direct excitation cross section computed by Roundtree (1977), which shows a strong resonance slightly above the threshold at 9.14 eV. Doering and Gulcicek did not make measurements below 13.9 eV, so they could not confirm the resonance, but it does not appear in the

more recent theoretical cross section of Tayal and Henry (1989). (Note that a similar resonance was present in the ^3S calculation of Roundtree and Henry (1972), but it also does not appear in the later calculations of either Julienne and Davis (1976) or Tayal and Henry (1988); see below.) So perhaps it is an artifact.

The largest contribution to cascade to ^5S comes from the ^5P state. The direct excitation of the ^5P state from the ^3P ground state has a peak cross section of 2.3×10^{-18} cm^2 (Gulcicek *et al.*, 1988). The theoretical peak is about 3.6×10^{-18} cm^2, occurring between two observed values (Tayal and Henry, 1989). Theory and experiment are consistent to within the uncertainties. Since there are no intermediate branches and the $^5P \rightarrow {}^5S$ transition is allowed, the cross sections of these two excited states can be summed, yielding 6.7×10^{-18} (ignoring any differences in the energy functions).

The total 1356 Å emission cross section measured by Stone and Zipf (1974) is 2.5×10^{-17} cm^2. If the downward revision of earlier O cross sections by Zipf and Erdman (1985) of a factor of 2.8 is applied to the Stone and Zipf 1356 Å value, the resulting 9×10^{-18} cm^2 agrees with the dayglow (Morrison and Meier, 1988; Conway *et al.*, 1988; Link *et al.*, 1988a, b). The difference between this value and the above sum of the ^5S and ^5P may be due to cascade from levels higher than ^5P. This conclusion is consistent with the other calculations tabulated by Julienne and Davis (1976), although their cascade contributions from levels above ^5P and therefore their total cross sections are slightly larger (6 and 12×10^{-18} cm^2, respectively). These cross sections are listed in Table XI, along with other states cascading to ^5S. The cascade cross sections have been multiplied by their respective probabilities of branching to ^5S.

Thus there is reasonable agreement on the magnitude of the peak emission cross section for 1356 Å. But nagging problems remain with the energy function. Uncertainties in the laboratory measurements (typically quoted as $\pm$ 30–50%), as well as in the theory, leave room for improved precision in future work.

O(^5S) initial volume excitation rates were presented in Figure 32 (solid lines) as examples of a photoelectron-excited atomic oxygen emission in the dayglow. The calculations were made using the cross section, model atmospheres and photoelectron fluxes in Figures 28, 30, and 31, respectively. Enhancements in the volume excitation rates due to multiple scattering (dashed curves in Figure 32) were computed using Equation (34) but with inclusion of (1) extinction by O_2, (2) the fine structure atomic levels, following the formalism of Strickland and Donahue (1970) and Strickland and Rees (1974), and (3) changes in the Boltzmann populations of the ground state angular momentum states with thermospheric temperature, as indicated in Figure 49.

The column emission rate for O I 1356 Å is given by Equation (30), using Equation (39) and incorporating the fine structure transitions in the following way:

$$4\pi I = \int j[\mathbf{s}]\,(B_5 T[\tau_5] + B_3 T[\tau_3])\,\mathrm{d}s\,, \tag{48}$$

where j is the volume excitation rate to the ^5S upper state, B_5 ($= A_{55}/(A_{55} + A_{53})$ is the branching ratio to the $g = 5$ ($J = 2$) lower level (Figure 49), and τ_5 is the optical depth

TABLE XI

O I photoelectron emission cross sections (10^{-18} cm^2) for 1356 and 1304 Å

Feature	Optical depth	Type	Direct	Cascade							Total cascade	Total	Ref.
				$3s'$	$3p$	$3d$	$4s$	$4p$	$4d$	$4f$	$n=5$			
1356 Å at 15 eV	Thin	Thy	2.9		2.6	1.5	0.9	1.1	1.0	0.05	1.4	8.6	11.5	1
	Thin	Lab	3.1		3.6									2, 4
	Thin	Lab											9	3
1304 Å at 20 eV	Thin	Thy	7.1	0.7	5.7	0.5	0.2	0.5	0.1	0.004	0.3	8	15	1
	Thick	Thy	7.1	6.6	5.7	2.5	1.4	1.8	1.5	0.02	2.6	22	29	1
(Revised)	Thin	Lab	11	10^{-4} [a]	7.7	0.7	(0.2)	(0.5)	(0.1)	(0.004)	(0.3)	9	20	2, 4, 5, 6
(Revised)	Thick	Lab	11	0.6 [b]	7.7	2.4	(1.4)	(1.8)	1.3	(0.02)	(2.6)	18	29	2, 4, 5, 6
	Thin	Thy	10.8		11.3									7
(Emission)	Thin	Lab											17	8

[a] 5.4 (Ref. 4) × 2 × 10^{-5} (Erdman and Zipf, 1983).

[b] 5.4 (Ref. 4) × 0.11 (see text).

( ) Assumes Ref. 1 values.

References

1. Julienne and Davis (1976).
2. Doering and Gulcicek (1989).
3. Stone and Zipf (1974) reduced by 2.8.
4. Gulcicek *et al.* (1988).
5. Vaughan and Doering (1988).
6. Gulcicek and Doering (1988).
7. Tayal and Henry (1988).
8. Zipf and Erdman (1985).

at line center for the $^3P_2 - {}^5S_2$ transition. Note that actual branching ratios must be used in accounting for branching into each of the two lines in the 1356 Å doublet, whereas in the formalism developed for the 1304 Å triplet, Strickland and Donahue (1970) and Strickland and Rees (1974) instead used ratios of statistical weights. This is correct for 1304 Å since the oscillator strengths of the three lines are virtually identical. In adapting the radiative transport code to 1356 Å, Strickland and Anderson (1983) also used statistical weight (instead of branching) ratios for 1356 Å. However, calculations have shown that little error is introduced in the total (doublet) column emission rate when the solar zenith angle is less than 60 deg or if the viewing direction is away from the region of greatest multiple scattering (which occurs below 150 km; see Figure 32). Link *et al.* (1988a) correctly used branching ratios (R. Gladstone, private communication, 1989).

Examples of vertical column emission rates for O I 1356 Å are shown in Figure 50 as functions of viewing altitude for observation zenith angles (OZA) of 0 and 180 deg. Both solar max and min atmospheres are illustrated. Excitation rates at the six solar zenith angles in Figure 32 were used in the computations. The two sets of curves in each panel represent (1) the correct calculation using Equation (48) including multiple scattering in j (dashed lines) and (2) the simplified case where optically thin conditions are assumed (no multiple scattering and unity T functions in Equation (48) (solid lines). In both cases, extinction by O_2 is included. The greatest error in ignoring multiple scattering occurs when viewing downward (OZA = 180 deg) from low altitudes at large solar zenith angles. There the initial excitation rate peaks above 200 km, so most of the emission observed comes from backscattering at lower altitudes. Under those viewing conditions, it is clear that neglect of multiple scattering leads to large errors. This is true even though the vertical resonant optical depth is only near unity. For other viewing conditions, the differences between the correct calculation and the optically thin approximation are less.

As with N_2 LBH-band emissions (Figure 44), the differences between altitude profiles at solar min and max are obvious indicators of the exospheric temperature. Remote sensing of 1356 Å altitude profiles gives information on both the magnitude and altitude distribution of atomic oxygen. When 1356 Å is combined with N_2 airglow measurements, the neutral atmospheric composition and altitude distribution can be specified, in principle. This has been done with rocket and satellite data in the past. Recent papers on the subject are by Meier *et al.* (1985), Link *et al.* (1988a, b), Conway *et al.* (1988), Morrison and Meier (1988), Morrison *et al.* (1991). Additional remote sensing concepts are discussed in Section 5.

The O I 1356 Å nightglow is produced by radiative recombination of O^+ and has an initial excitation rate slightly larger than the 911 Å volume emission rate seen in Figure 37 (also see Figure 17(b)). The excitation rate is given by Equation (41), except that the recombination coefficient is 4.9×10^{-13} cm^3 s^{-1} (Julienne *et al.*, 1970). An important difference between 911 and 1356 Å is that multiple scattering can cause a secondary low altitude peak in the total volume excitation rate of the ^5S level, while 911 Å is due to recombination to the ^3P ground state and the resulting continuum

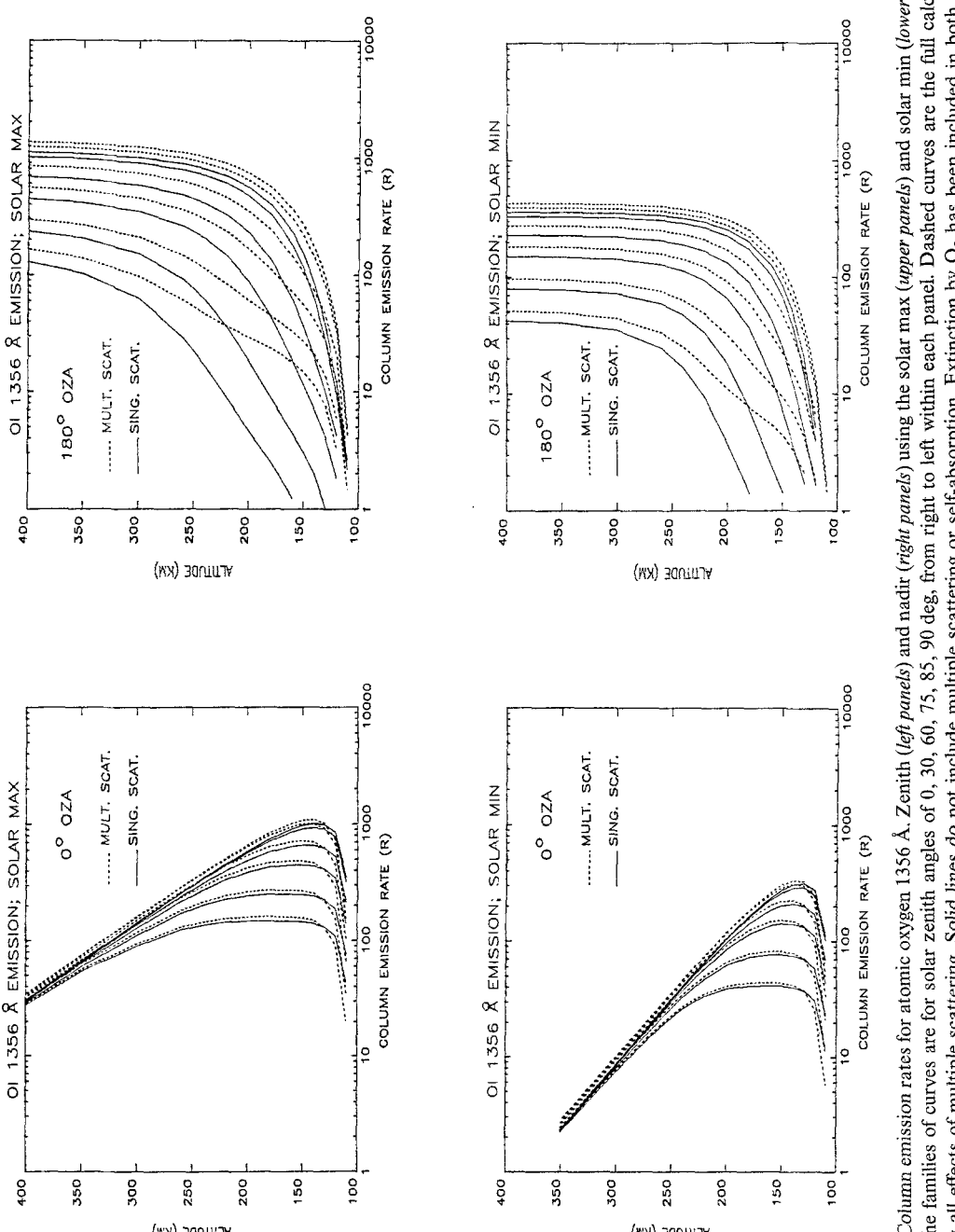

Fig. 50. *Column emission rates for atomic oxygen 1356 Å. Zenith (left panels) and nadir (right panels) using the solar max (upper panels) and solar min (lower panels) models. The families of curves are for solar zenith angles of 0, 30, 60, 75, 85, 90 deg, from right to left within each panel. Dashed curves are the full calculation including all effects of multiple scattering. Solid lines do not include multiple scattering or self-absorption. Extinction by* O_2 *has been included in both cases.*

radiation is not multiply scattered. Paxton *et al.* (1991) have studied the 1356 Å nightglow problem in some detail. An example of their calculations is shown in Figure 51.

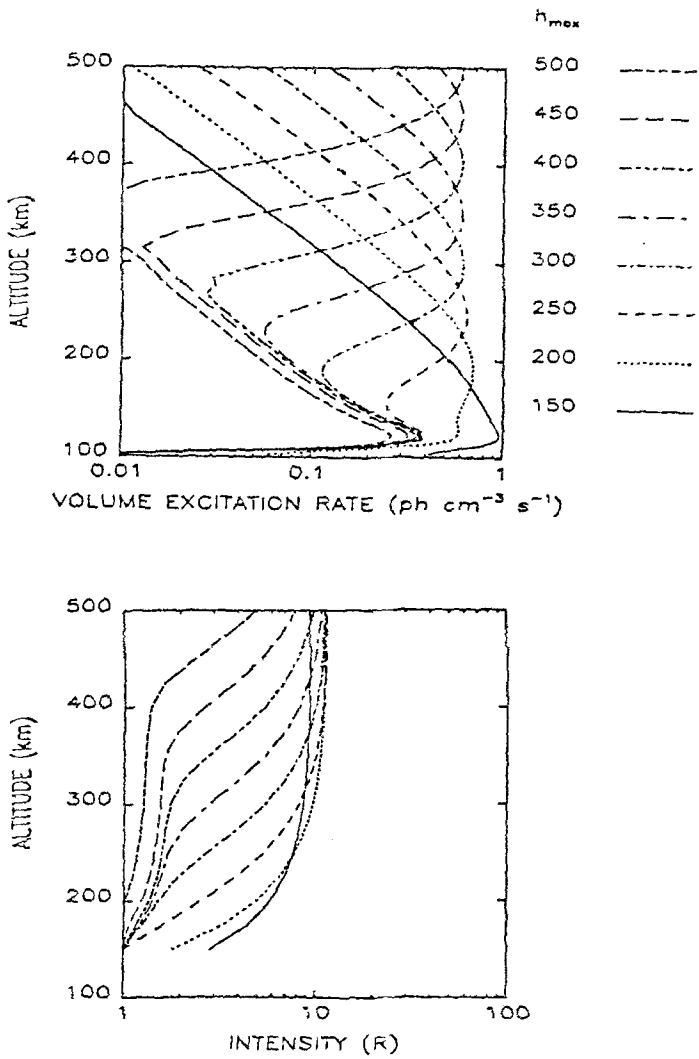

Fig. 51. *Upper panel*: Volume excitation of O(^5S) state for Chapman layer ionosphere peaking at the indicated heights. For each profile, the peak electron concentration was fixed at 10^6 cm^{-3} and the scale height was set at 60 km. Multiple scattering was included. *Lower panel*: Column emission rates vs observation altitude for nadir viewing. Each curve corresponds to the ionospheric layer in the upper panel.

The upper panel shows the total volume emission rate, including multiple scattering from a Chapman ionospheric layer with a peak concentration of 10^6 cm^{-3} and scale height of 60 km, but whose peak height varies from 150 to 500 km. The behavior is qualitatively similar to the dayglow: as the ionosphere rises, the initial excitation rate rises (as it does in the dayglow with increasing solar zenith angle) and separates from the secondary

peak at low altitudes due to multiple scattering. The magnitude of the primary peak, however remains the same (for $h_{max} > 150$ km) since the peak electron concentration was kept constant.

The column emission rate for an OZA of 180 deg is shown in the lower panel of Figure 51. For low altitude satellites such as S3-4, the bulk of the emission rate seen in the nadir from 150–250 km is due to multiple scattering, and consequently provides information about atomic oxygen as well as O^+. For higher altitude satellites such as STP 78-1, the effect of multiple scattering is to increase the nadir column emission rate by about 20%.

Early work by Meier and Opal (1973) showed a good correlation between the column emission rate observed from OGO-4 and the electron concentration observed during overpasses of ground ionosondes, and thereby confirmed the radiative recombination source proposed by Hanson (1969). Subsequent work (e.g., Chakrabarti, 1984; Abreu *et al.*, 1984, 1986; Paxton *et al.*, 1991) supports this conclusion.

4.1.3.2. *1304 and 1641 Å* ($2p^4\ ^3P - 3s\ ^3S$ *and* $2p^4\ ^1D - 3s\ ^3S$). It has long been hoped that the 1304 Å triplet could be used as a diagnostic of the concentration of atomic oxygen in the thermosphere because of its prominence in the FUV spectrum. The extremely large line-center opacity of the atmosphere at the center of these resonance lines has presented a formidable obstacle to the ready interpretation of observations. Early attempts at modelling the airglow (Strickland and Donahue, 1970) and aurora (Strickland and Rees, 1974) depended on the assumed validity of CFR in an isothermal scattering atmosphere. Later work by Meier and Lee (1982) showed that the details of frequency redistribution are important, that PFR must be employed to account for radiation transport in the wings of the line, and that isothermicity is not a valid approximation (also see Strickland, 1979, for additional details on this latter point). Still later work by Meier and Conway (1985) found that a branching transition at 1641 Å provides a sensitive indicator of atomic oxygen when combined with 1304 Å. The current status of the 1304 Å problem is discussed in this section.

Details of the 1304 Å triplet configuration are shown in Figure 49. Transition probabilities for the lines are given in Table IV. Both photoelectron excitation and resonant scattering of the solar 1304 Å lines are important for the dayglow, their relative strengths depending upon observation conditions. At night, radiative recombination of O^+ is the primary source.

Beginning with Stewart (1965), more than 15 theoretical and experimental determinations of the electron impact excitation cross section to the ^3S state have been made. As with ^5S, both direct and higher level cascade contributions are important. In contrast to the quintet manifold, the triplet cascade components have been categorized two ways. Those cascades which occur following direct excitation to upper levels in the triplet manifold are referred to as 'thin', since they begin with a single transition from the ground state to the upper state, followed by some probability of eventual branching to the ^3S state. However, when the scattering medium is optically thick, multiple scattering occurs between the ground state and many of the upper levels, thereby enhancing the

probability of cascade. In this case, the cascade is called 'thick' because the effective branching ratio can be much larger than under thin conditions. Julienne and Davis (1976) used the term 'thick' to refer to the limiting case of infinite opacity, in which so many scatterings occur that all atoms eventually relax via cascade transitions, yielding effective branching ratios of unity.

Theoretical calculations of direct and cascade contributions to the population of $O(^3S)$ were given by Julienne and Davis (1976); values for their cross sections at 20 eV are reproduced (from their Tables 1 and 2) in Table XI as the first two rows under the 1304 Å entry. The total excitation cross section is the sum of the direct and cascade components. The latter are obtained by summing the product of the cross sections for direct excitation to the cascade states times their respective branching ratios to ^3S (or to the intermediate states which lead to ^3S). This accounting is identified in the table as the 'thin' cross section. The 'thick' cross sections are obtained by the same method, except that unity branching ratios are used assuming the limiting case of an infinitely thick atmosphere. Listed are the main cross sections for transitions populating ^3S for use in comparing more recent observations and theory.

Perhaps the most important modification to the Julienne and Davis cascade accounting comes as a result of more recent information about the $3s'$ transition. They used a branching ratio of 0.11 for $3s'\ ^3D^0 - 3p\ ^3P$, taken from Wiese *et al.* (1966). Christensen and Cunningham (1978) later measured 4×10^{-4}, but Erdman and Zipf (1983) have since set the upper limit at 2×10^{-5}. In either case, it is clear that cascade to ^3S is much less significant than previously thought (Link *et al.*, 1988a). If the Erdman and Zipf upper limit is taken as the actual branching ratio, it accounts for 12% of the total $3s'$ loss. The remaining 88% loss from $3s'\ ^3D^0$ is another branch via 1172 Å, to the ^1D state (Morrison, 1985; Erdman and Zipf, 1986b). The issues about this transition are discussed in Section 4.1.3.4.

The most recent laboratory measurement of the cross section for direct excitation from ^3P to ^3S (11×10^{-18} cm^2) was made by Gulcicek and Doering (1988) and has been inserted in the third row of Table XI under 1304 Å. At 20 eV, their value is 55% larger than Julienne and Davis (1976).

In addition, Doering and colleagues have measured some of the direct excitation cross sections which contribute to ^3S through cascade. Cross sections for $3s'$, $3p$, $3d$, and $4d$ at 20 eV are listed in the third and fourth rows in Table XI (under 1304) as References 2, 4, 5, 6. The branching ratios used by Julienne and Davis have been applied to the thin cross sections, except for $3s'$ (see above) and $3d$ (see Section 4.1.3.3). As in the Julienne and Davis entries, those labelled 'thick' are the direct cross sections (except for $3s'$) times unity branching probability. Cross sections given parentheses were not measured by the Doering group, so those of Julienne and Davis are used. These two rows are considered 'revisions' (see discussion below) to the Julienne and Davis cross sections.

A new theoretical computation of the direct excitation cross section has been made by Tayal and Henry (1988). Apparently the theory has been much improved; the value at 20 eV is in excellent agreement with Gulcicek and Doering. A strong resonance in the cross section near threshold found in an earlier theoretical calculation by Roundtree

and Henry (1976) is not present in the new results. Tayal and Henry also computed the $3p\ ^3P$ excitation cross section, which was found to be more than a factor of two larger than the laboratory results of Gulcicek *et al.* (1988) for energies greater than 20 eV. The reason for this discrepancy is not known. The Gulcicek *et al.* laboratory measurements were used in the 'revised' entry for the $3s\ ^3P$ state in Table XI.

The cross section leading to *emission* of O I 1304 Å under optically thin laboratory conditions has been measured most recently by Zipf and Erdman (1985). This cross section includes direct excitation plus cascade, and is listed in Table XI as a total 'thin' cross section for comparison with the other entries.

Comparison of the last two rows in Table XI with the 'revised' Julienne and Davis tabulation shows good agreement. Of course, Table XI is only meant to be indicative. A more accurate assessment would include integration of excitation cross sections over photoelectron fluxes in actual atmospheres. Furthermore, Table XI is incomplete: while the strongest contributions are listed, additional cascading states measured by the Doering group should be included. Hopefully, a more complete evaluation will be possible in the near future.

The energy dependences of various 1304 Å cross sections are shown in Figure 52. The

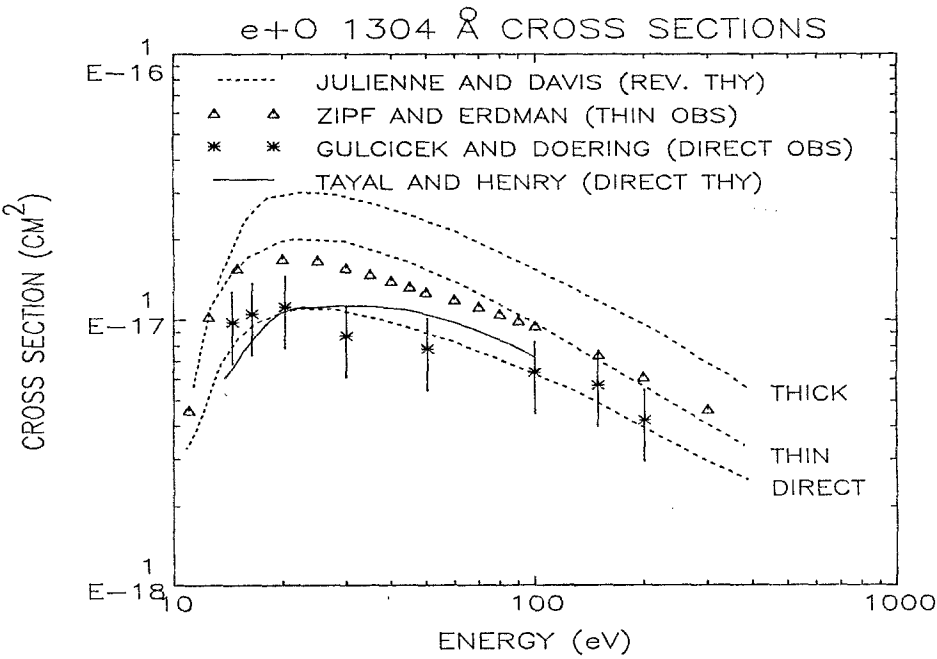

Fig. 52. Excitation cross sections for electron impact on atomic oxygen. 'Direct' is for excitation from the ground state to the ^3S state, 'thin' is direct excitation plus cascade, and 'thick' includes enhanced cascade due to multiple scattering in an optically thick atmosphere. The dashed curves are the cross sections of Julienne and Davis (1976), revised as discussed in the text and in Table XI. The solid line is the recent direct excitation theory of Tayal and Henry (1988), the asterisks are the direct excitation observations of Gulcicek and Doering (1988), and the triangles are the emission cross-section measurements of Zipf and Erdman (1985), which include direct and 'thin' cascade.

dashed lines use those given by Julienne and Davis (1976), but normalized at 20 eV, according to Table XI ('revised'). Their direct cross section agrees with the latest theory of Tayal and Henry (1988) to within 15%, and to within experimental error of the measurement of Gulcicek and Doering (1988). The 'revised' thin cross section agrees with Zipf and Erdman (1985), probably to within experimental error. The thick cross section is discussed next. Thus over a range of energies, the various determinations of ^3S cross sections are in good agreement.

Additional information on cross sections can be obtained from analyses of dayglow observations. Morrison and Meier (1988), using the energy function of Zipf and Erdman (1985) in a re-analysis of the 1978 and 1980 rocket (see Table I) data, argue that the 1304 Å airglow can be reproduced with a 'thick' cross section of 2.4×10^{-17} cm^2. This 42% increase over the Zipf and Erdman thin cross section is probably reasonable based on enhanced cascade due to multiple scattering in the optically thick atomic oxygen atmosphere. This conclusion agrees with Figure 52, as well as with unpublished laboratory data which show enhancements in both 1304 and 8446 Å emission cross sections as optically thick conditions are approached (E. Zipf, private communication, 1987). On the other hand, Link *et al.* (1988a) in analyses of STP 78-1 satellite data and the same 1978 and 1980 rocket data (Link *et al.*, 1988b) reached a different conclusion: that the dayglow can be matched using the Zipf and Erdman cross section without enhanced cascade. This dichotomy is probably rooted in modelling assumptions and is discussed later in this section. Excitation rates in this paper (Figure 33) were computed using the Zipf and Erdman energy function, adjusted to a peak value of 2.4×10^{-17} cm^2 (Figure 28).

The second source of excitation of O(^3S) is resonant scattering of the solar triplet. The solar irradiance is distributed approximately equally in the three lines. Earlier rocket measurements of the total triplet irradiance ranged from 6 to 14×10^9 ph cm^{-2} s^{-1} (Mount and Rottman, 1985). However, the Solar Mesospheric Explorer measurements showed a smaller solar cycle change from 8.6 to 6.6×10^9 from 1981 through 1986, with a weaker rotation modulation superimposed (G. Rottman, private communciation, 1988). The discrepancy with earlier rocket data at solar maximum may be due to calibration problems, although strong rotation modulation during that part of the solar cycle can lead to incorrect estimates of the average value if continual measurements are not available to provide perspective. As discussed earlier, the solar line profile used in the calculations of the airglow is that in Figure 34.

A second solar component to the O(^3S) population rate comes from the accidental resonance between the singlet transition of the $2p^4\ ^3P \rightarrow 3d\ ^3D^0$ multiplet and the solar Lβ line at 1025.76 Å (Meier *et al.*, 1987; see Section 4.1.3.3). The branching ratio from the $^3D^0$ state through channels which lead to ^3S is 29%. Since thermospheric oxygen is optically thick to the 1026 Å multiplet, the branching probability is enhanced significantly. Calculations using the model of Meier *et al.* (1987) show that the branching contribution is roughly 10% of the direct excitation by the solar 1304 Å triplet. This source is not included in the illustrations which follow.

Column emission rates or radiances for O I 1304 Å cannot be calculated directly from

excitation rates in Figures 33 and 35. The frequency profile of the emission rate must be known for the observation direction if the correct form of the radiance is to be used (Equation (16)). Because of the very large atmospheric optical depth at line center for the 1304 Å triplet, transport of radiation in the wings must be correctly modelled using the angle-dependent frequency redistribution function (Equation (16)). Atmospheric temperature gradients affect the cross section at line center, the line width, and the Boltzmann population of the ground state angular momentum levels. Figures 53 and 54 illustrate the former two effects. Figure 53 shows the resonant scattering cross section

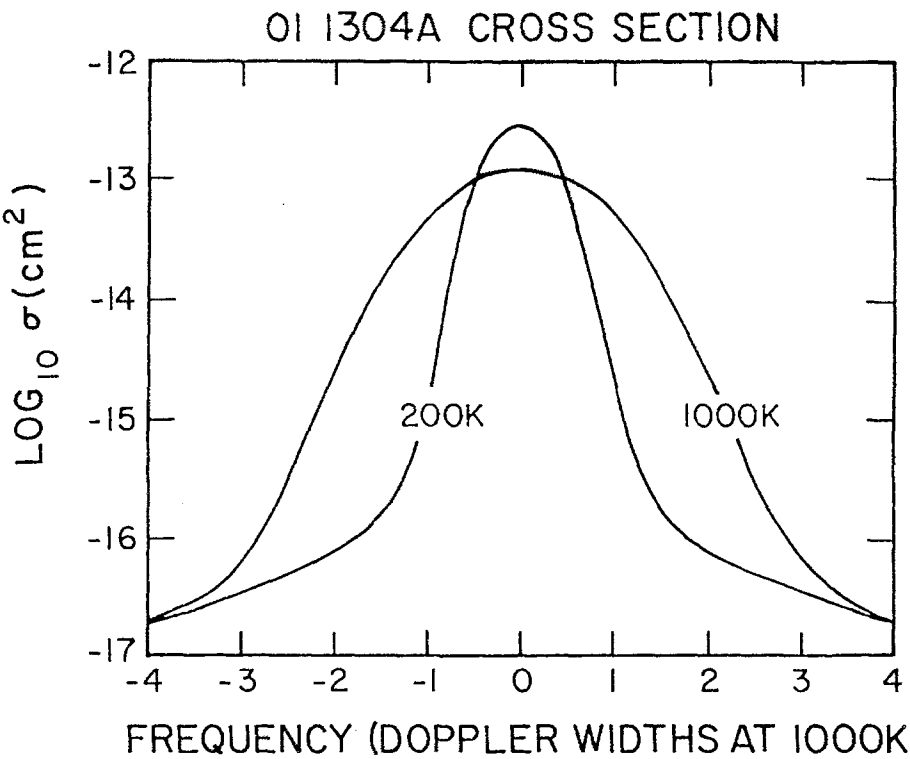

Fig. 53. Resonant scattering cross section for O I 1304 Å as a function of frequency, measured in Doppler widths at 1000 K (4.42 mÅ). See Equation (18) and Table IV.

(Equation (18)) for temperatures typical of the upper and lower thermosphere. To obtain the frequency profile of the optical depth, it is necessary to integrate along the line of sight, the product of the cross section at each frequency and the concentration of O atoms in the given level of the ground state (bottom of Figure 49), allowing for the atmospheric temperature gradient. The frequency profile of the vertical optical depth for the 1302.17 Å line at several altitudes is shown in Figure 54. Photons created at 100 km will not see unity optical depth, unless their frequency is larger than about 12 (exospheric temperature) Doppler widths. In going from 112 to 100 km, the atmosphere cools considerably and the optical depth between 1 and 2 Doppler widths from line center does not increase much.

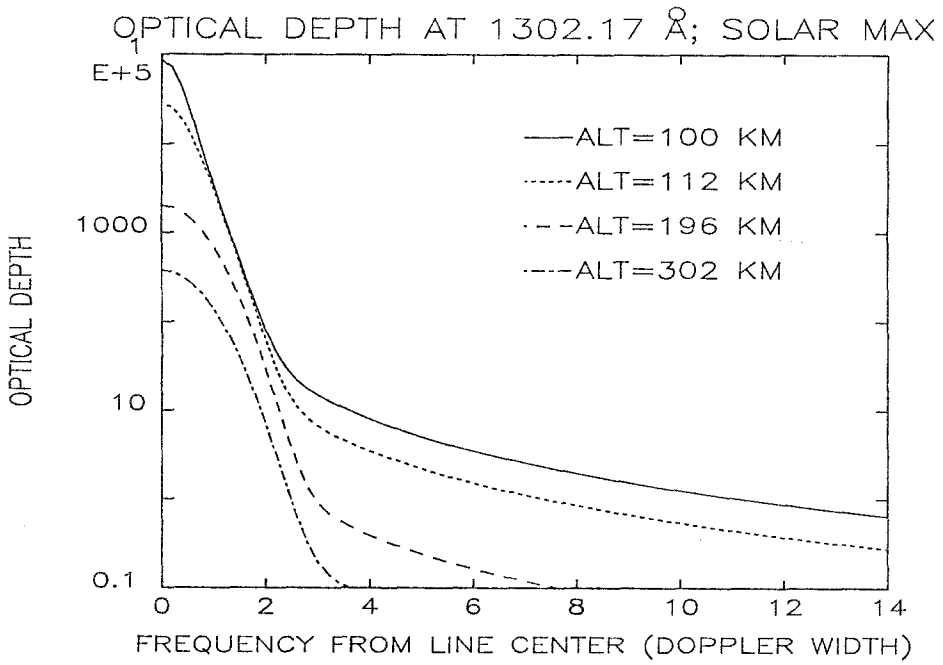

Fig. 54. Optical depth for the O I $^3P_2 \rightarrow {}^3S$ 1302.17 Å transition as a function of frequency in units of Doppler widths at 1191 K exospheric temperature (4.81 mÅ).

In addition to the vagaries of the optical depth variations, coupling among the fine structure levels and an accurate description of changes in frequency following photon scattering must be included in the radiative transport model to properly characterize the frequency distribution of the radiation field. Strickland and Donahue (1970) and Strickland and Rees (1974) describe the incorporation of fine structure, assuming CFR. The angle-dependent form of the redistribution function (Equation (16)) must be used for the scattering process. The Monte-Carlo model of Meier and Lee (1982) includes all of these effects (as well as pure absorption by O_2) and is used for the examples presented in this review.

Line profiles from calculations of the column emission rate are shown in Figures 55 (solar max) and 56 (solar min). The upper and lower panels are for photoelectron and solar excitation, respectively, and the right panels are for viewing upward vertically and the left for downward viewing at the indicated altitudes. Strong reversal is seen from the photoelectron source in the upper left panel as a consequence of entrapment of photons initially created near line center; photons escaping from the atmosphere do so in the optically thinner line wings. The thicker the line, the greater the displacement of the peaks from line center, as expected. Within the medium, however, the line profiles are flat-topped, again with the thicker lines being slightly broader. The solar-excited lines display a much different behavior. There is little or no reversal when viewing downward from 700 km, since the Doppler core of the line is filled in by photons backscattered from high altitudes. Notice how much broader the lines from the solar source are than

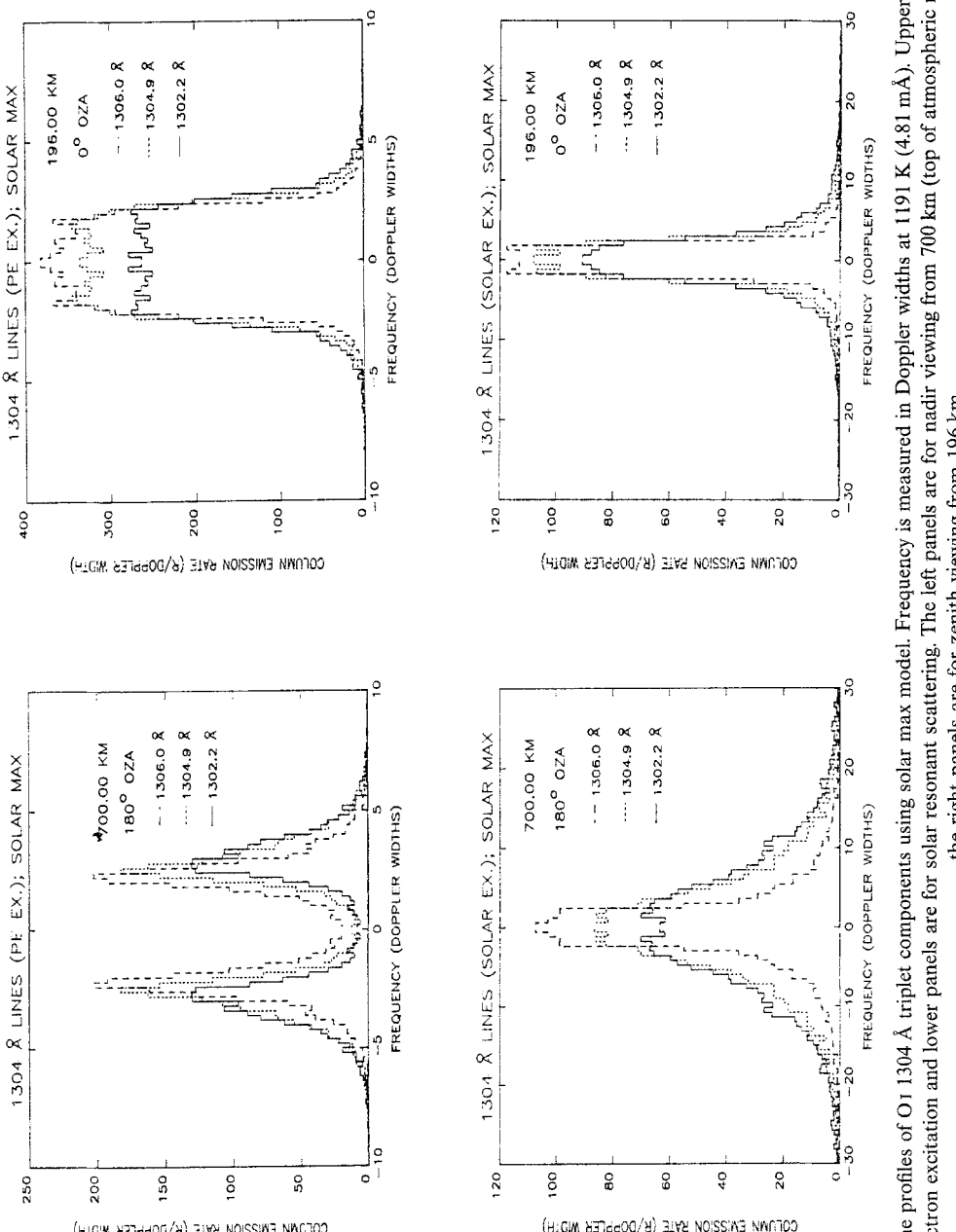

Fig. 55. Line profiles of O I 1304 Å triplet components using solar max model. Frequency is measured in Doppler widths at 1191 K (4.81 mÅ). Upper panels are for photoelectron excitation and lower panels are for solar resonant scattering. The left panels are for nadir viewing from 700 km (top of atmospheric model) and the right panels are for zenith viewing from 196 km.

those from photoelectrons. Backscattering of the wings of the solar lines from oxygen deep in the thermosphere contributes to the broad profiles. The thinner components of the triplet are significantly more narrow in the wings. The wings are broader at solar max due to the increased amount of scattering in the more dense oxygen atmosphere. Since the Doppler width is calculated using the exospheric temperature, the increase in line width is actually greater than appears from comparing Figures 55 and 56 by an additional factor of $\sqrt{1191\ \mathrm{K}/816\ \mathrm{K}} = 1.20$. Additional discussion of 1304 Å line profiles is given by Meier and Lee (1982) and Gladstone (1988).

Altitude profiles of the individual components of the 1304 Å triplet were observed with a high-resolution instrument during the 1980 rocket campaign (Christensen *et al.*, 1982; see Table I). While the resolution was insufficient to resolve the line shapes, radiances from each of the lines were resolved and were found to be about the same magnitude. This is the result of the large degree of multiple scattering and was predicted by Meier and Lee (1982).

Frequency-integrated column emission rates from photoelectron excitation are shown in the left panel of Figure 57 as functions of observing altitude for up and down viewing conditions. The upper left panel shows rates for the solar max model, and lower left, solar min. For nadir viewing, the emission rate increases with decreasing altitude as the observer approaches the region of maximum entrapment, and then decreases at lower altitudes. The zenith emission rate peaks at low altitude, and decreases with increasing altitude, eventually approaching the O scale height. The differences in scale heights and magnitudes between solar max and min are obvious.

As discussed above, because of the enormous opacity, it is not straightforward to relate the contribution of the column emission rate to the volume emission rate. One way to obtain some insight is to examine the 'contribution function'. Formally, the contribution function is obtained by computing the frequency-dependent vertical radiance due to emissions which occur in the altitude increment between an altitude grid level and the one just below (or above, in the case of upward viewing). Integrating over frequency the product of the radiance from that altitude interval and the frequency-dependent probability of reaching the observer (either at the top or bottom boundaries) yields the contribution function from that interval. Thus if the observer is located at the top or the bottom of the atmosphere, the contribution function describes the incremental contribution to the radiance leaving the top (or the bottom) of the atmosphere from each altitude interval. Contribution functions are plotted as functions of the altitude of the emitting interval in the right two panels of Figure 57, for viewing in the nadir from the 'top' of the atmosphere at 700 km, and for viewing in the zenith from the 'bottom' at 100 km. When viewing upward from 100 km, most of the contribution to the column emission rate comes from altitudes close to the 100 km level. In contrast, for nadir viewing from 700 km, the peak in the contribution function is at lower altitudes, but the function is broad, indicating sensitivity to a wide altitude span. This is especially true for the solar max situation. Simple summing of the individual points gives the total radiance leaving the atmosphere. Additional discussion of contribution functions is given by Meier (1987).

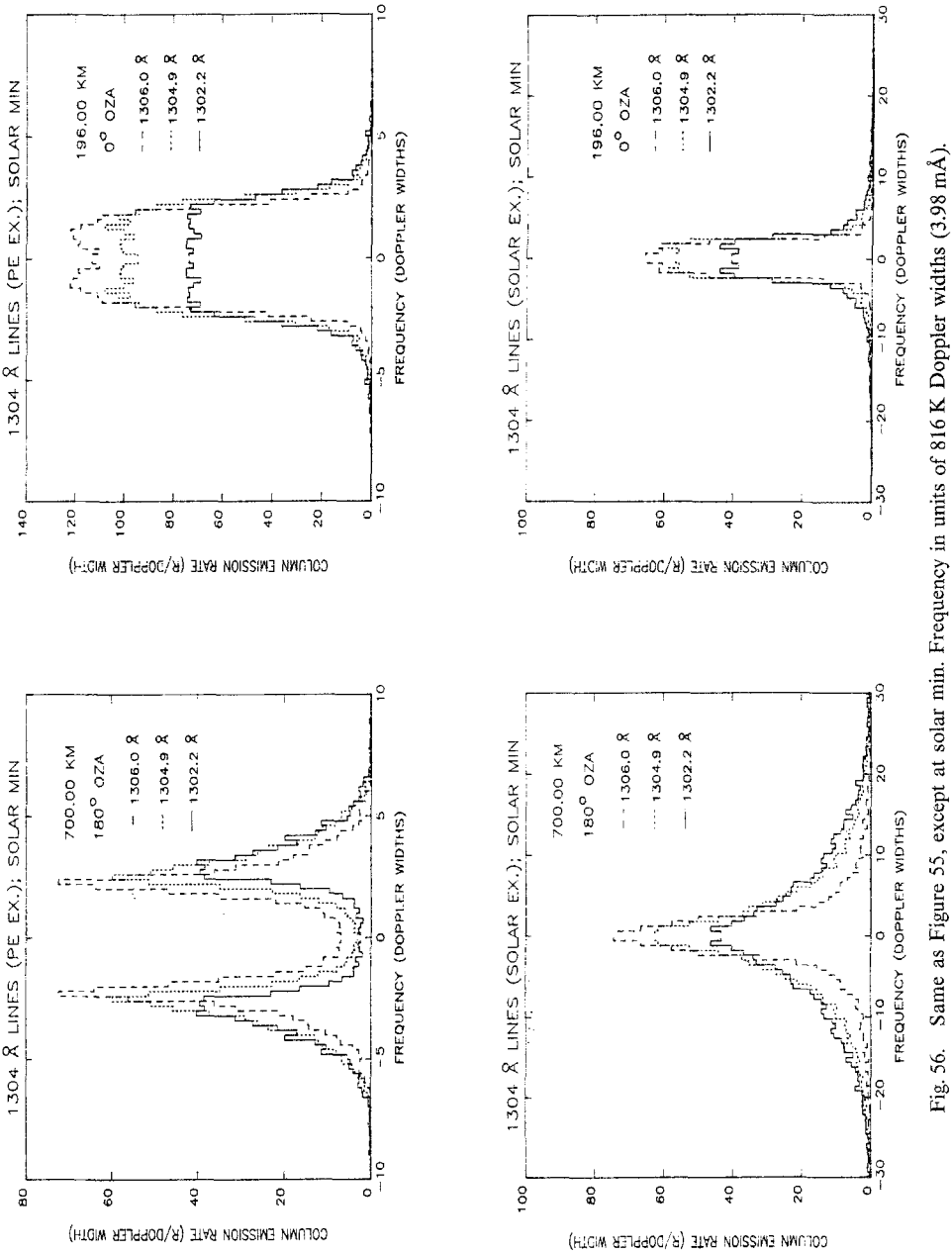

Fig. 56. Same as Figure 55, except at solar min. Frequency in units of 816 K Doppler widths (3.98 mÅ).

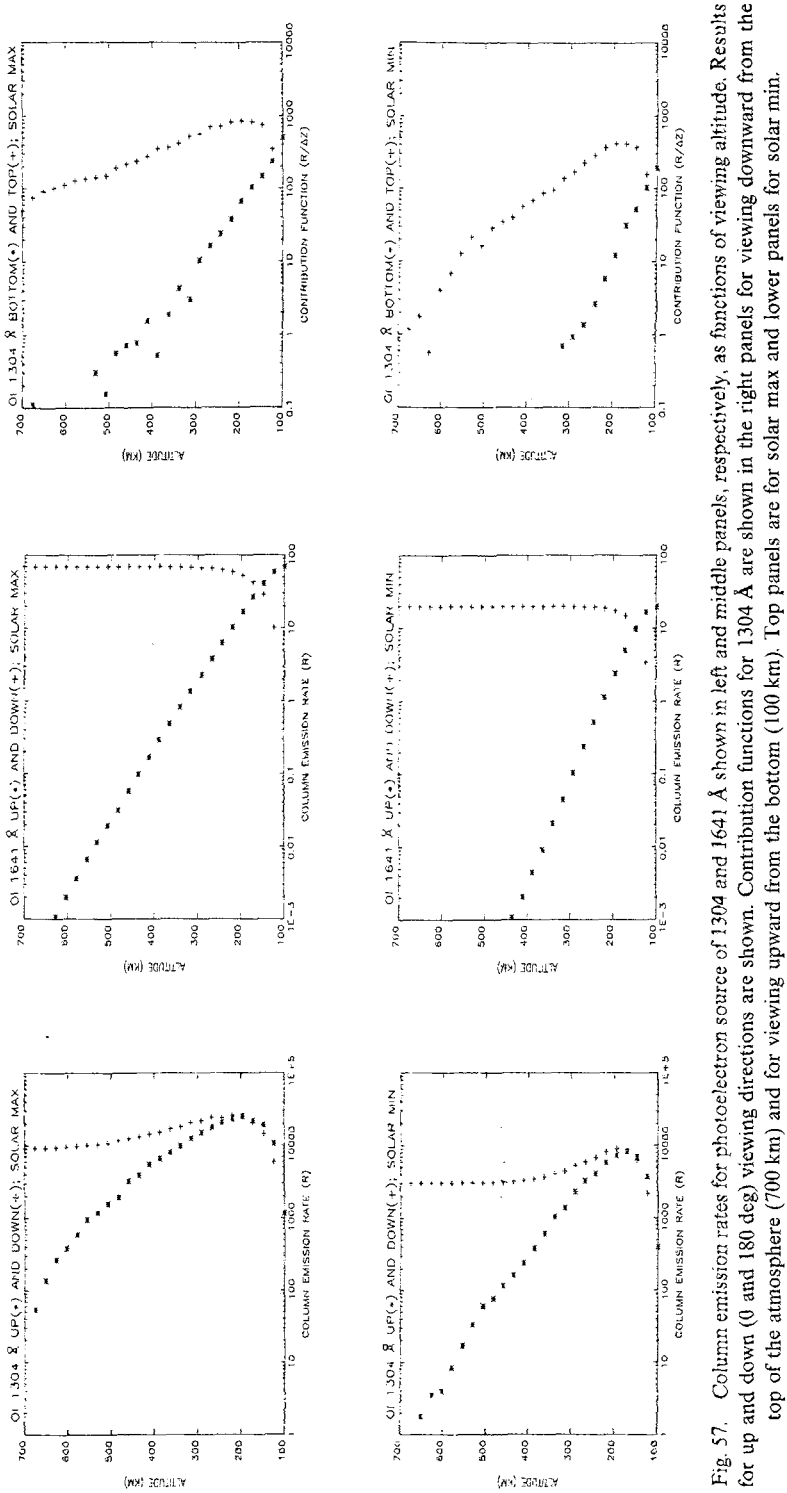

Fig. 57. Column emission rates for photoelectron source of 1304 and 1641 Å shown in left and middle panels, respectively, as functions of viewing altitude. Results for up and down (0 and 180 deg) viewing directions are shown. Contribution functions for 1304 Å are shown in the right panels for viewing downward from the top of the atmosphere (700 km) and for viewing upward from the bottom (100 km). Top panels are for solar max and lower panels for solar min.

Column emission rates and contribution functions for the solar source are shown in Figure 58, in the right and left panels, respectively. The degree of imprisonment is less than in the photoelectron case because of important contributions from scattering in the optically thin wings of the line. The contribution function is especially interesting, showing the important component of the nadir radiance at the top of the atmosphere from solar photons scattered near 100 km, and from the secondary peak at high altitudes, seen in the initial excitation rate (Figure 35).

The radiance due to the weak branch ($^3S \rightarrow {}^1D$) at 1641 Å is given by

$$I = \int \frac{B}{4\pi} j(z)\, \mathrm{d}s\,, \tag{49}$$

where the best estimate of the branching ratio, B, is 2.4×10^{-6} (see discussion and references of Conway *et al.*, 1988) and j is the volume excitation rate of $O(^3S)$, given in Figures 33 and 35. The column emission rate at 1641 Å is given in the central panels of Figures 57 and 58, after converting I to Rayleighs. Conway *et al.* (1988) and Meier and Conway (1985) showed that the ratio of 1641 to 1304 Å radiances depends on the O concentration, the proportionality being near-linear, depending on viewing conditions. This is a result of the relationship between the branching rate and the mean number of scatterings of photons before escaping, which in turn depends on the opacity of the medium. The utility of this ratio as a remote sensing observable is discussed in Section 5.

The 1304 Å dayglow observations reviewed in Section 2 have been analyzed by various authors. As noted in the discussion of the O I 1356 Å dayglow, recent work has been published by Meier *et al.* (1985), Link *et al.* (1988a, b), Conway *et al.* (1988), Morrison and Meier (1988), Morrison *et al.* (1991). With a few exceptions, the conclusions by those authors are in reasonable agreement. One exception pointed out earlier is the issue raised by Link *et al.* (1988a, b), who concluded that the electron impact excitation cross section of Zipf and Erdman (1985) can explain the dayglow without an enhancement in the contribution from multiple scattering within high lying cascade levels. Link *et al.* pointed out the disagreement with the work of Meier *et al.* (1985), who found that the upper limit of Julienne and Davis (1976) of a factor of two enhancement agreed with the 1978 and 1980 (reference Table I) rocket observations. With the revisions in the cross section for O by Zipf and Erdman (1985), and for N_2 by Ajello and Shemansky (1985), modification of the conclusions of Meier *et al.* (1985) became necessary. Morrison and Meier (1988) reported some of the revised conclusions. Among them was that agreement with the 1304 Å dayglow could be achieved if the electron impact excitation cross section in the optically thick atmosphere were 2.5×10^{-17} cm^2, some 31% lower that suggested earlier by Meier *et al.* (1985), but still larger that the optically thin Zipf and Erdman (1985) value advocated by Link *et al.* (1988b) in analyzing the same rocket data. However, for the sake of argument, if Link *et al.* were to use the correction factors for the photoelectron flux and the O concentration given in Table II of Morrison and Meier, the electron impact excitation cross section needed

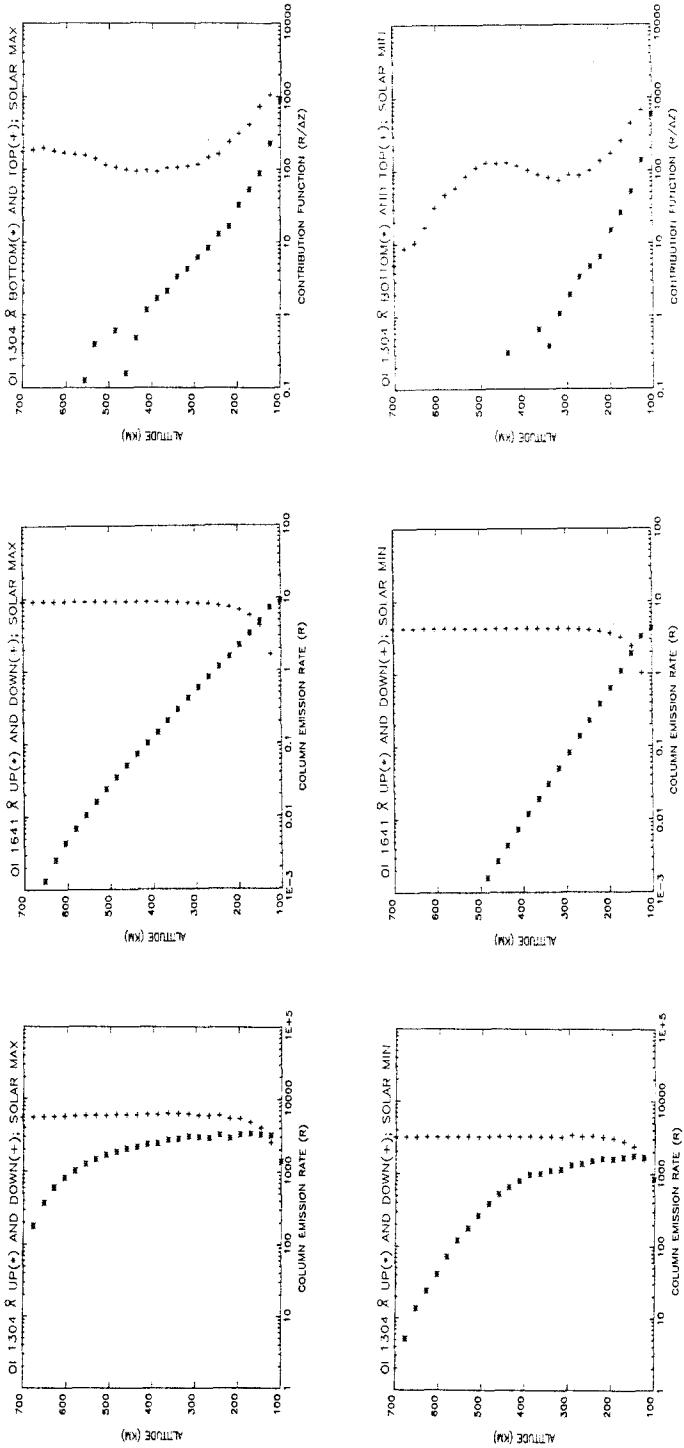

Fig. 58. Same as Figure 57, except for the solar resonant scattering source.

to fit the observations could be increased by as much as 35% from the Zipf and Erdman optically thin value. Furthermore, the discrepancy they found between the 1356 Å data in the 1980 rocket case and their airglow model (seen in their Figure 6) would be removed. Thus the absolute values and ratio of 1304 to 1356 Å in the airglow models of both Link *et al.* (1988b) and Morrison and Meier (1988) agree with the rocket data if both groups were to make similar adjustments to the model atmosphere and photoelectron flux. The enhanced 1304 Å cross section also agrees with S3-4 satellite data reported by Conway *et al.* (1988). It would appear that the 1304 Å cross-section picture displayed in Figure 52 is valid. The value of 2.5×10^{-17} cm^2 at 20 eV is between the thin and (infinitely) thick cases and is plausible for the Earth's thermosphere. Again, Link *et al.* (1988a, b) do not agree with these conclusions.

Unfortunately, the radiative transport modelling effort required to calculate radiances is quite substantial. Using a VAX 11/750 computer, the Monte-Carlo model of Meier and Lee (1982) takes many hours of CPU time in order to obtain a single altitude profile. Unless a synthesis of a large number of model results can be developed, rapid remote sensing analysis using this approach may not be feasible. But the 1641 to 1304 Å ratio shows promise as an algorithmic variable for deduction of O concentrations. The Feautrier technique of Gladstone (1988) is computationally much faster than Monte Carlo, but it requires angle averaging of the redistribution function which leads to some minor differences with the angle-dependent results. A new approach using doubling techniques also shows promise (Yelle and Wallace, 1987), but it, too uses angle-averaged redistribution functions.

At night, O I 1304 Å radiation is produced in the ionosphere by radiative recombination. The initial excitation rate is given by Equation (41) using a recombination coefficient of 2.8×10^{-13} cm^3 s^{-1} in an optically thick atmosphere at 1160 K (Julienne *et al.*, 1974). Little modelling of the 1304 Å nightglow has been reported. Anderson *et al.* (1976) performed some sample calculations for comparison with STP 72-1 satellite data using a CFR model. Other unpublished modelling by those authors has shown that if the ionosphere is at high altitude (where there is much less multiple scattering than during the day), and if the nightglow is also observed from a high altitude location, transport in the wings of the line (which are thick at low altitudes) is greatly reduced and the computationally fast CFR model can be used. It is important for remote sensing purposes to observe simultaneously both 1304 Å and another optically thinner feature such as 1356 Å, since the ratio is proportional to the height of the ionosphere: the higher the *F* region, the lower the amount of multiple scattering (Gerard *et al.*, 1977; Strickland and Anderson, 1977). Alternatively, if the height and strength of the radiative recombination source are known, say from a limb scan, the 1304 Å provides information about the O concentration at night.

4.1.3.3. *1026 Å* ($2p^4\,{}^3P - 3d\,{}^3D^0$). An emission feature at 1026 Å observed in the dayglow has been identified as the atomic oxygen multiplet and/or the atomic hydrogen Lβ line (Anderson *et al.*, 1980; Chakrabarti *et al.*, 1983). More recent work by Meier *et al.* (1987) has shown that the bulk of the emission at that wavelength seen from the

STP 78-1 satellite at 600 km is due to the oxygen lines, which are pumped by an accidental resonance with the solar Lβ line (Bowen fluorescence).

The 1026 Å transition is a six-line multiplet, consisting of a singlet, doublet and triplet. Details of the transition are given in Figure 59 and Table IV. The theoretical branching

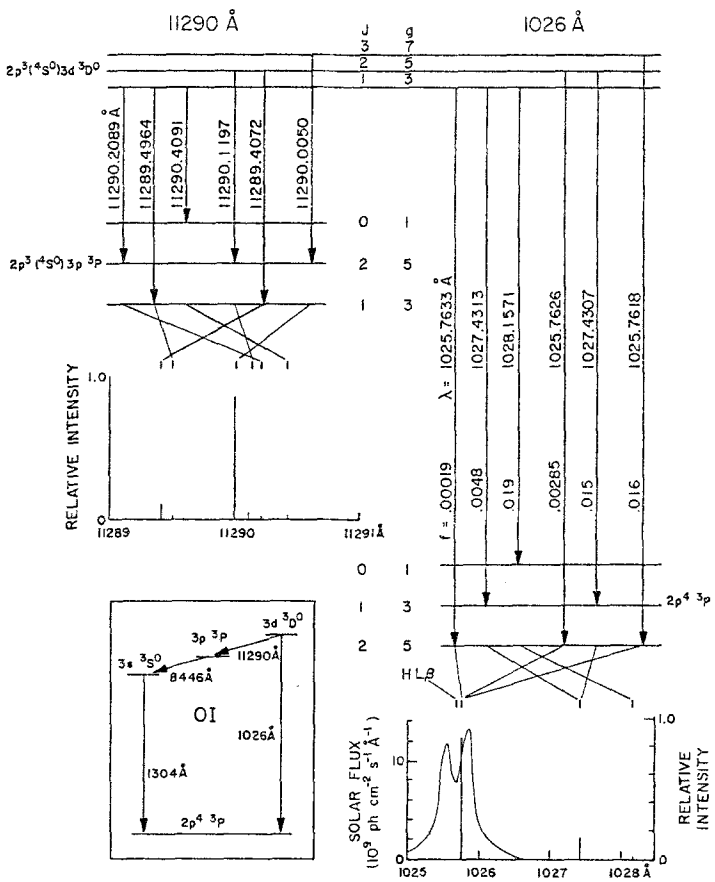

Fig. 59. Detailed energy level diagram for the 1026 and 11290 Å multiplets, showing the relative line strengths (below) for optically thin conditions. The accidental resonance with the solar Lβ line is shown in the lower right panel. The lower left panel shows the relationship of the multiplets to 1304 Å. Taken from Meier *et al.* (1987).

ratio for $3d\ ^3D^0$ atoms relaxing to the ground state is 0.72 (Pradhan and Saraph, 1977). Zipf *et al.* (1979) observed 0.74 from a lab experiment, in good agreement with theory. (Christensen and Cunningham (1978) measured a ratio of 0.9, also in the laboratory, but difficult corrections for multiple scattering were necessary and imply some uncertainty in this value; see below.) Since the optical depths above 100 km for the 1026 Å lines can surpass 10^4, multiple scattering enhances the loss of 1026 Å radiation via the 11 290 Å transition. The 1026 Å radiative transport problem is difficult to handle theoretically because of the near degeneracy among various lines of the multiplet; two

groups of lines are less than a Doppler width apart in wavelength, permitting mixing of photons among multiplet components. The accidental resonance between the solar Lβ line and three transitions of the multiplet originating from the $J = 2$ level of the ground state can be seen in the lower right panel of Figure 59. The oscillator strength and transition probability are much larger for the singlet transition, so most of the initial excitation radiation resides in that component. Furthermore, because of the large loss rate via branching, the mean number of scatterings is less than 4, and little mixing among levels is expected from the solar source. Some 85% of the radiation is expected to be in the singlet line (Meier *et al.*, 1987). Thus the model of Meier and Lee (1982) can be used to calculate the singlet line emission at 1025.7616 Å, without the substantial modification required for the theory to account for the various degeneracies.

Figure 60 shows zenith and nadir column emission rates for the singlet component

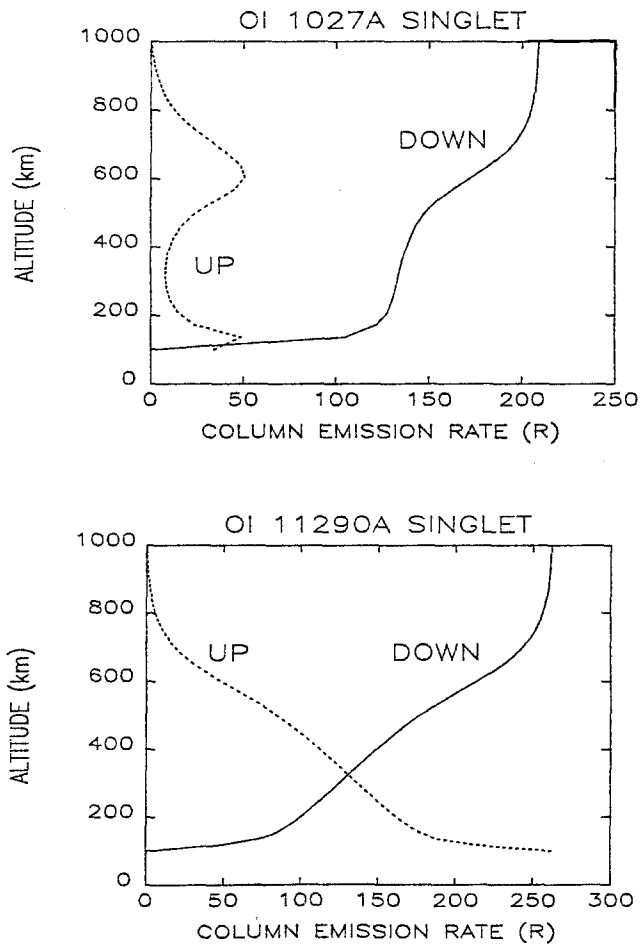

Fig. 60. Zenith and nadir column rates for 1026 and 11290 Å singlet transitions resulting from the accidental resonance with solar Lβ. The atmospheric model is that corresponding to STP 78-1 satellite observations in March 1979 (1300 K exospheric temperature). Taken from Meier *et al.* (1987).

of the multiplet computed by Meier *et al.* (1987). The model atmosphere used by them is appropriate for solar maximum. The solar flux used for the wavelength of the oxygen line was 9.6×10^9 ph cm^{-2} s^{-1} Å^{-1}. The solar zenith angle is 0 deg, and up and down viewing correspond to OZA's of 30 and 150 deg, respectively. The peculiar behaviour of the altitude profile of the 1026 Å emission is due to the shape of the volume excitation rate (similar to ^3S in Figure 35; see Meier *et al.*, 1987), and the effects of self-absorption. O I 11 290 Å does not have opacity effects, so it can be computed from Equation (49), with $B = 0.28$ and j given by the $3d\,^3D_3^0$ excitation rate.

Photoelectron excitation of O I 1026 Å takes place at a moderate rate; the peak cross section is given in Table V. In contrast to the solar source, all levels of the $^3D^0$ state are populated. Since the emission rate following the initial excitation is within the Doppler core of the line, nearly all of the radiation from the photoelectron source is strongly imprisoned and complete branching loss to the 11 290 Å line takes place after only a few scatterings. Thus, while self-absorption remains large, amplification of the 1026 volume emission rate is orders of magnitude less than for 1304, and the net 1026 Å radiance from this internal source is negligible. The 11 290 Å radiance is enhanced significantly. Because of the degeneracies, the correct coupling among the lines has not been included in the radiation transport description. Making the plausible assumption that the $3d\,^3D^0$ levels are completely degenerate for the photoelectron source, the model can treat the transitions in groups. Meier *et al.* found that the resulting 11 290 Å column emission rate was 450 *R* for the entire multiplet, some 70% larger than the solar excitation of the singlet shown in Figure 60. (As noted in the previous section, the photoelectron source is included in the accounting of the ^3S cascade population (Table XI), but the solar source is not.)

Several limb scans of the 1026 Å airglow measured from STP 78-1 were modelled by Meier *et al.* (1987). The atomic hydrogen Lβ emission amounted to only 20% of the O I 1026 Å radiance viewing in the nadir from 600 km, but the two emissions are comparable for observations upward. It would be useful to conduct additional studies with better signal-to-noise than STP 78-1 to further validate the model and to determine the sensitivity of the 1026 Å emission rate to the oxygen concentration.

A weak feature at 1026 Å was noted in he tropical nightglow by Chakrabarti (1984) (see Figure 12). The radiative recombination coefficient for the production of O I 1026 Å is about one-fourth that of 911 Å (Julienne *et al.*, 1974). However, because of the large branching losses, the 1026 Å radiance is expected to be very weak. Detailed calculations are required to determine whether the feature observed by Chakrabarti is O I or H I 1026 Å.

4.1.3.4. *989 ($2p^4\,^3P - 3s'\,^3D^0$), 1173 and 7990 Å.* The 989 Å feature is prominent in the EUV dayglow and auroral spectrum. Like 1026 Å, it consists of singlet, doublet, and triplet lines forming a sextuplet. Unlike 1026 Å, there is no mixing among lines because they are well separated; so each of the three multiplets can be treated independently. The term 989 Å refers to the full multiplet. Details of the transition are shown in Figure 61, taken from Morrison and Meier (1988). Atomic constants are given in

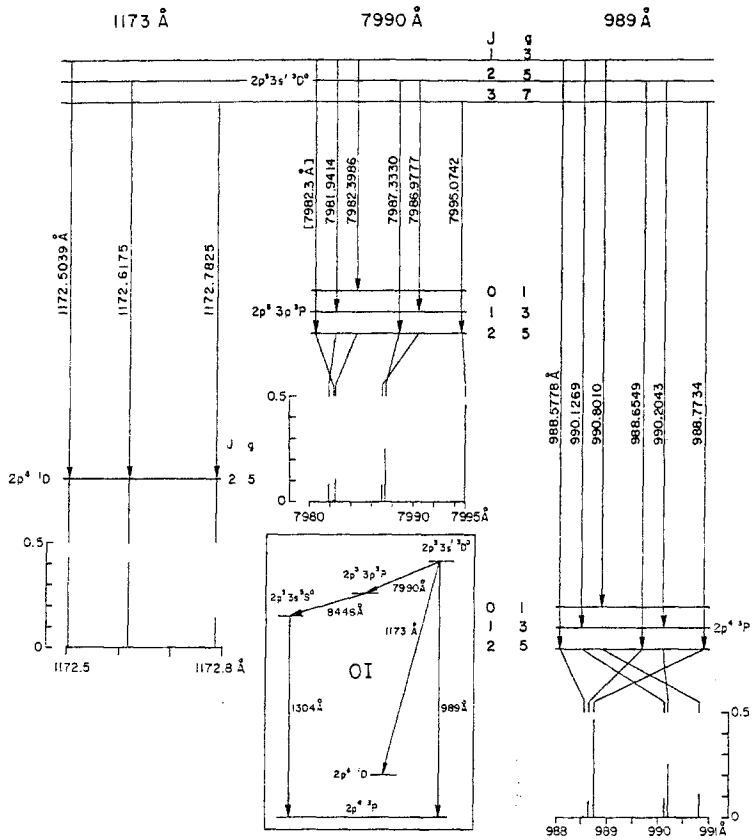

Fig. 61. Detailed energy level diagram for the 989, 7990, and 1173 Å multiplets. Relative line strengths for optically thin conditions are shown below each transition. The insert panel shows the relationship of the multiplet to O I 1304 Å. Taken from Morrison and Meier (1988).

Tables IV and XII, along with relative line strengths for optically thin conditions. Details of branch transitions at 1173 and 7990 Å are shown in Figure 61. Another intercombination branch to ^1S occurs at 1484 Å, but apparently is too weak to be observed.

The solar irradiance is small at 989 Å, so the excitation source in the dayglow is photoelectron impact. The cross section has undergone significant revision since the early estimate by Espy *et al.* (1979) of 8.4×10^{-18} cm^2. The emission cross section and energy function was measured by Zipf and Erdman (1985); their maximum value was 1.45×10^{-17} cm^2 at 50 eV. Vaughan and Doering (1987) measured a peak value for the direct excitation cross section of 5.87×10^{-17} cm^2, which was later confirmed by Gulcicek and Doering (1988) (but the latter authors revised upward the cross section at lower energies). The discrepancy between the direct and emission cross sections is too large to be explained by cascade, which was estimated at 25% (by Zipf and Erdman, 1985; for $e + O_2 \rightarrow O(^3D^0)$). Recent analyses by Gladstone *et al.* (1987),

TABLE XII

Atomic constants for 989 Å multiplet

Transition	g_{upper}	g_{lower}	λ_0, Å	Branching ratio	Line strength
Triplet					
$3s'\ ^3D_1^0 \rightarrow 2p^4\ ^3P_2$	3	5	988.5778	0.030	0.006
$3s'\ ^3D_1^0 \rightarrow 2p^4\ ^3P_1$	3	3	990.1269	0.429	0.0858
$3s'\ ^3D_1^0 \rightarrow 2p^4\ ^3P_0$	3	1	990.8010	0.541	0.1082
Doublet					
$3s'\ ^3D_2^0 \rightarrow 2p^4\ ^3P_2$	5	5	988.6549	0.254	0.0847
$3s'\ ^3D_2^0 \rightarrow 2p^4\ ^3P_1$	5	3	900.2043	0.746	0.2487
Singlet					
$3s'\ ^3D_3^0 \rightarrow 2p^4\ ^3P_2$	7	5	988.7734	1.0	0.4666

Morrison and Meier (1988), and Link *et al.* (1988a, b) have demonstrated that the 989 Å dayglow is consistent with the Gulcicek and Doering cross section, with perhaps a slight increase for cascade needed by Morrison and Meier. Smith *et al.* (1971) found no cascade to $O(^3D^0)$, whereas Zipf and Erdman (1985) state that the upper quantum states in the triplet manifold are populated even more efficiently by $e + O$ than $e + O_2$, so there may be a cascade component. This issue is not resolved.

Originally, it was thought that the principal branch loss of $O(^3s'\ ^3D^0)$ was via emission of 7990 Å radiation; the branching ratio calculated from the transition probabilities of Wiese *et al.* (1966) gave 0.11 for the $3s'\ ^3D^0 - 3p\ ^3P$ transition. However, a calculation of the transition probabilities by Pradhan and Saraph (1977) resulted in a branching ratio of 4×10^{-4}, a value which was later verified experimentally by Christensen and Cunningham (1978). This apparent resolution dissoluted when Erdman and Zipf (1983) were unable to observe 7990 Å emission in a laboratory experiment and set the upper limit to the branching ratio at 2.5×10^{-5}. In a further development, Morrison (1985) reported an intercombination transition at 1173 Å which could explain the loss of 989 Å photons; he determined the branching ratio to be 1.5×10^{-4}, a value later verified by Erdman and Zipf (1986b) to within experimental error (1.3×10^{-4}).

Information about branching losses from $O(3s'\ ^3D^0)$ is available from several rocket experiments. Simultaneous observations of the 989 and 1173 Å airglow by Bowers *et al.* (1987) were analyzed by Gladstone *et al.* (1987) and by Morrison and Meier (1988). Gladstone *et al.* assumed that all of the branching losses were due to the 1173 Å transition and concluded that the airglow data are in agreement with the laboratory values. Comparison of theoretical and observed altitude profiles of the two emissions are shown in the upper panel of Figure 62, taken from Gladstone *et al.*

Morrison and Meier took a slightly different approach, used the laboratory measurement of the 1173 Å branching ratio as the minimum possible, and examined the effect of additional branching channels. They found that at rocket altitudes, the 989/1173 intensity ratio is not particularly sensitive to the total (sum of 1173 Å and other channel)

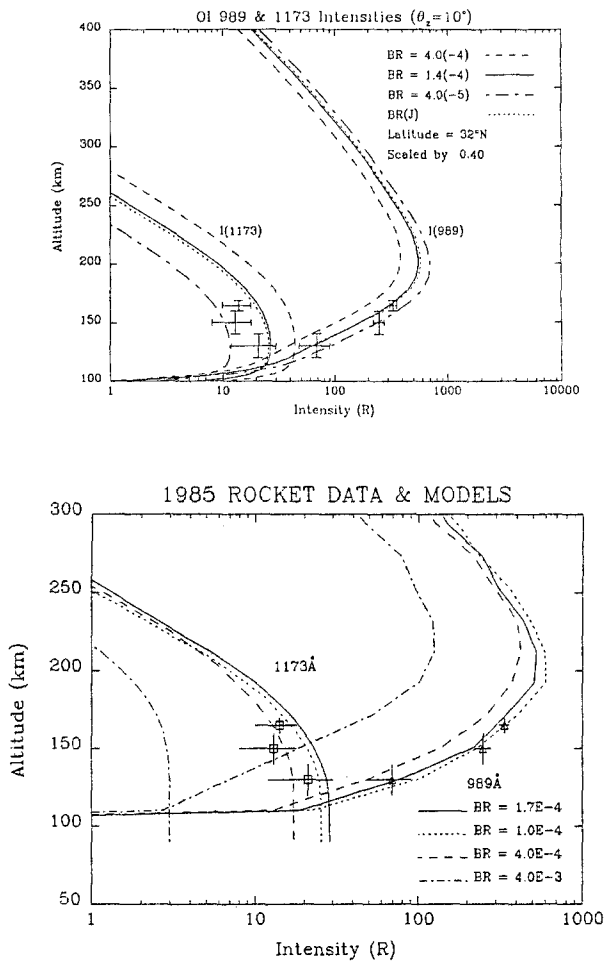

Fig. 62. Altitude profiles of 989 and 1173 Å appropriate to the solar min observations of Bowers *et al.* (1987). The upper panel is taken from Gladstone *et al.* (1987); they assumed that all branching is via 1173 Å and allowed that branching ratio to vary as a parameter of their model. The lower panel is from Morrison and Meier (1988), who assumed that the 1173 Å branching ratio was fixed at the laboratory value of 1.5×10^{-4}, and varied the total (sum of 1173 Å plus any other transitions) branching ratio.

branching ratio, and that the 1985 rocket observations were in agreement with the laboratory values of 1173 Å. The Morrison and Meier theoretical altitude profiles (see lower panel of Figure 62) are slightly different than Gladstone *et al.*, since Morrison and Meier varied the total branching ratio, but fixed the ratio for 1173 Å. In addition, Morrison and Meier analyzed data from the 1978 and 1980 rocket campaigns (see Table I). They concluded that the radiances from all three rocket experiments were consistent with a total branching ratio of $1.5–4 \times 10^{-4}$.

Another constraint on the branching issue is imposed by data obtained with a high-resolution spectrometer flown on the 1980 rocket (Christensen *et al.*, 1982). This instrument partially resolved the 989 Å multiplet components. Theoretically, as the total

branching ratio changes, the degree of multiple scattering in each member of the multiplet changes in different ways, providing a means of determining the branching loss. Figure 63 shows the observed multiplet profile at 1.3 Å resolution, compared with

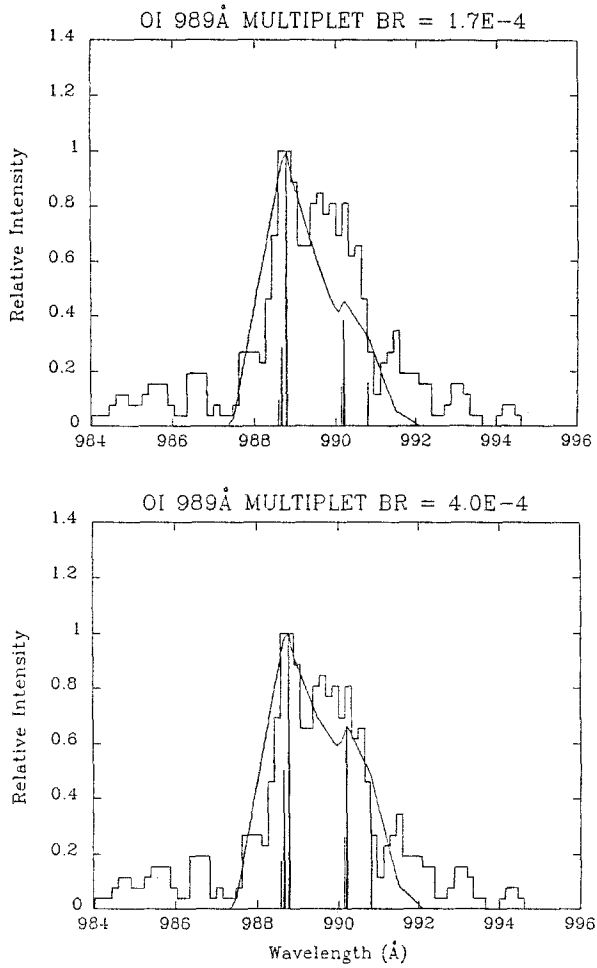

Fig. 63. O I 989 Å multiplet observed at 1.3 Å resolution from the 1980 rocket campaign of Christensen *et al.* (1982). Theoretical calculations of the relative intensities of the individual multiplet components are shown as vertical lines and at 1.3 Å resolution (solid lines). The upper panel assumes a branching ratio which is the sum of the laboratory value for 1173 Å (1.5×10^{-4}) and the upper limit of Erdman and Zipf (1983) for 7990 Å (2.5×10^{-5}). The lower panel uses a branching ratio of 4×10^{-4}, the best fit to the data. Taken from Morrison and Meier (1988).

total branching ratios of 1.7 and 4×10^{-4}, taken from Morrison and Meier (1988). Clearly, the latter value provides better agreement with the data. Fortuitously, the optically thin line strengths (Table XII) also agree with the flight data (see Figure 9 of Christensen *et al.* (1982) or Figure 5(e) of Morrison and Meier (1988)). This is a consequence of the grouping in wavelength of the multiplet components according to

the ground state levels (Figure 61) and the fact that although multiple scattering does redistribute photons within a multiplet, the sums of the line intensities within a wavelength group remain close to the optically thin value (if the branching ratio is 4×10^{-4}; Meier, 1982).

A conclusive way to resolve the 7990 Å branching issues would be to make simultaneous observations of 989, 1173, and 7990 Å in the dayglow or aurora, along with independent measurements of the atomic oxygen concentration. If reliable branching ratios were to be established, the ratios of the emission rates could be used to monitor routinely the atomic oxygen concentration (Meier, 1982; Morrison and Meier, 1988). It was further shown by Meier (1982) that ratios of individual components within the 7990 Å multiplet depend upon the O concentration, so that observations of the singlet-to-doublet or singlet-to-triplet ratio provide a means of ground-based monitoring of atomic oxygen.

A weak 989 Å emission in the tropical nightglow, which tracks 911 and 1356 Å emissions observed simultaneously from STP 78-1, was analyzed by Abreu *et al.* (1984). The emission rate is about an order of magnitude lower than at 911 Å. Because the $3s'\ ^3D^0$ state involves an excited O^+ core configuration, and because such oxygen ions are sparse at night, radiative recombination is an unlikely source of 989 Å radiation. However, dielectronic recombination into states above the ionization limit can occur, which than can radiate to $O(3s'\ ^3D^0)$ at 8229 or 7952 Å. This appears to be a plausible explanation for the 989 Å emission rate, although better determinations of the dielectronic recombination rate are required to account for the brightness quantitatively.

4.2. Minor Species

4.2.1. *Nitric Oxide*

NO γ-bands are produced in the dayglow (Figure 5) from resonance fluorescence of sunlight and in the nightglow (Figure 11) from N + O association, following C to A state cascade. The latter chemiluminescence process also produces the δ-bands. Transitions from D to X states produce the epsilon system which has been seen in the dayglow (Cleary, 1986). The relationships among the various bands can be seen in the partial energy level diagram of NO in Figure 64. Details of the production processes are given in Section 3.2.1.2 as examples of resonance fluorescence and in 3.2.2.2 as examples of chemiluminescence. Volume emission rates for the (0, 0) γ-band are shown in Figure 36 using the NO concentrations at solar max from McCoy (1983b) and the g-factor from Table VII. Volume excitation rates for total NO(C) production from chemiluminescence at solar max are shown in Figure 38.

The γ-band column emission rate from solar resonance fluorescence can be calculated by integrating the volume emission rates for the (0, 0)-band in Figure 36. The result is shown in Figure 65 for viewing vertically above 100 km. Emission rates for other bands may be obtained by scaling with the g-factors given in Table VII. Self-absorption (Cravens, 1977; Cleary, 1986) has not been included. Production of the (0, 0) γ-band from N + O association can be obtained by integrating the C-state production rates in

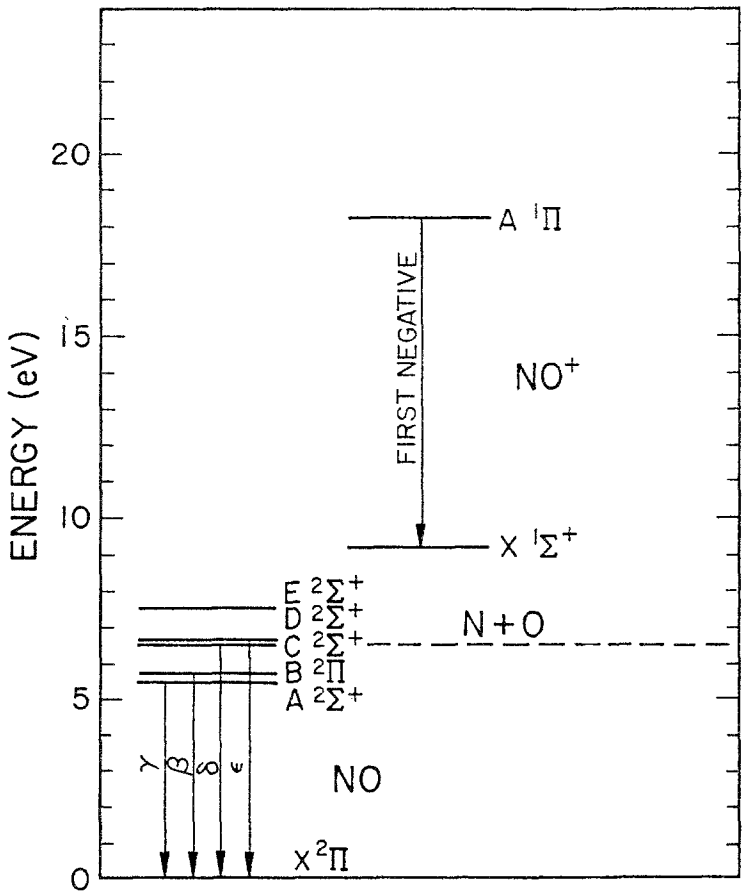

Fig. 64. Partial energy level diagram of NO and NO^+.

Figure 38, multiplying by the $C \rightarrow A$ branching ratio (0.23 from Rusch and Sharp, 1981; McCoy, 1983a, b; Tennyson *et al.*, 1986) and the fraction of A-state excitation resulting in (0, 0)-band emission. The latter values are given in Table XIII for the $v' = 0$ progressions of the δ- and γ-bands (obtained from R. McCoy, private communication, 1989; who used unpublished Franck–Condon factors supplied by D. Albritton; values of similar magnitude are given by Barth, 1966). Only the $v' = 0$ vibrational level of the C state is populated following N + O association. The same is true of the A state following a radiative transition (at 1.22μ) from the C state. The column emission rate of the (0, 0)-band from chemiluminescence is also shown in Figure 65. Clearly fluorescence is the dominant source during the day. Chemiluminescence emission in the other bands of the γ-system can be obtained by scaling with the fractional populations of the other states listed in the lower part of Table XIII. The δ-system can be calculated by using the ratio of the δ- to γ-systems (3.33), and by scaling with the fractional populations in the upper part of Table XIII.

Reported values for the fluorescence efficiency of the δ-bands are at odds. Because

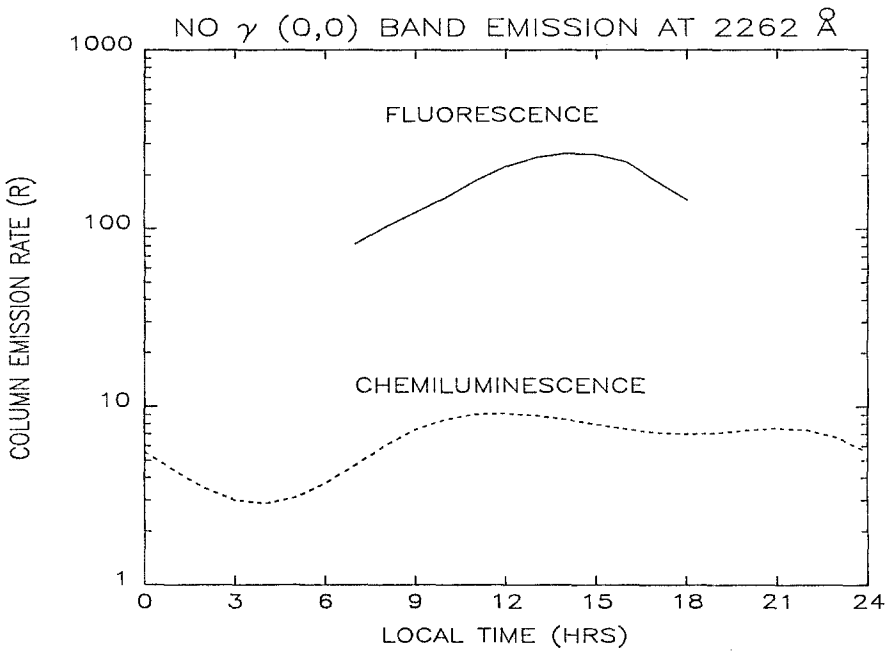

Fig. 65. Dependence of vertical column emission rate above 100 km on local time for the conditions of the rocket flight of McCoy (1983a), which took place on 7 November, 1979 from White Sands Missile Range, NM at 01 : 11 GMT. The solar 10.7 cm flux was 278 on the previous day, the 81-day average was 225, and A_p was 12. The fluorescence component was computed using the NO concentration given in Figure 5 of McCoy (1983b), and the O + N → NO(C) chemiluminescence component used the N and O concentrations from the MSIS 86 model atmosphere.

TABLE XIII

Percentage of total NO γ and δ emission into $v' = 0$ progressions

Band	Wavelength, Å	Emission, %
δ (0, 0)	1909	20.0
(0, 1)	1980	28.9
(0, 2)	2055	23.7
(0, 3)	2134	14.5
(0, 4)	2219	7.5
(0, 5)	2310	3.4
(0, 6)	2406	1.4
(0, 7)	2509	0.6
γ (0, 0)	2262	21.6
(0, 1)	2363	29.9
(0, 2)	2471	23.4
(0, 3)	2587	13.8
(0, 4)	2713	6.8
(0, 5)	2849	2.9
(0, 6)	2997	1.2
(0, 7)	3159	0.4

of the pre-dissociation of the C state, the fraction of excitation of the C state which results in γ-band radiation depends on the spectrum of the radiation source. Cleary (1986) discussed the issues and concluded that in the dayglow fluorescence is much stronger than chemiluminescence for producing the δ-band emission. The epsilon bands are also produced by fluorescence in the dayglow (Cleary, 1986).

Altitude profiles of the various fluorescence-produced dayglow emissions, obtained either from rockets or by limb-scanning satellites, can be inverted to obtain volume emission rates, which in turn can be divided by the g-factor to determine the NO concentration. This has become the standard method for observing NO during the day. McCoy (1983a, b) and Cleary (1986) discussed recent rocket observations employing this technique. NO was observed this way on the Atmospheric Explorer satellites (Cravens *et al.*, 1985; and references). More recently, Barth *et al.* (1988) and Siskind *et al.* (1989a, b) reported Solar Mesospheric Explorer (SME) satellite data.

Often the daytime NO concentrations derived using the fluorescence method peak lower in the atmosphere than predicted by odd nitrogen photochemical models (e.g., McCoy, 1983b). (The fluorescence excitation rates plotted in Figure 36 used McCoy's model results.) Recently, Barth *et al.* (1988) found that the NO concentration at 110 km covaries with solar activity in response to both solar rotation modulation and the 11-year cycle. They interpret this as a consequence of variations in soft solar X-rays which produce low altitude photoelectrons. These photoelectrons increase the production of odd N which reacts with O_2 to produce NO. An increase in the soft X-ray flux used in photochemical models could also move the peak in theoretical NO to lower altitudes, improving the agreement with the fluorescence data.

4.2.2. *Atomic Hydrogen*

No other UV airglow feature has been observed as much as the atomic hydrogen Lα line at 1215.67 Å. It was the first airglow feature observed from space (Byram *et al.*, 1957); a historical review can be found in the paper by Rairden *et al.* (1986). Images of the Lα corona surrounding the Earth are seen in Figures 25 and 26. Interpretation of Lα data has been the chief way of studying planetary exospheres. Because atomic hydrogen often has a scale height which is a sizeable fraction of a planetary radius, a spherical radiation scattering model is necessary to interpret observations. The principal excitation source of the geocoronal emission is resonant scattering of the strong solar Lα line (Figures 1 and 34). The opacity of hydrogen on the Earth is sufficient that significant multiple scattering takes place. Self-absorption by terrestrial H can be seen as the narrow absorption feature at the center of the solar line in the upper left panel of Figure 34. The combination of multiple scattering and large scale height enable hydrogen radiation to scatter around through the geocorona into the night sector and produce the nightglow.

The most sophisticated model of the hydrogen airglow developed so far is by Anderson and colleagues (Anderson and Hord, 1977; Anderson *et al.*, 1987a, b). Included in the model are (1) multiple scattering (assuming CFR), (2) asymmetric hydrogen density distribution, (3) temperature gradients, (4) asymmetric velocity dis-

tribution, and (5) molecular absorption. The model successfully reproduces the Lα airglow using recent geocoronal hydrogen models of Tinsley *et al.* (1986).

Observations made from very high altitudes (> 40 000 km) can be interpreted using optically thin models. An early example of data taken from the OGO-3 satellite is shown in Figure 66 (Mange and Meier, 1970). The three models are for different values of a

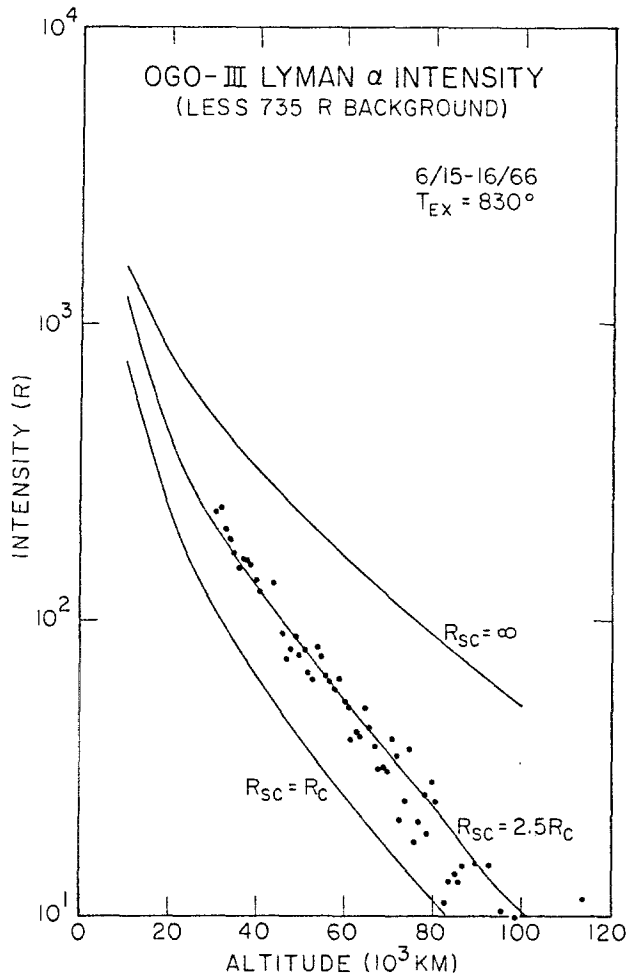

Fig. 66. Near-zenith geocoronal Lα airglow vs altitude of OGO-3 spacecraft, with background subtracted. Solid curves give normalized theoretical intensities based on the model of Chamberlain (1963). The parameter R_{sc} is a measure of the satellite population of hydrogen atoms, measured in units of the geocentric distance of the exobase. Figure taken from Mange and Meier (1970).

parameter of the Chamberlain (1963) exosphere model which adjust the populations of atoms in satellite orbits. The data require subtraction of an interplanetary background due to backscattering of sunlight by interstellar hydrogen atoms which have penetrated the solar system (for recent work see Ajello *et al.*, 1987; or Bertaux *et al.*, 1985). Moving

down in observation altitude, limb scan data from the DE-1 satellite (Figure 26) are shown in Figure 67 (Rairden *et al.*, 1986). The airglow models also employed a Chamberlain (1963) density distribution and show the sensitivity of the limb profiles to exospheric temperature.

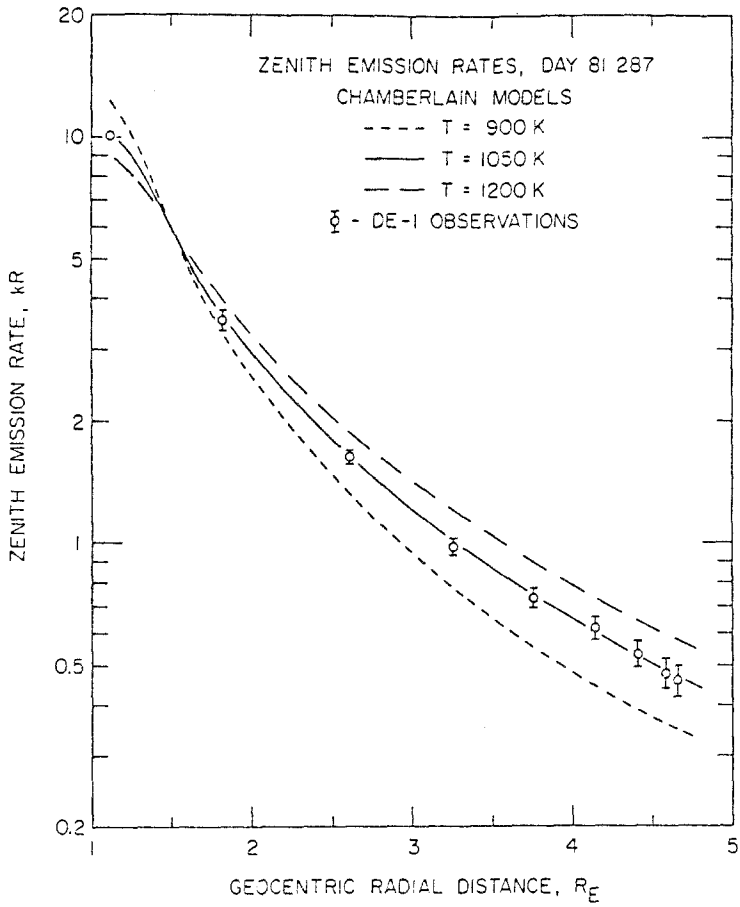

Fig. 67. H Lα emission rates in the zenith as a function of geocentric distance in earth radii, with background subtracted. Hydrogen exobase densities were 70000, 44000, and 31000 cm^{-3} for the (Chamberlain, 1963) model corresponding to exospheric temperatures of 900, 1050, and 1200 K, respectively. The critical satellite level $R_{sc} = 3R_c$. Figure taken from Rairden *et al.* (1986).

Limb scan data taken from low Earth orbit (600 km) in the optically thick region of the geocorona are shown in Figure 68 (Anderson *et al.*, 1987a). The upper panel of Figure 68 demonstrates the need for incorporating pure absorption and temperature gradients in the model. If they are ignored, the nadir emission rate is much too large. (The model shown in Figure 19 used an isothermal spherically-symmetric density distribution (Meier and Mange, 1973); the lower boundary of the radiative transport model was set at 100 km, in an attempt to mimic the observed nadir emission rate.) The middle panel of Figure 68 shows the sensitivity of limb scans to the exobase hydrogen concen-

tration (mainly a zenith effect). And the lower panel of Figure 68 shows the sensitivity to the flux of escaping hydrogen atoms (mainly a nadir effect). Anderson *et al.* (1987a) discuss the details of the sensitivity study. The important point of limb scanning is that

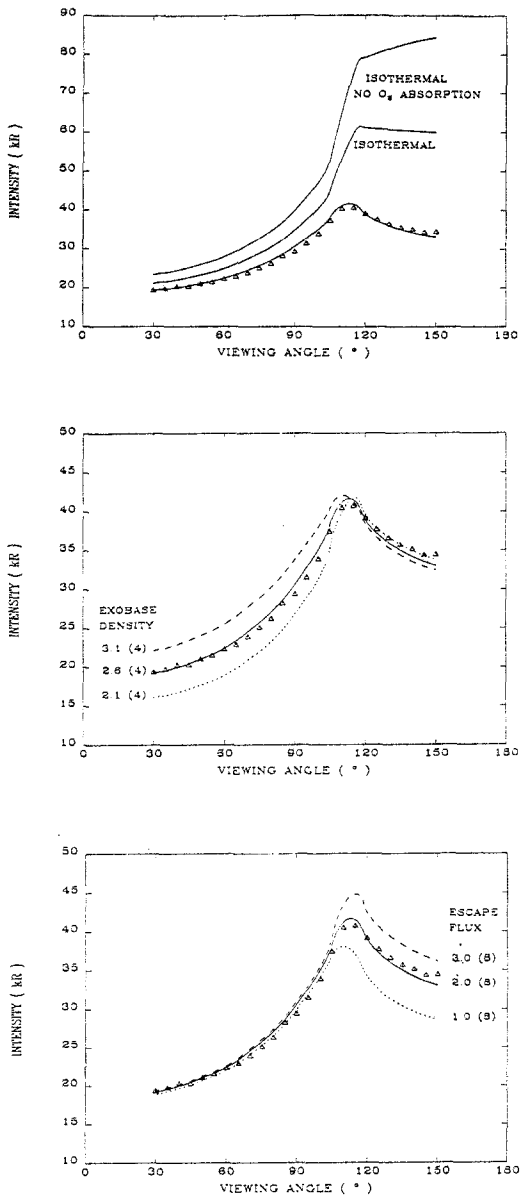

Fig. 68. Observed and modelled H Lα limb intensities for the conditions of the STP 78-1 satellite (Table I) on 30 March, 1979 at the subsolar position. The triangles represent data from 4 orbits in 10 deg viewing angle bins. Solid curves are best fits to data (exobase density of 26 000 cm^{-3} and escape flux of 2×10^8 cm^{-2} s^{-1}). *Upper panel*: various approximations to model; *middle panel*: sensitivity to exobase density; *lower panel*: sensitivity to escape flux. Taken from Andserson *et al.* (1987a).

the deductions are based on shapes, without resorting to absolute instrumental calibration. The hydrogen concentrations derived from such analyses agree with exospheric theory (Tinsley *et al.*, 1986) as well as with exchange equilibrium determinations of H (Breig *et al.*, 1985). After detrending the influence of the geocorona, long-term Lα airglow observations (see Figure 20) can be used to deduce the variation of the solar flux at line center. Such attempts have been found to agree with direct solar measurements (Thomas and Anderson, 1976). Thus the current understanding of the Lα airglow is good.

Such is not the case for the H Lβ emission at 1025.72 Å and the accompanying Balmer α branch at 6562.8 Å, produced by resonant scattering of the solar Lβ line (Figure 34). There have been far fewer measurements of either the Lβ airglow or the solar line profile. But many observations of the H Balmer α line, which branches from the $3p\,^2P$ Lβ upper level, have been made over the years. The Balmer α airglow, predicted by the same radiative transport model and hydrogen concentrations that have done so well with Lα, has perennially been too low by about a factor of 2 (Anderson *et al.*, 1987b).

While it might be argued that the problem resides in the dearth of solar Lβ line profile measurements, there is both direct and indirect evidence that the solar line-center flux is closely related to that of Lα. Lemaire *et al.* (1978) reported full solar disk observations of both Lα and Lβ line profiles, and these are shown in Figure 34. The Lβ line measurement is not of sufficient resolution to isolate the geocoronal absorption line, but Lemaire *et al.* estimate that the actual line center flux should be 10–20% larger than observed in Figure 34. If a mean of 15% is chosen, the ratio of the solar Lα to Lβ line center fluxes is 66. Interestingly, this is the same ratio needed to explain nearly 11 years worth of measurements by Voyager 2 of the interplanetary background emission produced by backscattering of the solar lines (Shemansky *et al.*, 1984). Remarkably, the interplanetary ratio does not change by more than $\pm$ 8% over the time-span of the observations, covering heliocentric distances from 1.5 to 10 AU. That solar Lα and Lβ should covary is also supported theoretically (Skumanich and Lites, 1986). Further discussion is given by Meier *et al.* (1987) and Anderson *et al.* (1987a). While the limited information available so far is consistent, more direct observations of the solar Lβ would be welcome.

Of course, direct observations of the geocoronal Lβ airglow would help resolve the Balmer α problem. But low altitude observations are contaminated by the O I 1027 Å emission (see Section 4.1.3.3). The only unambiguous observation of geocoronal Lβ was obtained during the Apollo 16 mission, when the camera was operated in the spectrographic mode (Carruthers and Page, 1976a). The Lβ emission rate was measured at high altitudes, well above the thermospheric oxygen 1026 Å airglow. The altitude profile is shown in Figure 69 (Meier *et al.*, 1977), along with a theoretical calculation based on the same model used to fit the Lα data (Carruthers *et al.*, 1976). The solar Lβ flux required was 8×10^9 ph cm^{-2} s^{-1} Å^{-1}, a factor of 50 lower than the solar Lα flux needed to match the airglow. This ratio is lower than discussed above, but is still consistent to within the estimated experimental calibration uncertainties associated with operating the Apollo 16 camera in spectrographic and imaging modes (G. Carruthers,

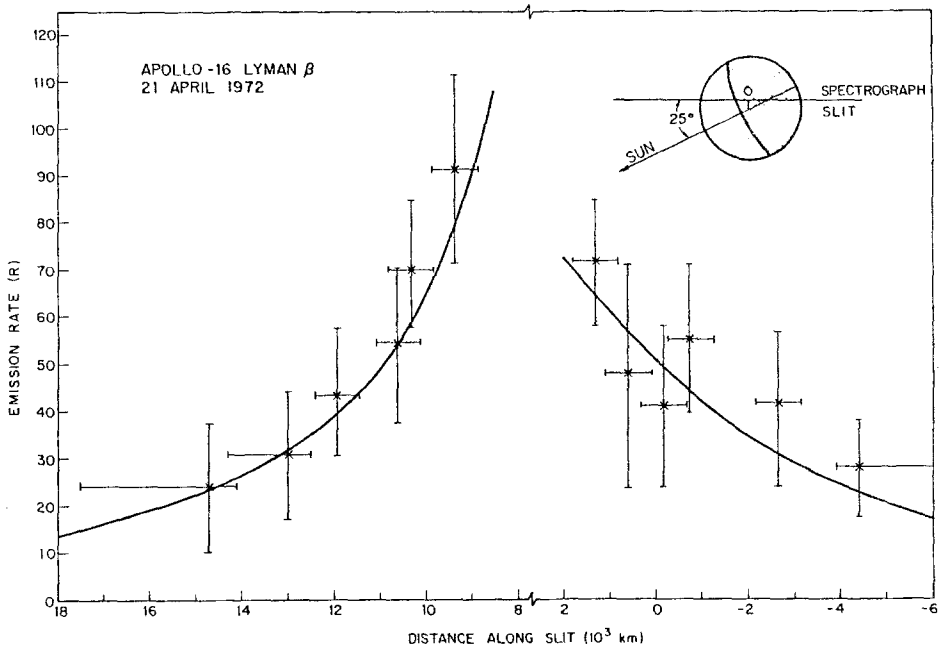

Fig. 69. Geophysical H Lβ emission rate as a function of distance along the Apollo 16 camera/spectrograph slit. The distance scale is measured from the closest approach of the slit to the center of the Earth, marked by '0' in the upper right insert. Positive distances are towards the Sun. The solid curve is a multiple scattering model. Figure taken from Meier *et al.* (1977).

private communication, 1989). Thus the Apollo 16 data as well as the O I 1027 Å data from STP 78-1 (see Section 4.1.3.3) are also consistent with the solar Lβ flux and the geocoronal H concentration. The factor-of-two Balmer α problem remains unresolved.

4.2.3. *Atomic Helium*

The first two resonance lines of atomic helium at 584 and 537 Å have been seen in the dayglow (Figures 3, 8, and 22 and Table II). Resonant scattering of the solar emission lines is the excitation source. Since the helium scale height is not as large as hydrogen, little radiation can be scattered beyond the terminator and the nightglow is negligible. (The zenith emission at night in Figure 22 is due to the interplanetary background.) Molecular extinction in the atmosphere prevents radiation at these wavelengths from reaching much below 160 km (Figure 2).

The 584 Å emission has been observed on a number of occasions from sounding rockets and satellites. The most comprehensive data set analyzed so far is the broad-band photometric observations from the STP 72-1 satellite at 740 km altitude (Meier and Weller, 1972; Anderson *et al.*, 1979; Figure 22 and Table I). Since helium does extend into the lower exosphere and its vertical opacity is some tens of optical depths at line center, a spherical radiative transport model must be employed to interpret observations. Such a model was used by Meier and Weller (1972) to reproduce the

theoretical curves in Figure 22. The solid curve employs a spherically-symmetric helium concentration, while the dashed curve includes the well-known bulge of helium atoms in the winter hemisphere. No model results are shown for the nadir, since the signal from the broad-band filter photometer was contaminated by other emissions in the passband from the lower thermosphere. A more comprehensive analysis of the data, including limb scans, was reported by Anderson *et al.* (1979). A sample of the limb scan data from two orbits is shown in Figure 70, along with model results which take into account the global variation of helium. Again, observations from below the spacecraft (> 90 deg zenith

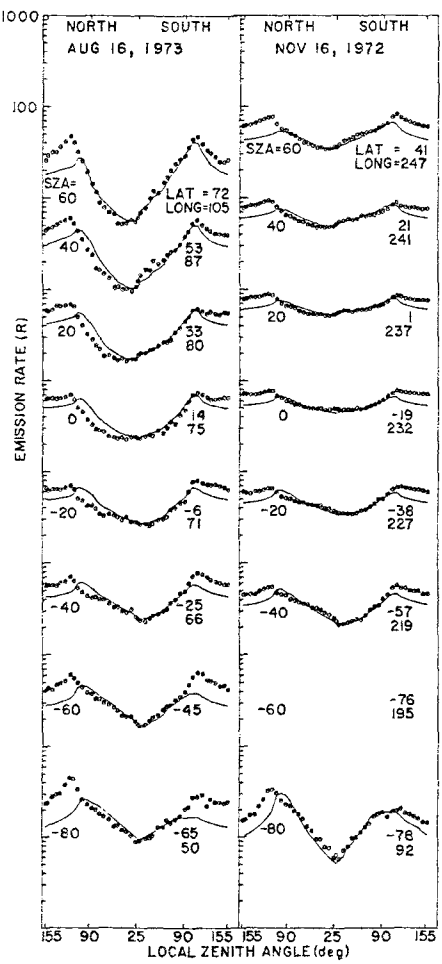

Fig. 70. Dependence of the He 584 Å emission rate on observation (local) zenith angle as observed from various orbital locations during two passes of the STP 72-1 spacecraft (Table I). The solar zenith angle and geographic location are indicated below each spin-scan. The best fit to the data is indicated by the solid lines. The scale for each spin-scan is displaced downward by a factor of 10 for clear viewing. North and south sides of the spin-scans are indicated at the top. The mismatch between data and models when looking down is due to other emissions in the photometer passband besides He 584 Å. Figure taken from Anderson *et al.* (1979).

angle) are not well reproduced by the model due to other contaminating emissions. Interestingly, Fahr and Smid (1982) suggested that differences between CFR and PFR models could account for some of the nadir discrepancy. This is surprising since the helium opacities are only of the order of tens of optical depths, and therefore significant transport should not be occurring in the line wings where CFR–PFR differences lead to important effects on the integrated radiance. This point may warrant further investigation.

The shape of limb scan observations from near the top of an optically thick atmosphere are particularly sensitive to the optical depth of the scatterer, as was shown in Figure 68 for H Lα. This is also true for He 584 Å. Figure 71 shows that as the opacity

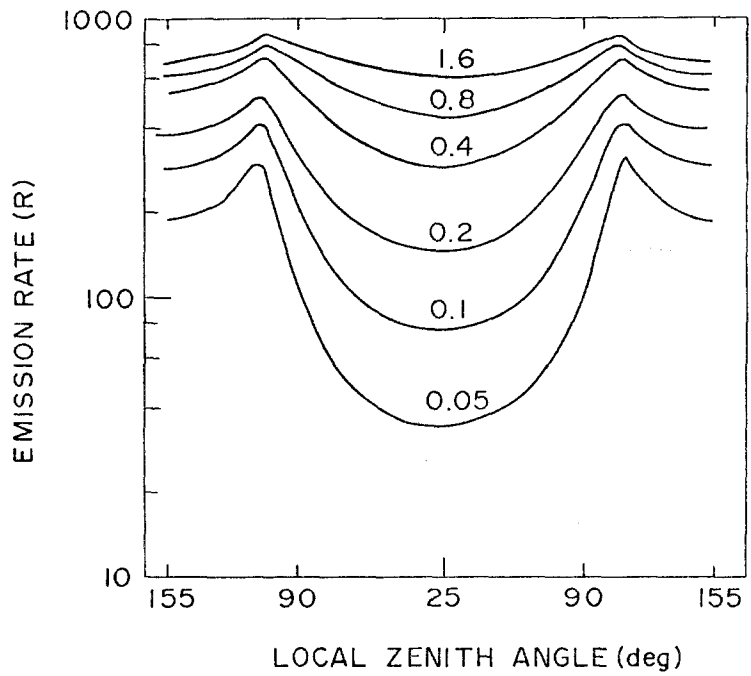

Fig. 71. Model calculations of the He 584 Å emission rate vs local (observation) zenith angle for a 900 K model atmosphere with the helium concentration scaled by the indicated multipliers. The solar zenith angle was 0° and the observation altitude was 740 km. See Anderson *et al.* (1979) for details.

of the atmosphere increases, the radiation field becomes more isotropic and *vice versa*. So it can be concluded that helium concentrations derived from fitting model profiles to data such as shown in Figure 70 can be used with confidence, without resort to absolute calibration.

The solar line profile observed by Doschek *et al.* (1974) (Figure 34), adjusted for terrestrial self-absorption, was used in the above modelling. Other measurements of solar line profiles using absorption cell technology are summarized by Ogawa *et al.* (1984) and appear to be consistent with the profile measured directly. A slight trend

towards narrowing of the solar line with increasing solar activity is indicated, but is within the uncertainty of the measurements.

Spectroscopic observations of the 584 Å line have been made from rockets (e.g., Gentieu *et al.*, 1984; Figure 8) and the STP 78-1 satellite (Chankrabarti *et al.*, 1983). Extremely high spectral resolution data were obtained with an absorption cell experiment by Fahr *et al.* (1986). The analysis by Fahr *et al.* using a radiative transport model showed agreement with the MSIS helium model, but a high solar 584 Å flux was required.

The He 537 Å line is severely contaminated by O II lines at 538 and 539 Å. These can be sorted out with high-resolution spectroscopy (Gentieu *et al.*, 1984) or by examining the limb profile of the emission rate, since O^+ and He have different altitude distributions. Recent work using this latter technique with STP 78-1 data has shown that when viewing downward from 600 km, O II emissions dominate, but that emissions seen upward are largely due to He 537 Å (Cleary *et al.*, 1991).

4.2.4. *Atomic Nitrogen*

Atomic nitrogen has several moderately bright lines in the FUV (1493, 1200, and 1135 Å) and many weak lines in the EUV. These are identified in the energy level

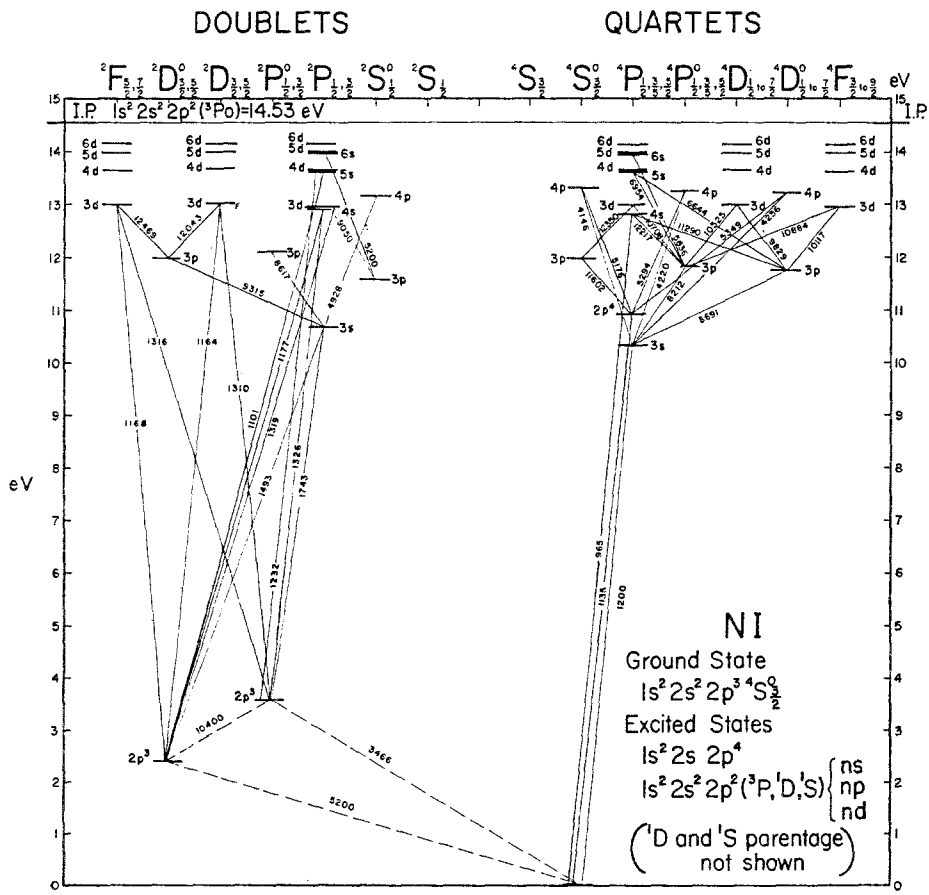

Fig. 72. Partial energy level diagram for atomic nitrogen. Adapted from Tinsley (1972).

diagram in Figure 72 and in Tables II and IV. The FUV lines are produced in varying amounts by photoelectron impact on N and N_2, and by photodissociative excitation of N_2. The solar spectrum is weak at 1200 and 1134 Å so that resonant scattering of sunlight is not an important source. But multiple scattering is important for these two lines; the line-center opacity for the 1200 Å lines can be more than 60 but is significantly less at 1134 Å. N I 1200 Å has a triplet upper state (^4P) and a single lower state. N I 1134 Å is also a triplet with wavelengths 1134.1653, 1134.4149, and 1134.9803 Å. The radiative transport issues are complicated by the molecular contributions to the excitation rate. Usually in a dissociative excitation process, the excited fragment atoms are kinetically hot, having emission temperatures of tens of thousands of kelvins (e.g., Wells *et al.*, 1976). Since the line width following dissociation is much larger than the ambient atmospheric absorption width, little multiple scattering should occur from this source and the contribution to the emission rate from this process should have optically thin altitude profiles with a N_2 scale height on the topside. Direct electron impact on N will have a thermal width, will be multiply scattered, and will have a flatter altitude profile.

There has been a long-standing issue regarding the N I 1200 Å lines: observed altitude profiles of the radiance have nearly always had the appearance of optically thick emissions, even though the molecular sources dominate the 1200 Å production rate in the lower thermosphere both in the dayglow and in the aurora (e.g., see Park *et al.*, 1977; Takacs and Feldman, 1977; Meier *et al.*, 1980; and their references). A solution to the problem was discussed by Meier *et al.* (1980) in which it was proposed that some 50–70% of the 1200 Å photons from dissociative excitation are produced within the ambient Doppler core of the line; i.e., a sizeable fraction of fragment atoms has low velocities following dissociation. The problem and the proposed resolution can be seen in the center panel of Figure 73, which compares the model of Meier *et al.* (1980) with

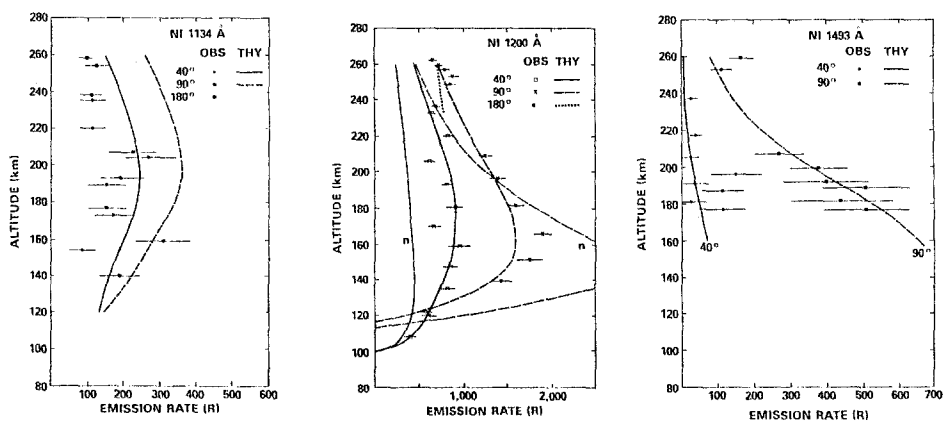

Fig. 73. Comparison with theory of altitude profiles of N I column emission rates taken during the 1978 rocket flight (Table I). *Left panel*: Compares multiple scattering model with dayglow data for 40 and 90 deg OZA. *Center panel*: N I 1200 Å triplet model results for optically thin case (indicated by '*n*' for 40 and 90 deg) and multiple scattering case for all three look directions. *Right panel*: N I 1493 Å column emission rate, shown only for observing above 160 km to avoid uncertainties in correcting the data for an underlying N_2 LBH band. Statistical error bars are shown for the 1σ level. Taken from Meier *et al.* (1980).

N I dayglow data from the 1978 rocket (Table I). Shown are data for three observational zenith angles. The curves labelled '*n*' are computed from optically thin volume emission rates and clearly show far too much limb brightening (from 40 to 90 deg OZA). The unlabeled curves use the above fraction of low-velocity emitters from the dissociation processes; much better agreement is then achieved. Subsequent to this analysis however, is new laboratory work on different aspects of N_2 dissociative excitation processes (Erdman and Zipf, 1983, 1987; Wu *et al.*, 1983). While direct information on the production of 1200 Å emission line profiles from dissociation is still not available, the conclusions of those authors based on indirect evidence strongly suggest that the dissociation products of N_2 are likely to be kinetically fast and that the proposed solution of Meier *et al.* (1980) may not be correct.

A number of additional new results have become available since the work of Meier *et al.* (1980): (1) A new measurement of the energetic electron impact excitation cross section of N_2 leading to $N(^4P)$ was made by Ajello and Shemansky (1985), which confirmed the earlier cross section of Mumma and Zipf (1971a) (after adjustment of the Mumma and Zipf value downward by 0.7 to account for the new H_2 Lα calibration standard (Shemansky *et al.*, 1985)). (2) The direct energetic electron impact cross section for $e + N(^4S) \rightarrow N(^4P)$ has been observed to have a peak value of near 10^{-16} cm^2 (Doering, private communication, 1990). This value is lower than the emission cross section of Stone and Zipf (1973): 2.5×10^{-16} cm^2. Cascade from higher levels would have to account for the major part of the population rate of $N(^4P)$ to avoid a discrepancy between direct excitation and emission (direct + cascade) cross sections. On the other hand, the Stone and Zipf cross section should certainly be lowered by 30% because of the change in the H_2 Lα calibration standard (see above), and probably other downward revisions may be needed (Zipf and Erdman, 1985). In any case, any hope that the optically thick/thin issue might be resolved with an increase in the $e + N$ contribution of the total $N(^4P)$ excitation rate is rapidly disappearing, since Meier *et al.* already used the larger Stone and Zipf cross section. (3) The photoelectron code of Strickland and Meier (1982) has been upgraded (Section 3.2.1.1). (4) New odd nitrogen photochemical models are available (McCoy, 1983; Cleary, 1986). (5) Additional work on the photodissociative excitation rate of N_2 has been reported by Wu *et al.* (1983). Clearly, the analysis of the FUV emissions of N I needs to be revisited.

Also shown in Figure 73 are the data and model fits to N I 1134 Å (left panel) and 1493 Å (right panel). The multiple scattering issues are not as severe with the 1134 Å resonance line because the optical depth is not as great as at 1200 Å. Still, constraints on the various production mechanisms of excited N atoms are available from data with good precision. The 1493 Å emission is contaminated by LBH-bands at low altitudes. At higher altitudes, the direct $e + N(^4S) \rightarrow N(3s\,^2P)$ accounts for the magnitude and altitude profile of the data. The electron impact cross section for $e + N(^4S) \rightarrow N(3s\,^2P)$ leading to 1493 Å emission was actually for the companion emission at 1743 Å, but scaled by the 1493/1743 transition probabilities (2.7 from Mumma and Zipf, 1971a). A re-analysis of these emissions should also be made, subject to many of the same revisions needed for the 1200 Å feature.

4.3. Ions

4.3.1. *Atomic Oxygen Ion*

A number of O II features have been observed in the dayglow. They are identified in Table II and Figures 7 and 8. The transitions are shown in the energy level diagram in Figure 74. The brightest feature by far is at 834 Å. It is a triplet emission

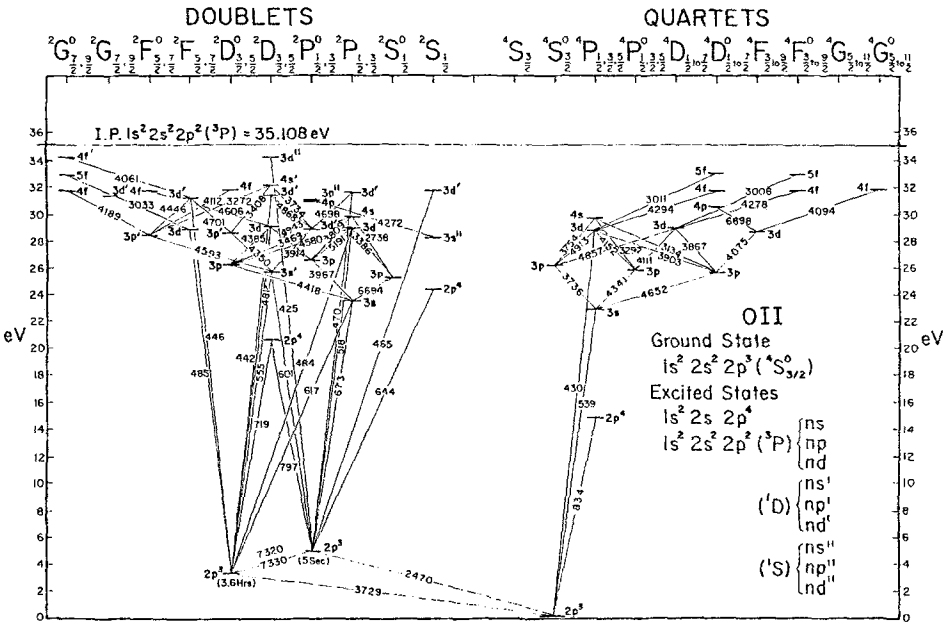

Fig. 74. Partial energy level diagram for O^+.

($2p^4\ ^4P \rightarrow 2p^3\ ^4S$), with a single lower level and a triplet upper level, producing the three lines listed in Table IV. There are three potential sources of excitation leading to 834 Å emission. The dominant source is photoionization of O leading to excited O^+. The cross section for this process is available from the compilation of Conway (1988), who combined the total photoionization cross section of Samson and Pareek (1985) with the branching ratio into the ^4P state (Henry, 1967). Integrating the product of the cross section and the solar ionizing irradiance at solar min and max (Table VI) results in g-factors of 9 and $22 \times 10^{-9}\ s^{-1}$, respectively. These are slightly lower than those computed by Torr and Torr (1985).

Electron impact ionization of O is a secondary source. The emission cross section for production of O II 834 Å was measured by Zipf *et al.* (1985); see Table V. Combining this cross section with the photoelectron fluxes in Figure 31 leads to peak g-factors (Equation (38)) of 7.5 and $20 \times 10^{-10}\ s^{-1}$ at solar min and max, respectively. After taking into account the altitude profiles of the excitation rates and multiple scattering, Cleary *et al.* (1989) found that this source contributed only 5% to the total column

emission rate. Earlier estimates of higher percentages (Feldman *et al.*, 1981; Anderson and Meier, 1985) were made prior to the laboratory measurement by Zipf *et al.* (1985).

A third even weaker source of O I 834 Å is resonant scattering of the solar emission lines. Feldman *et al.* (1981) estimated that the direct solar source should be no more than 10% of the other sources in the ionosphere. On the other hand, the solar source would be important for scattering by O^+ in the magnetosphere (Chakrabarti *et al.*, 1984; Chiu *et al.*, 1986, 1990; Akasofu, 1989; Swift *et al.*, 1989; Meier, 1990). An accurate assessment of the spectral irradiance has proven difficult because the solar 834 Å feature contains both O III and O II multiplets. Solar spectra published so far have not had sufficient spectral resolution to separate the individual lines. Recently, however, Meier (1990) reported on early rocket spectra obtained by Tousey *et al.* (1963) during a rocket flight on 22 August, 1962. The spectra at 834 Å apparently were not published and the original photographic plate has not been found. But a high quality reproduction was located which contained the 834 Å spectrum at about 0.14 Å resolution (FWHM). This was sufficient to determine the relative contributions of O II and O III, if it is assumed that the upper states of the ions are populated according to their statistical weights. Meier *et al.* (1990) found that 26% of the solar emission at 834 Å is due to O II. The 834 Å line in the solar min spectrum of Figure 1 contains 6.7×10^8 ph cm^{-2} s^{-1}. If the O II emission lines have FWHM of 0.065 Å (Meier *et al.*, 1990), then the resulting solar *g*-factors are those given in Table IV for the three lines of the O II multiplet (assuming a Gaussian line profile). If the O^+ concentration at the ionospheric peak were 10^6 cm^{-3}, the total volume excitation rate would be 1.5 cm^{-3} s^{-1}, a factor of more than 30 lower than the photoionization source peak production rate at solar min. Thus the solar source can be ignored in the ionosphere.

The ionosphere is usually optically thick to the 834 Å lines; line center optical depths approach 10 for the thickest transition when the peak O^+ concentration exceeds 10^6 cm^{-3}. Thus multiple scattering must be included in analyses of the 834 Å airglow. The initial production of $O^+(^4P)$ from photoionization of O occurs below 200 km during the day (see Figure 1 of Anderson and Meier, 1985). But the *F*-region of the ionosphere is usually much higher in altitude, thus posing an interesting radiative transport problem: the O^+ layer is essentially illuminated from below by a diffuse line radiation source. Multiple scattering causes the 834 Å airglow in the *F*-region to take on the character of the O^+ concentration. The details of the scattering model, which accommodates radiation initially produced either below or within the O^+ layer, have been worked out by Anderson and Meier (1985). (Earlier models were discussed by Feldman *et al.* (1981) and Kumar *et al.* (1983).) It should be noted that the oscillator strength used in the multiple scattering models (Kumar *et al.*, 1983; Anderson and Meier, 1985) was that given by Wiese *et al.* (1966): 0.43. A more recent tabulation by Ho and Henry (1983) showed that theory and experiment agreed upon a value near 0.25. Revised values are given in Table IV. Thus the earlier airglow work needs to be repeated using the lower oscillator strength.

Another important advance in modelling the O I 834 Å airglow was reported by Cleary *et al.* (1989), who showed that the agreement between the 834 Å airglow observed during

the 1978 rocket experiment (Table I) and an early version of the radiative transport model (Feldman *et al.*, 1981) was fortuitous. When the more accurate radiative transport model of Anderson and Meier (1985) was used, the theory turned out to be significantly lower in magnitude than the airglow below 200 km, a region where molecular absorption dominates the altitude profile. Cleary *et al.* concluded that agreement could be achieved if the N_2 absorption cross sections for the three lines of the 834 Å triplet were reduced by an order of magnitude. The justification is that earlier analyses (Kumar *et al.*, 1983; Anderson and Meier, 1985) used tabulations of absorption cross sections made with laboratory spectrographs which were unable to resolve the rotational structure of N_2. (The absorption character of N_2 in this wavelength region is dominated by rotational lines.) A careful investigation showed that it is unlikely that there are any accidental resonances between the O I emission lines and the N_2 absorption lines, so that extinction of the 834 Å dayglow by N_2 is much weaker than previously thought.

During the day, the 834 Å airglow can be used to determine the O^+ concentration through the proportionality introduced by multiple scattering of the line radiation produced from O photoionization. This was clearly seen in the STP 78-1 (Table I) data shown in Figure 21. In that figure, the model of Kumar *et al.* (1983) was used to compute the values given by the solid lines (S. Chakrabarti, private communication, 1989). Another perspective of the STP 78-1 data can be seen in Figure 75, where successive limb scans from a dayside pass of the satellite have been stacked and contoured to provide a scan angle-latitude plot of the 834 Å column emission rate (McCoy *et al.*, 1985). The strong upwelling of the ionosphere can again be seen over the geomagnetic equator (displaced to the north of the geographic equator). Individual limb scans can be analyzed to infer the local ionosphere plasma distribution from the airglow. Figure 76 shows the best fit of McCoy *et al.* to limb scans made near the equator and in the north. While the peak brightnesses were similar, the character of the elevated equatorial ionosphere is evident from the analysis (see caption of Figure 76). Additional discussion of O I 834 Å remote sensing is given in Section 5. At night, the *F*-region of the ionosphere can be remotely sensed using observations of the radiative recombination lines of atomic oxygen, as discussed earlier.

A number of other O II emission lines have been observed in the dayglow (Table II). Since excitation cross sections are generally not available for these features, most of the dayglow analyses have concentrated on line ratios because of the commonality of upper levels of various pairs of doublet features (see Figure 74). The upper states for four pairs of lines are listed in Table XIV, taken mostly from Gentieu *et al.* (1984). Sources of line ratios are the dayglow, laboratory observations and theory. Column 9 has been added to the table of Gentieu *et al.*, which gives ratios computed from best estimates of oscillator strengths from Ho and Henry (1983). Overall the agreement among the various sources is acceptable, considering that the uncertainties are typically greater than $\pm 30\%$.

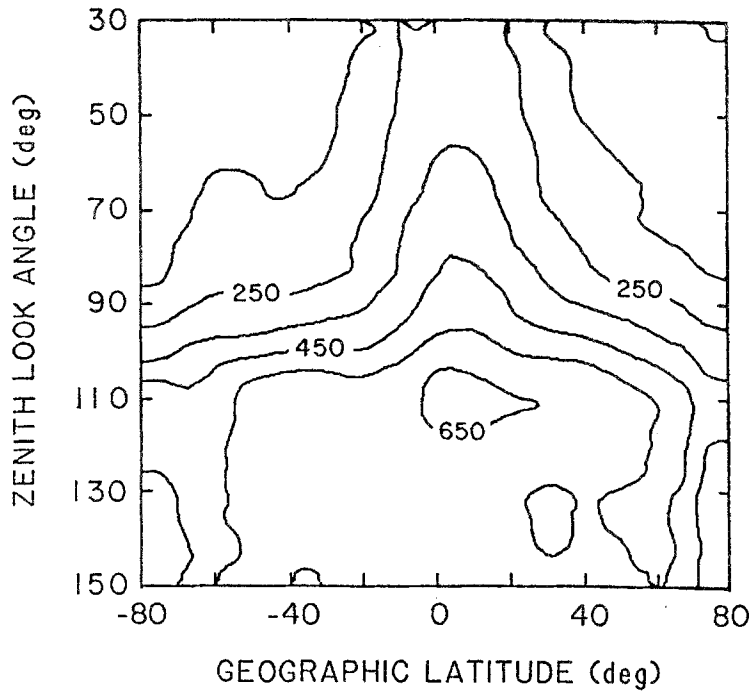

Fig. 75. O II 834 Å limb scans for a single dayside pass of the STP 78-1 satellite on 27 March, 1979. Contours are produced by combining radiances vs zenith look angle (OZA) for individual scans at each geographic latitude and plotting the data as isophotes. The upwelling ionosphere over the magnetic dip equator, displaced to the north of the geographic equator in this pass, is clearly seen in the data. There appears to be some auroral emission above the satellite (< 90 deg) in the south. Figure taken from McCoy *et al.* (1985).

TABLE XIV

Summary of O II branching ratios

Upper state	Transitions	Observations			Laboratory		Theory			
		1	2	3	4	5	6	7	8	9
$2s\,2p^4\,^2P$	538/581	3.0	>5.5	>5.8	2.6	1.65	3.3	3.3	3.2	2.4
$2p^2(^1D)3s\,^2D$	555/601	2.8	1.0	1.3–2.5	2.2	1.5	–	–	2.5	1.8
$2p^2(^3P)3s\,^2P$	617/673	5.7	3.6	7.5–12	5.5	4.2	–	6.0	4.5	6.7
$2s\,2p^4\,^2D$	718/797	5.0[a]	5.9[a]	>2.8[b]	9.7	6.95	6.4	–	7.7	8.6

[a] Corrected for pure absorption.
[b] Not corrected for pure absorption.

References

1. Gentieu *et al.* (1984).
2. Feldman *et al.* (1981).
3. Chakrabarti *et al.* (1983).
4. Morrison *et al.* (1981).
5. Morrison *et al.* (1983).
6. Cohen and Dalgarno (1964).
7. Luken and Sinanoglu (1976).
8. R. C. Cowan (private communication to Gentieu, 1980).
9. Estimated from Tabulation of Ho and Henry (1983).

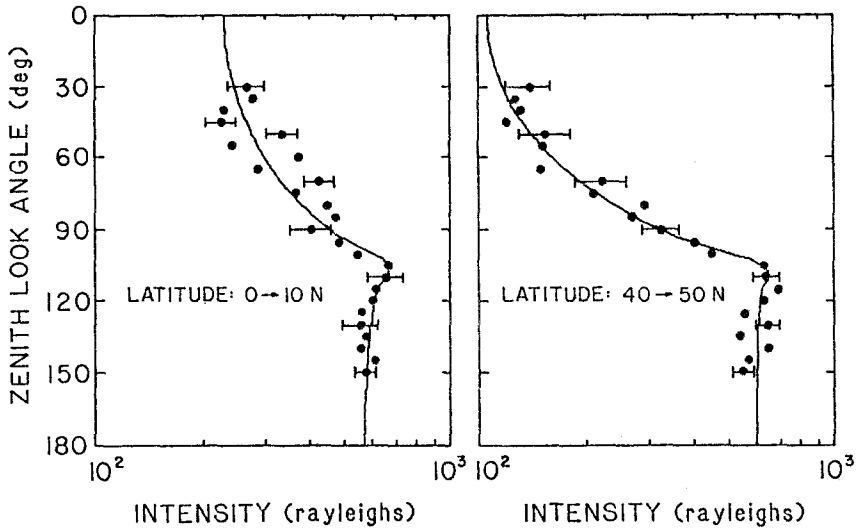

Fig. 76. Individual limb scans of the O II 834 Å dayglow in Figure 75 for mid-latitude and equatorial positions of the STP 78-1 satellite. Solid lines give the best-fit model results from McCoy *et al.* (1985). The ionospheric Chapman layer parameters in the model for the mid-latitude observation are, height of maximum: 400 km; peak concentration: 1.7×10^6 cm^{-3}; scale height: 65 km. At mid-latitude, the respective parameters are 400 km: 2×10^6 cm^{-3}; 75 km (mean values in range given by McCoy *et al.*). The concentrations have been scaled up by 1.7 to account for the revision in the 834 Å oscillator strength; see text. Figure taken from McCoy *et al.* (1985).

4.3.2. *Molecular Nitrogen Ion*

The (0, 0) band of the N_2^+ first negative system at 3914 Å is a bright dayglow feature (Figure 5), produced mostly through resonant scattering of sunlight by molecular nitrogen ions (Zipf and Fastie, 1964; Broadfoot, 1971). The transition is identified in the energy level diagram in Figure 39. While the concentration of N_2^+ in the ionosphere is low (e.g., see references in Bauer, 1973; and Breig *et al.*, 1983), the *g*-factor is large (Table VII), and the product yields a vertical column emission rate of 6.7 kR above 100 km, mid-afternoon near solar min (Zipf and Fastie, 1964). Few observations of the dayglow have been made because of the necessity to guard experiments against the bright Rayleigh-scattered continuum at low altitudes. Torr and Torr (1985) reported 3914 Å dayglow observations from Spacelab 1, but did not analyze the data in detail. The status of early twilight observations of 3914 Å was reviewed by Broadfoot (1971), who cited work by Wallace and McElroy (1966) showing that the twilight glow could also be accounted for by resonant scattering of sunlight. Recently new twilight studies have been reported preliminarily by Swift *et al.* (1989).

While N_2^+ is a minor component of the ionosphere, it is a tracer of key reactions, especially involving vibrationally excited ion chemistry. Models have consistently predicted a factor of two more N_2^+ than observed (see Breig (1987) for a recent review, and Breig *et al.* (1983) and Abdou *et al.* (1984) for discussions of the ion chemistry). Fox and Dalgarno (1985) have calculated vibrational distributions of the N_2^+ excited

state, and volume emission rates of 3914 Å. High spectral resolution monitoring of the vibrational distribution of the (0, 0) band would provide important information for the study of this important inospheric constituent.

4.3.3. *Atomic Nitrogen Ion*

The brightest N^+ emissions in the dayglow are at 2143, 1085, and 916 Å. Many weak lines are present in the FUV and EUV. Identifications are given in Table II, Figures 7 and 8, and in the energy level diagram in Figure 77. The concentration of N^+ in the

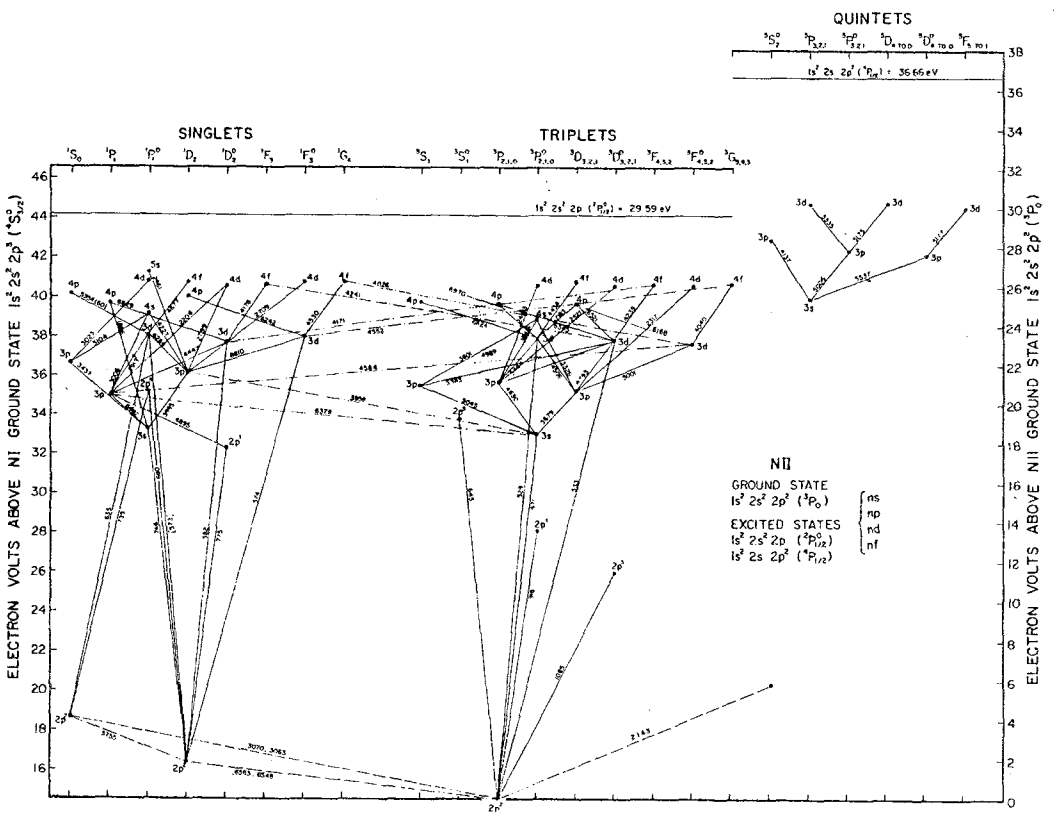

Fig. 77. Partial energy level diagram for N II.

ionosphere is so low that multiple scattering can be ignored completely in the modelling of these emission lines.

The N II emission at 2143 Å is a doublet at 2142.775 and 2139.007 Å, occurring via a transition of the ion from $^5S_2 \rightarrow {}^3P_2$ and $^3P_1$, respectively. The emission was first seen as a bright line in auroras and was referred to as the 'auroral mystery feature' because the identification was initially uncertain. Dick (1978) correctly identified the emission as an N II feature. Considerable controversy has surrounded the quantitive analysis of the excitation process. Apparently the only source in auroras with sufficient strength to produce the emission is electron impact dissociative ionization excitation of N_2. A cross section with magnitude of order 10^{-18} cm^2 is required for this process to explain auroral emissions. Knight (1982) measured a lower limit of just that value, in agreement with theory (Dalgarno *et al.*, 1981). But the laboratory work of Erdman and Zipf (1986)

resulted in a peak of 3×10^{-21} cm^2. The resolution of the discrepancy is embedded in the lifetime of the $N^+(^5S)$ metastable level. Theory yields values near 6 ms (Hibbert and Bates, 1981; Dalgarno *et al.*, 1981), while 5 μs is required by the Erdman and Zipf experiment. The longer lifetime could produce quenching of the metastable state in the laboratory, leading to an incorrect deduction of the magnitude of the cross section. However, Erdman and Zipf argue that quenching is not important in their measurement. Also, the excited fragments should be kinetically fast, leading to de-excitation by walls in the laboratory experiment if the lifetime is long. On another front, a recent rocket experiment by Siskind and Barth (1987) yielded cross sections and lifetimes (deduced from observed quenching of the altitude profile of the 2143 Å emission) consistent with the theoretical values. Earlier rocket observations by Sharp (1978) and by Feldman (1976) showed little and significant quenching, respectively. The quenching issue is still not resolved.

In the dayglow, photodissociative ionization of N_2 was suggested by Victor and Dalgarno (1982) as the excitation source of $N^+(^5S)$. This was confirmed by several rocket experiments (Barth and Steele, 1982; Gerard and Noel, 1986; Cleary and Barth, 1987; Bucsela and Sharp, 1989) and by Spacelab 1 observations (Torr and Torr, 1985). Cleary and Barth (1987) deduced an energy-dependent cross section for photodissociative ionization from the work of Wight *et al.* (1976) which has a peak value of about 2×10^{-18} cm^2 at 250 Å. They then deduced a yield for the production of $N^+(^5S)$ of 10% in order to reproduce their dayglow observations. A larger value of 20% was deduced by Torr and Torr (1985), but apparently they used a cross section at only 304 Å. In each case, the 2143 Å feature had to be separated from the blended NO γ-band. Quenching is not a significant factor for dayglow observations above 130 km.

While the 2143 Å dayglow observations can be explained plausibly with the atomic parameters discussed above, it would be very important to have confirmation with a laboratory measurement of the fluorescence cross section for photodissociative ionization excitation of N_2. Also it would be good to measure the dayglow in higher spectral resolution to better separate the 2143 Å doublet from the NO γ-band.

In the aurora, the N II sextuplet emissions at 1085 and 916 Å are produced by energetic electron impact excitation (Meier *et al.*, 1982b), but unpublished calculations by the author show that photoelectron impact excitation only accounts for 10% of the emission observed during the day. The remaining viable excitation processes are ionization of N and photodissociative ionization excitation of N_2. The cross sections for these processes have not been measured. Atomic nitrogen can be eliminated as a contender, not only because of its low concentration relative to N_2 (Figure 30), but also because of its much different altitude profile. The latter point can be illustrated by comparing the altitude profile of the N II 1085 Å column emission rate with that of the (4, 0) N_2 LBH-band at 1325 Å. Unpublished data from the 1980 rocket flight (Table I) kindly supplied by P. Gentieu are shown in Figure 78, along with smoothed 1325 Å data (Meier *et al.*, 1985). The EUV spectrometer viewed the airglow horizontally when the rocket was below about 235 km. Above that altitude, the payload was canted toward to 98 deg OZA from the local vertical. Substantial limb-brightening characteristic of the

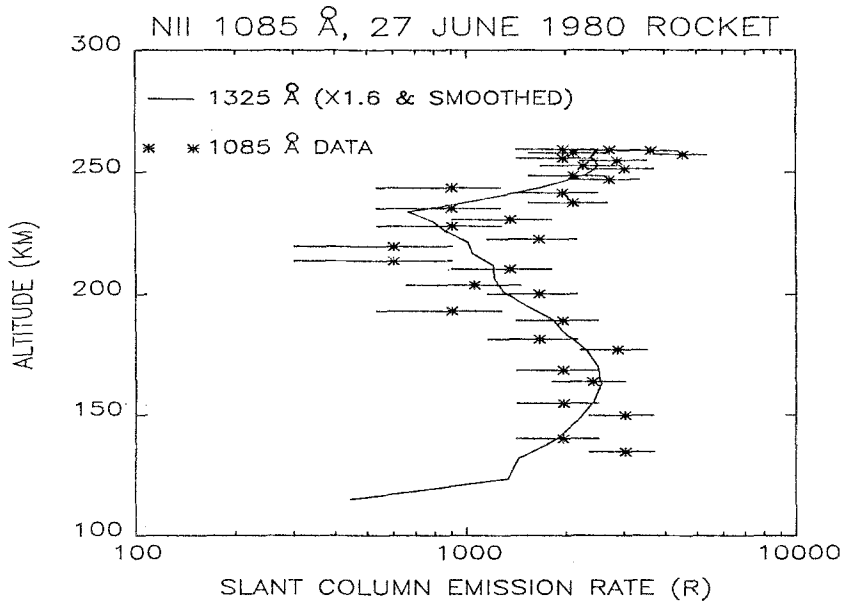

Fig. 78. N II 1085 Å column emission rate vs altitude from the 1980 rocket experiment (Table I; Gentieu *et al.*, 1981, 1984). The N II data are given by asterisks, with $+1\sigma$ statistical uncertainty shown. The solid line is the N_2 LBH (4, 0) band emission rate at 1325 Å, with a 5-point running smooth applied. (See Figure 6 of Meier *et al.* (1985) for the unsmoothed 1325 Å data.) The payload was pointed at 90 deg OZA below 235 km. Above that altitude, the line of sight was canted down to 98 deg to measure limb brightening. The unpublished 1085 Å data were provided through the courtesy of Peter Gentieu.

N_2 scale height can be seen in both the 1085 and 1325 Å data. The close correspondence between the two data sets leaves little doubt that the 1085 Å emission originates with N_2, in analogy with N II 2143 Å. The N II 916 Å emission probably has the same parentage.

4.3.4. *Helium Ion*

Johnson *et al.* (1971) first suggested that the Lα line of He^+ at 304 Å could be used to image the plasmasphere. They called the concept 'Magnetoglow'. The helium ion concentrations are sufficiently low that multiple scattering can be neglected. Subsequent work on rocket data (Meier and Weller, 1972; Paresce *et al.*, 1973, 1974), STP 72-1 satellite data (Weller and Meier, 1974), and Apollo–Souyez (Chakrabarti *et al.*, 1982) demonstrated that th 304 Å emission rate observed from low Earth orbit could be explained by resonant scattering of the bright solar line (Figures 1 and 34) using reasonable models of He^+ concentrations in the plasmasphere. A calculation taken from Weller and Meier (1974) can be seen in Figure 23, showing the sensitivity of the airglow to the plasmapause. In the night sector, the Earth's shadow acts as a height differentiator, revealing details of the plasmapause structure at large distances from the Earth where the line of sight of a sensor breaks into sunlight. The structure of the actual

plasmasphere is somewhat different than predicted by the *ad hoc* models shown in Figure 23.

There has been a resurgence of interest in magnetospheric imaging following the realization that measurable amounts of O^+ as well as He^+ are present outside the plasmasphere (Chiu *et al.*, 1986, 1990; Akasofu, 1989; Swift *et al.*, 1989). Swift *et al.* and Chiu *et al.* (1990) show theoretical images of O^+ 834 Å emission from the magnetosphere, but the radiance calculations neglect populations of fast moving ions which have their scattering centers Doppler shifted off the solar line. The correct procedure would be to compute the radiance from Equation (21), with a g-factor which is derived using a cross section (Equation (14a)) that has been integrated over the velocity distribution of ions including bulk motions. A recent paper by Meier (1990) examined the O^+ and O^{++} problems in detail and found lower excitation rates than previously estimated. The usual form for the g-factor given by Equation (23) assumes a continuum solar source, and consequently the velocity distribution of atoms is irrelevant, providing the scattering medium is optically thin. The solar 304 Å emission line is sufficiently broad (order 0.1 Å) compared with the thermal width of He^+ in the plasmasphere (about 8 mÅ for 4000 K; e.g., see Newberry *et al.*, 1989) that the continuum assumption is reasonable. Some examples of full global images of He^+ 304 Å from the plasmasphere are given in Section 5.

5. Remote Sensing Expectations

In Sections 3 and 4 of this review, the emphasis has been on understanding the physical mechanisms responsible for the production of the UV airglow and an assessment of the accuracy and precision of that knowledge. The present status of understanding of the airglow has been reached largely by pursuing what is known in the vernacular as 'forward modelling'. That is, one proceeds with an *ab initio* model to compute airglow radiances for comparison with observations, adjusting the model and iterating until agreement is achieved. While uniqueness is often difficult to demonstrate, confidence in conclusions improves as more observations are reproduced by the model. Section 4 has shown that many airglow features can be modelled to well within a factor of two uncertainty and often to better than the 20% or so typically quoted for observational accuracy. In this section, the discussion is turned to the inverse problem of determining atmospheric and inospheric parameters from the UV airglow.

For limited data sets, forward modelling is a reasonable approach. But with large data bases from satellite remote sensing missions, alternatives must be found. Two techniques which have been used are to apply simple inversion procedures to obtain altitude profiles of the emitters, or to use algorithms which relate empirically determined quantities, such as zenith-to-nadir ratios or emission line ratios, to the parameter sought. One of the more successful applications of the first method is to nitric oxide (e.g., Siskind *et al.*, 1989a, b). The γ-band g-factor for solar scattering is well-known (Table VII), and multiple scattering and self-absorption can be neglected. The altitude profile of NO can be obtained by inverting an altitude or limb profile of the radiance and dividing by the

g-factor. However, other cases are not so simple. Even if the radiance profile is free of absorption or multiple scattering, and can be inverted to obtain the volume emission rate, additional modelling is required to extract the concentration if the g-factor originates from photoelectron or photochemical sources. Consequently, algorithms must be employed for the rapid retrieval of parameters from the data. Examples of algorithms for photoelectron g-factors were given by Stewart (1970). When the emission process is more complicated, algorithms can be derived from parameter studies. For example, algorithms for the deduction of ionospheric parameters from the optically thick 834 Å dayglow were given by McCoy *et al.* (1985). Other examples will be noted in the following discussions.

Still another approach is to combine *ab initio* calculations with observations using predictor-corrector methodology (Strickland *et al.*, 1984; Decker *et al.*, 1986, 1988). The model initially calculates atmospheric conditions from first principles, but then compares observed parameters with model results, internally adjusting the unmeasured parameters to fit those observed, in a least-squares sense. The final model output contains values of the unmeasured parameters with uncertainties dictated by the measurements. But in order for this method to be used efficiently with large data bases, synthesized versions of the models or algorithms will probably be required.

A list of remote sensing observables is shown in Table XV. These are mostly gleaned from Section 4; a few are listed which were not discussed. The items are largely self-explanatory. References are provided for recent work on each emission. Additional details can be found in Section 4. The list is much too extensive to present a parameter sensitivity study for each observable. But it is worthwhile exploring possibilities for a limited number of somewhat diverse examples. To this end, a series of model calculations were made of dayglow emissions to be used for remote sensing of (1) the major thermospheric constituents, N_2, O_2, and O, (2) the dominant F-region ion, O^+, and (3) plasmaspheric He^+. For the neutral thermosphere, the radiances of photoelectron-excited O I dayglow lines and three N_2 LBH-bands were calculated for a variety of atmospheric conditions. Two remote sensing strategies were selected for illustration: limb scanning from low Earth orbit (850 km) and full global imaging from high Earth orbit. The two baseline model atmospheres used for illustration throughout the review are used in this section as well. Again, the conditions representing solar min and max are listed in Table VI and the concentrations are shown in Figure 30. In all cases considered in this section, as the atmospheric conditions changed the photoelectron flux was recomputed from first principles.

5.1. N_2, O_2, AND O FROM FUV DAYGLOW; LOW ALTITUDE ORBIT

A systematic study of FUV dayglow lines and bands of O and N_2 was carried out by Meier and Anderson (1983). The focus of their work was to identify the sensitivity of the dayglow to changes in atmopheric composition. This section extends their work to a wider range of observational and atmospheric conditions, using the upgraded photoelectron model described earlier in this review.

TABLE XV

Some UV remote sensing observables

Objective	Day/night	Approach	References
Neutral composition			
N_2	D	LBH, 2 PG AP[a], EP[b]	1
O_2	D	N_2 LBH absorption LR[c]	2, 3
	N	O I 1356 + 6300	4, 5
O	D	1304, 1356 AP, LR	3
		1641/1304 LR	6
		N_2 VK quenching, LR with 2 PG	Table VIII
		O_2 Herzberg?	
	N	O_2 Herzberg?	7
		O 2973 (5577)?	8, 9
Total density	D	Rayleigh scattering < 100 km	10
Temperature			
N_2	D	LBH, 2 PG scale height	1, 3, 11
	D	LBH, 2 PG rotational bands	11
O	D	1356 scale height	1, 3
NO	D	scale height	12
		Rotational band LR	27
Various	N	Rotational band LR; scale height	
Various	D, N	Line profiles	
Minor species			
NO	D	γ band AP	7, 12, 13
H	D, N	Lα, Lβ, AP	14, 15
He	D	584 AP	16
N	D	1200, 1493 AP	17
	N	NO: N + O and O from O_2 Herzberg	7
Mg	D	2852	17
Electron (ion) density			
F-region O^+	D	O II 834 AP, EP	18, 19, 20
	N	O + *e*: 911, 1304, 1356 AP	4, 5
F-region height	N	1356/1304 LR	22
Mg^+	D	2798 AP	23, 24
He^+	D, N	304 Å imaging	25, 26
O ionization rate	D	O II 834, 617, 540 ... AP	
N_2 ionization rate	D	N II 2143, 1085, 916 AP	
Photoelectron flux	D	Normalized model to N_2 LBH, 2 PG	3

[a] AP = using altitude profile (or limb scan).
[b] EP = using emission peak.
[c] LR = using line ratio.

References

1. Meier and Anderson (1983)
2. Strickland *et al.* (1983).
3. Meier *et al.* (1985).
4. Chandra *et al.* (1975).
5. Tinsley and Bittencourt (1975).
6. Conway *et al.* (1988).
7. McCoy (1983a, b).
8. Thomas and Young (1981).
9. Sharp and Siskind (1989).
10. Strickland *et al.* (1989).
11. Conway and Christensen (1985).
12. Siskind *et al.* (1989a, b).
13. Cleary (1986).
14. Anderson *et al.* (1987a).
15. Rairden *et al.* (1986).
16. Anderson *et al.* (1979).
17. Anderson and Barth (1971).
18. Anderson and Meier (1985).
19. McCoy *et al.* (1985).
20. Paxton and Strickland (1988).
21. Chakrabarti (1984).
22. Gerard *et al.* (1977).
23. Fesen and Hays (1982); Fesen *et al.* (1983).
24. Mende *et al.* (1985).
25. Weller and Meier (1976).
26. Chakrabarti *et al.* (1982).
27. McCoy (1981).

5.1.1. *Sensitivity to Solar Activity*

The N_2 LBH-band and O I 1356 Å excitation rates (Figure 32) used to compute the vertical column emission rates in Figures 44 and 50 are also the basis for calculating slant column emission rates from an observing altitude of 850 km. That altitude is typical of weather satellites such as TIROS or DMSP. Figure 79 shows three N_2

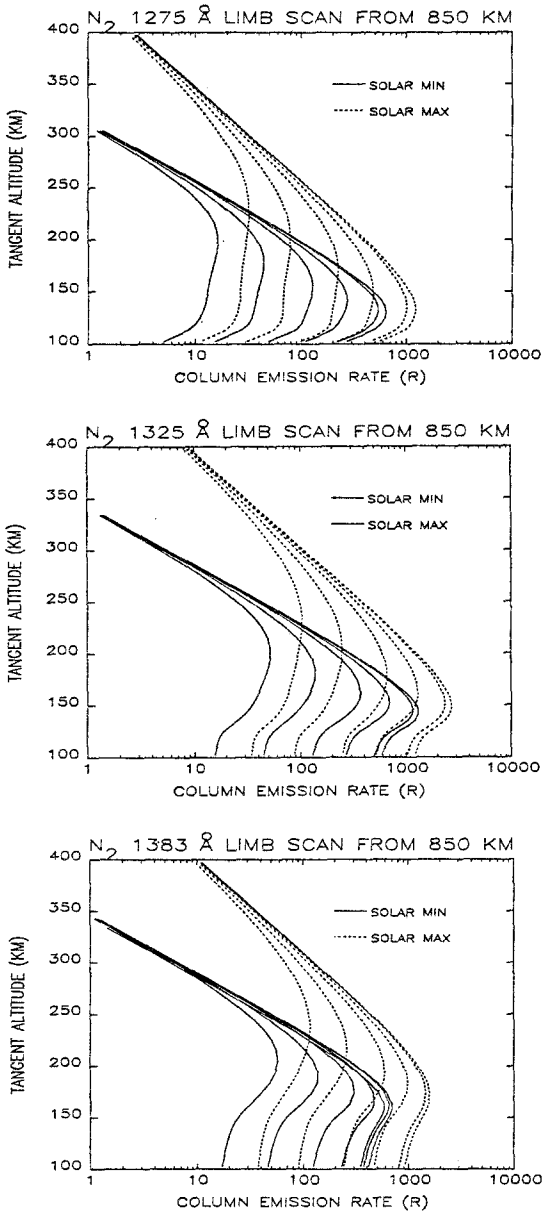

Fig. 79. Limb scans of three N_2 LBH bands for the solar min and max models given in Figure 30. Volume emission rates are given in Figure 32. Vertical column emission rates are given in Figure 44. The solar zenith angles are, from right to left within each panel: 0, 30, 60, 75, 85, 90 deg.

LBH-band slant emission rates vs altitude of the line-of-sight tangent for the 6 solar zenith angles used previously. Both solar min and max conditions are shown. The O I 1356 Å slant emission is shown in Figure 80. It is clear that the topside scale height can be determined from limb scans as well as from direct altitude profiles (Figures 44

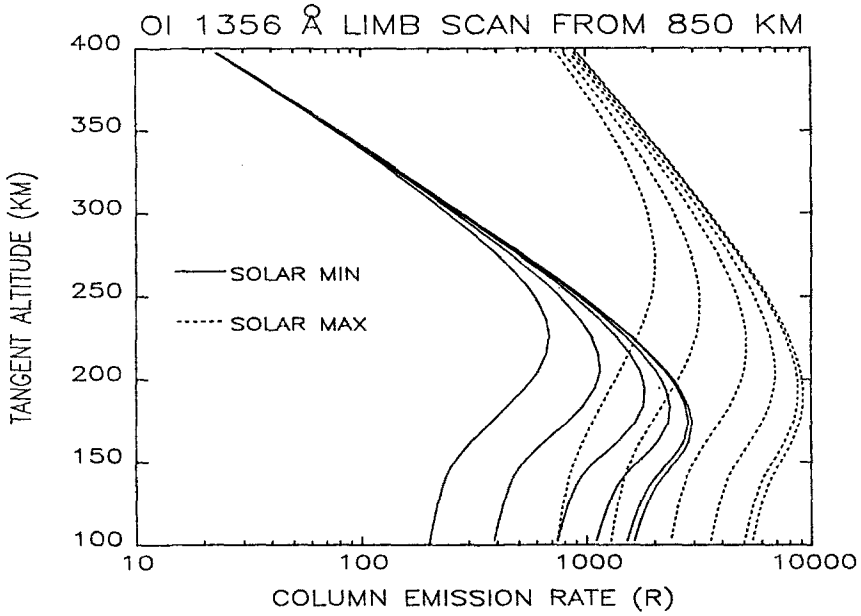

Fig. 80. Limb scans of O I 1356 Å for the models given in Figure 30. Volume and vertical volumn emission rates (including multiple scattering) are given in Figures 32 and 50, respectively. Solar zenith angles are, for right to left: 0, 30, 60, 75, 85, 90 deg.

and 50), and that the exospheric temperature can easily be obtained through the proportionality between the radiance and the N_2 or O concentration (Equation (21)). The shape of the emission peak varies considerably in Figures 79 and 80, primarily reflecting the altitude where the solar ionizing radiation is deposited. A rise in the altitude of peak excitation rate with increasing column concentration to the Sun is seen as both the solar zenith angle and solar activity increase. The emission peak also widens with increasing altitude due to the larger atmospheric scale height. Stewart (1970) and Richards and Torr (1985) have demonstrated the close relationship between the photoelectron flux and the attenuation of EUV sunlight.

The differences in the bottomside profiles of the three LBH bands in Figure 79 are caused by differential absorption by O_2 (Figure 47). This can be seen more clearly in Figure 81, where the ratios of the 1325 and 1383 to 1275 bands are shown. At high altitudes where extinction is negligible, the ratios are 3.2 and 3.8, respectively, as expected from Table IX. The strong sensitivity to O_2 can be seen in the large troughs below 200 km. The minima are smaller at larger solar zenith angles because the volume excitation rates (Figure 32) peak at higher altitudes where O_2 absorption is less. The rise

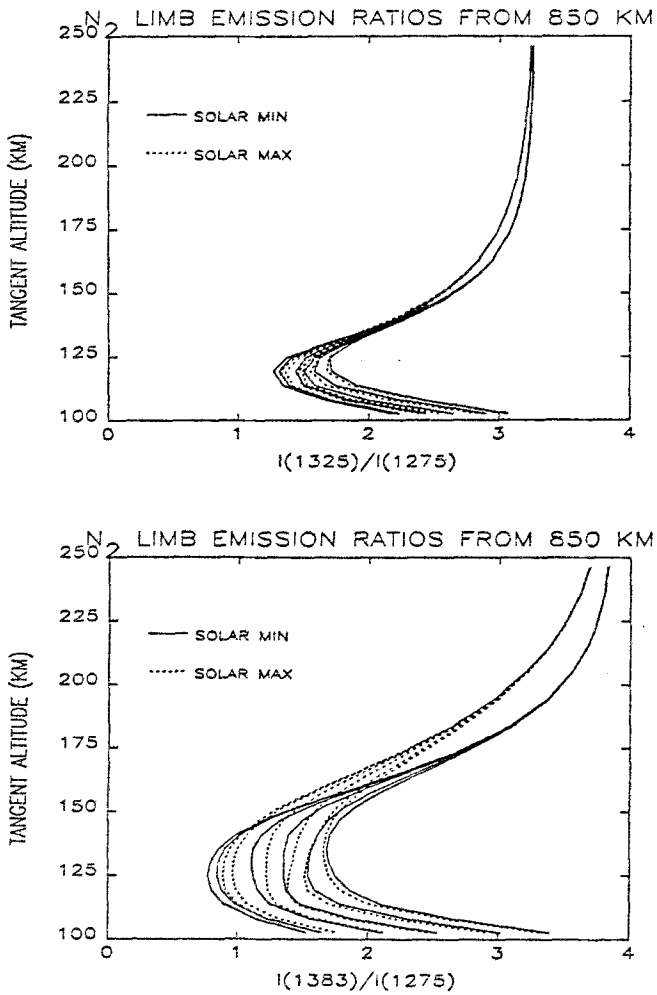

Fig. 81. LBH band ratios for the limb scans given in Figure 79. Solar zenith angles from right to left are 90, 85, 75, 60, 30, and 0 deg.

again in the ratios below 125 km occurs because O_2 absorption (actually the convolution of the volume excitation rate and the O_2 extinction profile) is less important than when viewing through long slant paths at 125 km tangent altitude (foreground emission dominates when viewing in the nadir).

The O/N_2 ratio is a well-known indicator of atmospheric energetics. The 1356/LBH emission rate ratio should provide a good measure of the concentration ratio because the *g*-factors are sensitive to the same photoelectron energy range (Figure 28), and to first order, cancel out in the ratio. Figure 82 shows the ratios for two LBH-bands. Significant changes are seen from solar min to max in both ratios. Again, the bottomside differences are due to O_2 absorption. The sensitivities to the O/N_2 ratio are explored more fully in the next section.

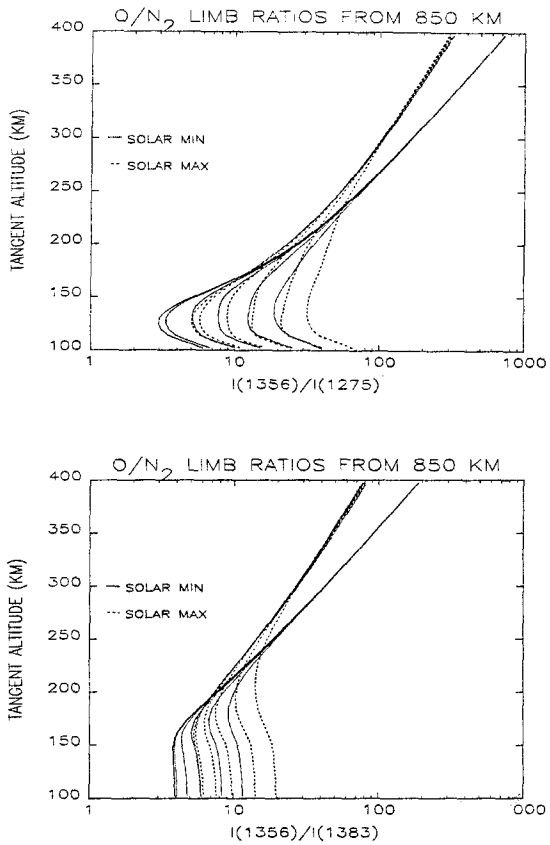

Fig. 82. O I 1356 Å emission divided by N_2 LBH band emissions for the models given in Figures 79 and 80. Solar zenith angles are as in Figure 81.

5.1.2. *Sensitivity to* O_2 *and* O *Composition*

The ability of the FUV airglow to discriminate among atmospheric models with different O_2 and O composition can be assessed by multiplying the concentration at all altitudes by constant factors. While this approach does not realistically simulate physical changes due to solar activity (last section) or geomagnetic activity (next section) it does serve as a simple basis for judging sensitivities. Only the solar max model is used for this demonstration.

As already noted a number of times, differential absorption of N_2 LBH-bands in the O_2 Schumann–Runge continuum (Figure 47) can be used to determine the O_2 abundance. The left panels in Figure 83 show the response of 1325/1275 and 1383/1275 LBH-band ratios to the multiplication and division of the O_2 concentration in Figure 30 by a factor of two. Only two solar zenith angle profiles are shown for clarity. The greater 1383/1275 sensitivity obviously reflects the larger O_2 absorption cross section at 1383 Å.

The right panels in Figure 83 display the effect of scaling the O concentration in the solar max model (keeping the O_2 concentration fixed at the model value). The LBH-

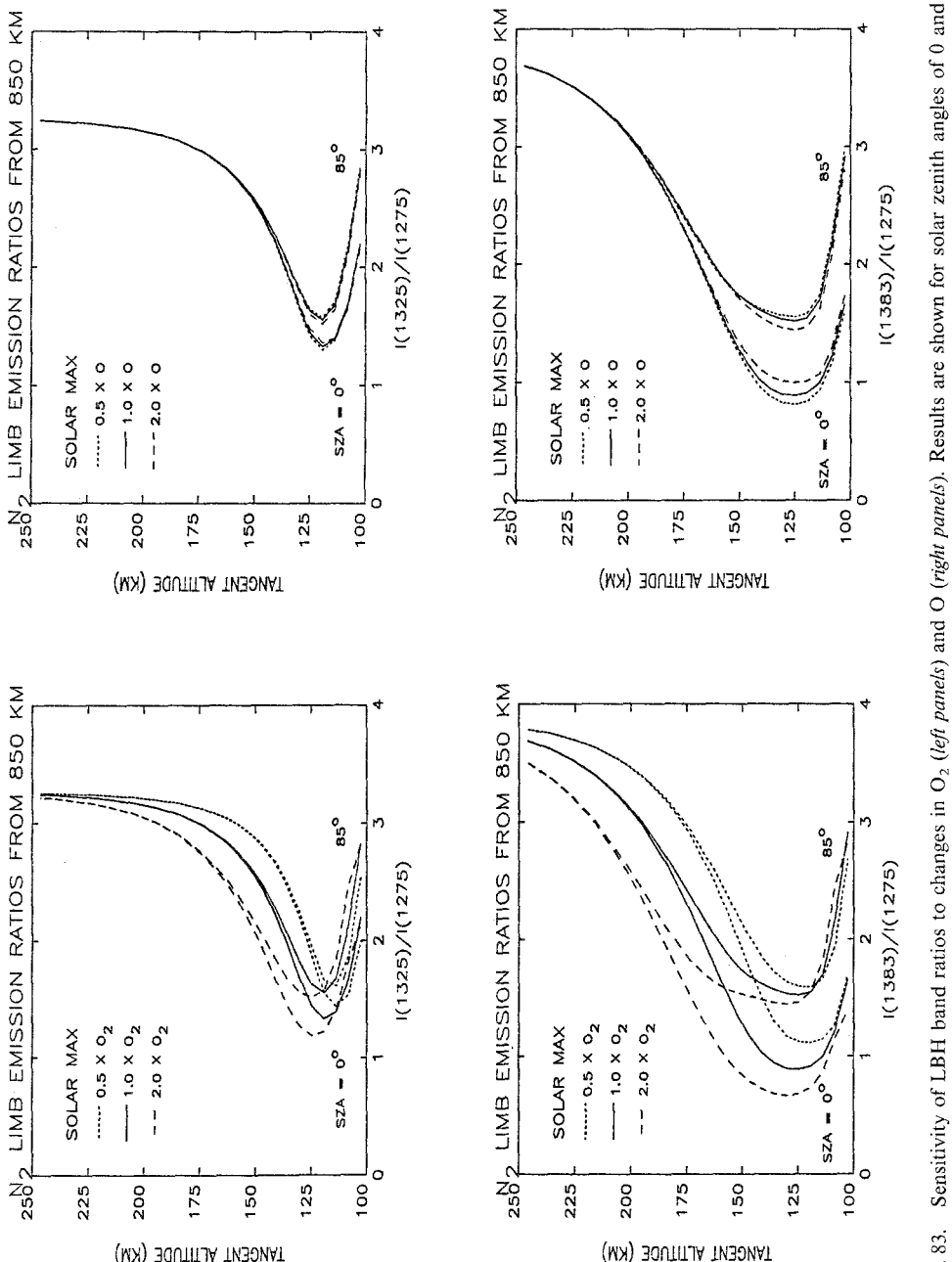

Fig. 83. Sensitivity of LBH band ratios to changes in O_2 (*left panels*) and O (*right panels*). Results are shown for solar zenith angles of 0 and 85 deg.

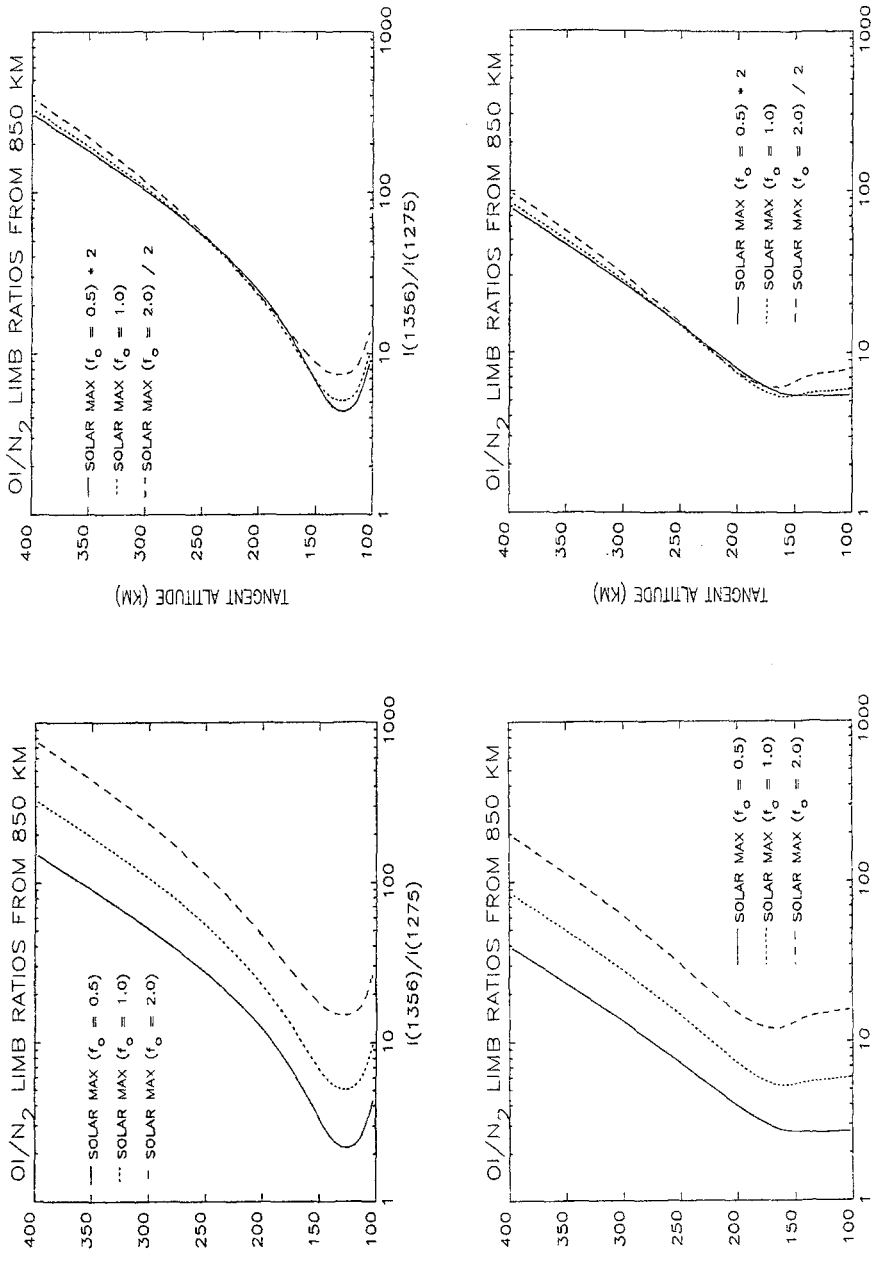

Fig. 84. Sensitivity of ratio of O I 1356 Å to two N_2 LBH bands obtained by dividing and multiplying the O concentration by a factor of 2 (*left panels*). *Right panels*: Show same results, but divided by O multiplier to remove first-order dependence of initial excitation rate on O concentrations.

band ratios are not very sensitive to the magnitude of atomic oxygen (at least within the range considered here).

A much greater response to O variations (relative to N_2) can be seen in the 1356 to LBH-band ratio. The left panels in Figure 84 show the 1356/1275 and 1356/1383 ratios for three O scalings at 0 deg solar zenith angle. The largest change is due to the linear dependence of the initial excitation rate (Equation (38)) on the concentration. This first-order effect can be detrended by dividing the 1356 Å radiances by the scaling factor. The resulting ratios are shown in the right panels of Figure 84. Secondary effects due to modifications of the photoelectron flux and to multiple scattering of 1356 Å radiation (see Figures 32 and 50) are now more evident. These are nonlinear influences and are difficult to disentangle without detailed investigation. Sample calculations show that some but not all of the increases which take place in the ratios at the highest and lowest altitudes when the O concentration is increased are due to multiple scattering. The qualitative differences in curvature from 100 to 150 km between using 1275 and 1383 Å emissions in the denominator of the ratio are due to O_2 absorption.

Yet another way of looking at the impact of changing atomic oxygen in the models is to take the ratio of a given radiance with a scaled O concentration to that with unscaled O. Plotted in the upper panel of Figure 85 are the N_2 1325 Å band radiances (scaling factor, f_0 = 0.5, 1, 2), ratioed to the unscaled radiance (f_0 = 1). The second-order effects noted in the previous figures are now seen more clearly. At low altitudes, there is more production of photoelectrons with lower O due to the reduced attenuation of the solar flux. But at higher altitudes, fewer photoelectrons are produced since O is the dominant species. A much different behavior is seen in O I 1356 Å, shown in the lower panel of Figure 85. Once again, the first-order effect is in the linear scaling of the O concentration in initial production rate of $O(^5P)$. But the combination of the modification of the g-factor by the atmospheric density changes and multiple scattering yield a qualitatively different response than seen in the LBH-band. Calculations show that extinction by O_2 has little bearing on the results displayed in Figure 85.

5.1.3. *Sensitivity to Geomagnetic Activity*

The response of the N_2 and O I FUV dayglow to geomagnetic activity is examined in this section. Again, the solar max model (Table VI) is used as the baseline. A very large geomagnetic disturbance can be simulated simply by increasing the A_p index in the MSIS-86 model to 200 (as occurred in the storm of early February 1986). Since the high- and mid-latitude thermospheres react significantly differently to localized heating induced by geomagnetic activity, the airglow response was calculated at two locations: the 'standard' 32 deg north in Table VI, and 60 deg north. The solar zenith angle was equated to the latitudes in each case. The relative changes in N_2, O_2, O and temperature as A_p increases from 10 to 200 in the model are shown in the upper two panels of Figure 86. Notice that at mid-latitude (left panel) all concentrations increase above 120 km in response to high A_p and that the molecular concentrations increase relative to atomic oxygen. At high latitude, however, there is substantial depletion of atomic oxygen relative to quiet conditions and the concentration of heavier species increases

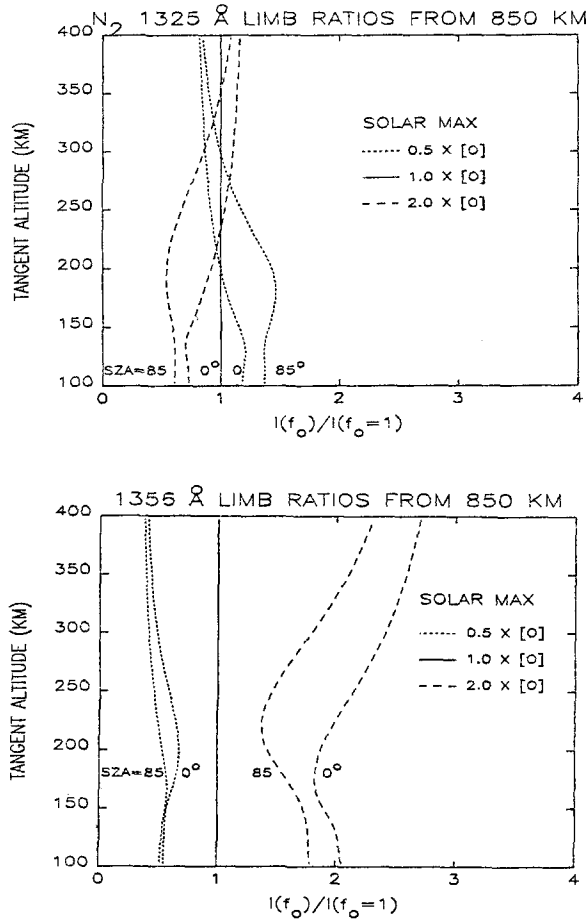

Fig. 85. *Upper panel*: Ratio of N_2 1325 Å band emission rate for various O multipliers to that at $f_0 = 1$. Two solar zenith angles are shown for solar max conditions. *Lower panel*: Same as upper panel, but for O I 1356 Å.

dramatically. This behavior of the MSIS model is also seen in thermospheric global circulation models (e.g., see the papers by Rees and Fuller-Rowell, 1988; Crowley *et al.*, 1989; and their many references to other work). (In fact, ground-based observations during the February 1986 storm indicate even greater depletions in atomic oxygen (Hecht *et al.*, 1989) than predicted by MSIS. The data base used to construct the MSIS model is not extensive at high geomagnetic activity, so it is not surprising that the prediction at $A_p = 200$ would not agree with observations.) Newer work by J. Hecht (private communciation, 1990) shows closer agreement with MSIS if the model is operated in the mode using the 3-hour A_p index.

The center panels in Figure 86 show the change in the 1356/1275 radiance ratio from low to high A_p, and the lower panels show the 1356/1383 ratio. The ratios are qualitatively similar to those in Figure 84. At mid-latitude, as geomagnetic activity increases,

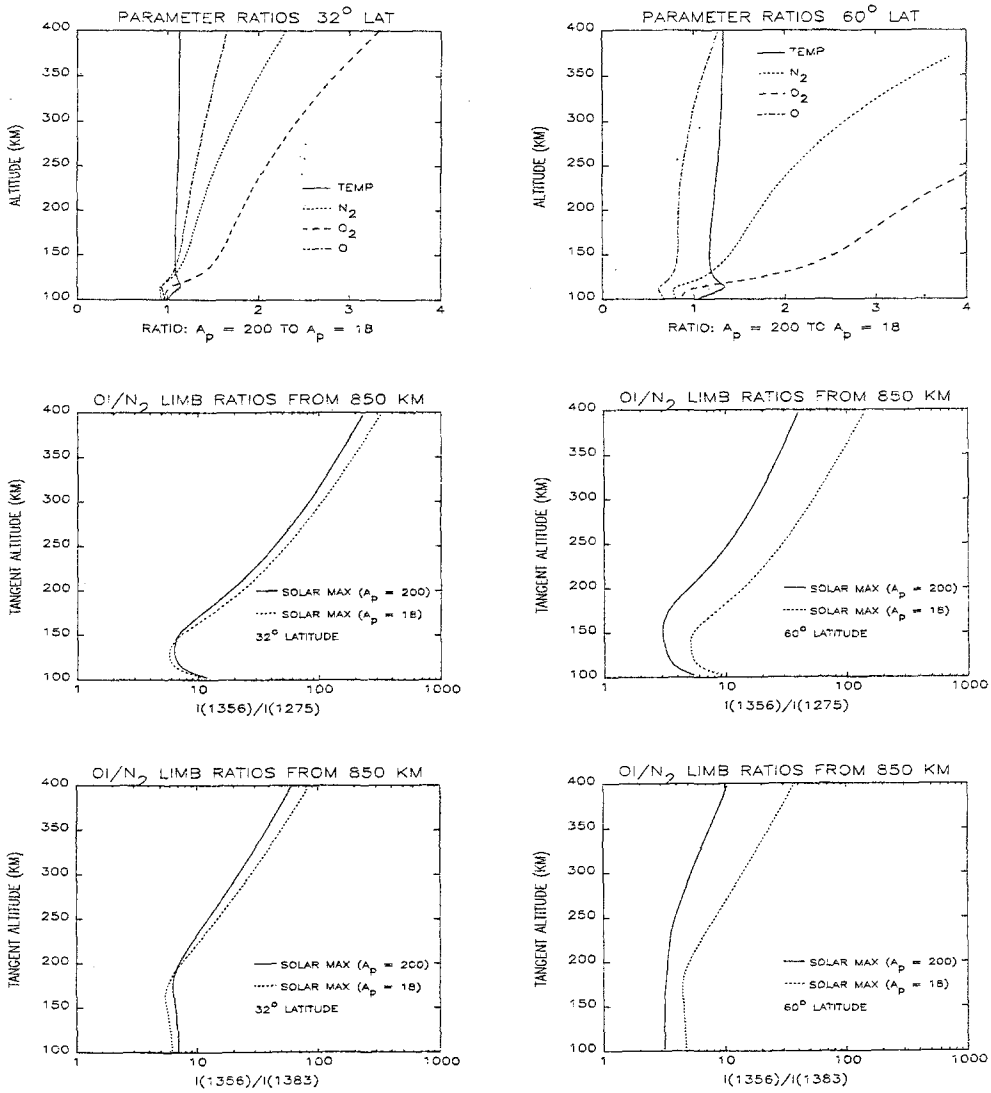

Fig. 86 *Upper panels*: Ratio of atmospheric parameters at $A_p = 200$ to those at $A_p = 18$, shown for latitudes of 32 (*left*) and 60 deg (*right*). Other geophysical conditions at solar max are given in Table VI and the concentrations are shown in Figure 30 for $A_p = 18$. *Center and lower panels*: Ratios of O I 1356 Å to two LBH bands for high (solid) and low (dashed) A_p at 32 (*left*) and 60 deg (*right*) latitude. The solar zenith angle equals the latitude in each case.

the O/N_2 ratio is not altered nearly as much as at high latitude, so the change in the radiance ratio is not nearly as large at 32 deg as at 60 deg. The differences in shape of the O_2 absorption trough below 200 km is partially due to the increase in the molecular oxygen concentration and to the increase in solar zenith angle at high latitude. Clearly, changes in the atmospheric composition during intense geomagnetic storms are easily discernable in the FUV airglow.

5.1.4. O I *Line Ratio Algorithms*

Because the various emission lines of atomic oxygen discussed in Section 4.1.3 have widely different optical depths for resonant scattering in the thermosphere, their ratios contain information about the concentration of O. As the first illustration, the power-law dependence of the ratio of 1641 to 1304 Å radiances on the O concentration found by Meier and Conway (1985) and Conway *et al.* (1988) is investigated. To illustrate this, the linear scaling factors for the O concentration are again employed. Column emission rates were computed for the solar max and min models. The view direction selected was in the nadir from 850 km with an overhead sun. The computations were made as described in Section 4.1.3.2, for linear multipliers of 0.5, 1, and 2 times [O]. The individual column emission rates are shown in Figure 87. At low O concentrations, the solar contribution to the total 1304 Å emission is equal to or greater than the photoelectron component. Note that this is not true for observations made at lower altitudes (Figures 57 and 58) where multiple scattering preferentially amplifies of the photoelectron source. The lower multiple scattering of solar radiation also leads to low 1641 Å emission from that source.

The ratios of 1641 to 1304 are shown in Figure 88, where the power-law behavior is evident. The vertical displacement of the two curves occurs because the initial radiation source is produced at a smaller optical depth from the upper boundary of the atmosphere at solar min. Consequently, there is less multiple scattering, with fewer photons branching through the 1641 Å channel. Additional information on the O concentration could be obtained from limb profiles.

The advantage in using this ratio to obtain an absolute magnitude of the O concentration is that both emissions originate from the same upper state, $O(^3S)$. On the other hand, the solar source has an important contribution to the 1304 Å emission, at least when viewing the thermosphere from above, so the relative strengths of the two sources must be known.

An alternative to using the weak 1641 Å emission is the 1356 to 1304 Å line ratio. These are often measured simultaneously, and both are bright features. Ratios are shown in Figure 88 for the same conditions as in Figures 86 and 87. The variation with O concentration is less than for 1641/1304. There is a displacement in the curves similar to that seen in Figure 87 even though the radiative transport conditions are much different. Of course, the disadvantage in using this ratio is that since the transitions are not from common electronic states, the relative photoelectron excitation cross sections must be known (in addition to accounting for the solar contribution to 1304 Å).

Another alternative ratio to use is 1173/989 (or equivalently 7990/989). Not only do these ratios involve common parent states, but also the only excitation source is photoelectron excitation. So neither the magnitude nor the energy function of the excitation cross section are issues. Unfortunately, the controversy regarding the respective branching ratios discussed in Section 4.1.3.4 must be resolved before these ratios can be used reliably. While this ratio was not computed for the present study, a set of values is available for solar min. Results from a model used by Morrison and Meier (1988) for analysis of data obtained from a rocket experiment on 17 January, 1985 are

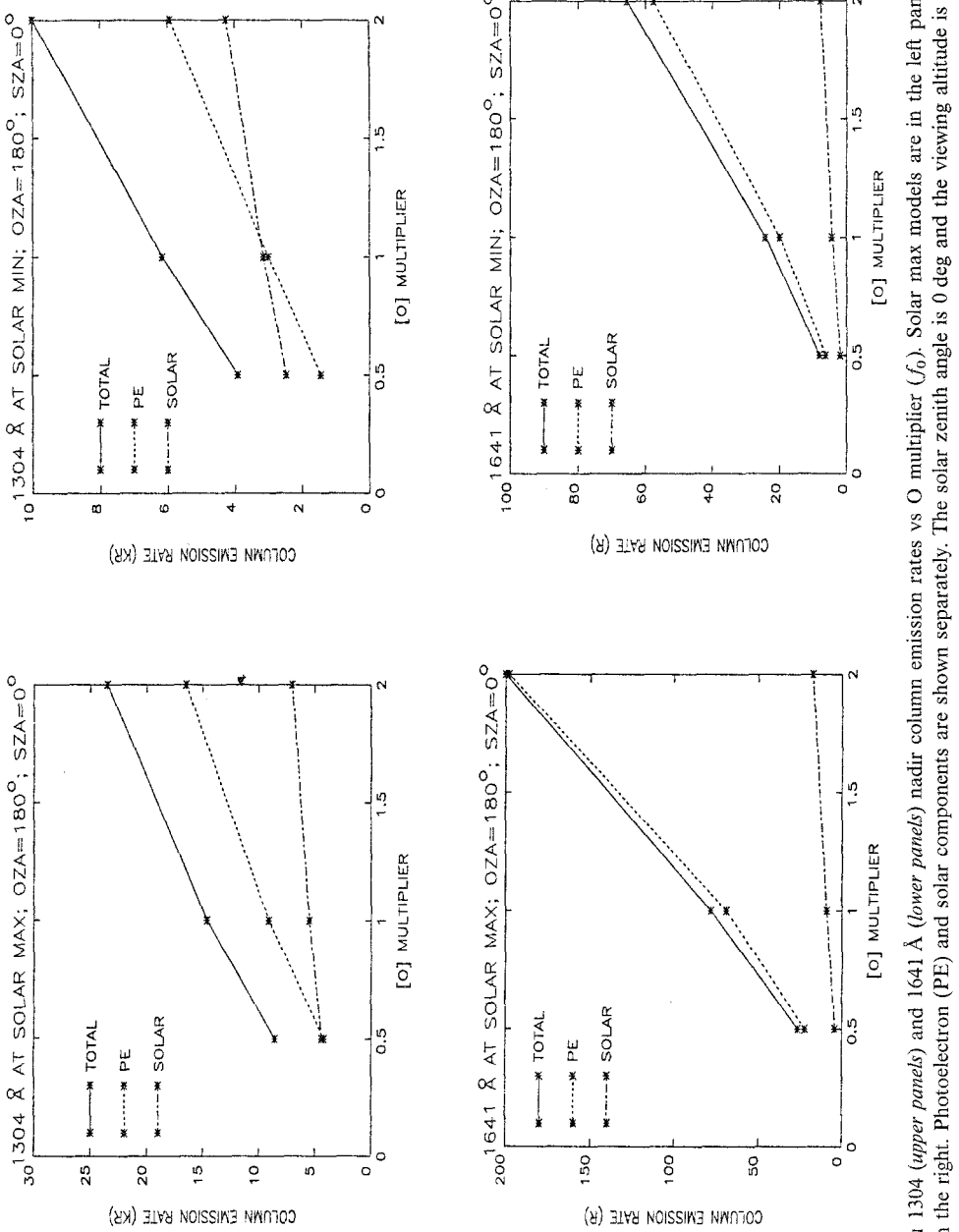

Fig. 87. O I 1304 (*upper panels*) and 1641 Å (*lower panels*) nadir column emission rates vs O multiplier (f_O). Solar max models are in the left panels and solar min on the right. Photoelectron (PE) and solar components are shown separately. The solar zenith angle is 0 deg and the viewing altitude is 850 km.

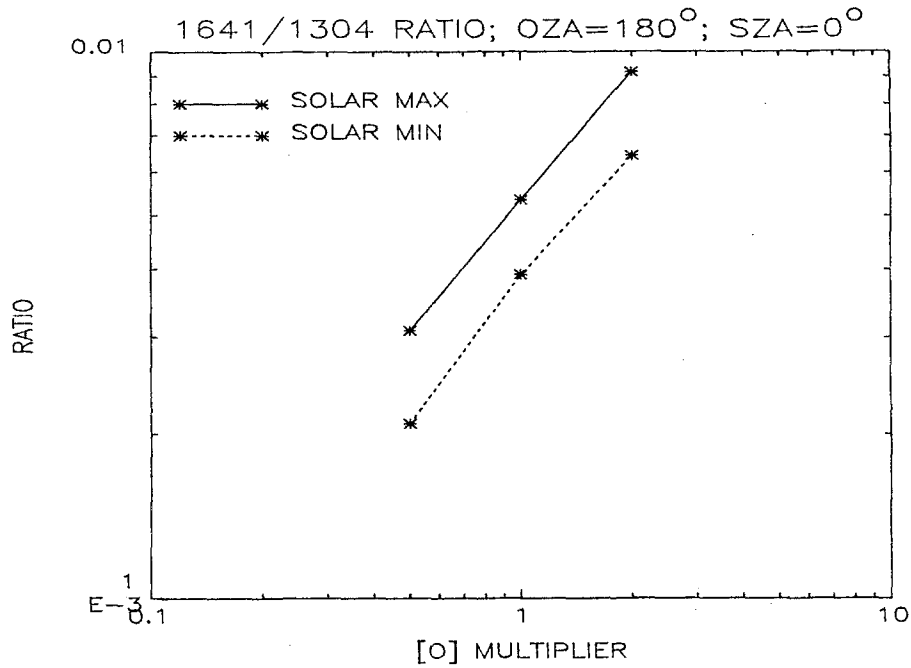

Fig. 88. Ratio of total 1641 to 1304 Å column emission rates from Figure 87 vs O multiplier.

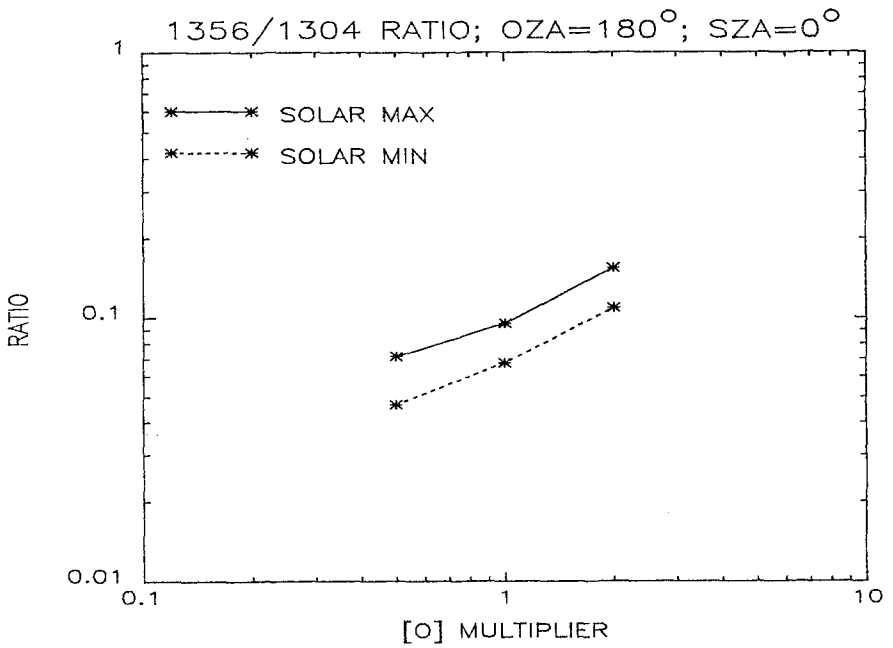

Fig. 89. Ratios of 1356 to total 1304 Å column emission rates vs O multiplier.

shown in Figure 90 (D. Morrison, private communication, 1990). The dependence of this ratio on f_0 is not as strong as 1641/1304, but the solar zenith angle is much larger

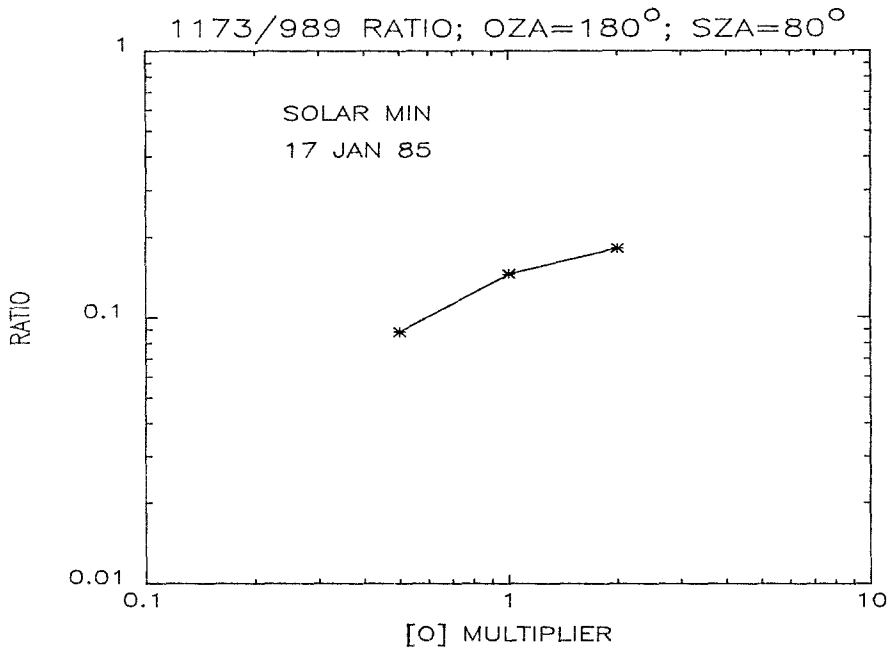

Fig. 90. Ratio of 1173 to 989 Å column emission rates for nadir viewing from 850 km. The conditions are appropriate for the 1985 rocket experiment discussed by Morrison and Meier (1988). The exospheric temperature from the MSIS model was 695 K. The total branching ratio for 1173 + 7990 is 1.7×10^{-4} and 1.5×10^{-4} for 1173 alone.

for the 1985 rocket and the atmospheric conditions are different. Also note that the 7990/989 ratio in a 6 keV aurora nearly tracks the change in O multiplier (Meier, 1982), showing that the branch-to-parent ratio vs f_0 depends on conditions.

5.1.5. *Remote Sensing Strategies for the Dayglow*

It is clear from the parameter studies in Section 5.1 that the functional dependences which exist between the airglow and the thermospheric composition are sufficient to obtain absolute concentrations. However, aside from some of the line ratio relationships, algorithms have not been derived for the rapid retrieval of physical parameters from airglow observations. In this section, one approach towards this end is described.

Ideally, one would like to use observables to obtain the absolute concentration of a species with as little dependence on instrumental calibration as possible. This approach avoids the need for accurate knowledge of the solar EUV irradiance or the photoelectron flux. The best technique so far identified uses line ratios of atomic oxygen. These have good sensitivity to the O abundance and are observationally dependent only on the relative instrumental calibration. The 1173/989 ratio appears to be the best candidate, once the branching ratio issues are resolved. However, the various ratios (Fig-

ures 88–89) also depend on the altitude profile for O and the viewing direction. Fortunately, information about the altitude profile can be obtained from limb scans of the relatively thin O I 1356 Å (Figure 80). So an algorithm which combines 1356 Å limb scans (altitude distribution) and line ratios (absolute value) should in principle give the desired atomic oxygen information. Of course, the exospheric temperature is obtained directly from the topside scale height.

Once the O concentration has been established, N_2 can be found from the O/N_2 ratio using one of the 1356/LBH-band ratios (e.g., Figures 82 or 84). Comparison with precomputed models or iterative fitting procedures could be used. Finally, the O_2 concentration can be acquired from LBH-band ratios (Figure 83).

An alternative technique combines limb scans of N_2 and O I emissions (Figures 79 and 80) which depend on the total atmospheric concentration ($[N_2] + [O] + O_2]$) through the attenuation of the solar irradiance, as well as the N_2, O, and O_2 concentrations individually. In principle, there is enough information (Figures 84 and 85) to solve the nonlinear problem numerically for the thermospheric composition without using O I line ratios. Although this is a much more difficult task, perhaps a predictor-corrector approach (Strickland *et al.*, 1984; Decker *et al.*, 1986, 1987; Meng *et al.*, 1986) would provide satisfactory results for data with high signal-to-noise.

5.2. Daytime O^+ from 834 Å: low altitude orbit

F-region O^+ is illuminated from below with 834 Å line radiation produced by photoionization of O (see Section 4.3.1). The ensuing multiple scattering of photons causes the radiation field to take on the character of the O^+ layer. In a detailed parametric study, McCoy *et al.* (1985) showed that limb scanning of the 834 Å emission rate from observing platforms at 300 and 600 km provides diagnostic information on the altitude distribution and magnitude of O^+. A crucial point is that as the O^+ distribution becomes optically thick to 834 Å radiation, the limb scan profiles have less structure and consequently are a measure of the ion abundance, independent of the magnitude of the radiance.

In this section, new computations of 834 Å limb scans are presented. These differ from those of McCoy *et al.* in that the observing altitude is 850 km, the lower oscillator strength reported by Ho and Henry (1983) is used (see Section 4.3.1), and the upgraded O photoionization cross section of Samson and Pareek (1985) (as tabulated by Conway, 1988) is applied (see also Angel and Samson, 1988). The solar max model (Table VI) again is the basis for computing the photoionization rate of O. Following McCoy *et al.*, a Chapman layer is used to describe the altitude profile of O^+:

$$N[Z] = N_m \exp\left[\frac{1}{2}\left(1 - \frac{Z - Z_m}{H} - \exp\left[-\frac{(Z - Z_m)}{H}\right]\right)\right],$$

where N_m is the peak concentration at altitude Z_m and H is the O scale height. The sensitivity of 834 Å limb scans to changes in each of these is presented next. Variations in individual components of the triplet are also discussed.

The dependence of the slant column emission rate on the altitude of the O^+ peak is shown in Figure 91. N_m and H are fixed at 10^6 cm^{-3} and 60 km, respectively. The

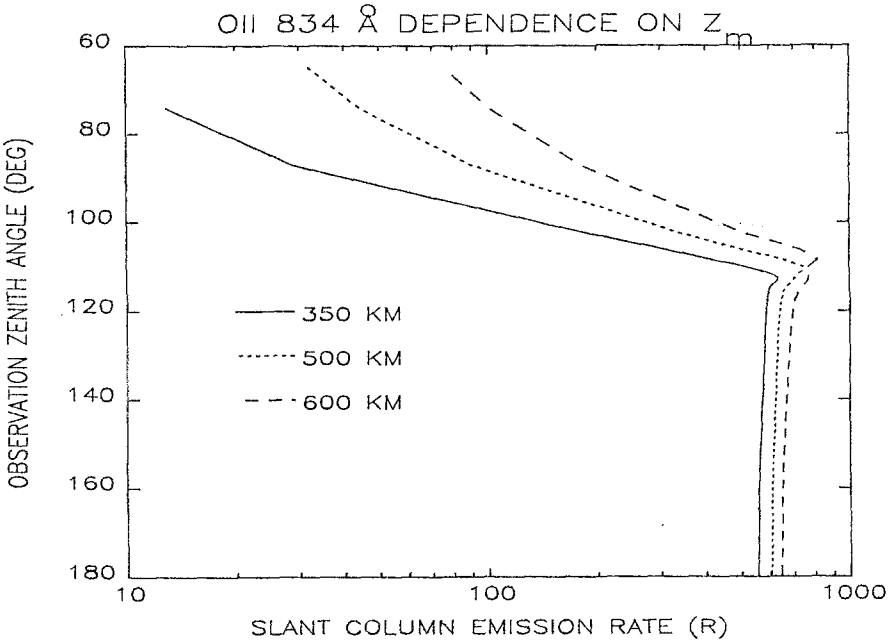

Fig. 91. OII 834 Å column emission rate vs OZA for three values of Z_m. H and N_m are 60 km and 10^6 cm^{-3}, respectively. The solar max model was used to calculate the initial excitation rate. The viewing altitude is 850 km and the solar zenith angle is 0 deg.

biggest effect is a rise in the brightness of the top side and in the angle of the peak of the emission rate. The latter point is better shown in Figure 92, which expands the profiles around their peaks. The emission rate also brightens as the layer moves up in altitude due to decreasing self-absorption. The vertical optical depth in the center (833.33 Å) line of the triplet is 2.5 for all three cases.

Effects of varying the scale height, H are seen in Figure 93, where N_m and Z_m are fixed at 10^6 cm^{-3} and 350 km, respectively. It is obvious that the topside expands when H is larger. But for downward viewing, the emission is brighter for smaller H. This is because the column abundance (and optical depth) of O^+ is lower and more 834 Å photons from the primary photoionization of O at lower altitudes are transmitted through to 850 km. (The vertical optical depths in the center line are 1.24, 2.5, and 3.6 for H = 30, 60, and 90 km, respectively.) The limb brightening is larger for H = 30 km, again because of the lower opacity.

The 834 Å dependence on N_m is shown in Figure 94, keeping Z_m and H fixed at 350 and 60 km, respectively. As N_m increases, the topside emission increases, and the nadir emission and the degree of limb brigtening decreases. These are all due to opacity effects. The vertical optical depths in the 833.33 Å line are 0.25, 2.5, and 25 for N_m = 10^5, 10^6, and 10^7 cm^{-3}, respectively. The zenith-to-nadir ratio is therefore a sensitive measure

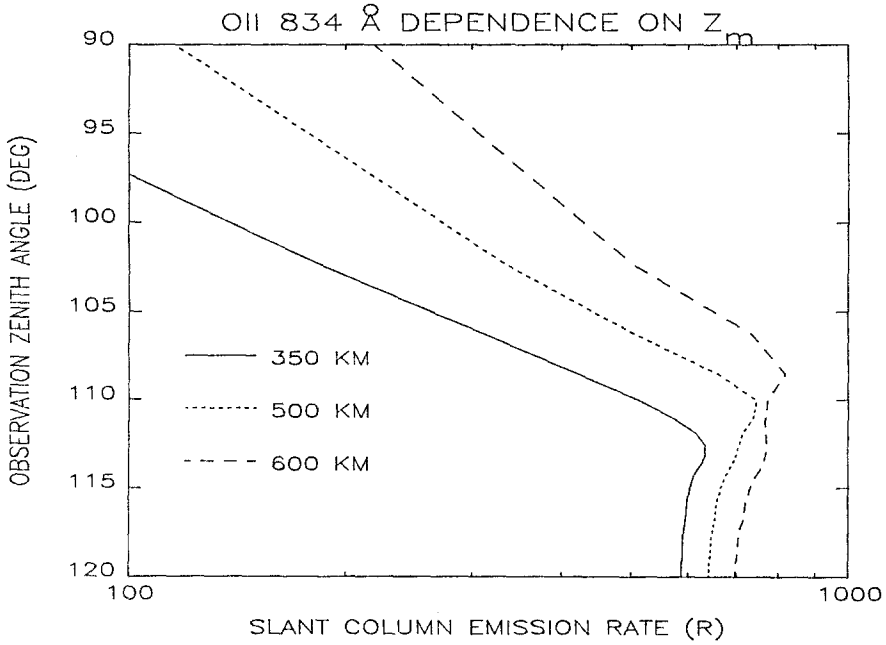

Fig. 92. Same as Figure 91, but with expanded scales. The inflection in the 600 km is real and is due to the separation in altitude of the *F* region and the low altitude photoionization source.

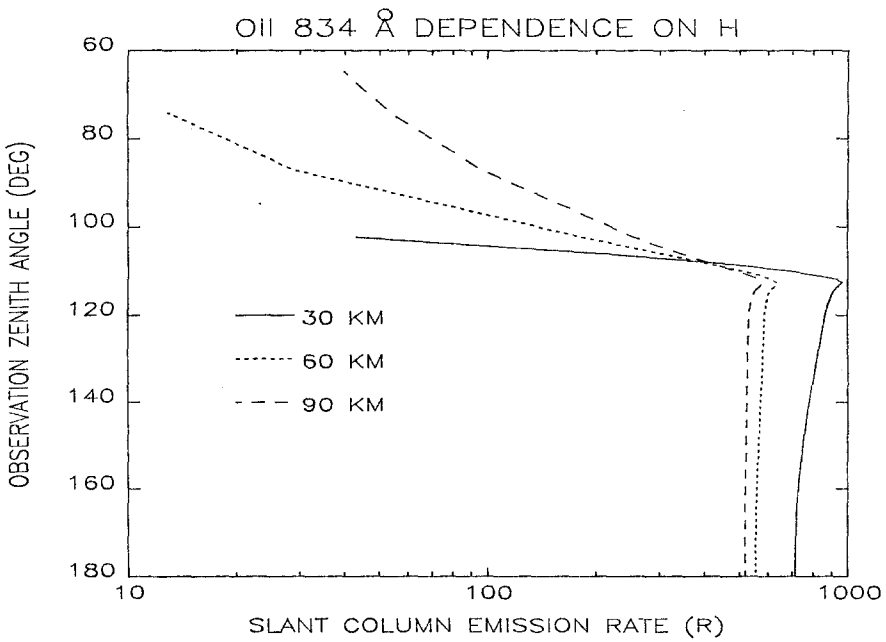

Fig. 93. O II 834 Å column emission rate vs OZA for three values of *H*. Z_m and N_m are 350 km and 10^6 cm^{-3}, respectively. See Figure 90 caption.

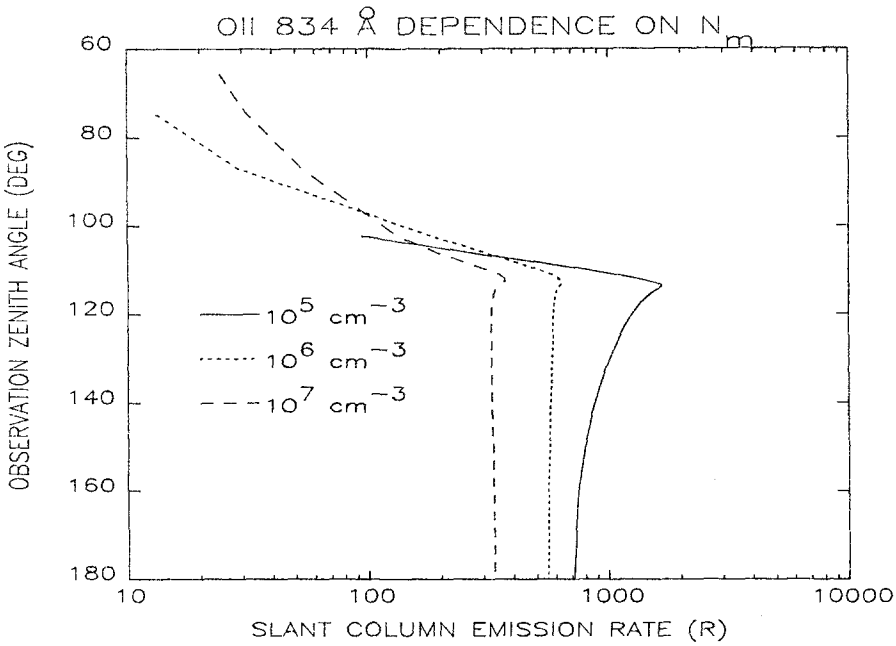

Fig. 94. O II 834 Å column emission rate vs OZA for three values of n_m. Z_m and H are 350 and 60 km, respectively. See Figure 90 caption.

of the absolute concentration of O^+, if Z_m and H have been determined (from applying the models in Figures 91–93; see McCoy *et al.*, 1985).

Additional information about the absolute concentration of O^+ is available from the observations of the individual components of the 834 Å triplet since their resonant optical depths differ by a factor of three (Table V; Anderson and Meier, 1985). For example, Figure 95 shows individual emission rates for the 823.76, 833.33, and 834.46 Å lines (left to right) for the case of Figure 94. The differences in limb brightening (from nadir to limb) can be seen for the thinnest case, but multiple scattering causes saturation of the lines for the thickest case, and the three profiles have similar shapes. However, there are differences among the individual triplet components when viewing above the limb, where the ionosphere becomes optically thin. A better way of seeing these effects is to plot line ratios for the three N_m cases. Ratios of the thickest-to-thinnest lines are shown in Figure 96. Differences in the line ratios provide yet another measure of the O^+ concentration.

McCoy *et al.* (1985) derived several algorithms relating various 834 Å observables to Chapman function parameters. Additional work on 834 Å remote sensing is presented by McCoy and Carruthers (1988), Paxton and Strickland (1988), and Conway *et al.* (1989). (Note that these papers and those references in Section 4.3.1 used old oscillator strengths and N_2 absorption cross sections.) While the 834 Å observational data base for validation of models is sparse, these papers and the above discussion serve to illustrate the considerable potential of this method for ionospheric remote sensing.

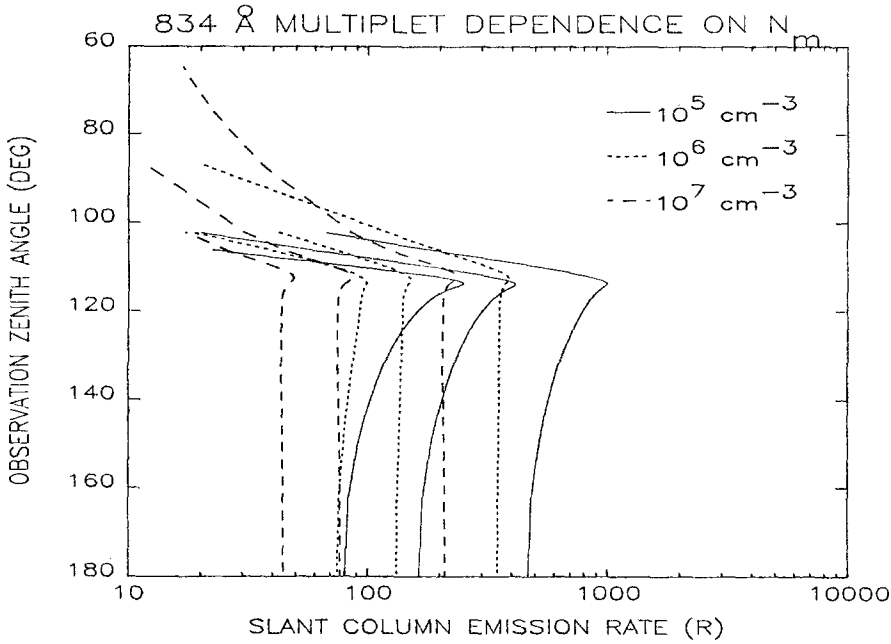

Fig. 95. O II 834 Å column emission rates vs OZA for three values of N_m. Individual components of the triplet, 832.76, 833.33, and 834.46 Å, are shown from left to right for each N_m. Z_m and H are 350 and 60 km, respectively. See Figure 90 caption.

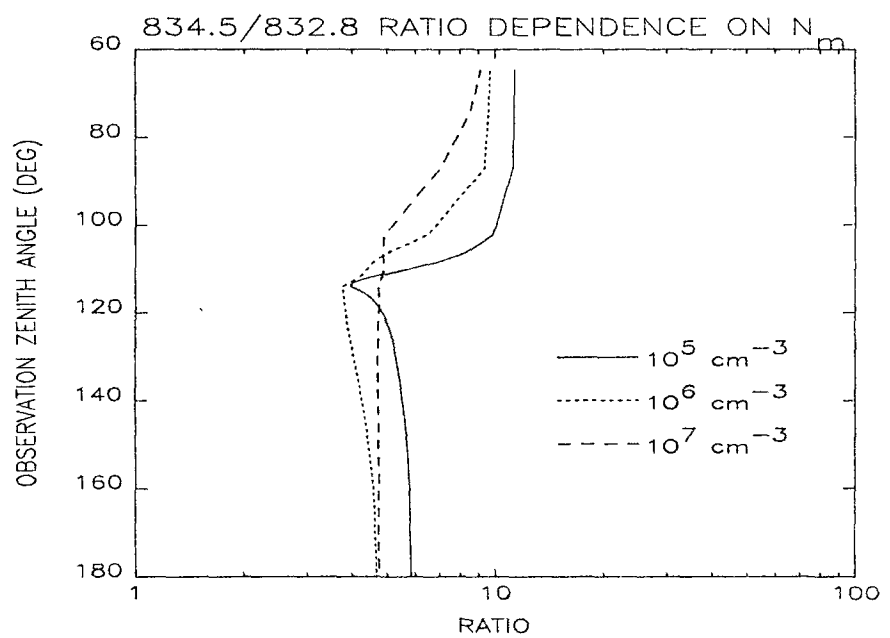

Fig. 96. Ratio of the strongest to the weakest O II 834 Å components for three values of N_m. Z_m and H are 350 and 60 km, respectively. See Figure 90 caption.

5.3. Global Scale Modelling: Images from High Altitude Orbit

Modelling of FUV airglow features on a global scale is computationally intense because of the changing atmospheric and viewing conditions. A technique has been developed by Strickland *et al.* (1991) which allows rapid production of images for generalized viewing conditions on a given date and time using a reasonably fine latitude-longitude-local time grid. The method involves computation of tables of radiance vs observation zenith angle for each emission feature at every model grid point. Computation of the photoionization rate, photoelectron flux, excitation rate, and any absorption or radiative transport effects, takes into account the local solar and geophysical conditions at the grid point. Then for a chosen observation location, the radiance for all lines-of-sight from the atmosphere accessible to the observer is found via table lookup and interpolation. Details are given by Strickland *et al.*

Applications of the technique are described by Paxton *et al.* (1990). Some of the results produced by Paxton *et al.* are presented in Section 5.3.1 as examples of monochromatic imaging expectations for the neutral composition of the thermosphere. The model of Strickland *et al.* has not yet incorporated the O I 1304 Å emission because of the large number of lengthy Monte-Carlo computations necessary. The broad-band images obtained from Apollo 16 or DE-1 (Section 2.4 and Figures 25 and 26) require the 1304 Å radiance for quantitative interpretation.

The second example of global imaging is the He II 304 Å emission from the plasmasphere. This is topic of Section 5.3.2.

5.3.1. *Global Images of* N_2 *and* O *Emissions*

In this section, the global response of the thermosphere to an intense geomagnetic storm is investigated, following the work of Paxton *et al.* (1991). The same set of conditions as for the limb scan analysis of Section 5.1.3 were used: solar max model with A_p = 18 and 200. For all of the images displayed here, the subsolar location is at 0 deg latitude and 0 deg longitude, and the observer is located at an altitude of 10 000 km and at 30 deg latitude and 30 deg longitude.

For orientation, the O and N_2 number densities at 150 km and their ratios are shown in Figure 97 for low geomagnetic conditions (A_p = 18). The O/N_2 ratio is higher in the morning in response to the lower temperature there. Figure 98 shows the same density images, but for high geomagnetic activity (A_p = 200). Comparison of the two figures shows the high latitude depletions in O and enhancements in N_2 at 150 km which occur during intense heating (see Figure 86). The increase in O at lower latitudes under storm conditions is also evident. These responses to high A_p are clearly seen in the O/N_2 ratio, as well.

Monochromatic global images of O I 1356 and N_2 LBH 1383 Å emissions are shown in the left and center panels of Figure 99, and their ratios in the right panel, for low A_p. Strong limb brightening is seen, especially to the lower left in the direction of the subsolar location. The dotted lines show contours of constant solar zenith angle. The emission rates track these lines, showing symmetry about the subsolar point. However, the images at high A_p, displayed in Figure 100, show substantial departure from this symmetry.

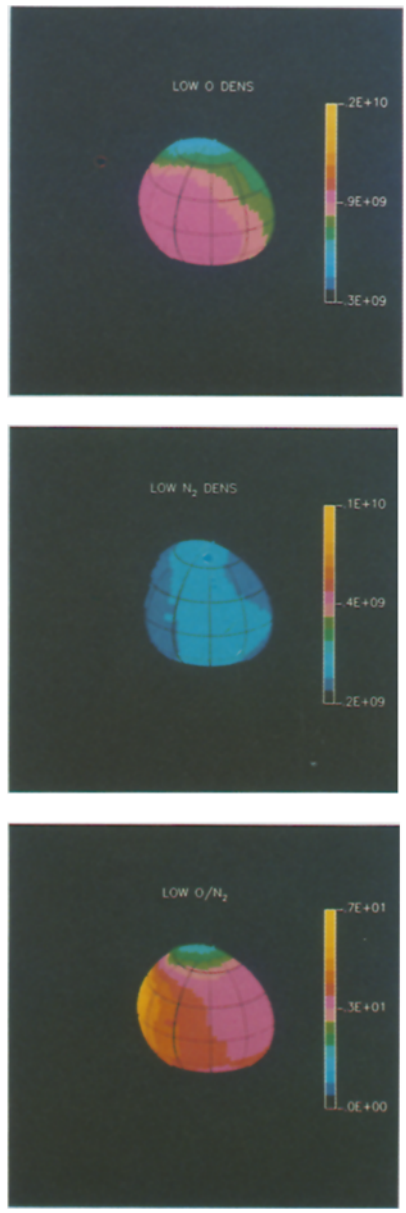

Fig. 97. Global image of the O (*top*) and N_2 (*center*) concentrations in cm^{-3} at 150 km and the O/N_2 ratio (*bottom*). The MSIS atmospheric model is for solar max (Table VI) conditions, with A_p = 18. The latitude and longitude of the subsolar point are 0 and 0 deg, and 30 and 30 deg for the observer. The altitude of the observer is 10000 km.

Similar departures from symmetry have been seen in DE-1 images (Craven and Frank, 1988). The response to geomagnetic activity is enhanced considerably when viewed in the ratio of 1356/1383. For low A_p, there is little structure in the ratio, except near the

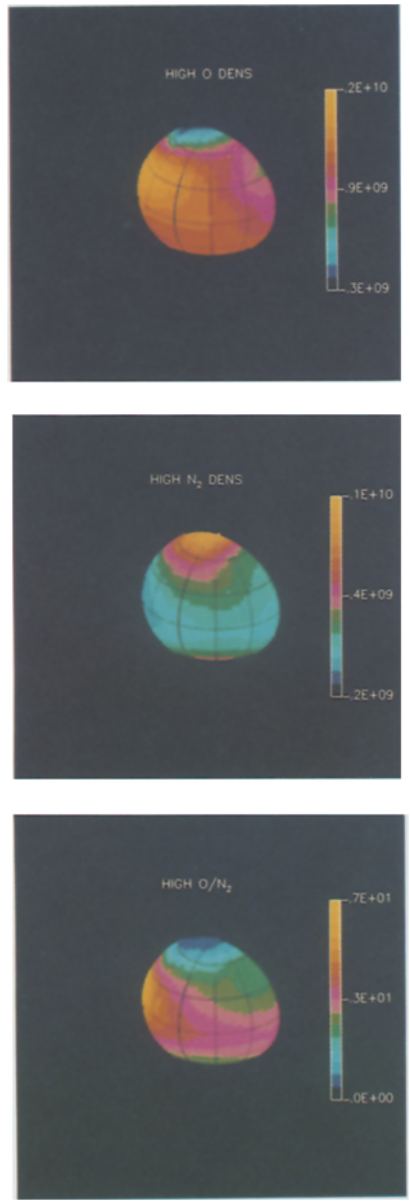

Fig. 98. Same as Figure 97, except that A_p = 200.

terminator, where 1383 decreases more rapidly with increasing solar zenith angle than 1356. As the terminator is approached, the altitude of maximum deposition of solar radiation rises, and the excitation of N_2 declines more rapidly than that of O (see Figure 32); this is also seen at high A_p in Figure 100. Again, the depletions in O relative to N_2 at high latitudes are reflected in the ratios of the irradiances.

Clearly, monochromatic imaging has much potential for studying thermospheric 'weather' on a global scale. Regions of localized energy deposition, as seen in the global circulation model results of Roble *et al.* (1987), Rees and Fuller-Rowell (1988), or Crowley *et al.* (1989) should be identifiable. Recombination radiation at night (Figures 25 and 26) or perhaps O II 834 Å radiation during the day should mimic ionospheric morphology and changes following geophysical or solar activity. Already broad-band imagery has confirmed the value of global remote sensing.

5.3.2. He II 304 Å: *Remote Sensing of the Plasmasphere*

Remote sensing provides a unique method of studying solar (wind)-magnetosphere-ionosphere energetics and dynamics as a global system. So far the only opportunities to do so have come from low altitude rocket and satellite observations. These can be powerful in their own right, especially when making sky scans of the polar (plasmapause) region or when using the Earth's shadow as a differentiator of the height variation of the optically thin emissions. Both *ad hoc* representations and physical models of the plasmaspheric He^+ concentration have successfully reproduced low altitude observations of the 304 Å sky brightness (see references in Sections 2.3 and 4.3.4). These same models can be used to predict what might be seen from high altitude orbit where the entire system is visible.

To illustrate the power of global imaging, the fictitious observing system was placed in a polar, twilight orbit at 10 earth radii and moved from the equator to the pole. Images of the plasmasphere were constructured using the model described by Weller and Meier (1974) and (shown in Figure 23 for low altitude observing). The plasmapause is set at 4.25 earth radii, independent of local time. The helium ion concentration is 400 cm^{-3} at 1000 km and 60 deg magnetic latitude. Guided by mass spectrometer measurements of H^+, the concentration is assumed to decrease by a factor of three from 60 deg to the equator, and to have an exponential altitude dependence with a scale height of 30 000 km. Beyond the plasmapause, the ion concentration decreases rapidly with a Gaussian topside. Below 1000 km, the altitude dependence is described by a representation of low altitude data (Meier and Weller, 1972). The subsolar point is set at (0 deg, 0 deg), geographic latitude and longitude; the solar 304 Å irradiance is 10^{10} cm^{-2} s^{-1} within a Gaussian line of 0.15 Å FWHM. Multiple scattering is ignored, since the He^+ concentration is small.

Four 304 Å images of the plasmasphere are shown in Figure 101, for satellite locations of 0, 30, 60, and 90 deg geographic latitude, from top to bottom. The geographic latitude is set to 90 deg (evening terminator). The top image reflects the dipole character of the plasmasphere, with sunlight incident from the left. The Earth shadow can be seen on the right. While no radiation emanates from within the shadow (no multiple scattering of sunlight into the shadowed plasmasphere), foreground and background radiation is present. The plasmapause is seen clearly to large distances. The slight tilt of the image is due to the offset of the magnetic pole (away from the image plane at 78 deg N latitude and 291 deg longitude) relative to the geographic pole, which is in the plane of the figure. The brightening at high latitudes is due to both the increase of He^+ away from the

equator and the effect of the long path through the plasmasphere edge at low altitudes where the ion concentration is largest. Even though there are no helium ions present over the poles in this model, foreground (mostly over the north polar cap) and background (southern cap) emission provides illumination from this viewing perspective. The characteristic doughnut shape of the plasmasphere is in evidence in the second view from 30 deg latitude. The foreground and background roles are now somewhat reversed. Moving on to 60 deg, the image becomes more circular and the dark polar cap can now be seen. Finally, a polar view is provided in the bottom image. The image is almost symmetric about the solar direction, as expected from the He^+ model used. The dark polar cap is now entirely visible.

These images provide just a glimpse of the accessibility of the plasmasphere from remote sensing. Local time effects and plasma tail extensions would certainly be seen in real images. The well-known decrease in the plasmapause in response to geomagnetic events would easily be visible. Concentration changes as field lines are emptied would be observable.

The development of multilayer thin film optical coatings promises a new wave of efficient photon collectors, capable of detecting weak EUV missions from the plasmasphere and magnetosphere. Both HeII 304 Å and OII 834 Å emission lines are candidates for this new technology. (See references of Section 4.3.4.) The 'magnetoglow' concept of Johnson *et al.* (1971) appears to be within reach.

6. Current and Future Prospects

The trend in terrestrial environmental research has, in recent years, become holistic. Interdisciplinary studies have become focussed toward what has been called 'Earth system science', a global approach. Activities in five principal disciplines, the atmosphere, oceans, lithosphere, biosphere, and solar-terrestrial system, have been coordinated within the framework of the IGBP (International Geosphere-Biosphere Program). Terrestrial research imperatives for the decades from 1995 to 2015 have been defined in a seven volume report from the US National Academy of Sciences, called *Space Science in the Twenty-First Century* (National Academy Press, 1988). A recurring theme throughout the report is the pressing need for a comprehensive understanding of the entire atmosphere system. The relatively poor understanding of global processes in the upper atmosphere is summarized in the Overview volume:

"On Earth, the upper atmosphere/ionosphere acts as the intermediary between the plasma-dominated magnetosphere and the bulk of the neutral atmosphere below. The region is highly complex. Interacting dynamical, chemical, radiative, and electrical variations occur there that couple the magnetosphere and middle atmosphere. To understand how these coupled elements interact to produce the great variability characteristic of the system is one of the major problems in solar-planetary relations. For example, the three-dimensional circulation of the thermosphere changes during and following geomagnetic storms; yet the consequence of the change of circulation on the

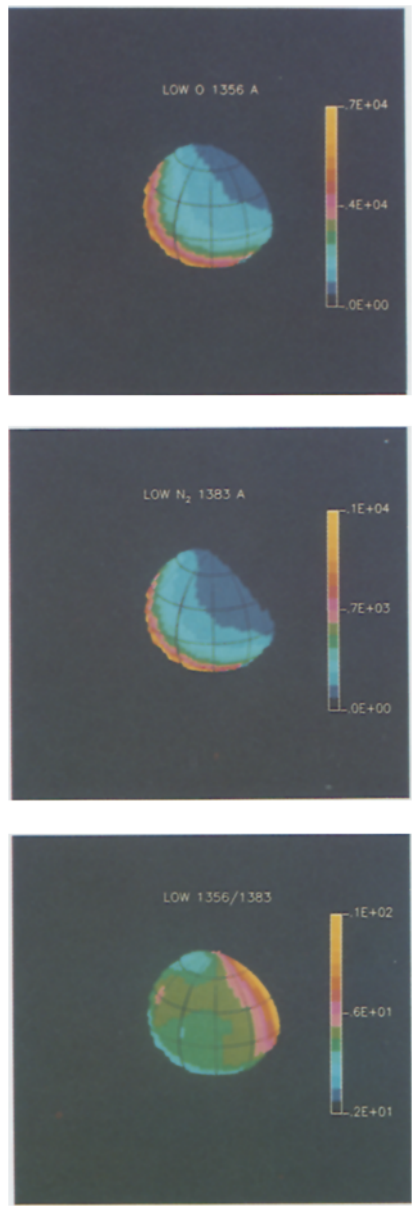

Fig. 99. Global images of O I 1356 Å (*top*) and N_2 1383 Å LBH band (*center*) column emission rates in Rayleighs and the 1356/1383 ratio (*bottom*), for the model in Figure 97 (A_p = 18). Viewing is as in Figure 97.

temperature, density, composition, and electric currents of the region are poorly understood."

The need for comprehensive studies of atmospheric systems is also cited in a National Research Council report entitled *Long-Term Solar-Terrestrial Observations* (National

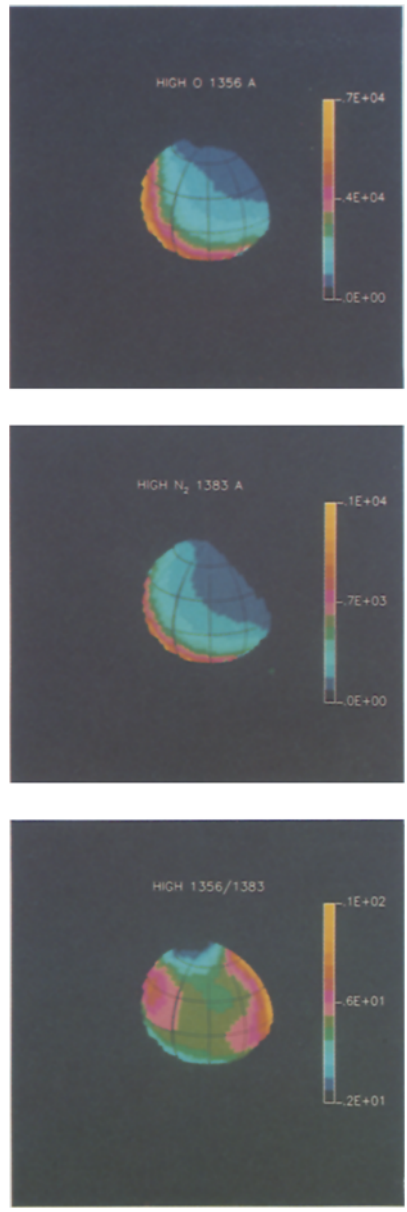

Fig. 100. Same as Figure 99, except that $A_p = 200$.

Academy Press, 1988), as well as in a September 1988 Science Strategy Workshop report to NASA, entitled *Solar-Terrestrial Sciences*.

In spite of the issues raised in these and other reports, no space-based mission to observe and monitor the upper atmosphere and ionosphere has been launched for a decade. Nor are the prospects particularly good. Although the Upper Atmospheric Research Satellite (UARS) is a remote sensing mission, it will not observe routinely above about 110 km. The next generation global measurements program, the Earth

Observing System (EOS), relies heavily on remote sensing, but again, does not include significant measurements of the upper atmosphere/ionosphere. A review of Earth System Science prepared by the Earth System Sciences Committe of the NASA Advisory Council in May 1986, shows little research in this area from space-based platforms until perhaps the end of the 1990's. Only the ground-based NSF CEDAR (Coupling, Energetics, and Dynamics of Atmospheric Regions) Program addresses the research issues in a focussed manner. While the U.S. Air Force Air Weather Service is moving toward a program of space weather monitoring, its focus is on operational needs, rather than on basic research. Clearly, space-based observing of the mesosphere, thermosphere, and ionosphere has fallen through the crack between the magnetosphere and the lower atmosphere in the US space program. Ironically, at the same time, evidence is accumulating that the interactions between the lower atmosphere and upper atmosphere are much more significant than previously thought. For example, an unexpected correlation between the QBO (Quasi-Biennial Oscillation) in equatorial stratospheric winds and solar-activity in the lower atmosphere has been discovered (Chanin *et al.*, 1989); carbon dioxide and methane production may actually modify the structure of the mesosphere and thermosphere (Roble and Dickinson, 1989).

While there is no coordinated space-based program in mesosphere/thermosphere/ionosphere research currently underway, there are a few UV remote sensing activities planned for satellite missions. Those which have been manifested for flight at the time of this writing are listed in Table XVI. Instrument details are given in Table XVII. While

TABLE XVI

Upcoming UV missions

Name	PI	Flight date	Carrier
UVLIM	R. R. Conway (NRL)	April, 1991	Shuttle
HUP	R. E. Huffman (GL)	April, 1991	Shuttle
FUV CAM	G. R. Carruthers	April, 1991	Shuttle
ISO	M. R. Torr (NASA/MSFC)	March, 1992	Shuttle/Atlas 1
RAIDS	R. P. McCoy (NRL)	October, 1992	TIROS-J
UVI	M. R. Torr (NASA/MSFC)	June, 1993	ISTP
MAHRSI	R. R. Conway (NRL)	January, 1994	Shuttle/SPAS

shuttle missions do not provide the long-term data bases needed for synoptic studies, they are included because of their global coverage. A brief description of the scientific objectives of each mission follows.

UVLIM

The Ultraviolet Limb Imager (UVLIM) is a set of two spectrographs designed to observe the limb of the ionosphere and thermosphere in the EUV and FUV (Conway *et al.*, 1989). The UVLIM will fly on the Shuttle as a Hitchhiker payload. The instrument will observe the full range of species which emit between 580 and 1800 Å. The principal objectives are to determine the composition of the atmosphere and ionosphere, with

TABLE XVII

UV flight instrumentation

Payload	Instrument	Type[a]	Wavelength range (Å)	Resolution (Å)	Field of view (deg)
UVLIM	EUV	WS	570–1080	5	0.1 × 4.2
	FUV	EFS	1150–1650	4	0.05 × 4.0
HUP	FUV	EFS	1100–1800	5	0.047 × 1.45
FUV CAM	FUV 1	ESC	1100–1600	250–300	20/3′ pixel
	FUV 2	ESC	1250–2000	250–600	20/3′ pixel
ISO	1	CTS	3800–8400	5	0.65
	2	CTS	2100–4300	2.5	0.65
	3	CTS	3070–3113	0.35	0.65
	4	CTS	990–2350	1.5	0.65
	5	CTS	220–1240	5	0.65
RAIDS	EUV	WS	500–1100	12	0.1 × 2.6
	FUV	WS	1300–1700	8	0.1 × 4
	MUV	EFS	1900–3200	11	0.1 × 2.1
	NUV	EFS	2950–4000	9	0.1 × 2.1
	NIR	EFS	7250–8700	7	0.1 × 2.1
	5890	P	5890	20	0.4 × 2.1
	6300	P	6300	20	0.2 × 2.1
	7774	P	7774	20	0.2 × 2.1
UVI	Camera	Imaging	1216	TBD	8
		(Filters)	1304, 1356	TBD	8
			1400–1600	TBD	8
			1600–1800	TBD	8
			1456	TBD	8
			2150	TBD	8
MAHRSI	MUV	CTS	1980–3100	0.1	0.01 × 1.15

[a] WS: Wadsworth spectrograph.
EFS: Ebert–Fastie spectrometer.
CTS: Czerny–Turner spectrograph.
P: photometer.
ESC: electrographic Schmidt camera.

special attention to the O^+ emissions. The global and diurnal variations of the atmosphere will be characterized for a number of orbits at an inclination of 57 deg. The vertical structure will be observed by maneuvering the orbiter to scan the instrumental fields-of-view through the local horizon.

HUP

The Horizon Ultraviolet (HUP) spectrometer is planned for flight on the shuttle in April 1991. The purpose of the mission is to obtain high spatial resolution FUV scans of the limb (near 1 milliradian). This will allow good altitude profiles of the dayglow and nightglow in this spectral range. Details of the instrumental concept are given by Huffman *et al.* (1981).

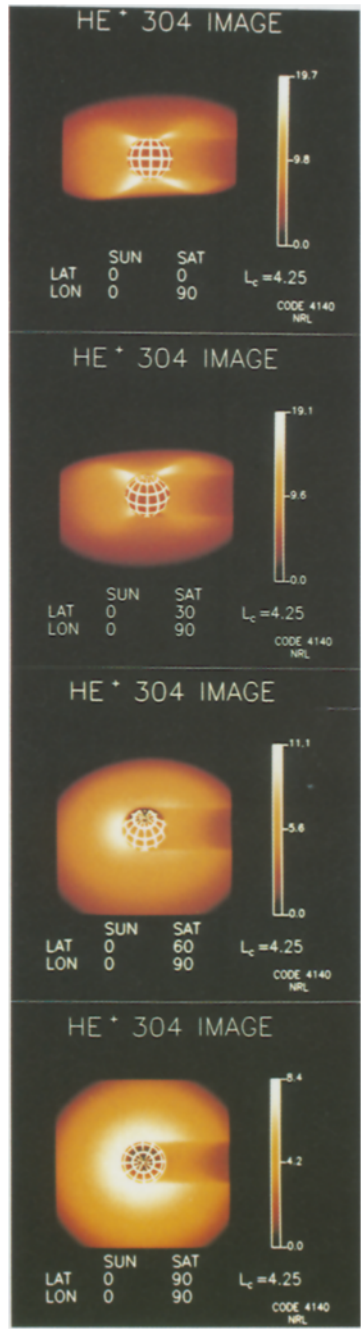

Fig. 101. Images of the Earth's plasmaspheric He II 304 Å emission in Rayleighs. The plasmapause is set at 4.25 earth radii (at the magnetic equator). The Sun is to the left; the subsolar location is at 0 deg geographic latitude and 0 deg longitude. The observer is at 10 earth radii, 90 deg longitude and 0 (*top*), 30 (*upper center*), 60 (*lower center*), and 90 (*bottom*) deg latitude. The Earth's shadow can be seen on the right passing through the plasmasphere. The depletion of helium ions seen at high latitudes is indicative of open magnetic field lines. Other details of the He^+ model and the images are given in the text.

FUVCAM

The Far Ultraviolet Camera payload consists of a two-camera system for obtaining imagery and photometry of natural and artificial sources of FUV radiation, particularly focusing on faint, diffuse sources such as the nightglow, diffuse nebulae and galactic background. The observation plan is to survey various sources, including the tropical ionospheric arcs, using wide field coverage with moderate spatial and spectral resolution. The instruments are located on a dedicated pointing platform with a fine stabilization system for long exposures on celestial targets, and a low light level television camera for pointing verification. A description of the cameras is given by Carruthers (1986).

ISO

The Imaging Spectrometric Observatory (ISO) is a group of five spectrographs planned for flight on the Atlas 1 Shuttle mission. The primary scientific objectives are: (1) studies of photochemical-dynamical coupling of the lower thermosphere and mesosphere; (2) studies of the effects of neutral particle precipitation on the mid- and low-latitude thermosphere; (3) retrieval of thermospheric ion and neutral densities, the neutral temperature and integrated solar EUV and photoelectron fluxes from optical emissions in support of the NSF CEDAR program; and (4) absolute intensity measurements of the solar EUV flux. See Torr *et al.* (1982) for instrument details.

RAIDS

The Remote Atmospheric and Ionospheric Detection System (RAIDS) consists of eight optical sensors for remote sensing of the upper atmosphere and ionosphere. Seven of the instruments reside on a mechanical platform which will scan the limb from 75 to 750 km. The eighth instrument is a non-moving FUV spectrograph which will image simultaneously the limb from 100 to 300 km, and the spectrum from 1300–1700 Å. The scientific objectives are to measure the airglow from 500 to 8700 Å and provide altitude profiles of ion and neutral constituents of the upper atmosphere and ionosphere. RAIDS is a proof-of-concept mission for ionospheric and neutral atmospheric remote sensing. RAIDS will fly on TIROS-J, with a nominal altitude of 850 km, 98 deg inclination, and a Sun-synchronous orbit at 07 : 30 local time. See McCoy *et al.* (1986, 1987) for descriptions of RAIDS.

UVI

The Ultraviolet Imager (UVI) is a filtered camera planned for flight on the International and Terrestrial Physics mission. The primary function of UVI is to obtain coherent global images of auroral features which in turn will provide the energy flux of precipitating particles, and the characteristic energy of the carriers. The UVI will be capable of measurements of these parameters both day and night, since solar blind detectors are employed in the instrument. The data will monitor precipitating particles to be used in three-dimensional ionospheric/thermospheric auroral and airglow models. A discussion of the optical design used by UVI is given by Johnson (1988).

MAHRSI

The Middle Atmosphere High Resolution Spectrographic Instrument (MAHRSI) is designed with the primary objective of measuring OH and NO emissions in the MUV and NUV against the strong Rayleigh scattered continuum. The intention is to observe the limb of the Earth from 40 to 120 km. The radiances due to solar fluorescence will be inverted to obtain altitude profiles of those middle atmosphere species. Other emissions from molecular nitrogen and oxygen in the lower thermosphere will also be observed. At the present time, flight is planned on the CRISTA/SPAS shuttle pallet along with ATLAS-3 in 1994. Discussion of the payload and observing objectives is in a report by Conway *et al.* (1988).

7. Concluding Remarks

This review has: (1) summarized the morphology and variability of the terrestrial ultraviolet airglow from an observational perspective, (2) outlined the basic principles of excitation and emission processes, (3) examined the current understanding of the major emission features, and (4) discussed selected remote sensing applications, exploiting the relationships of the UV airglow to the distribution of upper atmospheric and inospheric constituents. Attention has been drawn to models and algorithms required for the rapid extraction of atmospheric parameters from observations and to critical measurements needed in the future.

In the same way that visible, infrared and microwave measurements are key elements of lower atmosphere remote sensing programs, monochromatic UV imaging and spectroscopy are an essential part of comprehensive studies of the upper atmosphere. As national programs in atmospheric science are being formulated in response to the recommendations of the various studies, it is hoped that the dearth of mesosphere/thermosphere/ionosphere observations will be rectified. UV remote sensing is expected to play a central role in such programs. As stated by H. Friedman in his preface to *Toward an International Geosphere-Biosphere Program: A Study of Global Change* (National Academy Press, 1983). 'Ultraviolet imaging from space has literally shown us the Earth in a new light'.

Acknowledgements

I would like to thank the following for kindly supplying data, results or figures: C. Barth, S. Chakrabarti, A. Christensen, C. Deehr, J. Doering, L. Frank, P. Gentieu, R. Gladstone, J. Jasperse, J. Lean, R. McCoy, D. Morrison, G. Rottman, D. Strickland, B. Tinsley, and M. VanHoosier. I owe much gratitude to J. Lean, S. Chakrabarti, R. Gladstone, and R. Link for reading and suggesting improvements in the manuscript. R. Conway, R. McCoy, and T. Slanger also reviewed sections of the manuscript. S. Thonnard and S. Bailey provided computational support for the global image displays. D. Donaldson and B. Schmitt provided outstanding word processing support. Financial support for this effort came from the Office of Naval Research under

the Atmospheric and Ionospheric Remote Sensing (AIRS) Accelerated Research Initiative. The Defense Meteorological Satellite Program supported the dayglow sensitivity study.

References

Abdou, W. A., Torr, D. G., Richards, P. G., and Torr, M. R.: 1982, 'The Effect on Thermospheric Chemistry of a Resonant Charge Exchange Reaction Involving Vibrationally Excited N_2^+ Ions with Atomic Oxygen', *J. Geophys. Res.* **87**, 6324.

Abreu, V. J., Dalgarno, A., Yee, J. H., Chakrabarti, S., and Solomon, S. C.: 1984, 'The O I 989-Å Tropical Nightglow', *Geophys. Res. Letters* **11**, 569.

Abreu, V. J., Eastes, R. W., Yee, J. H., Solomon, S. C., and Chakrabarti, S.: 1986, 'Ultraviolet Nightglow Production Near the Magnetic Equator by Neutral Particle Production', *J. Geophys. Res.* **91**, 11365.

Ajello, J. M.: 1969, 'Emission Cross Sections of N_2 in the Vacuum UV by Electron Impact with Application to the Aurora', Ph.D. Thesis, University of Colorado, Boulder.

Ajello, J. M. and Franklin, B.: 1985, 'A Study of the Extreme UV Spectrum of O_2 by Electron Impact', *J. Chem. Phys.* **82**, 2519.

Ajello, J. M. and Shemansky, D. E.: 1985, 'A Re-Examination of Important N_2 Cross Sections by Electron Impact with Application to the Dayglow: The Lyman–Birge–Hopfield Band System and N I (119.99 nm)', *J. Geophys. Res.* **90**, 9845.

Ajello, J. M., James, G. K., Franklin, B. O., and Shemansky, D. E.: 1989, 'Medium-Resolution Studies of Extreme Ultraviolet Emission from N_2 by Electron Impact: Vibrational Perturbations and Cross Sections of the $c_4' \, ^1\Sigma_u^+$ and $b' \, ^1\Sigma_u^+$ States', *Phys. Rev.* **A40**, 3524.

Ajello, J. M., Stewart, A. I., Thomas, G. E., and Graps, A.: 1987, 'Solar Cycle Study of Interplanetary Lyman-alpha Variations: Pioneer Venus Orbiter Sky Background Results', *Astrophys. J.* **317**, 964.

Akasofu, S.-I.: 1989, 'Future of Magnetospheric Substorm-Storm Research', *EOS* **70**, 529.

Anderson, D. E., Jr. and Meier, R. R.: 1983, 'Determination of Atmospheric Composition and Temperature from the UV Airglow', *Planetary Space Sci.* **9**, 967.

Anderson, D. E., Jr. and Meier, R. R.: 1985, 'The O II 834 Å Dayglow: A General Model for Excitation Rate and Intensity Calculations', *Planetary Space Sci.* **33**, 1179.

Anderson, D. E., Jr. and Strickland, D. J.: 1988, 'Synthetic Dayglow Spectra and the Rayleigh Scattering Background from the Far UV to the Visible', *SPIE–UV Technology II* **932**.

Anderson, D. E., Jr., Feldman, P. D., Gentieu, E. P., and Meier, R. R.: 1980, 'The UV Dayglow 2, Lyα and Lyβ Emissions and the H Distribution in the Mesosphere and Thermosphere', *Geophys. Res. Letters* **7**, 529.

Anderson, D. E., Jr., Meier, R. R., and Weller, C. S.: 1976, 'Observations of Far and Extreme Ultraviolet O I Emissions in the Tropical Ionosphere', *Planetary Space Sci.* **24**, 945.

Anderson, D. E., Jr., Meier, R. R., and Weller, C. S.: 1979, 'The Seasonal-Latitudinal Variation of Exospheric Helium from He 584 Å Dayglow Emissions', *J. Geophys. Res.* **84**, 1914.

Anderson, D. E., Jr., Paxton,L. J., McCoy, R. P., Meier, R. R., and Chakrabarti, S.: 1987a, 'The Atomic Hydrogen Distribution and Solar Lyman-α Flux Deduced from STP 78-1 EUV Spectrometer Observations', *J. Geophys. Res.* **92**, 8759.

Anderson, D. E., Jr., Meier, R. R., Hodges, R. R., and Tinsley, B. A.: 1987b, 'H Balmer Alpha Intensity Distributions and Line Profiles from Multiple Scattering Theory Using Realistic Geocoronal Models', *J. Geophys. Res.* **92**, 7619.

Anderson, J. G. and Barth, C. A.: 1971, 'Rocket Investigation of the Mg I and Mg II Dayglow', *J. Geophys. Res.* **76**, 3723.

Angel, G. C. and Samson, J. A. R.: 1988, 'Total Photoionization Cross Sections of Atomic Oxygen from Threshold to 44.3 Å', *Phys. Rev.* **A38**, 5578.

Ånger, C. D., Murphree, J. S., Vallance Jones, A., King, R. A., Broadfoot, A. L., Cogger, L. L., Creutzberg, F., Gattinger, R. L., Gustafsson, G., Harris, F. R., Haslett, J. W., Llewellyn, E. J., McConnell, J. C., McEwen, D. J., Richardson, E. H., Rostoker, G., Sandel, B. R., Shepherd, G. G., Venkatesan, D., Wallis, D. D., and Witt, G.: 1987, 'Scientific Results from the Viking Ultraviolet Imager: An Introduction', *Geophys. Res. Letters* **14**, 383.

Barth, C. A.: 1964, 'Rocket Measurement of the Nitric Oxide Dayglow', *J. Geophys. Res.* **69**.

Barth, C. A.: 1965, *Ultraviolet Spectroscopy of Planets*, Jet Propulsion Laboratory Tech. Rept. 32-822, Pasadena, California.

Barth, C. A.: 1966, in A. E. S. Green (ed.), 'The Ultraviolet Spectroscopy of Planets', *The Middle Ultraviolet: Its Science and Technology*, John Wiley and Sons, Inc. New York.

Barth, C. A. and Schaffner, S.: 1970, 'OGO 4 Spectrometer Measurements of the Tropical Ultraviolet Airglow', *J. Geophys. Res.* **75**, 4299.

Barth, C. A. and Steele, R. E.: 1982, 'Rocket Observation of the N II 2143 Dayglow', *Geophys. Res. Letters* **9**, 559.

Barth, C. A., Tobiska, W. K., and Siskind, D. E.: 1988, 'Solar-Terrestrial Coupling: Low-Latitude Thermospheric Nitric Oxide', *Geophys. Res. Letters* **15**, 92.

Bates, D. R.: 1988a, 'Transition Probabilities of the Bands of the Oxygen Systems of the Nightglow', *Planetary Space Sci.* **36**, 869.

Bates, D. R.: 1988b, 'Excitation and Quenching of the Oxygen Bands in the Nightglow', *Planetary Space Sci.* **36**, 875.

Bates, D. R.: 1988c, 'Excitation of 557.7-nm O I Line in Nightglow', *Planetary Space Sci.* **36**, 883.

Bates, D. R.: 1989, 'Oxygen Band System Transition Arrays', *Planetary Space Sci.* **37**, 881.

Bauer, S. J.: 1973, *Physics of Planetary Ionospheres*, Springer-Verlag, New York.

Beiting, E. J. and Feldman, P. D.: 1979, 'Ultraviolet Spectrum of the Aurora (2000–2800 Å), *J. Geophys. Res.* **84**, 1287.

Bertaux, J. L. and Blamont, J. E.: 1973, 'Interpretation of OGO 5 Lyman-Alpha Measurements in the Upper Geocorona', *J. Geophys. Res.* **78**, 80.

Bertaux, J. L., Lallement, R., Kurt, V. G., and Mironova, E. N.: 1985, 'Characteristics of the Local Interstellar Hydrogen Determined from PROGNOZ 5 and 6 Interplanetary Lyman α Line Profile Measurements with a Hydrogen Absorption Cell', *Astron. Astrophys.* **150**, 1.

Blake, A. J., Carver, J. H., and Haddad, G. N.: 1966, 'Photo-Absorption Cross Sections of Molecular Oxygen between 1250 and 23350 Å', *J. Quant. Spectr. Rad. Trans.* **6**, 451.

Borst, W. L. and Zipf, E. C.: 1970, 'Cross Section for Electron-Impact Excitation of the (0, 0) First Negative Band of N_2^+ from Threshold to 3 keV', *Phys. Rev.* **A1**, 834.

Borst, W. L. and Zipf, E. C.: 1971, 'Lifetimes of Metastable CO and N_2 Molecules', *Phys. Rev.* **A3**, 979.

Bowers, C. W., Feldman, P. D., Tennyson, P. D., and Kane, M.: 1987, 'Observations of the O I Ultraviolet Intercombination Emissions in the Terrestrial Dayglow', *J. Geophys. Res.* **92**, 239.

Breig, E. L.: 1987, 'Thermospheric Ion and Neutral Composition and Chemistry', *Rev. Geophys. Space Phys.* **25**, 455.

Breig, E. L., Hanson, W. B., Hoffman, J. H., and Abdou, W. A.: 1983, 'Photochemistry of N_2^+ in the Daytime *F* Region', *J. Geophys. Res.* **88**, 7190.

Breig, E. L., Sanatini, S., and Hanson, W. B.: 1985, 'Thermospheric Hydrogen: The Long-Term Solar Influence', *J. Geophys. Res.* **90**, 5247.

Broadfoot, A. L.: 1971, in B. M. McCormac (ed.), 'Dayglow Nitrogen Band Systems', *The Radiating Atmosphere*, D. Reidel Publ. Co., Dordrecht, Holland.

Broadfoot, A. L. and Kendall, K. R.: 1968, 'The Airglow Spectrum, 3100–10000 Å', *J. Geophys. Res.* **73**, 426.

Brooks, N. H., Rohrlich, D., and Smith, Wm. H.: 1977, 'Transition Probabilities and Absolute Oscillator Strengths for Transitions of C I, O I, and N I Observed in Absorption in H I Regions', *Astrophys. J.* **214**, 328.

Brueckner, G. E. and VanHoosier, M. E.: 1991, 'The Ultraviolet Solar Spectrum 120–400 nm Results from the SUSIM Experiment Onboard Spacelab-2', *J. Geophys. Res.* (to be submitted).

Bruner, E. C., Jr. and Rense, W. A.: 1969, 'Rocket Observations of Profiles of Solar Ultraviolet Emission Lines', *Astrophys. J.* **157**, 417.

Brunger, M. J. and Teubner, P. J. O.: 1990, 'Differential Cross Sections for Electron-Impact Excitation of the Electronic States of N_2', *Phys. Rev.* **A41**, 1413.

Bucsela, E. J. and Sharp, W. E.: 1989, 'The Relative Line Strength and Intensity of the N II 2143 Doublet', *J. Geophys. Res.* **94**, 12069.

Byram, E. T., Chubb, T. A., Friedman, H., and Kupperian, J. E.: 1957, in M. Zlikoff (ed.), 'Far UV Radiation in the Night Sky', *The Threshold of Space*, Pergamon Press, London.

Carruthers, G. R.: 1986, 'The Far UV Cameras (NRL 803) Space Test Program Shuttle Experiment', *SPIE Ultraviolet Technology* **687**, 11.

Carruthers, G. R. and Page, T.: 1972, 'Apollo 16 Far-Ultraviolet Camera/Spectrograph: Earth Observations', *Science* **177**, 788.

Carruthers, G. R. and Page, T.: 1976a, 'Apollo 16 Far-Ultraviolet Spectra of the Terrestrial Airglow', *J. Geophys. Res.* **81**, 1683.

Carruthers, G. R. and Page, T.: 1976b, 'Apollo 16 Far-Ultraviolet Imagery of the Polar Auroras, Tropical Airglow Belts, and General Airglow', *J. Geophys. Res.* **81**, 483.

Carruthers, G. R., Page, T., and Meier, R. R.: 1976, 'Apollo 16 Lyman α Imagery of the Hydrogen Geocorona', *J. Geophys. Res.* **81**, 1664.

Cartwright, D. C.: 1978, 'Vibrational Population of the Excited States of N_2 under Auroral Conditions', *J. Geophys. Res.* **83**, 517.

Cartwright, D. C., Trajmar, S., Chutjian, A., and Williams, W.: 1977, 'Electron Impact Excitation of the Electronic States of N_2. II. Integral Cross Sections at Incident Energies from 10 to 50 eV', *Phys. Rev.* **A16**, 1041.

Cazes, S. and Emerich, C.: 1980, 'Nonpermanent Nighttime H Lyman Alpha Emissions at Low and Middle Latitudes, Detected from the D2A Satellite', *J. Geophys. Res.* **85**, 6049.

Chakrabarti, S.: 1984, 'EUV (800–1400 Å) Observations of the Tropical Airglow', *Geophys. Res. Letters* **6**, 565.

Chakrabarti, S., Kimble, R., and Bowyer, S.: 1984, 'Spectroscopy of the EUV (350–1400 Å) Nightglow', *J. Geophys. Res.* **89**, 5660.

Chakrabarti, S., Paresce, F., Bowyer, S., Chiu, Y. T., and Aikin, A.: 1982, 'Plasmaspheric Helium Ion Distribution from Satellite Observations of He II 304 Å', *Geophys. Res. Letters* **9**, 151.

Chakrabarti, S., Paresce, F., Bowyer, S., Kimble, R., and Kumar, S.: 1983, 'The Extreme Ultraviolet Day Airglow', *J. Geophys. Res.* **88**, 4898.

Chamberlain, J. W.: 1963, 'Planetary Coronae and Atmospheric Evaporation', *Planetary Space Sci.* **11**, 901.

Chamberlain, J. W. and Hunten, D. M.: 1987, *Theory of Planetary Atmospheres,* Academic Pres, Orlando, Fla.

Chandra, S., Reed, E. I., Meier, R. R., Opal, C. B., and Hicks, G. T.: 1975, 'Remote Sensing of the Ionospheric F Layer by Use of O I 6300 Å and O I 1356 Å Observations', *J. Geophys. Res.* **80**, 2327.

Chanin, M. L., Keckhut, P., Hauchecorne, A., and Labitzke, K.: 1989, 'The Solar Activity – Q.B.O. Effect in the Lower Thermosphere', *Ann. Geophys.* **7**, 463.

Cheung, A. S.-C., Yoshino, K., Parkinson, W. H., and Freeman, D. E.: 1986, 'Molecular Spectroscopic Constants of O_2 ($^3\Sigma_u^-$), the Upper State of the Schumann–Runge Bands', *J. Molec. Spectr.* **119**, 1.

Chiu, Y. T., Robinson, R. M., Collin, H. L., Chakrabarti, S., and Gladstone, G. R.: 1990, 'Magnetospheric and Exospheric Imaging in the Extreme Ultraviolet', *Geophys. Res. Letters* **17**, 267.

Chiu, Y. T., Robinson, R. M., Swenson, G. R., Chakrabarti, S., and Evans, D. S.: 1986, 'Concept and Verification of Imaging the Outflow of Ionospheric Ions into the Magnetosphere', *Nature* **322**, 441.

Christensen, A. B. and Cunningham, A. J.: 1978, 'Laboratory Study of O I (7990 Å) Branching Ratio', *J. Geophys. Res.* **83**, 4393.

Christensen, A. B., Eastes, R. W., Feldman, P. D., and Gentieu, E. P.: 1982, 'High-Resolution Dayglow O I (1304 Å) and O I (989 Å) Rocket Observations', *J. Geophys. Res.* **87**, 6317.

Cleary, D. D.: 1986, 'Daytime High-Latitude Rocket Observation of the NO γ, δ, and ε Bands', *J. Geophys. Res.* **91**, 11337.

Cleary, D. D. and Barth, C. A.: 1987, 'The N II 2143 Å Emission in the Dayglow', *J. Geophys. Res.* **92**, 13635.

Cleary, D. D., McCoy, R. P., Harada, L. K., and Chakrabarti, S.: 1991, 'Extreme Ultraviolet Emission Lines of He I and O II in the Spectral Interval (500–900 Å) Observed with the STP 78-1 Satellite', *J. Geophys. Res.* (submitted).

Cleary, D. D., Meier, R. R., Gentieu, E. P., Feldman, P. D., and Christensen, A. B.: 1989, 'An Analysis of the Effects of N_2 Absorption on the O^+ 834 Å Emission from Rocket Observations', *J. Geophys. Res.* **94**, 17281.

Cohen, M. and Dalgarno, A.: 1964, 'An Expansion Method for Calculating Atomic Properties, IV, Transition Probabilities', *Proc. Roy. Soc.* **A280**, 258.

Cohen, L., Feldman, U., and Doschek, G. A.: 1978, 'XUV Spectra of the 1973 June 15 Solar Flare Observed from Skylab III. A List of Spectral Lines from 1000 to 1940 Å', *Astrophys. J. Suppl.* **37**, 393.

Conway, R. R.: 1982, 'Self-Absorption of the N_2 Lyman–Birge–Hopfield Bands in the Far Ultraviolet Dayglow', *J. Geophys. Res.* **87**, 859.

Conway, R. R.: 1983a, 'Multiple Fluorescent Scattering of N_2 Ultraviolet Emissions in the Atmospheres of the Earth and Titan', *J. Geophys. Res.* **88**, 4784.

Conway, R. R.: 1983b, 'Comments on the Interpretation of 3371 Å Filter-Photometer Observations and Its Implications for the AE–E Photoelectron Fluxes', *Planetary Space Sci.* **31**, 1223.

Conway, R. R.: 1988, 'Photoabsorption and Photoionization Cross Sections of O, O_2, and N_2 for Photoelectron Production Calculations: A Compilation of Recent Laboratory Measurements', *NRL Memo. Rept. 6155.*

Conway, R. R. and Christensen, A. C.: 1985, 'The Ultraviolet Dayglow at Solar Maximum 2. Photometer Observations of N_2 Second Positive (0, 0) Band Emission', *J. Geophys. Res.* **90**, 6601.

Conway, R. R., Anderson, D. E., Jr., Budzien, S. A., and Feldman, P. D.: 1989b, 'Ultraviolet Limb Imaging Experiment', *SPIE, Ultraviolet Technology III* **1158**, 2.

Conway, R. R., Meier, R. R., and Huffman, R. E.: 1987, 'The Far Ultraviolet Vehicle Glow on the S3-4 Satellite', *Geophys. Res. Letters* **14**, 628.

Conway, R. R., Meier, R. R., and Huffman, R. E.: 1988, 'Abundance of Atomic Oxygen in the Lower Thermosphere from Satellite Observations of the O I 1641 Å Dayglow', *Planetary Space Sci.* **36**, 963.

Conway, R. R., Prinz, D. K., and Mount, G. H.: 1988, 'Middle Atmosphere High Resolution Spectrograph', *SPIE, UV Technology II* **932**.

Craven, J. D. and Frank, L. A.: 1988, 'A Signature in the UV Dayglow of Modification to the Upper Atmosphere During Auroral Substorms', Paper C1.2, COSPAR XXVII, Espoo, Finland.

Cravens, T. E.: 1977, 'Nitric Oxide Gamma Band Emission Rate Factor', *Planetary Space Sci.* **25**, 369.

Cravens, T. E. and Killeen, T. L.: 1988, 'Longitudinally Asymmetric Transport of Nitric Oxide in the E-Region', *Planetary Space Sci.* **36**, 11.

Cravens, T. E., Gerard, J. C., LeCompte, M., Stewart, A. I., and Rusch, D. W.: 1985, 'The Global Distribution of Nitric Oxide in the Thermosphere as Determined by the Atmosphere Explorer D Satellite', *J. Geophys. Res.* **90**, 9862.

Crowley, G., Emery, B. A., Roble, R. G., Carlson, H. C., Jr., and Knipp, D. J.: 1989, 'Thermosphere Dynamics During September 18–19, 1984, 1, Model Simulations', *J. Geophys. Res.* **94**, 16885.

Dahl, F. and Oddershede, J.: 1986, 'Radiative Lifetime of the "Forbidden" a $^1\Pi_g \leftarrow X\,^1\Sigma_g^+$ Transition of N_2', *Phys. Scripta* **33**, 135.

Dalgarno, A., Victor, G. A., and Hartquist, T. W.: 1981, 'The Auroral 2145 Å Feature', *Geophys. Res. Letters* **8**, 603.

Daniell, R. E., Jr. and Strickland, D. J.: 1986, 'Dependence of Auroral Middle UV Emissions on the Incident Electron Spectrum and Neutral Atmosphere', *J. Geophys. Res.* **91**, 321.

De Souza, A. R., Gousset, G., Touzeau, M., and Tu Khiet: 1985, 'Note on the Determination of the Efficiency of the Reaction $N_2(A^3\Sigma) + O(^3P) \rightarrow N_2 + O(^1S)$', *J. Phys.* **B18**, L661.

Decker, D. T., Daniell, R. E., Jr., Jasperse, J. R., and Strickland, D. J.: 1986, 'Determination of Ionospheric Electron Density Profiles from Satellite UV Emission Measurements', *Proc. SPIE Ultraviolet Technology* **687**, 73.

Decker, D. T., Retterer, J. M., Jasperse, J. R., Anderson, D. N., Eastes, R. W., DelGreco, F. P., Huffman, R. E., and Foster, J. C.: 1988, 'Determination of Daytime Midlatitude Electron Density Profiles from Satellite UV and In-Situ Data', *Proc. SPIE* **932**, 24.

Degen, V.: 1969, 'Vibrational Populations of $O_2(A\,^3\Sigma_u^+)$ and Synthetic Spectra of the Herzberg Bands in the Night Airglow', *J. Geophys. Res.* **74**, 5145.

Degen, V.: 1982, 'Synthetic Spectra for Auroral Studies: The N_2 Vegard–Kaplan Band System', *J. Geophys. Res.* **87**, 10541.

Dick, K. A.: 1970, 'Tentative Identification of Several N_2 $c' - a$ Bands in Auroras', *J. Geophys. Res.* **75**, 5609.

Doering, J. P. and Gulcicek, E. E.: 1989, 'Absolute Differential and Integral Electron Excitation Cross Sections for Atomic Oxygen 8. The $^3P - {}^5S^0$ Transition (1356 Å) from 13.9 to 30 eV', *J. Geophys. Res.* **94**, 2733.

Doering, J. P., Fastie, W. G., and Feldman, P. D.: 1970, 'Photoelectron Excitation of N_2 in the Day Airglow', *J. Geophys. Res.* **75**.

Doering, J. P., Gulcicek, E. E., and Vaughan, S. O.: 1985, 'Electron Impact Measurement of Oscillator Strengths for Dipole-Allowed Transitions of Atomic Oxygen', *J. Geophys. Res.* **90**, 5279.

Donahue, T. M.: 1965, 'Some Considerations Concerning Radiation Transport in the O I 1304 Triplet in the Upper Atmosphere', *Planetary Space Sci.* **13**, 871.

Donahue, T. M. and Fastie, W. G.: 1964, 'Observation and Interpretation of Resonance Scattering of Lyman-α and O I (1300) in the Upper Atmosphere', *Space Res.* **IV**, 304.

Donahue, T. M. and Foderaro, A.: 1955, 'The Effect of Resonance Absorption on the Determination of the Height of Airglow Layers', *J. Geophys. Res.* **60**, 75.

Donahue, T. M. and Kumer, J. B.: 1971, 'An Observation of the Helium I 584 Å Dayglow Radiation Between 400 and 1000 km', *J. Geophys. Res.* **76**, 145.

Donahue, T. M. and Meier, R. R.: 1967, 'Distribution of Sodium in the Daytime Upper Atmosphere as Measured by a Rocket Experiment', *J. Geophys. Res.* **72**, 2803.

Donnelly, R. F. and Pope, J. H.: 1973, *The 1–3000 Å Solar Flux for a Moderate Level of Solar Activity for Use in Modeling the Ionosphere and Upper Atmosphere*, NAOO Tech. Rpt. ERL 276–SEL 25.

Doschek, G. A., Behring, W. E., and Feldman, U.: 1974, 'The Widths of the Solar He I and He II Lines at 584, 537, and 304 Å', *Astrophys. J.* **190**, L141.

Doschek, G. A. and Donahue, T. M.: 1970, 'Transport of Resonance Radiation in Optically Thick Media', *Astrophys. J.* **161**, 737.

Douglas, A. E. and Herzberg, G.: 1951, 'Predissociation and Dissociation of the N_2 Molecule', *Can. J. Phys.* **29**, 294.

Eastes, R. W. and Sharp, W. E.: 1987, 'Rocket-Borne Spectroscopic Measurements in the Ultraviolet Aurora: The Lyman–Birge–Hopfield Bands', *J. Geophys. Res.* **92**, 10095.

Eastes, R. W., Feldman, P. D., Gentieu, E. P., and Christensen, A. B.: 1985, 'The Ultraviolet Dayglow at Solar Maximum. I. FUV Spectroscopy at 3.5 Å Resolution', *J. Geophys. Res.* **90**, 6594.

Erdman, P. W. and Zipf, E. C.: 1983, 'Electron Impact Excitation of O I 7990-Å Multiplet', *J. Geophys. Res.* **88**, 7245.

Erdman, P. W. and Zipf, E. C.: 1986a, 'Electron Impact Excitation of the O I 1614.3 Å Line Emission', *Geophys. Res. Letters* **13**, 506.

Erdman, P. W. and Zipf, E. C.: 1986b, 'Electron Impact Excitation of the O I 1172.6 Å Multiplet', *Planetary Space Sci.* **34**, 1155.

Erdman, P. W. and Zipf, E. C.: 1986c, 'Dissociative Excitation of the $N^+(^5S)$ State by Electron Impact: Excitation Function and Quenching by N_2', *J. Geophys. Res.* **91**, 11345.

Erdman, P. W. and Zipf, E. C.: 1987, 'A Laboratory Measurement of the Doppler Broadened N II λ5005.15 Å Emission Line-Width Produced by Electron Impact Excitation of N_2', *Planetary Space Sci.* **35**, 1471.

Espy, P. J., Erdman, P. W., and Zipf, E. C.: 1979, 'Electron Impact Excitation of the Terrestrial EUV Airglow', *EOS* **60**, 901.

Fahr, H. J. and Smid, T.: 1982, 'The Contribution of Singly Scattered Photons to the Optically Thick Resonance Radiation Field of the Helium Geocorona', *J. Geophys. Res.* **87**, 2487.

Fahr, H. J. and Smid, T.: 1986, 'Spectrophotometric EUV-observations and the Theoretical Modelling of the Geocoronal He I 584/537 Å Radiation Field', *Ann. Geophys.* **4**, 447.

Feldman, P. D. and Gentieu, E. P.: 1982, 'The Ultraviolet Spectrum of an Aurora 530–1520 Å', *J. Geophys. Res.* **87**, 2453.

Feldman, P. D., Anderson, D. E., Jr., Meier, R. R., and Gentieu, E. P.: 1981, 'The Ultraviolet Dayglow, 4, The Spectrum and Excitation of Singly Ionized Oxygen', *J. Geophys. Res.* **86**, 3583.

Fesen, C. and Hays, P. B.: 1982, 'Mg^+ Morphology from Visual Airglow Experiment Observations', *J. Geophys. Res.* **87**, 9217.

Fesen, C., Hays, P. B., and Anderson, D. N.: 1983, 'Theoretical Modeling of Low-Latitude Mg^+', *J. Geophys. Res.* **88**, 3211.

Filippelli, A. R., Chung, S., and Liu, C. C.: 1984, 'Electron-Impact Excitation of the $D^3\Sigma$ and $c_4'^1\Sigma$ Rydberg States of N_2', *Phys. Rev.* **A29**, 1709.

Fischer, F. and Schmidtke, G.: 1980, 'Rocket-Borne Auroral EUV Measurements', *J. Geophys. Res.* **85**, 4716.

Fox, J. L. and Dalgarno, A.: 1985, 'The Vibrational Distribution of N_2^+ in the Terrestrial Ionosphere', *J. Geophys. Res.* **90**, 7557.

Frank, L. A. and Craven, J. D.: 1988, 'Imaging Results from Dynamics Explorer I', *Rev. Geophys.* **26**, 249.

Frank, L. A., Sigwarth, J. B., and Craven, J. D.: 1986a, 'On the Influx of Small Comets into the Earth's Upper Atmosphere, I, Observations', *Geophys. Res. Letters* **13**, 303.

Frank, L. A., Sigwarth, J. B., and Craven, J. D.: 1986b, 'On the Influx of Small Comets into the Earth's Upper Atmosphere, II, Interpretation', *Geophys. Res. Letters* **13**, 307.

Freund, R. S.: 1972, 'Radiative Lifetime of $N_2(a\,^1\Pi_g)$ and the Formation of Metastable $N_2(a'\,^1\Sigma_u^-)$', *J. Chem. Phys.* **56**, 4344.

Friedman, H., Lichtman, S. W., and Byram, E. T.: 1951, 'Photon Counter Measurements of Solar X-Rays and Extreme Ultraviolet Light', *Phys. Rev.* **83**, 1025.

Gattinger, R. L., Harris, F. R., and Valance Jones, A.: 1985, 'The Height Spectrum and Mechanism of Type-B Aurora and its Bearing on the Excitation of $O(^1S)$ in Aurora', *Planetary Space Sci.* **33**, 207.

Geiger, J. and Schroder, B.: 1969, 'Intensity Perturbations Due to Configuration Interaction Observed in the Electron Energy-Loss Spectrum of N_2', *J. Chem. Phys.* **50**, 7.

Gentieu, E. P., Feldman, P. D., and Meier, R. R.: 1979, 'Spectroscopy of the Extreme Ultraviolet Dayglow at 6.5 Å Resolution: Atomic and Ionic Emissions Between 530 and 1240 Å', *Geophys. Res. Letters* **6**, 325.

Gentieu, E. P., Feldman, P. D., Eastes, R. W., and Christensen, A. B.: 1984, 'EUV Airglow During Active Solar Conditions 2. Emission Between 530 and 930 Å', *J. Geophys. Res.* **89**, 11053.

Gentieu, E. P., Feldman, P. D., Eastes, R. W., and Christensen, A. B.: 1981, 'Spectroscopy of the Extreme Ultraviolet Dayglow During Active Solar Conditions', *Geophys. Res. Letters* **8**, 1242.

Gerard, J. C. and Noel, C. E.: 1986, 'AE–D Measurements of the NO Geomagnetic Latitudinal Distribution and Contamination by $N^+(^5S)$ Emission', *J. Geophys. Res.* **91**, 10136.

Gerard, J. C., Anderson, D. N., and Matsushita, S.: 1977, 'Magnetic Storm Effects on the Tropical Ultraviolet Airglow', *J. Geophys. Res.* **82**.

Gilmore, F. F.: 1965, 'Potential Energy Curves for N_2, NO, O_2 and Corresponding Ions', *J. Quant. Spectr. Rad. Trans.* **5**, 369.

Gladstone, G. R.: 1982, 'Radiative Transfer with Partial Frequency Redistribution in Inhomogeneous Atmospheres: Application to the Jovian Aurora', *J. Quant. Spectr. Rad. Trans.* **27**, 545.

Gladstone, G. R.: 1988, 'UV Resonance Line Dayglow Emissions on Earth and Jupiter', *J. Geophys. Res.* **93**, 14623.

Gladstone, G. R., Link, R., Chakrabarti, S., and McConnell, J. C.: 1987, 'Modeling of the O I 989 Å to 1173-Å Ratio in the Terrestrial Dayglow', *J. Geophys. Res.* **92**, 12445.

Gross, R. W. F. and Cohen, N.: 1968, 'Temperature Dependence of Chemiluminescent Reaction, II, Nitric Oxide Afterglow', *J. Chem. Phys.* **48**, 2582.

Gulcicek, E. E. and Doering, J. P.: 1988, 'Absolute Differential and Integral Electron Excitation Cross Sections for Atomic Oxygen 5. Revised Values for the $^3P - {}^3S^0$ (1304 Å) and $^3P - {}^3D^0$ (989 Å) Transition Below 30 eV', *J. Geophys. Res.* **93**, 5879.

Gulcicek, E. E., Doering, J. P., and Vaughan, S. O.: 1988, 'Absolute Differential and Integral Electron Excitation Cross Sections for Atomic Oxygen 6. The $^3P - {}^3P$ and $^3P - {}^5P$ Transitions from 13.87 to 100 eV', *J. Geophys. Res.* **93**, 5885.

Hanson, W. B.: 1969, 'Radiative Recombination of Atomic Oxygen Ions in the Night-Time F-Region', *J. Geophys. Res.* **74**, 3720.

Hays, P. B., Abreu, V. J., Solomon, S. C., and Jeng-hwa Yee: 1988, 'The Visible Airglow Experiment, a Review', *Planetary Space Sci.* **36**, 21.

Heath, D. F. and Schlesinger, B. M.: 1986, 'The MG 280-nm Doublet as a Monitor of Changes in Solar Ultraviolet Irradiance', *J. Geophys. Res.* **91**, 8672.

Hecht, J. H. and Christensen, A. B.: 1989, 'Deducing Composition and Incident Electron Spectra from Ground-Based Auroral Optical Measurements: Variations in Oxygen Density', *J. Geophys. Res.* **94**, 13553.

Hedin, A. E.: 1987, 'MSIS-86 Thermospheric Model', *J. Geophys. Res.* **92**, 4649.

Hedin, A. E., Niemann, H. B., Kasprzak, W. T., and Seiff, A.: 1983, 'Global Empirical Model of the Venus Thermosphere', *J. Geophys. Res.* **81**, 73.

Hennes, J. P.: 1966, 'Measurement of the Ultraviolet Nightglow Spectrum', *J. Geophys. Res.* **71**, 763.

Henriksen, K. and Egeland, A.: 1988, 'The Interpretation of the Auroral Green Line: A Historic Preamble and the Present State of Knowledge', *EOS* **69**, 721.

Henry, R. J. W.: 1967, 'Photoionization Cross Sections for Atomic Oxygen, *Planetary Space Sci.* **15**, 1747.

Hernandez, S. P., Doering, J. P., Abreu, V. J., and Victor, G. A.: 1983, 'Comparison of Absolute Photoelectron Fluxes Measured on AE–C and AE–E with Theoretical Fluxes and Predicted and Measured N_2 2 PG 3371 Å Volume Emission Rates', *Planetary Space Sci.* **31**, 221.

Hibbert, A. and Bates, D. R.: 1981, 'Quantal Calculation of the Lifetime of $N^+(^5S)$ and the λ2145 Å Auroral Mystery Feature', *Planetary Space Sci.* **29**, 263.

Hicks, G. T. and Chubb, T. A.: 1970, 'Equatorial Aurora/Airglow in the Far Ultraviolet', *J. Geophys. Res.* **75**, 6233.

Hinteregger, H. E., Fukui, K., and Gilson, B. R.: 1981, 'Observational, Reference and Model Data on Solar EUV from Measurements on AE–E', *Geophys. Res. Letters* **8**, 1147.

Ho, Y. K. and Henry, R. J. W.: 1983, 'Oscillator Strengths and Collision Strengths for O II and O III', *Astrophys. J.* **264**, 733.

Holland, R. F.: 1969, 'Excitation of Nitrogen by Electrons: The Lyman–Birge–Hopfield System of N_2', *J. Chem. Phys.* **51**, 3940.

Holstein, T.: 1947, 'Imprisonment of Resonance Radiation in Gases', *Phys. Rev.* **72**, 1212.

Holstein, T.: 1951, 'Imprisonment of Resonance Radiation in Gases, II', *Phys. Rev.* **83**, 1159.

Hovestadt, D., Hausler, B., and Scholer, M.: 1972, 'Observation of Energetic Particles at Very Low Altitudes Near the Geomagnetic Equator', *Phys. Rev. Letters* **28**, 1340.

Huffman, R. E., LeBlanc, F. J., Larrabee, J. C., and Paulsen, D. E.: 1980, 'Satellite Vacuum Ultraviolet Airglow and Auroral Observations', *J. Geophys. Res.* **85**, 2201.

Huffman, R. E., LeBlanc, F. J., Paulson, D. E., and Larrabee, J. C.: 1981, 'Ultraviolet Horizon Sensing from Space', *SPIE* **265**, 290.

Hummer, D. G.: 1962, 'Non-Coherent Scattering, I. The Redistribution Functions with Doppler Broadening', *Monthly Notices Roy. Astron. Soc.* **125**, 21.

Hummer, D. G.: 1969, 'Non-Coherent Scattering, VI. Solutions of the Transfer Problem with a Frequency-Dependent Source Function', *Monthly Notices Roy. Astron. Soc.* **145**, 95.

Ishimoto, M., Meng, C. I., Romick, G. J., and Huffman, R. E.: 1988, 'Auroral Electron Energy and Flux from Molecular Nitrogen Ultraviolet Emissions Observed by the S3-4 Satellite', *J. Geophys. Res.* **93**, 9854.

Ishimoto, M., Torr, M. R., Richards, P. G., and Torr, D. G.: 1986, 'The Role of Energetic O^+ Precipitation in a Mid-Latitude Aurora', *J. Geophys. Res.* **91**, 5793.

Jacchia, L. G.: 1971, 'Revised Static Models of the Thermosphere and Exosphere with Empirical Temperature Profiles', *Smithsonian Astrophys. Obs. Spec. Rept.* **332**.

Jacchia, L. G.: 1977, 'Thermospheric Temperature, Density and Composition: New Models', *Smithsonian Astrophys. Obs. Spec. Rept.* **375**.

Jasperse, J. R.: 1977, 'Electron Distribution Function and Ion Concentrations in the Earth's Lower Ionosphere from Boltzmann–Fokker–Planck Theory', *Planetary Space Sci.* **25**, 743.

Jasperse, J. R.: 1981, 'The Photoelectron Distribution Function in the Terrestrial Ionosphere', *Proc. SPIE Conference, Phys. Space Plasmas* **4**, 53.

Jefferies, J. T.: 1968, *Spectral Line Formation*, Blaisdell Publ. Co., Waltham.

Jefferies, J. T. and White, O. R.: 1960, 'Source Function in a Non-Equilibrium Atmosphere. VI. The Frequency Dependence of the Source Function for Resonance Lines', *Astrophys. J.* **132**, 767.

Johnson, R. Barry: 1988, 'Wide Field of View 3-Mirror Telescopes Having Common Axes', *Opt. Eng.* **27**, 1046.

Johnson, C. Y., Young, J. M., and Holmes, J. C.: 1971, 'Magnetoglow – a New Geophysical Resource', *Science* **171**, 379.

Julienne, P. S. and Davis, J.: 1976, 'Cascade and Radiation Trapping Effects on Atmospheric Atomic Oxygen Emission Excited by Electron Impact', *J. Geophys. Res.* **81**, 1397.

Julienne, P. S., Davis, J., and Oran, E.: 1974, 'Oxygen Recombination in the Tropical Nightglow', *J. Geophys. Res.* **79**, 2540.

Kaneda, E., Mukai, T., and Hirao, K.: 1981, in S. I. Akasofu and J. R. Kan (eds.), 'Synoptic Features of Auroral System and Corresponding Electron Precipitation Observed by Kyokko', *Physics of Auroral Arc Formation*, Am. Geophys. U., Washington, D.C.

Kelly, Raymond L.: 1987, 'Atomic and Ionic Spectrum Lines Below 2000 Angstroms: Hydrogen through Krypton Part 1 (H–Cr)', *J. Phys. Chem. Ref. Data* **16**, 1.

Kenner, R. D. and Ogryzlo, E. A.: 1984, 'Quenching of the O_2 (A, $v = 2 \rightarrow X$, $v = 5$) Herzberg I Band by O_2 and O', *Can. J. Phys.* **62**, 1599.

Kirby, K., Constantinides, E. R., Babeu, S., Oppenheimer, M., and Victor, G. A.: 1979, 'Photoionization and Photoabsorption Cross Sections of He, O, N_2 and O_2 for Aeronomic Calculations', *At. Nucl. Data Tables* **23**, 63.

Knight, R. D.: 1982, 'Radiative Lifetime of the $^5S_2$ Metastable State of N^+', *Phys. Rev. Letters* **48**, 792.

Kofsky, I. L.: 1988, 'Excitation of N_2 Lyman–Birge–Hopfield Bands Emission by Low Earth Orbiting Spacecraft', *Geophys. Res. Letters* **15**, 241.

Kopp, J. P., Rusch, P. W., Roble, R. G., Victor, G. A., and Hays, P. B.: 1977, 'Photoemission in the Second Positive System of Molecular Nitrogen in the Earth's Dayglow', *J. Geophys. Res.* **82**, 555.

Kumar, S., Chakrabarti, S., Paresce, F., and Bowyer, S.: 1983, 'The O^+ 834-Å Dayglow: Satellite Observations and Interpretation with a Radiation Transfer Model', *J. Geophys. Res.* **88**, 9271.

Kumer, J. B.: 1974, 'Polarization of Multiple Scattered Light in Planetary Atmospheres from Solution of the Coupled Linear Integral Equations Derived for Mixed Rayleigh-Isotropic Scattering', *J. Quant. Spectr. Rad. Trans.* **14**, 165.

Kumer, J. B. and James, T. C.: 1974, '$CO_2(001)$ and N_2 Vibrational Temperatures in the $50 \leq Z \leq 130$ km Altitude Range', *J. Geophys. Res.* **79**, 638.

Kupperian, J. E., Jr., Byram, E. T., Chubb, T. A., and Friedman, H.: 1959, 'Far Ultraviolet Radiation in the Night Sky', *Planetary Space Sci.* **1**, 3.

Lean, J.: 1987, 'Solar Ultraviolet Irradiance Variations: A Review', *J. Geophys. Res.* **92**, 839.

Lean, J.: 1988, 'Solar EUV Irradiances and Indices', *Adv. Space Res.* **8**, 263.

Lee, Jong-Sen: 1974a, 'Monte Carlo Simulation of Voigt Distribution in Photon Diffusion Problems', *Astrophys. J.* **187**, 159.

Lee, Jong-Sen: 1974b, 'Monte Carlo Simulation of Emission Frequencies from Partial Frequency Redistribution Functions', *Astrophys. J.* **192**, 465.

Lee, Jong-Sen: 1977, 'Simulation of Emission Frequencies from Angle-Dependent Partial Frequency Redistributions', *Astrophys. J.* **218**, 857.

Lee, Jong-Sen and Meier, R. R.: 1980, 'Angle-Dependent Frequency Redistribution in a Plane Parallel Medium: External Source Case', *Astrophys. J.* **240**, 185.

Lee, J. S., Doering, J. P., Potemra, T. A., and Brace, L. H.: 1980a, 'Measurements of the Ambient Photoelectron Spectrum from Atmosphere Explorer: I. AE–E Measurements Below 300 km During Solar Minimum Conditions', *Planetary Space Sci.* **28**, 947.

Lee, J. S., Doering, J. P., Potemra, T. A., and Brace, L. H.: 1980b, 'Measurements of the Ambient Photoelectron Spectrum from Atmosphere Explorer: II. AE–E Measurements from 300 to 1000 km During Solar Minimum Conditions', *Planetary Space Sci.* **28**, 973.

Lemaire, P., Charra, J., Jouchoux, A., Vidal-Madjar, A., Artzner, G. E., Vial, J. C., Bonnet, R. M., and Skumanich, A.: 1978, 'Calibrated Full Disk H I Lyman-α and Lyman-β Profiles', *Astrophys. J.* **223**, L55.

Levasseur, A. C.: 1976, 'Observations Atmospheriques et Astronomiques au Voisinage de 6563 A a Bord du Satellite D2A', Ph.D. Thesis, Univ. of Paris, Paris.

Levasseur, A. C. and Blamont, J. E.: 1973, 'Satellite Observations of Strong Balmer Alpha Atmospheric Emissions Around the Magnetic Equator', *J. Geophys. Res.* **78**, 3881.

Lewis, B. R., Berzins, L., and Carver, J. H.: 1986, 'Oscillator Strengths for the Schumann–Runge Bands of $^{16}O_2$', *J. Quant. Spectr. Rad. Trans.* **36**, 209.

Link, R., Chakrabarti, S., Gladstone, G. R., and McConnell, J. C.: 1988a, 'An Analysis of Satellite Observations of the O I EUV Dayglow', *J. Geophys. Res.* **93**, 2693.

Link, R., Gladstone, G. R., and Chakrabarti, S.: 1988b, 'A Reanalysis of Rocket Measurements of the Ultraviolet Dayglow', *J. Geophys. Res.* **93**, 14631.

Luken, W. L. and Sinanoglu, O.: 1976, 'Oscillator Strengths for Transitions Involving Excited States Not Lowest of Their Symmetry Oxygen I and Oxygen II Transition', *J. Chem. Phys.* **64**, 1495.

Mandleman, M., Carrington, T., and Young, R. A.: 1973, 'Predissociation and Its Inverse, Using Resonance Absorption NO $(C\,^2\Pi) - N + O$', *J. Chem. Phys.* **58**, 84.

Mange, P. and Meier, R. R.: 1970, 'OGO III Observations of the Lyman-Alpha Intensity and the Hydrogen Concentration Beyond 5 Earth Radii', *J. Geophys. Res.* **75**, 1837.

Marinelli, W. J., Green, B. D., DeFaccio, M. A., and Blumberg, W. A. M.: 1988, 'Vibrational Relaxation and Intersystem Crossing in $N_2(a\,^1\Pi_g)$', *J. Phys. Chem.* **92**, 3429.

Marinelli, W. J., Kessler, W. J., Green, B. D., and Blumberg, W. A. M.: 1989, 'The Radiative Lifetime of $N_2(a\,^1\Pi_g, v = 0\text{–}2)$', *J. Phys. Chem.* **91**, 71.

Mason, N. J. and Newell, W. R.: 1987, 'Electron Impact Total Excitation Cross Section of the $a\,^1\Pi_g$ State of N_2', *J. Phys. B: At. Mol. Phys.* **20**, 3913.

McCoy, R. P.: 1981, 'Rocket Measurements of Thermospheric Odd Nitrogen and Comparisons with a Diffusive Transport Chemical Model', Ph.D. Thesis, Univ. of Colorado, Boulder.

McCoy, R. P.: 1983a, 'Thermospheric Odd Nitrogen 1. NO, N(4*S*) and O(3*P*) Densities from Rocket Measurements of the NO Delta and Gamma Bands and the O_2 Herzberg I Bands', *J. Geophys. Res.* **88**, 3197.

McCoy, R. P.: 1983b, 'Thermospheric Odd Nitrogen 2. Comparisons of Rocket Observations with a Diffusive Transport Chemical Model', *J. Geophys. Res.* **88**, 3206.

McCoy, R. P. and Carruthers, G. R.: 1988, 'Spartan-282: The High Resolution Airglow/Aurora Spectrograph (HIRAAS)', *SPIE, Ultraviolet Tech. II* **932**, 297.

McCoy, R. P., Anderson, D. E., Jr., and Chakrabarti, S.: 1985, 'F2 Region Ion Densities from Analysis of O^+ 834-Å Airglow: A Parametric Study and Comparison with Satellite Data', *J. Geophys. Res.* **90**, 12257.

McCoy, R. P., Paxton, L. J., Meier, R. R., Cleary, D. D., Prinz, D. K., Wolfram, K. D., Christensen, A. B., Pranke, J. B., and Kayser, D. C.: 1987, in J. M. Goodman (ed.), 'RAIDS: An Orbiting Observatory for Ionospheric Remote Sensing from Space', *Effect of the Ionosphere on Communication, Navigation and Surveillance Systems*, Naval Research Laboratory, Washington, D.C., p. 519.

McCoy, R. P., Wolfram, K. D., Meier, R. R., Paxton, L. J., Cleary, D. D., Prinz, D. K., Anderson, D. E., Jr., Christensen, A. B., Pranke, J. B., Sivjee, G. G., and Kayser, D. C.: 1986, 'The Remote Atmospheric and Ionospheric Detection System', *SPIE-UV Technology* **687**, 142.

McDade, I. C. and Llewellyn, E. J.: 1984, 'Atomic Oxygen Concentrations in the Auroral Ionosphere', *Geophys. Res. Letters* **11**, 247.

McLaughlin, R. W.: 1977, 'Vacuum Ultraviolet and Visible Radiation from Electron Impact Excitation of Nitrogen, Hydrogen, Oxygen, the Light Hydrocarbons and the Rare Gases', Ph.D. Thesis, Univ. of Pittsburgh.

Meier, R. R.: 1969, 'Balmer-Alpha and Lyman-Beta in the Hydrogen Geocorona', *J. Geophys. Res.* **74**.

Meier, R. R.: 1975, 'Resonance Scattering from Optically Thin Expanding Cometary Atmospheres', *Astron. Astrophys.* **40**, 373.

Meier, R. R.: 1977, 'Some Optical and Kinetic Properties of the Nearby Interstellar Medium', *Astron. Astrophys.* **55**, 211.

Meier, R. R.: 1981, 'A Study of Partial Frequency Redistribution of Monochromatic Source Radiation', *J. Quant. Spectr. Rad. Trans.* **25**, 1137.

Meier, R. R.: 1982, 'Spectroscopy of the O I 989- and 7990-Å Multiplets in the Dayglow Airglow', *J. Geophys. Res.* **87**, 6307.

Meier, R. R.: 1987a, 'Thermospheric Aurora and Airglow', *Rev. Geophys.* **25**, 471.

Meier, R. R.: 1987b, 'Issues Relating to "Holes" in the O I 1304 Å Far UV Dayglow', *Planetary Space Sci.* **35**, 1297.

Meier, R. R.: 1990, 'The Scattering Rate of Solar 834 Å Radiation by Magnetospheric O^+ and O^{++}', *Geophys. Res. Letters* **17**, 1613.

Meier, R. R. and Anderson, D. E., Jr.: 1983, 'Determination of Atmospheric Composition and Temperature from the UV Dayglow', *Planetary Space Sci.* **31**, 967.

Meier, R. R. and Conway, R. R.: 1983, 'On the N_2 Lyman–Birge–Hopfield Band Nightglow', *J. Geophys. Res.* **88**, 4929.

Meier, R. R. and Conway, R. R.: 1985, 'The $^1D - {}^3S$ Transition in Atomic Oxygen: A New Method of Measuring the O Abundance in Planetary Thermospheres', *Geophys. Res. Letters* **12**, 601.

Meier, R. R. and Lee, Jong-Sen: 1981, 'Angle-Dependent Frequency Redistribution: Internal Source Case', *Astrophys. J.* **250**, 376.

Meier, R. R. and Lee, Jong-Sen: 1982, 'An Analysis of the O I 1304 Å Dayglow Using a Monte Carlo Resonant Scattering Model with Partial Frequency Redistribution', *Planetary Space Sci.* **30**, 439.

Meier, R. R. and Mange, P.: 1970, 'Geocoronal Hydrogen: An Analysis of the Lyman-α Airglow from OGO-4', *Planetary Space Sci.* **18**, 303.

Meier, R. R. and Mange, P.: 1973, 'Spatial and Temporal Variations of the Lyman Alpha Airglow and Related Atomic Hydrogen Distributions', *Planetary Space Sci.* **21**, 309.

Meier, R. R. and Opal, C. B.: 1973, 'Tropical UV Arcs: Comparison of Brightness with foF2', *J. Geophys. Res.* **78**, 3189.

Meier, R. R. and Prinz, D. K.: 1971, 'Observations of the O I 1304 Å Airglow from OGO-4', *J. Geophys. Res.* **76**, 4608.

Meier, R. R. and Weller, C. S.: 1972, 'EUV Resonance Radiation from Helium Atoms and Ions in the Geocorona', *J. Geophys. Res.* **77**, 1190.

Meier, R. R. and Weller, C. S.: 1974, 'Extreme Ultraviolet Observations of the Latitudinal Variation of Helium', *J. Geophys. Res.* **79**, 1575.

Meier, R. R. and Weller, C. S.: 1975, 'Observations of Equatorial EUV Bands: Evidence for Low-Altitude Precipitation of Ring Current Helium', *J. Geophys. Res.* **80**, 2813.

Meier, R. R., Anderson, D. E., Jr., and Nicolet, M.: 1982, 'Radiation Field in the Troposphere and Stratosphere from 240–1000 nm. I. General Analysis', *Planetary Space Sci.* **30**, 923.

Meier, R. R., Anderson, D. E., Jr., Paxton, L. J., McCoy, R. P., and Chakrabarti, S.: 1987, 'The O I $3d\,{}^3D^0 - 2p^4\,{}^3P$ Transition at 1026 Å in the Day Airglow', *J. Geophys. Res.* **92**, 8767.

Meier, R. R., Carruthers, G. R., Page, T. L., and Levasseur-Regourd, A. C.: 1977, 'Geocoronal Ly-Beta and Ba-Alpha Emissions Measured During the Apollo-16 Mission', *J. Geophys. Res.* **82**, 737.

Meier, R. R., Conway, R. R., Feldman, P. D., Strickland, D. J., and Gentieu, E. P.: 1982, 'Analysis of Nitrogen and Oxygen Far Ultraviolet Auroral Emissions', *J. Geophys. Res.* **87**, 2444.

Meier, R. R., Conway, R. R., Anderson, D. E., Jr., Feldman, P. D., Eastes, R. W., Gentieu, E. P., and Christensen, A. B.: 1985, 'The Ultraviolet Dayglow at Solar Maximum 3. Photoelectron-Excited Emissions of N_2 and O', *J. Geophys. Res.* **90**, 6608.

Meier, R. R., Strickland, D. J., Feldman, P. D., and Gentieu, E. P.: 1980, 'The Ultraviolet Dayglow 1. Far UV Emissions of N and N_2', *J. Geophys. Res.* **85**, 2177.

Meier, R. R., Strickland, D. J., Hecht, J. H., and Christensen, A. B.: 1989, 'Deducing Composition and Incident Electron Spectra from Ground-Based Auroral Optical Measurements: A Study of Auroral Red Line Processes', *J. Geophys. Res.* **94**, 13541.

Meier, R. R., Widing, K., and Feldman, U.: 1991, 'Analysis of Solar O II/O III Multiplets at 834 Å: Implications for the Emission Measure Distribution in the Vicinity of 40000 K', *Astrophys. J.* **369**, 570.

Mende, S. B., Swenson, G. R., and Miller, K. L.: 1985, 'Observations of E and F Region Mg^+ from Spacelab 1', *J. Geophys. Res.* **90**, 6667.

Meng, C.-I. and Huffman, R. E.: 1984, 'Ultraviolet Imaging from Space of the Aurora Under Full Sunlight', *Geophys. Res. Letters* **11**, 315.

Meng, C.-I. and Huffman, R. E.: 1987, *Preliminary Observations from the Auroral and Ionospheric Remote Sensing Imager,* Johns Hopkins Applied Physics Lab Technical Digest, Vol. 8.

Meng, C.-I., Huffman, R. E., Skrivanek, R. A., Strickland, D. J., and Daniell, R. E.: 1987, 'Remote Sensing of Ionosphere by Using Ultraviolet and Visible Emissions', *SPIE-UV Technology* **687**, 2.

Meyerott, R. E. and Swenson, G. R.: 1990, 'A Surface Chemistry Model for the Production of N_2 LBH Spacecraft Glow', *Planetary Space Sci.* **38**, 555.

Mihalas, D.: 1978, *Stellar Atmospheres*, W. H. Freeman and Co., San Francisco.

Mitchell, A. C. G. and Zemansky, M. W.: 1961, *Resonance Radiation and Excited Atoms,* Cambridge University Press, Cambridge, 1961.

Molina, L. T. and Molina, M. J.: 1986, 'Absolute Absorption Cross Sections of Ozone in the 185- to 350-nm Wavelength Range', *J. Geophys. Res.* **91**, 14501.

Morrison, M. D.: 1985, 'Laboratory Measurement of the O I 1173/989 Å Branching Ratio', *Planetary Space Sci.* **33**, 135.

Morrison, M. D. and Meier, R. R.: 1988, 'The O I 989 and 1173 Å Multiplets in the Dayglow', *Planetary Space Sci.* **36**, 987.

Morrison, M. D., Bowers, C. W., Feldman, P. D., and Meier, R. R.: 1990, 'The EUV Dayglow at High Spectral Resolution', *J. Geophys. Res.* **95**, 4113.

Morrison, D., Christensen, A. B., and Cunningham, A. J.: 1981, 'Measured Branching Ratios for O II ^2D and ^2P Transitions in the Wavelength Range 530 to 800 Å', *J. Geophys. Res.* **86**, 3589.

Morrison, M. D., Cunningham, A. J., and Christensen, A. B.: 1983, 'EUV Branching Ratios for Ionized Nitrogen and Oxygen Emissions', *J. Quant. Spectr. Rad. Trans.* **29**, 137.

Mount, G. H. and Rottman, G. J.: 1983, 'The Solar Absolute Spectral Irradiance at 1216 Å and 1800–3173 Å: January 12, 1983', *J. Geophys. Res.* **88**, 6807.

Mount, G. H. and Rottman, G. J.: 1985, 'Solar Absolute Spectral Irradiance 118–300 nm: July 25, 1983', *J. Geophys. Res.* **90**, 13031.

Mumma, M. J. and Zipf, E. C.: 1971a, 'Dissociative Excitation of Vacuum-Ultraviolet Emission Features by Electron Impact on Molecular Gases. II. N_2', *J. Chem. Phys.* **55**, 5582.

Mumma, M. J. and Zipf, E. C.: 1971b, 'Dissociative Excitation of Vacuum Ultraviolet Emission Features by Electron Impact on Molecular Gases. I. H_2 and O_2', *J. Chem. Phys.* **55**, 1661.

Murtagh, D. P.: 1988, 'The O_2 Schumann–Runge System: New Calculations of Photodissociation Cross-Sections', *Planetary Space Sci.* **36**, 819.

Murtagh, D. P., McDade, I. C., Greer, R. G. H., Stegman, J., Witt, G., and Llewellyn, E. J.: 1986, 'ETON 4: An Experimental Investigation of the Altitude Dependence of the $O_2(A\ ^3\Sigma_u^+)$ Vibrational Populations in the Nightglow', *Planetary Space Sci.* **34**, 811.

Newberry, I. Y., Comfort, R. H., Richards, P. G., and Chappell, C. R.: 1989, 'Thermal He^+ in the Plasmasphere: Comparison of Observations with Numerical Calculations', *J. Geophys. Res.* **94**, 15265.

Nicolet, M., Cieslik, S., and Kennes, R.: 1988, 'Aeronomic Problems of Molecular Oxygen Photodissocia-

tion. II. Theoretical Absorption Cross-Sections of the Schumann–Runge Bands at 79 K', *Planetary Space Sci.* **36**, 1039.

Nicolet, M. and Kennes, R.: 1988a, 'Aeronomic Problems of Molecular Oxygen Photodissociation. III. Solar Spectral Irradiances in the Region of the O_2 Herzberg Continuum, Schumann–Runge Bands and Continuum', *Planetary Space Sci.* **36**, 1059.

Nicolet, M. and Kennes, R.: 1988b, 'Aeronomic Problems of Molecular Oxygen Photodissociation. IV. The Various Parameters for the Herzberg Continuum', *Planetary Space Sci.* **36**, 1069.

O'Neil, R. R., Lee, E. T. P., and Huppi, E. R.: 1979, 'Auroral O(^1S) Production and Loss Processes: Ground-Based Measurements of the Artificial Auroral Experiment, Precede', *J. Geophys. Res.* **84**, 823.

Ogawa, H. S. and Judge, D. L.: 1986, 'Absolute Solar Flux Measurements Shortward of 575 Å', *J. Geophys. Res.* **91**, 7089.

Ogawa, H. S., Phillips, E., and Judge, D. L.: 1984, 'Line Width of the Solar EUV He I Resonance Emissions at 584 and 537 Å', *J. Geophys. Res.* **89**, 7537.

Opal, C. B.: 1973, 'Enhancements of the Photoelectron-Excited Dayglow During Solar Flares', *Space Res.* **13**, 797.

Oran, E. S. and Strickland, D. J.: 1978, 'Photoelectron Flux in the Earth's Ionosphere', *Planetary Space Sci.* **26**, 1161.

Paresce, F.: 1979, 'EUV Observations of the Equatorial Aurora', *J. Geophys. Res.* **84**, 4409.

Paresce, F., Bowyer, S., and Kumar, S.: 1973, 'Observations of the He II 304-Å Radiation in the Night Sky', *J. Geophys. Res.* **78**, 71.

Paresce, F., Bowyer, S., and Kumar, S.: 1974, 'On the Distribution of He^+ in the Plasmasphere from Observations of Resonantly Scattered He II 304-Å Radiation', *J. Geophys. Res.* **79**, 174.

Parisot, J. P.: 1986, 'Excitation of Herzberg I and II Bands in the Atmospheres of Earth and Venus', *Ann. Geophys.* **4**, 481.

Park, H., Feldman, P. D., and Fastie, W. G.: 1977, 'The Extreme Ultraviolet (750–1230 Å) Spectrum of an Aurora', *Geophys. Res. Letters* **4**, 41.

Paxton, L. J. and Strickland, D. J.: 1988, 'EUV Imaging of the Ionosphere from Space', *Proc. SPIE-UV Technology II* **932**, 190.

Paxton, L. J., Anderson, D. E., Jr., and Huffman, R. E.: 1991, 'Satellite Observations of the O I 1356 Å Nightglow', *J. Geophys. Res.* (submitted).

Paxton, L. J., Cox, R., Strickland, D. J., and Meier, R. R.: 1991, 'Global Modelling of the FUV Airglow', *J. Geophys. Res.* (to be submitted).

Piper, L. G.: 1982, 'The Excitation of O(^1S) in the Reaction Between $N_2(A\ ^3\Sigma_u^+)$ and O(^3P)', *J. Chem. Phys.* **77**(5), 2372.

Piper, L. G. and Caledonia, G. E.: 1981, 'Rate Constants for Deactivation of $N_2(A\ ^3\Sigma_u^-, v' = 0, 1)$ by O', *J. Chem. Phys.* **75**, 2847.

Porter, H. S., Jackman, C. H., and Green, A. E. S.: 1976, 'Efficiencies for Production of Atomic Oxygen by Relativistic Proton Impact in Air', *J. Chem. Phys.* **65**, 154.

Pradhan, A. K. and Saraph, H. E.: 1977, 'Oscillator Strengths for Dipole Transitions in Neutral Oxygen', *J. Phys.* **B10**, 3365.

Prinz, D. K. and Meier, R. R.: 1971, 'OGO-4 Observations of the Lyman–Birge–Hopfield Bands in the Day Airglow', *J. Geophys. Res.* **76**, 6146.

Rairden, R. L. and Craven, J. D.: 1986, 'Geocoronal Imaging with Dynamics Explorer', *J. Geophys. Res.* **91**, 13613.

Rees, D. and Fuller-Rowell, T. J.: 1988, 'Understanding the Transport of Atomic Oxygen within the Thermosphere Using a Numerical Global Thermospheric Model', *Planetary Space Sci.* **36**, 935.

Richards, P. G. and Torr, D. G.: 1984, 'An Investigation of the Consistency of the Ionospheric Measurements of the Photoelectron Flux and Solar EUV Flux', *J. Geophys. Res.* **89**, 5625.

Richards, P. G. and Torr, D. G.: 1985, 'The Altitude Variation of the Ionospheric Photoelectron Flux: A Comparison of Theory and Measurement', *J. Geophys. Res.* **90**, 2877.

Roble, R. G. and Dickinson, R. E.: 1989, 'How Will Changes in Carbon Dioxide and Methane Modify the Mean Structure of the Mesosphere and Thermosphere?', *Geophys. Res. Letters* **16**, 1441.

Roble, R. G., Forbes, J. M., and Marcos, F. A.: 1987, 'Thermospheric Dynamics During the March 22, 1979, Magnetic Storm', *J. Geophys. Res.* **92**, 6045.

Rohrbaugh, R. P., Tinsley, B. A., Rassoul, H., Sahai, Y., Teixeira, N. R., Tull, R. G., Doss, D. R., Cochran,

A. L., Cochran, W. D., and Barker, E. S.: 1983, 'Observations of Optical Emissions from Precipitation of Energetic Neutral Atoms and Ions from the Ring Current', *J. Geophys. Res.* **88**, 6317.

Rottman, G. J.: 1985a, in C. S. Zerefos and A. Ghazi (eds.), 'Solar Ultraviolet Irradiance 1982 and 1983', *Atmospheric Ozone, Proceedings of the Quadrennial Ozone Symposium*, D. Reidel Publ. Co., Dordrecht, Holland.

Rottman, G. J.: 1985b, 'Solar Cycle Variation of Ultraviolet, 120–200 nm, Irradiance Measured by the Solar Mesosphere Explorer, 1982 through 1985', *EOS* **66**, 1009.

Rountree, S. P.: 1977, 'Electron-Impact Excitation of Atomic Oxygen: $^3P - 3s\,^5S^0$ and $^3P - 3s\,^3S^0$', *J. Phys. B: Atom. Molec. Phys.* **10**, 2719.

Rountree, S. P. and Henry, R. J. W.: 1972, 'Electron-Impact Excitation Cross Sections for Atomic Oxygen: $^3P - {}^3S$', *Phys. Rev.* **A6**, 2106.

Rusch, D. W. and Sharp, W. E.: 1981, 'Nitric Oxide Delta Band Emission in the Earth's Atmosphere: Comparison of a Measurement and a Theory', *J. Geophys. Res.* **86**, 10111.

Samson, J. A. R. and Pareek, P. N.: 1985, 'Absolute Photoionization Cross Sections of Atomic Oxygen', *Phys. Rev.* **A31**, 1470.

Scholer, M., Hovestadt, D., and Morfill, G.: 1975, 'Energetic He^+ Ions from the Radiation Belt at Low Altitudes Near the Geomagnetic Equator', *J. Geophys. Res.* **80**, 80.

Sharp, W. E.: 1971, 'Rocket-Borne Spectroscopic Measurements in the Ultraviolet Aurora: Nitrogen Vegard–Kaplan Bands', *J. Geophys. Res.* **76**, 987.

Sharp, W. E.: 1978, 'The Ultraviolet Aurora: The Spectrum Between 2100 Å and 2300 Å', *Geophys. Res. Letters* **5**, 703.

Sharp, W. E.: 1986, 'Sources of the Emission Features Between 2000 and 8000 Å in the Thermosphere', *Can. J. Phys.* **64**, 1594.

Sharp, W. E. and Rusch, D. W.: 1981, 'Chemiluminescence of Nitric Oxide: The NO ($C\,^2\Pi - A\,^2\Sigma^+$) Rate Constant', *J. Quant. Spectr. Rad. Trans.* **25**, 413.

Sharp, W. E. and Siskind, D. E.: 1989, 'Atomic Emission in the Ultraviolet Nightglow', *Geophys. Res. Letters* **16**, 1453.

Sharp, W. E., Rees, M. H., and Stewart, A. I.: 1979, 'Coordinated Rocket and Satellite Measurements of an Auroral Event. 2. The Rocket Observations and Analysis', *J. Geophys. Res.* **84**, 1977.

Shemansky, D. E. and Broadfoot, A. L.: 1971, 'Excitation of N_2 and N_2^+ Systems by Electron, II, Excitation Cross Sections and N_2 IPG Low Pressure Afterglow', *J. Quant. Spectr. Rad. Trans.* **11**, 1401.

Shemansky, D. E., Ajello, J. M., and Hall, D. T.: 1985, 'Electron Impact Excitation of H_2: Rydberg Band Systems and the Benchmark Dissociative Cross Section for H Lyman-Alpha', *Astrophys. J.* **296**, 765.

Shemansky, D. E., Judge, D. L., and Jessen, J. M.: 1984, in Y. Kondo, F. C. Bruhweiler, and B. D. Savage (eds.), 'Pioneer 10 and Voyager Observations of the Interstellar Medium in Scattered Emission of the He 584-Å and HLyα 1216-Å Lines', *Local Interstellar Medium*, NASA Conf. Publ. 2345, p. 24.

Shepherd, G. G.: 1984, 'Atomic Oxygen Concentrations in the Auroral Thermosphere: Application of a Thermospheric Temperature Criterion', *Geophys. Res. Letters* **11**, 1117.

Siskind, D. E. and Barth, C. A.: 1987, 'Rocket Observation of the N II 2143 Å Emission in an Aurora', *Geophys. Res. Letters* **14**, 479.

Siskind, D. E., Barth, C. A., and Roble, R. G.: 1989a, 'The Reponse of Thermospheric Nitric Oxide to an Auroral Storm, 1, Low and Middle Latitudes', *J. Geophys. Res.* **94**, 16885.

Siskind, D. E., Barth, C. A., Evans, D. S., and Roble, R. G.: 1989b, 'The Response of Thermospheric Nitric Oxide to an Auroral Storm, 2, Auroral Latitudes', *J. Geophys. Res.* **94**, 16899.

Sivjee, G. G.: 1983, 'Differences in Near UV (~3400–4300 Å) Optical Emissions from Midday Cusp and Nighttime Auroras', *J. Geophys. Res.* **88**, 435.

Skumanich, A. and Lites, B. W.: 1986, 'Radiative Transfer Diagnostics: Understanding Multilevel Transfer Calculations, I, Analysis of the Full Statistical Equilibrium Equations', *Astrophys. J.* **310**, 419.

Slanger, T. G.: 1983, 'Auroral N_2 Emission', *Planetary Space Sci.* **31**, 1525.

Slanger, T. G.: 1986, 'Auroral $N_2(c_4'\,^1\Sigma_u^+ \rightarrow a\,^1\Pi_g)$ Emission, II', *Planetary Space Sci.* **34**, 399.

Slanger, T. G. and Degen, V.: 1986, 'The Rotationally-Resolved Oxygen Afterglow, 373–474 nm', *Planetary Space Sci.* **34**, 931.

Slanger, T. G. and Huestis, D. L.: 1981, '$O_2(c\,^1\Sigma_u^- \rightarrow X\,^3\Sigma_g^-)$ Emission in the Terrestrial Nightglow', *J. Geophys. Res.* **86**, 3551.

Stahel, D., Leoni, M., and Dressler, K.: 1983, 'Nonadiabatic Representations of the $^1\Sigma_u^+$ and $^1\Pi_u$ States of the N_2 Molecule', *J. Chem. Phys.* **79**(6), 2541.

Stegman, J. and Murtagh, D. P.: 1988, 'High Resolution Spectroscopy of Oxygen U.V. Airglow', *Planetary Space Sci.* **36**, 927.

Stewart, A. I.: 1965, 'Fast Photoelectrons and the Dayglow', Ph.D. Thesis, Queen's University, Belfast.

Stewart, A. I.: 1970, 'Photoionization Coefficients and Photoelectron Impact Excitation Efficiencies in the Daytime Ionosphere', *J. Geophys. Res.* **75**, 6333.

Stone, E. J. and Zipf, E. C.: 1973, 'Excitation of Atomic Nitrogen by Electron Impact', *J. Chem. Phys.* **58**, 4278.

Stone, E. J. and Zipf, E. C.: 1974, 'Electron Impact Excitation of the $^3S^0$ and $^5S^0$ States of Atomic Oxygen', *J. Chem. Phys.* **60**, 4237.

Strickland, D. J.: 1979, 'The Transport of Resonance Radiation in a Non-Isothermal Medium-Effect of Varying Doppler Width', *J. Geophys. Res.* **84**, 5890.

Strickland, D. J. and Anderson, D. E., Jr.: 1977, 'The O I 1304 Å Nadir Intensity/Column Production Rate Ratio and its Application to Airglow Studies', *J. Geophys. Res.* **82**, 1013.

Strickland, D. J. and Anderson, D. E., Jr.: 1983, 'Radiation Transport Effects on the 1356 Å Limb Intensity Profile in the Dayglow', *J. Geophys. Res.* **88**, 9260.

Strickland, D. J. and Christensen, A. B.: 1988, *Dayglow Optical Backgrounds: Calculated Spectra and Limb Profiles from 1200–8000 Å*, Aerospace Report No. TOR-0088(3409–91)-1, Aerospace Corp., Los Angeles.

Strickland, D. J. and Donahue, T. M.: 1970, 'Excitation and Radiative Transport of O I 1304 Å Resonance Radiation, I', *Planetary Space Sci.* **18**, 661.

Strickland, D. J. and Meier, R. R.: 1982, *A Photoelectron Model for the Rapid Computation of Atmospheric Excitation Rates*, NRL Memorandum Report 5004.

Strickland, D. J. and Rees, M. H.: 1974, 'The O I 1304 and 1356 Emissions in Aurorae', *Planetary Space Sci.* **22**, 465.

Strickland, D. J., Barnes, R. P., and Andersen, D. E., Jr.: 1988, *UV Background Calculations: Rayleigh Scattered and Dayglow Backgrounds from 1200–3000 Å*, AFGL-TR-88-0200, Geophysics Laboratory, Hanscomb Air Force Base, Mass.

Strickland, D. J., Cox, R., Barnes, R., Paxton, L., and Meier, R. R.: 1991, *A Model for UV Global Imaging* (in preparation).

Strickland, D. J., Daniell, R. E., Jr., Decker, D., Jasperse, J. R., and Carlson, H. C.: 1984, *Determination of Ionospheric Electron Density Profiles from Satellite UV Emission Measurements*, Air Force Geophysics Lab Technical Report 84–0140.

Strickland, D. J., Jasperse, J. R., and Whalen, J. A.: 1983, 'Dependence of Auroral FUV Emissions on the Incident Electron Spectrum and Neutral Atmosphere', *J. Geophys. Res.* **88**, 8051.

Strickland, D. J., Meier, R. R., Hecht, J. H., and Christensen, A. B.: 1989, 'Deducing Composition and Incident Electron Spectra from Ground-Based Auroral Optical Measurements: Theory and Model Results', *J. Geophys. Res.* **94**, 13527.

Strobel, D. F. and Shemansky, D. E.: 1982, 'EUV Emission from Titan's Upper Atmosphere: Voyager 1 Encounter', *J. Geophys. Res.* **87**, 1361.

Swenson, G. R. and Meyerott, R. E.: 1988, 'Spacecraft Ram Cloud Atom Exchange and N_2 LBH Glow', *Geophys. Res. Letters* **15**, 245.

Swift, D. W., Smith, R. W., and Akasofu, S.-I.: 1989, 'Imaging the Earth's Magnetosphere', *Planetary Space Sci.* **37**, 379.

Swift, W. R., Torr, D. G., Richards, P. G., Bhatt, P. P., Hamilton, C. M., and Goodwin, R. L.: 1989, 'Twilight Observations and Modelling of the N_2^+ First Negative Bands', *EOS* **70**, 1234.

Takacs, P. Z. and Feldman, P. D.: 1977, 'Far Ultraviolet Atomic and Molecular Nitrogen Emission in the Dayglow', *J. Geophys. Res.* **82**, 5011.

Tayal, S. S. and Henry, R. J. W.: 1988, 'Electron-Impact Excitation of Atomic Oxygen', *Phys. Rev.* **A38**, 5945.

Tayal, S. S. and Henry, R. J. W.: 1989, 'Oscillator Strengths and Electron Collisional Excitation Cross Sections for Atomic Oxygen', *Phys. Rev.* **A39**, 4531.

Tennyson, P. D., Feldman, P. D., Hartig, G. F., and Henry, R. C.: 1986, 'Near-Midnight Observations of Nitric Oxide δ- and γ-Band Chemiluminescence', *J. Geophys. Res.* **91**, 10141.

Thomas, G. E.: 1963, 'Lyman Alpha Scattering in the Earth's Hydrogen Geocorona, I', *J. Geophys. Res.* **68**, 2639.

Thomas, G. E. and Anderson, D. E., Jr.: 1976, 'Global Atomic Hydrogen Density Derived from OGO-6 Lyman Alpha Measurements', *Planetary Space Sci.* **24**, 303.

Thomas, G. E. and Bohlin, R. C.: 1972, 'Lyman-Alpha Measurements of Neutral Hydrogen in the Outer Geocorona and in Interplanetary Space', *J. Geophys. Res.* **77**, 2752.

Thomas, J. M. and Kaufman, F.: 1985, 'Rate Constants of the Reactions of Metastable $N_2(A\,^3\Sigma_u^+)$ in $v = 0, 1, 2$, and 3 with Ground State O_2 and O', *J. Chem. Phys.* **83**, 2900.

Thomas, R. J.: 1981, 'Analyses of Atomic Oxygen, the Green Line, and Herzberg Bands in the Lower Thermosphere', *J. Geophys. Res.* **86**, 206.

Thomas, R. J. and Young, R. A.: 1981, 'Measurements of Atomic Oxygen and Related Airglows in the Lower Thermosphere', *J. Geophys. Res.* **86**, 7389.

Thomas, R. N.: 1957, 'The Source Function in a non-Equilibrium Atmosphere. I. The Resonance Lines', *Astrophys. J.* **125**, 260.

Timothy, J. G.: 1977, in Oran R. White (ed.), 'The Solar Spectrum Between 300 and 1200 Å', *The Solar Output and Its Variation*, Colorado Associated University Press, Boulder.

Tinsley, B. A.: 1972, 'O I and N I Allowed Transitions in the Airglow and Aurora', *Ann. Geophys.* **28**, 155.

Tinsley, B. A.: 1976a, 'Evidence that the Recovery Phase Ring Current Consists of Helium Ions', *J. Geophys. Res.* **81**, 6193.

Tinsley, B. A.: 1976b, 'Energetic Neutral Atom Precipitation During Magnetic Storms: Optical Emission, Ionization, and Energy Deposition at Low and Middle Latitudes', *J. Geophys. Res.* **84**, 1855.

Tinsley, B. A.: 1981, 'Neutral Atom Precipitation – A Review', *J. Atmospheric Terrest. Phys.* **43**, 617.

Tinsley, B. A. and Bittencourt, J. A.: 1975, 'Determination of F Region Height and Peak Electron Density at Night Using Airglow Emissions from Atomic Oxygen', *J. Geophys. Res.* **80**, 2333.

Tinsley, B. A., Christensen, A. B., Bittencourt, J. A., Gouveia, H., Angreji, P. D., and Takahashi, H.: 1973, 'Excitation of Oxygen Line Emissions in the Tropical Nightglow', *J. Geophys. Res.* **78**, 1174.

Tinsley, B. A., Rohrbaugh, R. P., Sahai, Y., and Teixeira, N. R.: 1982, 'Energetic Oxygen Precipitation as a Source of Vibrationally Excited N_2^+ 1N Emissions Observed at Low Latitudes', *Geophys. Res. Letters* **9**, 543.

Torr, D. G. and Sharp, W. E.: 1979, 'The Concentration of Atomic Oxygen in the Auroral Lower Thermosphere', *Geophys. Res. Letters* **6**, 860.

Torr, M. R. and Torr, D. G.: 1982, 'The Role of Metastable Species in the Thermosphere', *Rev. Geophys. Space Phys.* **20**, 91.

Torr, M. R. and Torr, D. G.: 1985, 'Ionization Frequencies for Solar Cycle 21: Revised', *J. Geophys. Res.* **90**, 6675.

Torr, M. R., Torr, D. G., Ong, R. A., and Hinteregger, H. E.: 1979, 'Ionization Frequencies for Major Thermospheric Constituents as a Function of Solar Cycle 21', *Geophys. Res. Letters* **6**, 771.

Torr, M. R., Torr, D. G., and Eun, J. W.: 1985, 'A Spectral Search for Lyman–Birge–Hopfield Band Nightglow from Spacelab 1', *J. Geophys. Res.* **90**, 4427.

Tousey, R., Purcell, J.D., Austin, W. E., Garrett, D. L., and Widing, K. G.: 1963, 'New Photographic Spectra of the Sun in the Extreme Ultraviolet', *Space Res.* **IV**, 703.

Vallance Jones, A.: 1971, 'Auroral Spectroscopy', *Space Sci. Rev.* **11**, 776.

Vallance Jones, A.: 1974, *Aurora*, D. Reidel Publ. Co., Dordrecht, Holland.

Vallance Jones, A. and Gattinger, R. L.: 1976, 'Quenching of the N_2 Vegard–Kaplan System in Aurora', *J. Geophys. Res.* **81**, 497.

Vallance Jones, A., Meier, R. R., and Shefov, N. N.: 1985, 'Atmospheric Quantal Emissions: A Review of Recent Results', *J. Atmospheric Terrest. Phys.* **47**, 623.

Vaughn, S. O. and Doering, J. P.: 1987, 'Absolute Experimental Differential and Integral Electron Excitation Cross Sections for Atomic Oxygen 3. The $(^3P \rightarrow {}^3D^0)$ Transition (989 Å) from 20 to 200 eV with Improved Values for the $(^3P \rightarrow {}^3S^0)$ Transition (1304 Å)', *J. Geophys. Res.* **92**, 7749.

Victor, G. A. and Dalgarno, A.: 1982, 'The 2145 Å Dayglow and the High Altitude Nitric Oxide Density', *Geophys. Res. Letters* **9**, 866.

Wallace, L. and McElroy, M. B.: 1966, 'The Visual Dayglow', *Planetary Space Sci.* **14**, 677.

Wallace, L., Barth, C. A., Pearce, J. B., Kelly, K. K., Anderson, D. E., Jr., and Fastie, W. G.: 1970, 'Mariner 5 Measurement of the Earth's Lyman Alpha Emission', *J. Geophys. Res.* **75**, 3769.

Watanabe, K.: 1958, in H. E. Landsberg and J. van Mieghem (eds.), 'Ultraviolet Absorption Processes in the Upper Atmosphere', *Advances in Geophysics*, Academic Press, New York.

Weller, C. S. and Meier, R. R.: 1974, 'First Satellite Observations of the He^+ 304 Å Radiation and Its Interpretation', *J. Geophys. Res.* **79**, 1572.

Wells, W. C., Borst, W. L., and Zipf, E. C.: 1971, 'Absolute Cross Section for the Production of $O(^5S^0)$ by Electron Impact Dissociation of O_2', *Chem. Phys. Letters* **12**, 288.

Wells, W. C., Borst, W. L., and Zipf, E. C.: 1976, 'Translational Spectroscopy of Metastable Fragments Produced by Dissociative Excitation of Atmospheric Gases by Electron Impact. I. Nitrogen', *Phys. Rev.* **A14**, 695.

White, O. R.: 1977, *The Solar Output and Its Variation*, Colorado Associated University Press, Boulder.

Wiese, W. L., Smith, M. W., and Glennon, B. M.: 1966, *Atomic Transition Probabilities*, NSRDS-NBS4, Vol. 1, U.S. Government Printing Office, Washington, D.C.

Wight, G. R., van der Wiel, M. J., and Brion, C. E.: 1976, 'Dipole Excitation Ionization and Fragmentation of N_2 and CO in the 10–60 eV Region', *J. Phys. Sect.* **B9**, 675.

Wu, C. Y. R., Chen, J. K., and Judge, D. L.: 1983, 'Atomic Nitrogen Emissions from Photodissociation of N_2', *J. Geophys. Res.* **88**, 2163.

Yelle, R. V. and Wallace, L.: 1989, 'Resonance Line Transfer Calculations by Doubling Thin Layers. I. Comparison with Other Techniques', *Astrophys. J.* **346**, 481.

Yoshino, K. and Tanaka, Y.: 1977, 'High Resolution VUV Absorption Spectrum of N_2, Homogeneous Perturbation Between $c_4'(0)\,{}^1\Sigma_u^+$ and $b'(1)\,{}^1\Sigma_u^+$ Levels', *J. Mol. Spectr.* **66**, 219.

Yoshino, K., Freeman, D. E., Esmond, J. R., and Parkinson, W. H.: 1983, 'High Resolution Absorption Cross Section Measurements and Band Oscillator Strengths of the (1, 0)–(12, 0) Shumann–Runge Bands of O_2', *Planetary Space Sci.* **31**, 339.

Yoshino, K., Freeman, J. R., Esmond, J. R., and Parkinson, W. H.: 1987, 'High Resolution Absorption Cross Sections and Band Oscillator Strengths of the Schumann–Runge Bands of Oxygen at 79 K', *Planetary Space Sci.* **34**.

Yung, Y. L. and Goody, R. M.: 1976, 'Photometric Properties of Io and Their Influence on Line Formation in the Atmosphere', *Icarus* **29**, 57.

Zeippen, C. J. M., Seaton, M. J., and Morton, D. C.: 1977, 'Some O I Oscillator Strengths and the Interstellar Abundance of Oxygen', *Monthly Notices Roy. Astron. Soc.* **181**, 527.

Zipf, E. C. and Erdman, P. W.: 1985, 'Electron Impact Excitation of Atomic Oxygen: Revised Cross Sections', *J. Geophys. Res.* **90**, 11 087.

Zipf, E. C. and Fastie, W. G.: 1964, 'An Observation of the (0, 0) Negative Band of N_2^+ in the Dayglow', *J. Geophys. Res.* **69**, 2357.

Zipf, E. C. and Gorman, M. R.: 1980, 'Electron-Impact Excitation of the Singlet States of N_2, 1, The Birge–Hopfield System $(b\,{}^1\Pi_u - X\,{}^1\Sigma_g^+)$', *J. Chem. Phys.* **73**, 813.

Zipf, E. C. and McLaughlin, R. W.: 1978, 'On the Dissociation of Nitrogen by Electron Impact and by EUV Photoabsorption', *Planetary Space Sci.* **26**, 449.

Zipf, E. C., Kao, W. W., and Erdman, P. W.: 1985, 'On the Simultaneous Ionization-Excitation of the O II (834 Å) Resonance Transition by Electron Impact on Atomic Oxygen', *Planetary Space Sci.* **33**, 1309.

Zipf, E. C., McLaughlin, R. W., and Gorman, M. R.: 1979, 'A Study of the Excitation and Radiative Decay of the $3s'\,{}^3D^0$ and $3d\,{}^3D^0$ Levels of Atomic Oxygen', *Planetary Space Sci.* **27**, 719.